Driving a Strongly Interacting Superfluid out of Equilibrium

Dissertation
zur
Erlangung des Doktorgrades (Dr. rer. nat.)
der
Mathematisch-Naturwissenschaftlichen Fakultät
der
Rheinischen Friedrich-Wilhelms-Universität Bonn

von
Alexandra Bianca Behrle
aus
Friedrichshafen, Deutschland

Bonn, 27.07.2017

Dieser Forschungsbericht wurde als Dissertation von der
Mathematisch-Naturwissenschaftlichen Fakultät der Universität Bonn angenommen
und ist auf dem Hochschulschriftenserver der ULB Bonn
`http://hss.ulb.uni-bonn.de/diss_online` elektronisch publiziert.

1. Gutachter: Prof. Dr. Michael Köhl
2. Gutachter: Prof. Dr. Stefan Linden

Tag der Promotion: 21.12.2017
Erscheinungsjahr: 2018

To my parents and my sister

"Fortunately science, like that nature to which it belongs,
is neither limited by time nor by space.
It belongs to the world, and is of no country and no age.
The more we know, the more we feel our ignorance;
the more we feel how much remains unknown..."

-Humphry Davy,

the discoverer of the element sodium and the eponym of our experiment.

Abstract

A new field of research, which gained interest in the past years, is the field of non-equilibrium physics of strongly interacting fermionic systems. In this thesis we present a novel apparatus to study an ultracold strongly interacting superfluid Fermi gas driven out of equilibrium. In more detail, we study the excitation of a collective mode, the Higgs mode, and the dynamics occurring after a rapid quench of the interaction strength. Ultracold gases are ideal candidates to explore the physics of strongly interacting Fermi gases due to their purity and the possibility to continuously change many different system parameters, such as the interaction strength.

The novel apparatus enabling the experiments outlined below is built from scratch. The setup is described and characterized in detail. We produce a fermionic superfluid of 4×10^6 ^{6}Li atoms at a temperature of $T/T_F = 0.07 \pm 0.02$, where T_F is the Fermi temperature. This is achieved within 23 s by a combination of laser cooling, radio frequency evaporation of ^{23}Na and simultaneous sympathetic cooling of ^{6}Li in an optical plugged magnetic trap and subsequent evaporative cooling of ^{6}Li in a dipole trap.

In this thesis we provide the first experimental evidence of the Higgs mode in a strongly interacting Fermi gas in the crossover from a BCS superfluid to a molecular Bose-Einstein condensate. We develop a novel excitation method, which directly couples to the amplitude of the order parameter. This is achieved by continuously changing the population of one spin component by driving a radio frequency transition to a previously unoccupied third hyperfine state. This effectively modulates the interaction strength and the amplitude of the order parameter. We spectroscopically observe a resonance behavior at twice the gap frequency. For strong coupling, the peak width broadens and eventually the Higgs mode disappears when the Cooper pairs turn into tightly bound dimers signaling the instability of the Higgs mode. It has been suggested [1] that the Higgs mode frequency is a precise measure of the superconducting gap in the BEC-BCS crossover, where the exact value of the gap is yet unknown and numerical calculations are challenging. Hence, our novel method provides a unique technique to determine the superconducting gap.

Moreover, we perform rapid variations of the interaction parameter and vary both the initial interaction strength and the amplitude of the quench. The rapid quenches are performed by rapidly transferring one spin component of a two-component spin mixture into a third state with a different interaction strength by using a radio frequency transition. Using this novel method, we can perform the quenches in half the Fermi time, which is experimentally very close to a sudden change and to date faster than any other research group performing interaction quenches with ultra cold gases. In the experiment, we observe a fast relaxation to a zero order parameter for large quenches, whereas for small quenches we observe, after a sudden drop, a revival of the order parameter and equilibration to a long-term superfluid steady state. Our measurement provides the first evidence of the collapse and subsequent revival of order in a strongly interacting fermionic system.

Parts of this thesis will be published in the following articles:

A. Behrle, T. Harrison, J. Kombe, K. Gao, M. Link, J.-S. Bernier, C. Kollath, and M. Köhl, *Observation of the Higgs mode in a strongly interacting fermionic superfluid* (2017), in preparation.

T. Harrison, A. Behrle, K. Gao, M. Link, and M. Köhl, *Collapse and revival of order in a quenched superfluid* (2017), in preparation.

Contents

CHAPTER 1

Introduction

Fermions are the building blocks of nature. They appear as elementary particles, such as electrons and quarks, or as composite particles, such as protons and neutrons. Composite fermions consist of an odd number of elementary fermions. Their behavior is fundamental to the understanding of the universe and the matter surrounding us. Adding strong interactions to a fermionic system increases their complexity enormously and to date, besides great effort and success of condensed matter research, still only little of their emerging collective behavior is completely understood. Examples for strongly interacting fermionic systems include superconductors, neutron stars, quark-gluon-plasma and ultracold Fermi gases [2–4]. The latter can be realized in the laboratory and are ideal candidates to study strongly interacting fermions experimentally since many system parameters including the interaction strength can be tuned continuously [2]. Furthermore, the purity of such systems allows understanding from first principles. Ultracold Fermi gases thus have great potential to contribute to our understanding of the fundamental physical ground states of such systems.

A new field of research, which gained interest in the past years, is the field of non-equilibrium physics of strongly interacting fermionic systems, which is very challenging to treat theoretically [5, 6]. In this thesis we present a novel apparatus to study an ultracold strongly interacting superfluid Fermi gas driven out of equilibrium. In more detail we study the excitation of a collective mode, the Higgs mode, and the dynamics occurring after a rapid quench of the interaction strength.

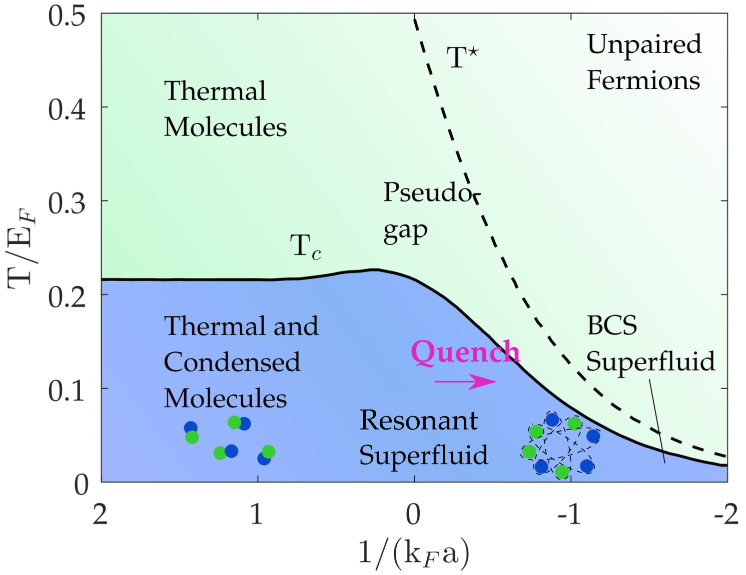

Figure 1.1: Phase diagram of an interacting fermionic spin mixture as a function of temperature and interaction parameter $1/(k_F a)$. The solid line shows the critical temperature T_c, beneath which superfluidity occurs. The formation of pairs starts at higher temperatures, which is denoted by the dashed line and the corresponding temperature $T^\star$. The figure illustrates the crossover from a molecular Bose-Einstein condensate (BEC) to weakly bound Cooper pairs as a function of the interaction parameter $1/(k_F a)$. The purple arrow illustrates a possible quench using our novel technique. The plot is adapted from [7, 8].

An attractively interacting two-component Fermi gas undergoes a second-order phase transition to a superfluid state at a critical temperature [2]. The accompanied decrease in free energy in the superfluid phase is enabled by the formation of pairs between particles of opposite spin. Depending on the interaction strength, there are two different extremes of pairs, either weakly bound Cooper pairs or tightly bound molecules, which can be interpreted as composite bosons. The superfluid physics of Cooper pairs is described by the Bardeen-Cooper-Schrieffer (BCS) theory [9, 10], whereas the superfluid nature of the composite bosons is characterized by the theory of interacting Bose-Einstein condensates (BEC) [11–13]. The crossover between a strongly-interacting Bose-Einstein condensate of dimers and a weakly interacting gas of Cooper pairs is a smooth transition and the non-equilibrium experiments presented in this thesis are performed in this crossover region. The crossover and the phase diagram of an interacting fermionic spin mixture is illustrated in Figure 1.1.

The order parameter indicates the degree of order across a phase transition [14]. Typically, it is zero in the normal phase and ranges from nonzero to a finite value below the critical point of the phase transition. An example of the order parameter is the net magnetization of a ferromagnet, which is zero in the normal phase and finite in the ferromagnetic phase. Phase transitions, which are characterized by more than one parameter, can be described by complex order parameters. In this case, the magnitude of the order parameter is zero in the normal phase and nonzero below the phase transition. One example of a complex order parameter is the order parameter of a superconducting state. Here, the order parameter is related to the density of the superconducting component.

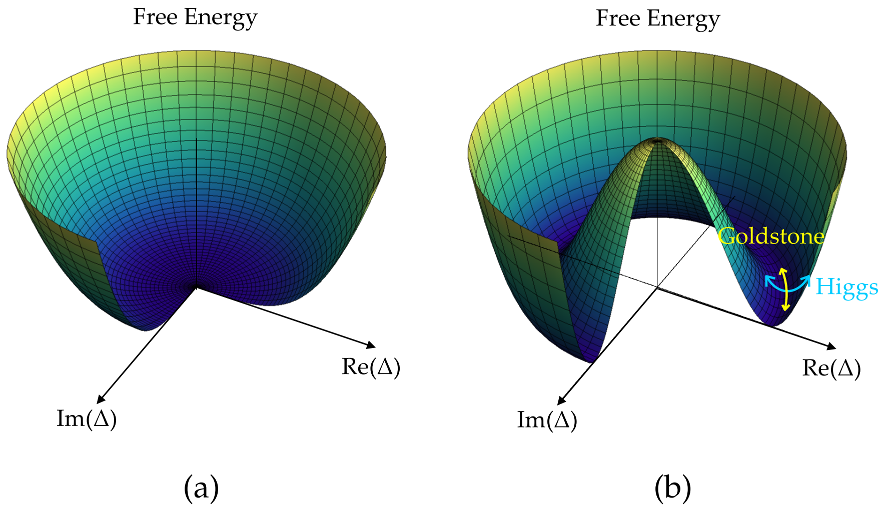

Figure 1.2: Spontaneous breaking of a continuous symmetry. **(a)** Free energy of a system in the normal phase as a function of the real and imaginary part of the complex order parameter Δ. **(b)** Mexican hat potential of the free energy in the superconducting state. The order parameter of the equilibrium state spontaneously takes one of the values at the energy minimum. Two collective modes arise: a Goldstone mode (yellow curve) varying the phase of the order parameter and a Higgs mode (blue curve) altering its amplitude.

The phase transition from a normal to superfluid state is accompanied with a change in the potential landscape of the free energy [14] describing the system as illustrated in Figure 1.2. Here, the free energy is plotted as a function of the real and imaginary part of the complex order parameter Δ. Above the critical temperature, the system is in the normal state (Figure 1.2 (a)) and its thermal equilibrium state (the minimum of the potential) is described by a vanishing order parameter Δ. The system is U(1) symmetric. Below the critical temperature, the continuous symmetry is spontaneously broken as the steady state is now given by an arbitrary point along the circle of the Mexican hat potential with minimum energy. The order parameter of this state is defined by an amplitude, which is different from zero and a phase depending on the position along the minimum of the potential. Besides characterizing the order of the superconducting state, Δ describes the gap in the single-particle spectrum of the superconductor.

Starting from the equilibrium state below the critical temperature, two possible collective modes arise: the Higgs and the Goldstone mode [5]. The Goldstone mode is gapless and describes variations of the phase of the order parameter, which correspond to fluctuations along the minimum of the potential. In contrast, the Higgs mode is gapped and alters the amplitude of the order parameter, which corresponds to radial fluctuations in the Mexican hat potential.

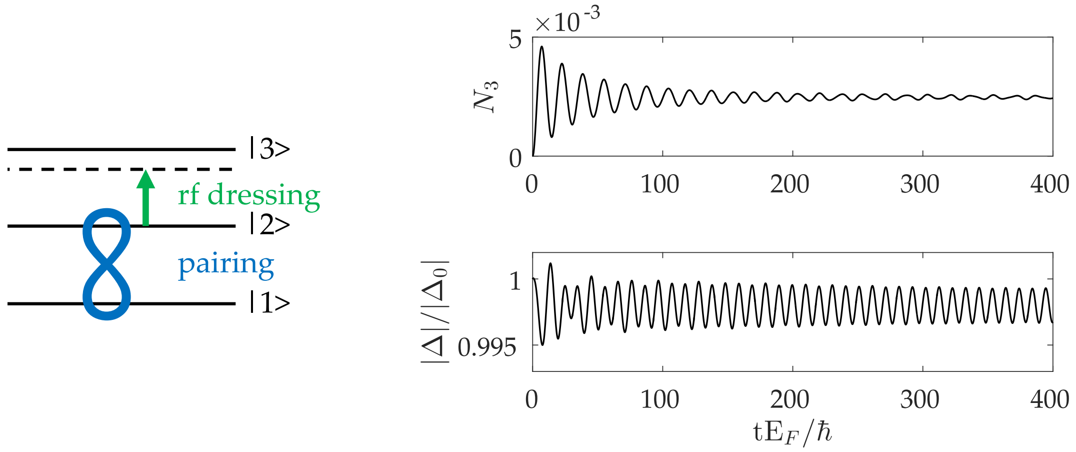

(a)

(b)

Figure 1.3: Higgs mode excitation scheme. **(a)** The excitation scheme employs a radio frequency (rf) field dressing of the $|2\rangle$ state with the initially unoccupied hyperfine state ($|3\rangle$ state) thereby modulating the pairing between the states $|1\rangle$ and $|2\rangle$. **(b)** Top: Theoretically modeled population of the $|3\rangle$ state N_3 during the modulation time (see chapter 9). The amplitude of the oscillation is only half a percent of the population of either the $|1\rangle$ state or the $|2\rangle$ state. The decay of the amplitude with time is due to dephasing induced by many-body physics. Bottom: Time evolution of the amplitude of the order parameter induced by the rf dressing shown in **(a)**.

In this thesis we provide the first experimental evidence of the Higgs mode in a strongly interacting Fermi gas in the crossover from a BCS superfluid to a molecular Bose-Einstein condensate. We prepare a spin mixture of ultracold fermionic lithium atoms in a three-dimensional harmonic trap and develop a novel excitation method, which couples directly to the amplitude of the order parameter Δ. The excitation scheme, shown in Figure 1.3 (a) employs a radio frequency (rf) field dressing of the $|2\rangle$ state with the initially unoccupied hyperfine state ($|3\rangle$ state) thereby modulating the pairing between the states $|1\rangle$ and $|2\rangle$. This effectively modulates the interaction strength and the amplitude of the order parameter Δ as illustrated in Figure 1.3 (b). We spectroscopically observe a resonance behavior at twice the gap frequency ($2\Delta/h$, where h is the Planck constant). This resonance behavior broadens for increasing interaction strength signaling the disappearance of the Higgs mode when Cooper pairs turn into strongly bound dimers. In addition, we show experimentally that our novel excitation scheme couples directly to the amplitude of the order parameter and does not create single-particle excitations.

While a Goldstone mode appears necessarily when a continuous symmetry is broken, the Higgs mode, however, requires an additional symmetry to prevent decay mechanisms of collective excitations to lower lying modes, such as the Goldstone mode. The probably best known example of a Higgs mode appears in the Standard Model of particle physics giving elementary particle their mass [15]. After decades of intensive research the existence of the Higgs boson was finally proven experimentally by [16, 17] completing the electro-weak theory of the Standard Model of particle physics. The stability of the Higgs mode in particle physics is ensured by Lorentz invariance. In the context of condensed-matter physics, this role can be taken over by particle-hole symmetry [18]. An example of a particle-hole symmetric system hosting a stable Higgs mode is the Bardeen-Cooper-Schrieffer (BCS) model, which describes weakly interacting superconductors [18, 19]. In a Fermi sea of weakly interacting Cooper pairs the addition of a quasiparticle compared to a hole does not change the physics of the system, hence it is particle-hole symmetric. In contrast, the addition of a quasiparticle to a strongly interacting cloud of dimers on the BEC side is not symmetric to addition of a quasihole. The quasiparticle can interact with the dimers, whereas the hole cannot.

In the context of condensed matter, the existence of the Higgs mode in weakly interacting superconductors and conventional BCS superconductors [20–22] has been proven experimentally. Yet, the excitation mechanisms have only been indirect. By exciting other modes, such as the charge density wave mode in a superconductor [23], spectral weight is transferred to the Higgs mode, which can be detected by Raman scattering. In contrast, in the realm of strongly correlated superconductors particle-hole symmetry is not precisely fulfilled. The question whether a stable Higgs mode exists in such systems has been subject of numerous discussions [1, 5, 24–27]. Moreover, the Higgs mode has been observed in systems such as antiferromagnets [28], liquid ^{3}He [29], ultracold bosonic atoms near the superfluid/Mott-insulator transition [30, 31], spinor gases [32] and Bose gases strongly coupled to optical fields [33]. However, weakly interacting Bose-Einstein condensates do not show a stable Higgs mode as particle-hole symmetry is not fulfilled.

For the understanding of an interacting many-body system it is fundamental to understand the excitation spectrum and the fundamental modes of the system. To date, it is impossible to answer these questions for strongly interacting fermionic systems from a theoretical point of view as the theoretical treatment is too complex and experiments are necessary to provide evidence of their existence. Our experiment proves the existence of the Higgs mode in a strongly interacting fermionic gas for the first time by employing a direct coupling scheme. Furthermore, the Higgs mode was proposed to be a good measure of the gap parameter. Hence, our method can give insight into the evolution of the gap in a system driven out of equilibrium and into spin-imbalanced systems. Moreover, our findings provide a route to better understand strongly-correlated superconductors, the lifetime of the Higgs mode and its decay mechanism, which is also important for elementary particle physics, where the existence of particles is often proven by the detection of the remaining particles after a decay.

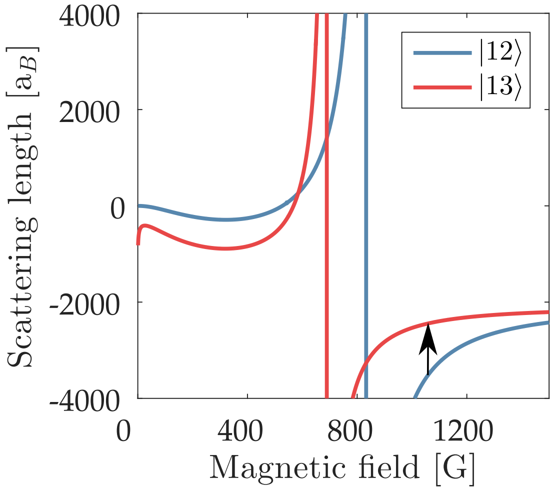

Figure 1.4: Illustration of experimental technique for performing interaction quenches. The figure shows the scattering length of different spin mixtures of the three lowest hyperfine states of ^{6}Li as a function of an external magnetic field. The black arrow illustrates the population transfer and shows the change in scattering length when performing such a spin-flip. The data is taken from [34].

Motivated by our novel excitation technique to modulate the order parameter and to excite the Higgs mode, we further investigate the regime of rapid quenches of the order parameter and subsequent dynamics. This is illustrated in Figure 1.1 and Figure 1.4. The phase diagram of an interacting fermionic spin mixture as a function of temperature and the interaction parameter $1/(k_F a)$ is shown in Figure 1.1. We prepare our sample in a superfluid state beneath the critical temperature T_c and rapidly change the interaction parameter $1/(k_F a)$. This is indicated by the purple arrow. The quenches are performed by rapidly transferring one spin component of a two-component spin mixture into a third state by using a radio frequency transition, see Figure 1.4 (b). Due to the different interaction strengths between the different spin mixtures, we can rapidly change the interactions between the particles. Previously, such quenches were proposed by changing the magnetic field in proximity of a Feshbach resonance. Experimentally, the necessary changes of the magnetic field cannot be performed faster than the internal time scales of the system due to eddy currents in the vacuum chamber. The relevant time scale in the strongly interacting regime is the Fermi time, which sets the time scale for collision rates and thermalization and which is for our system approximately 50 µs. Using our novel method, we can perform the quenches in half the Fermi time, which is experimentally very close to a sudden change and to date faster than any other research group performing interaction quenches with ultra cold gases. Moreover, we vary both the initial interaction strength and the amplitude of the quench.

In general, quantum mechanical quenches of the order parameter provide insight into the energy spectrum of the system's Hamiltonian and the time scales, in which the system responds to changes. In addition, time-dependent amplitudes of the quantum state can interfere during the evolution and - provided the coherence time is long enough - interference can lead to a revival of the order. Collapse and revival of the matter wave field have been observed in Bose–Einstein condensates [35].

Volkov and Kogan [36] showed in 1973 that the order parameter of a BCS superconductor exhibits oscillations with a power law decay when the system is brought out of equilibrium by a small perturbation. In the mid-2000s their work was extended to different interacting regimes and long time scales after the quench [6, 37–39]. However, for strong interactions and non-integrable systems these models are not completely applicable and major questions are still to be answered.

In our experiment we observe a fast relaxation of the initially finite order parameter to zero for large quenches, whereas for small quenches we observe, after a sudden drop, a revival of the order parameter and equilibration to a long-term superfluid steady state. This revival of the order parameter can be connected with a critical quench parameter. This signalizes the possible interpretation of a dynamical quantum phase transition [40]. A dynamical phase transition indicates a non-analytical behavior at a critical point in time, similar to a temperature driven phase transition, where this behavior occurs in the free energy density at a critical temperature. Our measurement provides the first evidence of a collapse and subsequent revival of order in a strongly interacting fermionic system. In addition, we observe that the time scale of the initial sudden drop depends on the amplitude of the quench. For large quenches the decay follows h/Δ, whereas for small quenches the decay follows the quasiparticle relaxation time. Hence, our experiments provide insight into the intrinsic mechanisms occurring after a sudden interaction quench and study a strongly interacting Fermi gas driven out of equilibrium.

Thesis Structure

The non-equilibrium experiments presented in this thesis have been conducted in a novel apparatus for ultracold gases. Hence, a major part of this thesis explains the experimental setup, which was newly designed and built from scratch. To start with an introduction to the scattering properties of ultracold gases and an explanation how the interaction between atoms can be tailored by means of a Feshbach resonance is given in chapter 2. This is not only important for the investigation of the Higgs mode across different interactions but also for the interaction quenches explained afterwards.

We present the vacuum system, the laser system, the trap and cooling strategies necessary to exploit the variety of strongly interacting fermionic superfluids in chapter 3-chapter 8. In order to meet the experimental challenge to cool, trap and manipulate two different atomic species simultaneously, we designed the vacuum system presented in chapter 3. In the following chapter 4 we demonstrate how a stable laser cooling system was achieved at first stage with a variable pitch spin-flip Zeeman slower providing high atomic fluxes and at second stage inside a magneto-optical trap containing higher or comparable atom number than other groups. The laser setups to cool, trap, manipulate and image both our species are presented as well. After the atoms have been laser cooled, they are transferred to the magnetic trap, which is outlined in chapter 5. We demonstrate efficient radio frequency evaporation of sodium atoms ^{23}Na in an optically plugged magnetic trap in only 5 s and simultaneous sympathetic cooling of lithium ^{6}Na. Further cooling of lithium is achieved by preparing a spin mixture of the two lowest hyperfine states after they have been transferred from the magnetic trap to an optical dipole trap. Subsequent enhancing of the scattering length by means of a Feshbach resonance and lowering of the dipole trap potential allows for efficient evaporation and cooling the cloud to quantum degeneracy in chapter 6.

The last two technical chapters describe the magnetic field coils and radio frequency coils (chapter 7) and the detection methods (chapter 8). The sophisticated design of the radio frequency coils allowing rapid quenches of the interaction parameter is presented in chapter 10. In addition, we show how we measure our main observable, the condensate fraction, using the established rapid ramp technique, which gives a measure of the order parameter of the system.

After the preparation of our ultracold gas chapter 9 tochapter 11 show the main scientific results of this thesis. In chapter 9 we present the first observation of the Higgs mode in a strongly interacting Fermi gas. We exploit a spectroscopic method to excite and detect the Higgs mode. Further results were achieved on non-equilibrium dynamics of a strongly interacting Fermi gas. By quickly changing the interaction strength using fast radio frequency transfers we are able to explore different regimes of the quench phase diagram for the first time as presented in chapter 10 and chapter 11. Figure 1.5 illustrates an atom's way through the experiment and aims to guide the reader through this thesis.

The work presented in this thesis was carried out in close collaborations with Timothy Harrison, Kuiyi Gao and Martin Link.

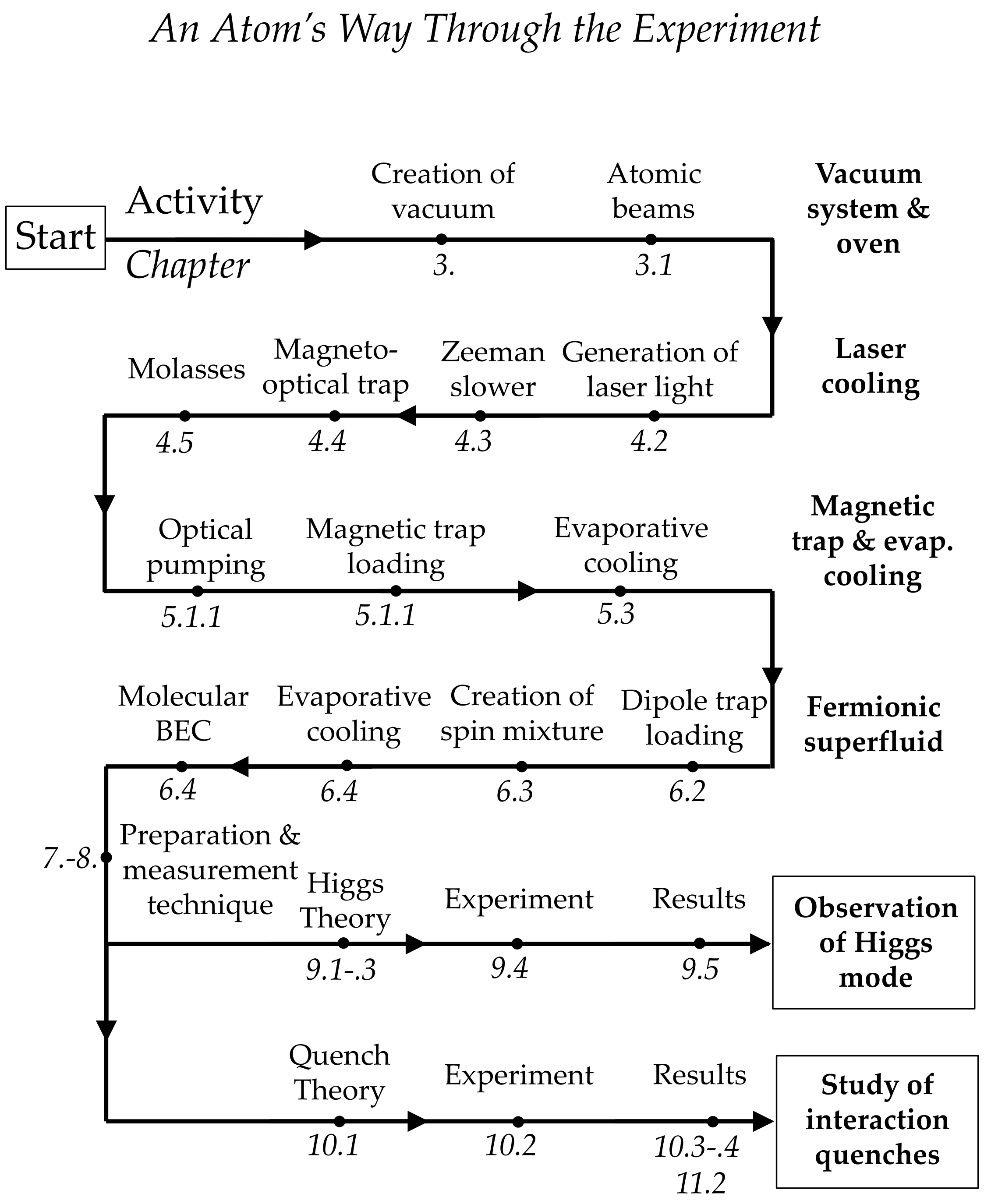

Figure 1.5: Illustration of an atom's way through the experiment. This figure aims to guide the reader through this thesis

CHAPTER 2

Ultracold Atoms and Their Scattering Properties

The state of a particle is described by its internal and external degrees of freedom. The internal state is given by the electronic (hyperfine) state and even at room temperature atoms are usually in their internal electronic ground state. The behavior of the external state depends on the confining potential and temperature and is for example specified by the kinetic energy. Classically, the statistics of an ideal gas is described by the Maxwell-Boltzmann distribution [41]. An ideal gas consists of randomly moving particles, which can only undergo perfect elastic collisions. However, at low temperature quantum statistics come into play and the nature of the particles becomes important. One distinguishes between two different kinds of particles, between bosons and fermions. If the wavefunction of a system is symmetric under particle exchange, the particles are called bosons. They carry an integer spin. In contrast, if the wavefunction is anti-symmetric under particle exchange, the particles are called fermions. They carry half integer spin.

In our experiment we work with both kinds, namely sodium ^{23}Na and lithium ^{6}Li. ^{23}Na obeys Bose-Einstein statistics, whereas ^{6}Li follows the Fermi-Dirac statistics. The distinction between fermionic lithium and bosonic sodium is due to the fact that the total spin of all constituents of ^{6}Li (three protons, three neutrons and one valance electron) is half integer. In the same way, the addition of spins of the individual components of ^{23}Na results in a total integer spin.

Their occupation probability (for an ideal non-interacting gas) is given by [42]

$$f_{B,F}(E,T) = \frac{1}{e^{(E-\mu)/k_B T} \mp 1} \quad . \tag{2.1}$$

Here, E is the energy, T the temperature, μ the chemical potential and k_B is the Boltzmann constant.

For a system containing identical fermions at zero temperature each energy states is occupied with a single particle (due to the Pauli exclusion principle) up to the Fermi energy E_F. In case of a harmonic trap each confining direction can be associated with a trapping frequency ω_i ($i = x, y, z$). Together with the atom number N the Fermi energy is then given by [43]

$$E_F = (6N)^{1/3} \hbar (\omega_x \omega_y \omega_z)^{1/3} \quad . \tag{2.2}$$

This equation defines the energy necessary to add another particle to the system. At finite temperature the occupation softens around the Fermi surface and higher states can be occupied. On the contrary, bosons in their ground state at low but finite temperatures all occupy the same state and form a Bose-Einstein condensate.

2.1 Scattering Between Ultracold Atoms

In order to create a molecular Bose-Einstein condensate it is essential to understand the principles of ultracold atoms interaction and the impact on the required cooling techniques. Therefore, this section gives a brief outline about scattering processes in quantum mechanics. A more detailed introduction can be found in [44–46]. The next section explains how the interaction strength can be tuned, which is crucial in the experiments presented in this thesis.

Quantum mechanically the scattering process is described by the corresponding Schrödinger equation in center-of-mass coordinates with distance vector $\mathbf{r}$ (with $r = |\mathbf{r}|$), reduced mass $m/2$ and potential $V(\mathbf{r})$

$$\left(\nabla^2 + k^2\right) \psi_{\mathbf{k}}(\mathbf{r}) = v\left(r\right) \psi_{\mathbf{k}}(\mathbf{r}) \quad \text{with} \quad k^2 = \frac{mE}{\hbar^2} \quad \text{and} \quad v\left(r\right) = \frac{mV\left(r\right)}{\hbar^2} \quad . \tag{2.3}$$

The incoming wavefunction is typically simplified by a plane wave with momentum $\mathbf{k}$. At long distances relative to the characteristic length scale of the scattering potential, the wavefunction of the outgoing wave can be described by an spherical scattered wave in the direction $\mathbf{k'}$ [46]

$$\psi_{\mathbf{k}}(\mathbf{r}) \sim e^{i\mathbf{k}\cdot\mathbf{r}} + f(\mathbf{k'},\mathbf{k})\frac{e^{ikr}}{r} \quad , \tag{2.4}$$

where $f(\mathbf{k'},\mathbf{k})$ describes the scattering amplitude. For a radial symmetric potential the scattering amplitude can be expanded into partial waves with angular momentum l (see for example [44]). In the long wavelength or low energy limit only the lowest angular momentum state $l = 0$ contributes [44, 45], which is called s-wave scattering. It can be shown that a phase shift δ [44] between scattered and unscattered wave occurs. In addition, this phase shift scales linearly with the wavevector amplitude and the ratio

$$a := -\lim_{k \ll 1/r_0} \frac{\tan \delta_{l=0}(k)}{k} \tag{2.5}$$

is called the scattering length. A positive scattering length describes a repulsive scattering potential, whereas an attractive interaction potential results in a negative scattering potential.

The thermal de Broglie wavelength ($\lambda_{dB} = h/\sqrt{2\pi m k_B T}$, here h is the Planck constant and m the mass) and the interparticle distance of ultracold colliding particles is large compared to the range of the scattering potential, which is the Van der Waals potential [47]. Hence, the details of the scattering potential are not resolved. In the low energy limit, where s-wave scattering is the dominant process, the scattering event is specified by a single parameter, the scattering length a. In order to obtain qualitative information, the calculations of the scattering process can be simplified by replacing the interaction potential by a pseudopotential V, which acts as an effective interaction potential and is not dependent on the microscopic properties of the system but gives the correct results. This pseudopotential can be written as [48]

$$\hat{V}\psi(\mathbf{r}) = g\delta(\mathbf{r})\frac{\partial}{\partial r}\left[r\psi(\mathbf{r})\right] \quad , \tag{2.6}$$

where g is the interaction parameter. Using this pseudopotential in the Schrödinger equation it can be shown [48] that the corresponding s-wave scattering length is given by $a = mg/(2\pi\hbar^2)$

In case of s-wave scattering the orbital wavefunction of the two colliding particles is symmetric. As the total wavefunction of two fermions is anti-symmetric, the total wavefunction of the spin has to be anti-symmetric (the fermions have to be in two different spin states and hence are distinguishable). A result of this consideration is that collisions and hence thermalizations between identical fermions is not possible in the low temperature limit. Thermalization and cooling is therefore only possible by for example adding a second species (sympathetic cooling, section 5.3) or by making the atoms distinguishable through their internal state (section 6.3).

2.2 Feshbach Resonances

Feshbach resonances in fermionic gases offer a powerful tool to explore the versatility of differently interacting systems. For example by increasing the scattering length thermalization can be enhanced, allowing for quick thermalization during evaporative cooling. In contrast to bosonic gases, the molecules close to resonance are stable, which is a result of the Pauli principle [49].

For a given interatomic potential the background scattering length a_{bg} is a fixed quantity. However, in case of resonant scattering the scattering length can be dependent on the magnetic field and it can be tuned from large negative to large positive values in the vicinity of a Feshbach resonance. This phenomenon is explained in more detail in this section using the Feshbach resonance of ^{6}Li as an example.

At high magnetic fields (B$\gtrsim$ 140 G) the electronic and the nuclear spin of the ground state are decoupled. In addition, the orbital angular momentum quantum number of alkali atoms L in the ground state is equal to zero. Hence, the three lowest states in lithium have the same electronic spin (m$_s$=-1/2, see Figure 5.1) and a spin mixture of two of these states is in a triplet configuration. This is illustrated in Figure 2.1. Two incoming colliding particles have aligned spins with an energy E$_c$. Usually the triplet state cannot couple to the singlet state as the continuum of the singlet state lies at higher energies (that is the reason why it is called closed channel). However, if the triplet state is brought to resonance with a bound state of the singlet state, coupling between these two states can lead to an enhancement of the scattering length. The total spin of the colliding atoms $F_{total} = L_{total} + S_{total} + I_{total}$ is a conserved quantity during the scattering process ($L_{total} = 0$ for alkali atoms in their ground state). In contrast, the total electronic spin $S_{total} = S_1 + S_2$ and the total nuclear spin $I_{total} = I_1 + I_2$ do not have to be conserved separately. As a consequence, the electronic spin can flip from a triplet into a singlet state. The energy difference between the two states depends on the magnetic field value and the difference of their magnetic moments. The spins of the singlet states are anti-aligned and therefore have a negligible net magnetic moment. In contrast, the aligned spins of the triplet state have a net magnetic moment and its energy can be tuned due to the Zeeman shift with an external magnetic field and thus can be brought into resonance with the closed channel.

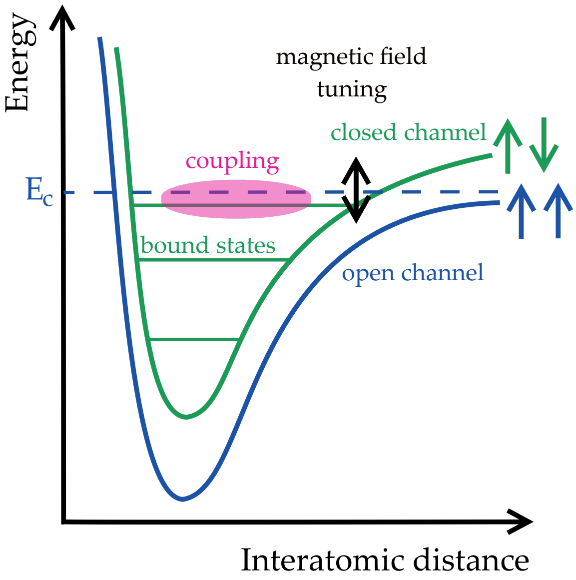

Figure 2.1: Interatomic potential of two colliding particles, which are initially in the triplet state (open channel). By tuning an external magnetic field the triplet state can be brought to resonance with a bound state of a closed singlet state. Coupling between these two states leads to an enhancement of the scattering length.

The dependence of the scattering length on the magnetic field can be expressed as [46]

$$a(B) = a_{bg}\left(1 - \frac{\Delta B}{B - B_0}\right) \quad , \tag{2.7}$$

where a_{bg} describes the scattering length resulting from collision processes solely in the open channel, ΔB is the width of the resonance and B_0 the resonance position. The width of the resonance depends on the coupling strength g, the difference in magnetic moment $\Delta\mu$ and the background scattering length a_{bg} through $\Delta B \propto g^2/(\Delta\mu\, a_{bg})$.

Due to its broad Feshbach resonances, ^{6}Li is an ideal candidate to explore different interaction regimes in the laboratory. The resonances are located at around 800 G and a width of $100 - 300$ G (depending of the spin mixture used) allows experimental fine tuning of the scattering length. In addition, due to the broad feature of the resonance, the stability and reproducibility of the magnetic field is not as critical as in experiments with ^{40}K, where the resonance (at $\sim$ 200 G) is only ten's of Gauss wide.

Figure 2.2 shows the scattering length of ^{6}Li for different spin mixtures of the three lowest states in the vicinity of the Feshbach resonance located at 800 G. This plot shows an important property of lithium, which is used in the experiments described in chapter 10 and chapter 11: if a spin mixture is prepared at a certain field and it is suddenly transferred into a different spin mixture, the scattering length and thereby the interaction between the particles is changed. A huge advantage of this technique is the fast time scale on which this change of interaction strength can be performed on. To be more precise, we can complete this transfer within 20 μs, whereas magnetic field changes take much longer (100 G in 50 μs), which is due to induced currents in the steel chamber.

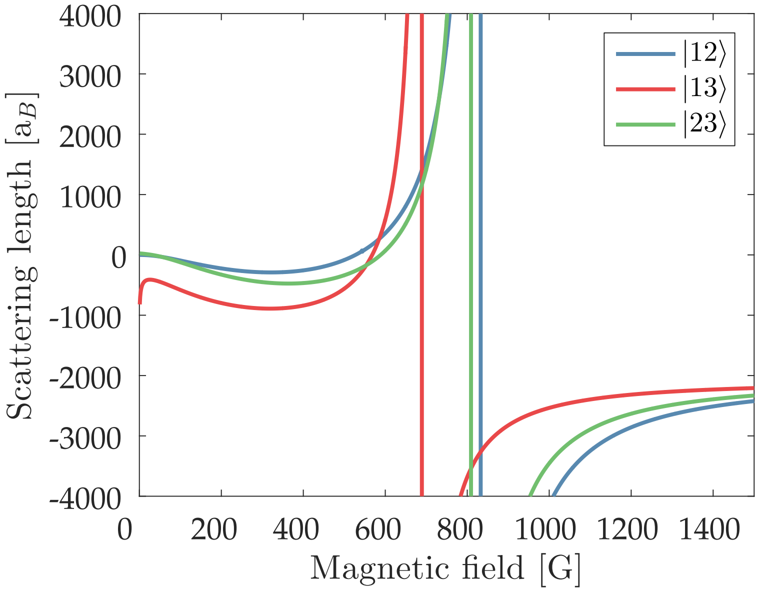

Figure 2.2: Scattering length of different spin mixtures of the three lowest hyperfine states of ^{6}Li as a function of an external magnetic field at the Feshbach resonance at 690 G for $|13\rangle$, 811 G for $|23\rangle$ and 834 G for $|12\rangle$. The data is taken from [34].

2.3 The BEC-BCS Crossover

The results presented in chapter 9 to chapter 11 has been performed in the crossover between a Bose-Einstein condensate (BEC) of dimers and a BCS (Bardeen-Cooper-Schrieffer) superfluid. At zero temperature this crossover describes the continuous transition from a molecular Bose-Einstein to a superfluid gas of Cooper pairs. These pairs consist of two particles with opposite momentum and spin. The phase diagram as a function of the dimensionless interaction parameter $1/(k_F a)$ and temperature is depicted in Figure 2.3. In fact, the interaction parameter depends on the Fermi wavevector k_F, which is related to the Fermi energy by $E_F = \hbar^2 k_F^2/(2m)$, and on the scattering length a. The scattering length can be changed by means of a Feshbach resonance as explained in section 2.2. As the Fermi wavevector depends on the Fermi energy it can be changed in our experiment by changing the atom number or trapping frequencies (see Equation 2.2). Changing these two parameters together with the temperature allows accessing different regimes of the phase diagram presented in Figure 2.3. The solid line shows the critical temperature T_c beneath which superfluidity occurs. Above T_c the gas is a normal Bose gas of dimers, which dissociate at the temperature $T^\star$.

At low temperature $T < T_c$ on the BEC side of the resonance ($1/(k_F a) > 0$) a bound state exists and the atoms can form molecules. The size of the molecules is much smaller than the interparticle distance and the molecules condense into a Bose-Einstein condensate. Close to resonance $1/(k_F a) \sim 0$, called the unitary regime, the pairs are strongly interacting and their size is of the order of the interparticle spacing. In this region the only relevant time scale setting for example the scattering rate, is the Fermi time $\tau_F = \hbar/E_F$ and the relevant energy scale is the Fermi energy. Far on the BCS side (($1/(k_F a) << 0$) pairing is a many-body effect and the pair size is much bigger than the inter particle distance. At low temperature this leads to the formation of pairs in momentum space [50] (Cooper pairs), which are responsible for superfluidity in this region. A full description of this system was developed by Bardeen, Cooper and Schrieffer [9] in 1957, the BCS theory.

The region where $-1 < 1/(k_F a) < 1$ is the strongly interacting regime and often called the crossover region. As the scattering length diverges the only relevant energy scale is the Fermi energy E_F and the corresponding time scale $\tau_F = h/E_F$. Most of the experiments described in this thesis (chapter 9, chapter 10 and chapter 11) are conducted in the strongly interacting regime. The transition between the state where pairing occurs in real space (BEC) to a state where pairing exists in momentum space (BCS) is a smooth crossover. This was first realized by Leggett [51] (built on work of Popov [52], Keldysh [53] and Eagle [54]). First experimental realizations of gases in the crossover region were achieved between 2004-2005 [55–61].

Figure 2.3 shows another feature of the BEC-BCS crossover, which is important for the out-of-equilibrium dynamics studied in chapter 10 and chapter 11. Assuming the temperature is kept constant and $1/(k_F a)$ is changed rapidly one can rapidly cross the phase transition. Systems, which are initially in the superfluid regime can be quenched to a state, which at equilibrium would not be superfluid. When the quenches happen much faster than all internal time scales interesting dynamics can be studied, see chapter 10. Also systems initially in the normal state can be quenched into the superfluid regime and the formation of a condensate can be observed (chapter 11).

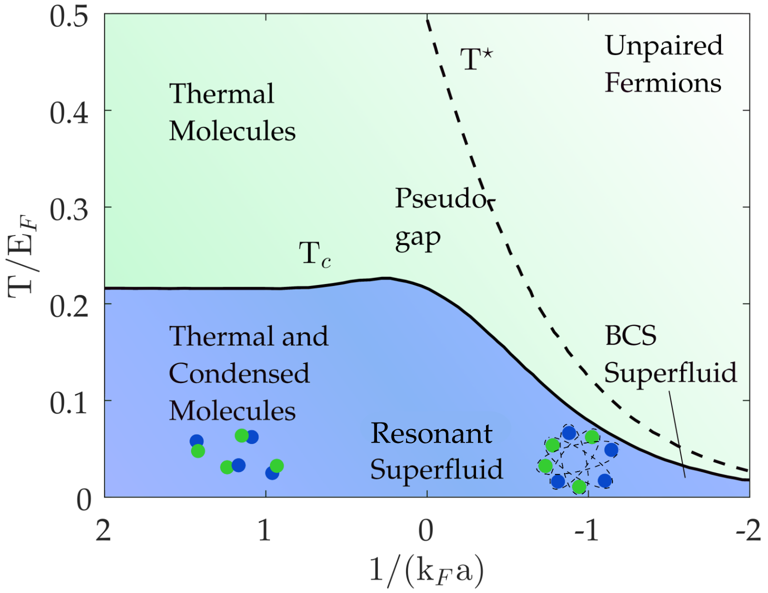

Figure 2.3: Illustration of the phase diagram of an interacting fermionic spin mixture as a function of temperature and interaction parameter $1/(k_F a)$. The solid line shows the critical temperature T_c beneath which superfluidity occurs. The formation of pairs starts at higher temperatures already, which is denoted by the dashed line and the corresponding temperature $T^\star$. This plot is adapted from [7, 8].

A detailed description of the BEC-BCS crossover can be found in [14, 46, 62, 63] (and references therein). In the following section both regimes, the BEC and the BCS region, are discussed further.

2.3.1 Molecular BEC

On the BEC side of the Feshbach resonance, where the scattering length is positive ($a > 0$), a molecular bound state exists, which can be populated by two fermions with different spin states. The binding energy is given by [46]

$$E_b = -\frac{\hbar^2}{m\,a^2} \quad . \tag{2.8}$$

If the binding energy is higher than the energy scale defined by the temperature and if the pair size is small, the molecules behave like point-like bosons and below the critical temperature T_c they form a Bose-Einstein condensate.

The high scattering cross section close to the resonance results in a fast thermalization of the sample. This is used in our experiment during evaporation of the spin mixture in the dipole trap. In addition, molecules are formed during the evaporation process. Due to the higher polarizability of molecules (twice as high as for single atoms), molecules experience a deeper trapping potential than single atoms and preferably stay in the trap while single atoms are evaporated from the trap. If the temperature is low enough, a Bose-Einstein condensate of tightly bound molecules is formed. After the release from the trap and free expansion the atomic distribution shows the distinct feature of a BEC, the bimodal momentum distribution with a dense central core and a low density Gaussian distribution of thermal molecules (see Figure 6.7).

2.3.2 Cooper Pairs: The BCS Region

On the BCS side of the resonance, where the scattering length is negative and ($1/(k_F a) \ll -1$), pair formation is a many-body phenomenon. The Hamiltonian, which describes this system is given by [14, 63]

$$H_{BCS} = \sum_{k,\sigma} \epsilon_k c^\dagger_{k,\sigma} c_{k,\sigma} + \frac{g}{V} \sum_{k,q} c^\dagger_{q,\uparrow} c^\dagger_{-q,\downarrow} c_{-k,\downarrow} c_{k,\uparrow} \quad , \tag{2.9}$$

where $\epsilon_k = \hbar^2 k^2 / (2m)$ is the single-particle dispersion. The operator $c^\dagger_{k,\sigma}$ ($c_{k,\sigma}$) creates (annihilates) a fermion with spin σ and momentum k. The interaction strength is given by g and V is the volume. The first term describes the free energy of the particle and the second term characterizes the interaction. A closer look at the second term shows that pairs with different spin and different momentum are formed. This Hamiltonian is an approximation as only pairs with vanishing total momentum are considered, which eliminates density fluctuations. However, pairs with zero total momentum are the main contributors of the superfluid. Assuming a spin mixture of two different states and introducing a mean field decoupling [14] with an order parameter

$$\Delta = \frac{g}{V} \sum_k \langle c_{-k,\downarrow} c_{k,\uparrow} \rangle \tag{2.10}$$

leads to the following simplified Hamiltonian

$$H^{mf}_{BCS} = \sum_k \epsilon_k \left(n_{k,\uparrow} + n_{k,\downarrow} \right) + \sum_k \left\{ \Delta^\star c_{-k,\downarrow} c_{k,\uparrow} + \Delta c^\dagger_{k,\uparrow} c^\dagger_{-k,\downarrow} \right\} \quad . \tag{2.11}$$

Here, $n_{k,\uparrow(\downarrow)}$ denotes the number of atoms with momentum k and spin $\uparrow$ $(\downarrow)$. The BCS order parameter Δ is an important parameter throughout this thesis. It is zero in the normal phase and finite in the superfluid phase and can be expressed in experimental accessible parameters [46] within the mean-field frame work presented above

$$\Delta_{\mathrm{BCS}} = \frac{8}{e^2} e^{-\pi/(2k_F|a|)} \quad . \tag{2.12}$$

In addition, in a simplified picture it specifies the binding energy of the Cooper pair and from Equation 2.12 it can be seen that the further the system resides in the BCS regime, the more loosely the pairs are bound. This challenges the experimental detection of BCS pairs as they can easily break when the cloud is released from the trap for time-of-flight imaging. A solution to this problem is explained in section 8.2.

A more accurate description of the order parameter Δ for the BEC-BCS crossover can be found within the solution of the time-dependent Bogoliubov-de Gennes equations [1]

$$\Delta = \tilde{g} \sum_\eta u_\eta v^\star_\eta \quad . \tag{2.13}$$

The interaction parameter $\tilde{g}$ is defined via the relation $1/(k_F a) = 8\pi E_F/(\tilde{g} k_F^3) + \sqrt{4E_c/(\pi^2 E_F)}$, where E_c is a cutoff energy avoiding the ultraviolet divergence in the Bogoliubov-de Gennes equation with contact potentials. We use this relation to calculate the order parameter Δ in chapter 9 to chapter 11.

The ground state wavefunction of a BCS state is given by [14]

$$|\phi_{\mathrm{BCS}}\rangle = \prod_k \left(u_k + v_k c^\dagger_{k,\uparrow} c^\dagger_{-k,\downarrow}\right) |0\rangle \quad . \tag{2.14}$$

The probabilities $|u_k|^2$ and $|v_k|^2$ describe whether a Cooper pair with momentum k is empty or occupied. Within mean-field BCS theory the critical temperature is proportional to the order parameter and it is given by

$$T_{c,\mathrm{BCS}} = \frac{1.78}{\pi} \Delta_{\mathrm{BCS}} \quad . \tag{2.15}$$

Usually the critical temperature is low due to the exponential factor. However, close to unitary $|k_F a| \sim 1$ temperatures below $T_{c,\mathrm{BCS}}$ can be realized in the experiment. For example, at $|k_F a| = 1$ the critical temperature is $T_c \approx 0.2\, T_F$ (see Figure 2.3) and clouds as cold as $0.06\, T_F$ can be prepared (chapter 6).

To summarize, this chapter explains how the interaction between spin mixtures of fermions can be changed using resonant scattering. This occurrence of enhanced scattering is called a Feshbach resonance. By changing the scattering length different regions of the BEC-BCS crossover can be accessed. In addition, parameters such as the order parameter have been defined, which are important throughout the thesis.

CHAPTER 3

Vacuum System

In order to achieve ultra low temperatures and to study Bose-Einstein condensates and ultracold degenerate Fermi gases, it is necessary to isolate the atomic sample from its environment. This is done by levitating the atoms inside an ultra high vacuum chamber by trapping them magnetically or optically (see chapter 5 and section 6.1). The trapped atoms can couple to the environment by thermal radiation, fluctuations of the trapping potential or by collisions with the background gas [64]. Indeed, background gas collisions are the main limiting factor of the lifetime of the atoms in the trap. Therefore, it is necessary to establish ultra high vacuum in proximity of the trap. Pressures of $< 10^{-11}$ mbar have to be reached in order to have a reasonable lifetime and to be able to perform experiments with highly degenerate clouds.

In addition, a high repetition rate of the experimental cycle is favorable because optimizing system parameters and data taking can be done faster while the system is less likely to drift during the time the measurement is performed. One step of the experimental cycle, which is on the order of seconds and therefore can make the cycle long, is the loading of the first trap, the magneto-optical trap (MOT). In order to minimize the trap loading time, a high flux of atoms from the oven towards the MOT is necessary. This can be achieved by an effusive oven. Typically, the flux of sodium atoms is on the order of 10^{12} atoms per second. The partial pressure in the reservoir cups is high ($10^{-6} - 10^{-4}$ mbar) and the separation between the high pressure region and the UHV region has to be accomplished carefully. One way to do so is to place a long tube with low conductance between the two parts of the vacuum chamber. This method, which is called differential pumping, is described in section 3.2.

The vacuum system described in this thesis can be divided into three main parts: the oven, the differential pumping section and the main chamber (with the pumping chamber attached). A CAD drawing of the vacuum system is shown in Figure 3.1 and a real picture of the vacuum system can be found in Figure A.1. In the following, a detailed description of each part is given.

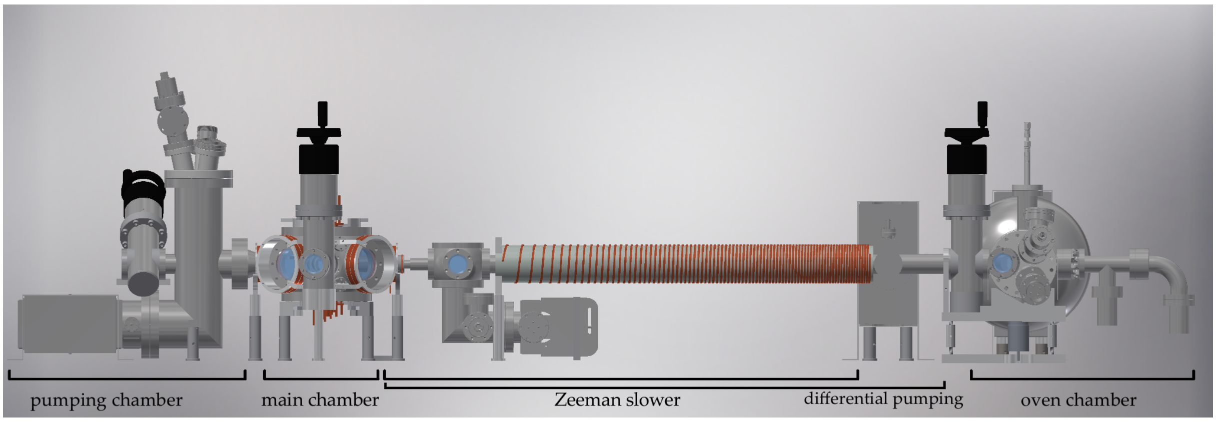

Figure 3.1: CAD drawing of vacuum system. From right to left: The atomic beam is created in the **oven**. Next to the oven a **differential pumping** section is placed in order to separate the high pressure region (**oven**) from the low pressure region (**main chamber**). The first stage of slowing the atoms is achieved by a **Zeeman slower**. Afterwards, the atoms reach the magneto-optical trap (MOT) inside the **main chamber**. Further pumping of the main vacuum chamber is achieved by vacuum pumps connected to the **pumping chamber**. A picture of the vacuum system can be found in Figure A.1.

3.1 Oven

The oven for the two atomic species experiment consists of two reservoirs (for ^{6}Li and ^{23}Na respectively), a mixing chamber and an oven nozzle, which creates the atomic beam containing both species. The design of the oven resembles the oven built at MIT [65] and is shown in Figure 3.2. This two chamber design is necessary because the partial pressure of sodium and lithium at the same temperature differs by three orders of magnitude. Having two different reservoirs instead of only one allows independent control over the atomic flux of each species. As long as there is no condensation of sodium in the mixing chamber the flux of sodium through the oven nozzle is equal to the flux through the mixing nozzle. The mixing and the oven nozzle are made from a standard CF40 flange. The mixing nozzle consists of a hole with a diameter of 2 mm and a length of 32 mm, whereas the diameter of the oven nozzle is 4 mm.

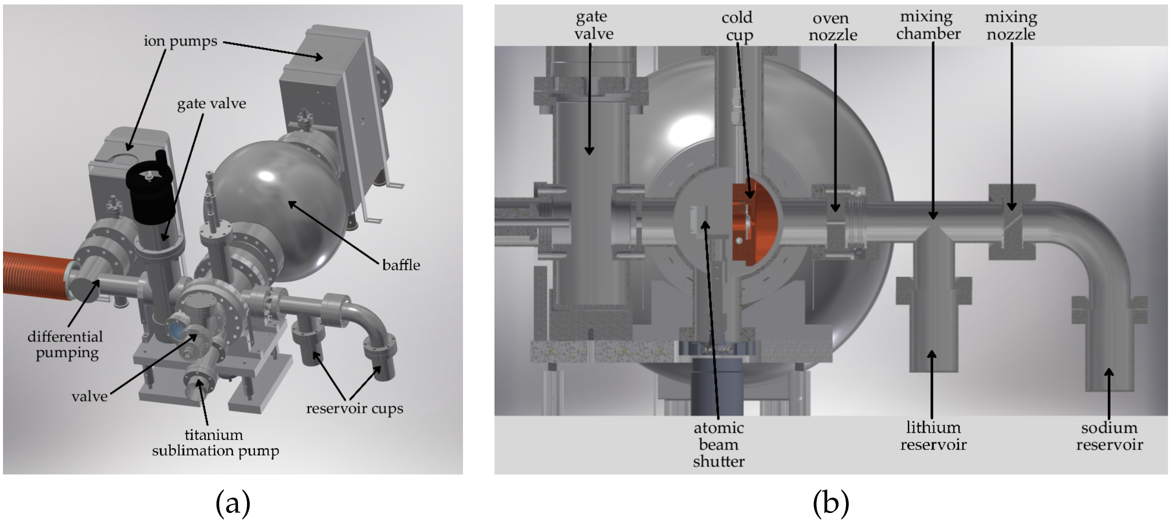

(a) (b)

Figure 3.2: CAD images of oven: **(a)** Overview of the oven chamber and neighboring components containing the reservoirs, vacuum pumps (ion pumps and titanium sublimation pump), valves and a baffle. **(b)** A cut through of the oven chamber: The two-species oven consists of two reservoirs connected by the mixing nozzle. Behind the oven nozzle, an atomic beam containing both sodium and lithium is created. The cold cup collects diverging atoms of the atomic beam, which would not reach the position of the first trap. The cup can be taken out for cleaning purposes. The mechanical shutter consists of a shutter flag (with a mirror attached used for diagnostic purposes), a magnetic feedthrough and it is only opened for the duration of the MOT loading.

Each reservoir is heated with a flange heater[1] to the desired temperature. The sodium reservoir is heated up to 330°C and the lithium reservoir to 390°C. In order to avoid clogging of the nozzles through condensation, they have to be the hottest part of the oven chamber. The mixing nozzle and the oven nozzle are therefore heated up to $\sim$ 490°C. A baffle protects the ion pump close to the oven from contamination due to high pressure; A majority of the atoms condense on a plate inside the baffle. The large size of the baffle ensures that the pumping conductance is not reduced. Wherever high operating temperatures are necessary nickel gaskets instead of standard copper gaskets are used since they are better suited for high temperatures. In addition, nickel gaskets react less likely with lithium than copper gaskets and they are therefore the

---

[1] Tempco, Mi-Plus Band Heater, $400 - 600$W

better vacuum sealant in regions where the concentration of lithium is high. The oven is thermally isolated from the environment using aluminum foil and fiber glass mats.

After some operation time the oven gets empty. Mainly sodium is consumed over time and has to be refilled. This is mainly due to the fact that the sodium flux is kept higher to obtain large sodium MOTs providing an excellent starting point for sympathetic cooling. The sodium consumption rate of sodium is approximately 1 µg per second (see section A.3 for more information). To avoid a bake-out of the whole chamber a gate valve is placed between oven and main chamber. This can be closed whenever the oven has to be opened for refilling or cleaning.

The purpose of the cold cup, which is placed behind the oven nozzle, is to collect all atoms which would not reach the MOT position but contaminate the vacuum or deposit inside the gate valve instead (which would make it unusable). This collector plate can be water cooled such that the atoms efficiently stick to the plate. In order to block the atomic beam while it is not needed, a mechanical shutter is used. This shutter consists of a shutter flag connected to a magnetic feedthrough (MagiDrive MD25DXMZ from UHV Design). The feedthrough is driven by a stepper motor and rotates the flag by 90°. Next to the shutter an optical viewport allows diagnosing proper shutter operation and oven operation, see Figure 3.3. In addition, it is used to monitor the fluorescence of the atomic beams over time. This is helpful to judge whether the reservoirs are empty.

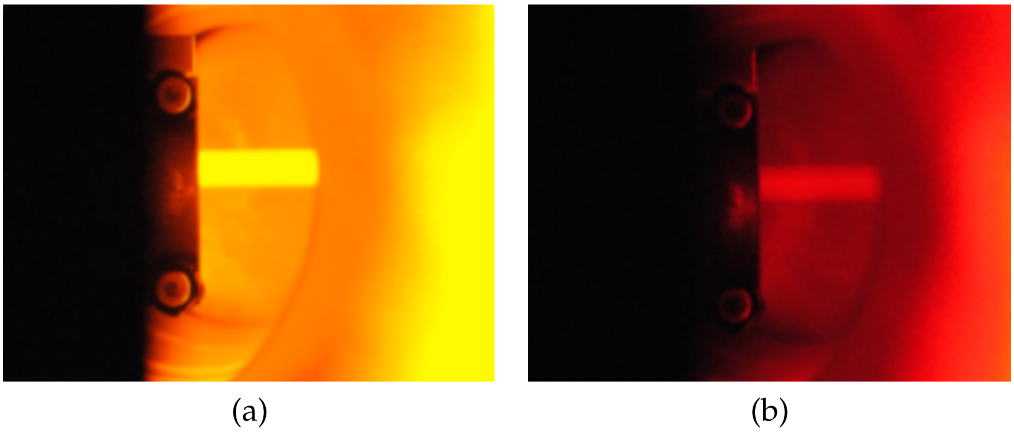

(a) (b)

Figure 3.3: Atomic beams coming out of the oven (on the right) and before entering the Zeeman slower (on the left) field: **(a)** sodium beam and **(b)**lithium. Images were taken trough the optical viewport attached to the oven chamber.

3.2 Differential Pumping Section

As mentioned earlier, a long tube with low conductivity is used to separate the high pressure region (the oven) from the low pressure experimental environment. This differential pumping tube essentially limits the flow of gas towards the low pressure region (see Figure 3.4). The tube starts directly after the gate valve and is extended into the Zeeman slower where it is conical shaped. This shape accounts for the expanding beam and prevents collisions of atoms in the beam, which are backscattered from the inside of the tube. Further pumping is carried out by an ion pump connected to a small chamber, which separates the two parts of the spin-flip Zeeman slower. The optical access gained by this pumping chamber could be used for transverse cooling of the atomic beam relative to the Zeeman slower. As our atom number in the MOT is not limited by the atom flux, we haven't implemented this additional cooling stage thus far. This differential pumping layout including all ion pumps and vacuum parts can maintain a pressure difference of 10^{-5} between oven and main chamber. This number is an approximation not including outgassing of hydrogen in the steel chamber, which is a limiting factor of reaching ultra high vacuum. However, by comparing the setup of other ultracold gas experiments a conclusion regarding the desired pumping speed of pumps can be made (see for example [66]). At a background pressure of $\sim 10^{-11}$ mbar long enough lifetimes in a magnetic trap have been reported ([64] and references therein). A description of the analysis of conductance between vacuum parts and pressure in the system can be found in section A.2.

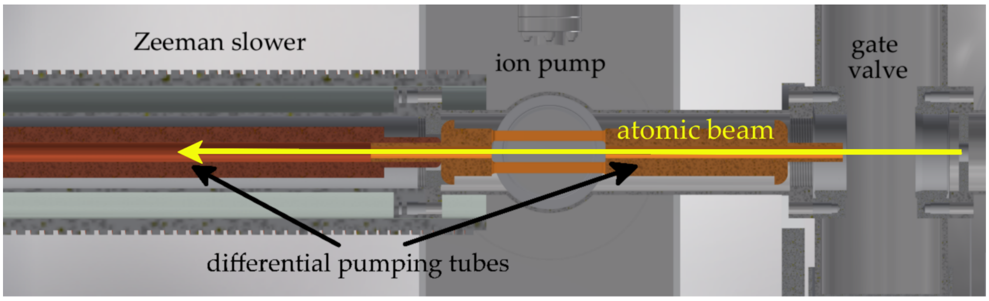

Figure 3.4: CAD image of differential pumping section. The differential pumping tubes are highlighted in orange and red to make the individual parts better visible.

3.3 Main Chamber and Surrounding Components

After the atoms have been initially slowed by the Zeeman slower they reach the magneto-optical trap (MOT) in the main chamber. A CAD image of the main chamber is shown in Figure 3.5. As mentioned above, one design goal was to reach a high number of sodium atoms in the MOT. This ensures that the cooling capacity for sympathetic cooling of lithium is as high as possible. For this reason we made sure that not only the atomic flux is high but also that we lose as few atoms as possible between the end of the Zeeman slower and the MOT. This is achieved by keeping the distance between the end of the Zeeman slower and the MOT position small (4.5 cm). Further cooling is realized by optical molasses of sodium. Afterwards, the anti-Helmholtz field of the initial magnetic field trap generated by the MOT coils is switched on. The transfer to the final magnetic trap position is completed by ramping on the final magnetic field of the trap coils while simultaneously ramping down the MOT fields. The final magnetic trap coils in Helmholtz configuration are later used to generate a homogeneous field for tuning the interactions between the lithium atoms when they are in the dipole trap. The final position of the atoms is defined by the final magnetic trap coils and is designed to be 3 mm below the fused silica window. This short distance to the window is intentional to place a high resolution objective (from Special Optics, tested in our group [67], NA= 0.72, resolution:600 µm) right on top of the window.

Several offset and gradient coils along the x-, y- and z-direction are used to cancel the earth magnetic field and stray fields and to have independent control over the magnetic fields during the experimental cycle.

Additional coils used as a radio and microwave source are are mounted inside and outside the chamber in proximity to the final position of the atoms. They are used for manipulation of the hyperfine state of the atoms, e.g. for the radio frequency (rf) evaporation of sodium in the magnetic trap and for the creation of a spin mixture of lithium in the lowest two hyperfine states. In the beginning we used the coils inside the vacuum chamber for rf evaporation and hyperfine manipulation. However, after testing and optimizing we noticed that we achieve better evaporation and transfer efficiencies with the antennas outside the vacuum. The coils inside the vacuum are now used as pick-up coils for diagnosis purposes.

In addition to the ion pump connected to the pumping chamber (Figure 3.1), a titanium sublimation pump, also attached to the pumping chamber, maintains the ultra high vacuum in the main chamber. The titanium sublimation pump pumps among others hydrogen, which is the primary load contributor at low pressures. Due to the fact that these pumps are not very close to the final position, we were worried about remaining hydrogen outgassing from the steel chamber. This is why we added some non evaporable getters purchased from SAES group. They were activated during the final bake-out and are pumping sine then. However, the effect of these is hard to quantify.

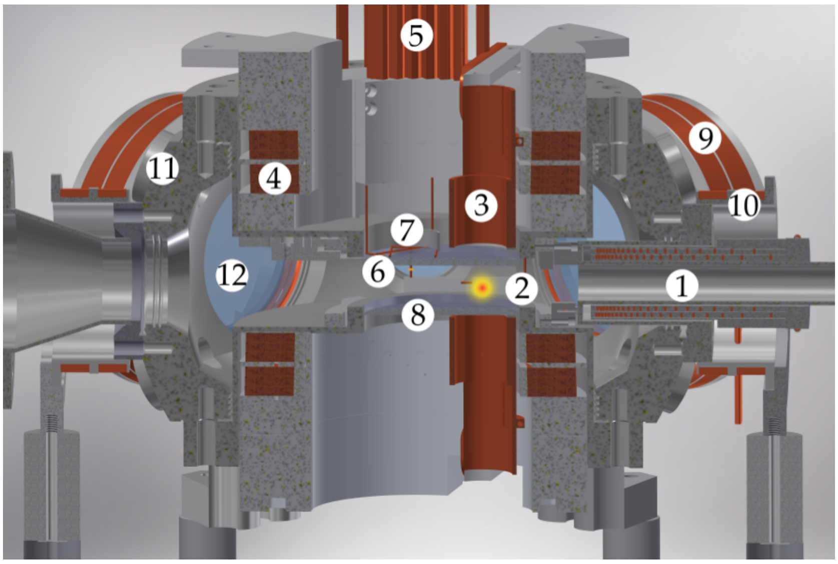

Figure 3.5: CAD image of main chamber: (1) Second part of the spin-flip Zeeman slower. (2) Magneto-optical trap (MOT) position, the two-species MOT is indicated by the yellow (sodium) and red (lithium) dot. (3) MOT coils and MOT coil mounts. (4) Final magnetic trap coils, Feshbach coils and general offset and gradient coils along the z-direction. (5) Leads of previous mentioned coils. (6) Final position of atoms indicated by orange dot 3 mm below the vacuum window. (7) Radio frequency and microwave antennas for hyperfine manipulation and magnetic field coils for displacing the atoms inside the dipole trap (used for dipole trap frequency measurements). (8) Inverted optical viewport made by the special techniques group at UKAEA. (9) Gradient and offset coils for compensating earth magnetic and stray fields along x- and y-direction. (10) Coils for canceling magnetic fields arising from the Zeeman slower at the position of the MOT (only the one opposite the Zeeman slower is used). (11) CF16 ports used for electrical feedthroughs for (pick-up) antennas. In addition, some of them are connected to non evaporable getters from SAES group. (12) Optical viewports with large optical access, see section A.4.

The optical viewports surrounding the main chamber are homemade. The design principle follows the idea by Scott Crane and Christopher Ekstrom [68]. Their sealing method relies on crushing thin copper knife-edges between glass and steel chamber and therefore sealing the vacuum up to UHV. This can have several advantages: The first one being larger optical access. Many standard optical viewports have reduced optical access due to the method they are sealed to the flange. The second one being the free choice of glass material and coating. In addition, the glass can be coated before attaching it to the flange guaranteeing a coated area up to the steel flange. In contrast, this is not the case for standard viewports, which are coated after being sealed to the flange and therefore have an uncoated ring on the edge. The choice of glass material is also important. A material with low birefringence is favorable for all applications related to optical trapping of ultracold atoms. A drawing of these homemade viewports can be found in section A.4.

3.4 Bake-out

In order to do experiments with Bose-Einstein condensates and degenerate Fermi gases a background pressure of $< 10^{-11}$ mbar is necessary. The main limiting factor of reaching and maintaining such low pressures is the desorption of gas from the inner surfaces of the vacuum system. While for example water can be removed at modest temperatures (100°C), significant removal of hydrogen from steel is more difficult and requires temperatures of around 300°C for several days. Nevertheless, this has to be performed as remaining hydrogen is usually the limiting factor at low pressures. During high temperatures bake-outs hydrogen diffuses from the bulk to the surface and is pumped away. This method reduces the outgassing rate of hydrogen at room temperature significantly and makes it possible to reach pressures below 10^{-11}mbar [69, 70].

We started with a high temperature bake-out of the main chamber and the pumping chamber during which the system was heated up to 300°C and kept at this temperature for two weeks. All ports of the main chamber were covered with blank flanges and the magnets of the ion pump were removed. For the final bake-out the main chamber with the homemade optical viewports was heated up to 150°C, other parts like gate valves and chambers with standard viewports to 200°C and ion pumps up to 280°C. The oven was heated up to 300°C. During the manufacturing process of lithium, lithium hydride can be created, which has to be removed before operation. With the intention of removing lithium hydride and other hydrogen from the lithium reservoir, the reservoir was brought to a temperature of 500°C for about 20 min. In addition, the filaments of the titanium sublimation pumps were fired and the non-evaporative getters were activated.

Following the cool down and firing the titanium sublimation pumps multiple times a pressure of approximately 10^{-11} mbar was recorded on the ion pump and ion gauge next to the main chamber. Therefore, the desired pressure of an ultra high vacuum system was established ready to study ultracold atoms.

CHAPTER 4

Laser Cooled Atoms

One of the main challenges of this new experiment is to achieve highly efficient laser cooling resulting in an excellent starting condition for further evaporative cooling in a magnetic trap. To do so, a dedicated laser system has been developed as described in this chapter.

The atoms leaving the oven have a peak velocity of $\sim 500\,\mathrm{m\,s^{-1}}$ for sodium and $\sim 1\,200\,\mathrm{m\,s^{-1}}$ for lithium depending on the species and the temperature of the reservoir. In order to be able to capture them in a magneto-optical trap, the speed of the atoms has to be reduced to tens of $\mathrm{m\,s^{-1}}$. To achieve this goal the technique of laser cooling is applied. This chapter begins with an explanation of the working principle of laser cooling, continues with the description of the laser systems for the two species, explains the construction of the Zeeman slower and concludes with the characterization of the magneto-optical trap. As a result excellent flow rates of slowed atoms to the MOT are achieved and high atom numbers in the MOT.

4.1 Theory of Laser Cooling

Laser cooling is the essential technique, which enables the production of ultracold gases. It took several decades from the very first idea to its first realization. The work performed in this area was a milestone for the atomic physics community and Steven Chu, Claude Cohen-Tannoudji and Willian Daniel Phillips were awarded with the Nobel prize in 1997 for their accomplishments. The principles of their work are explained in this section; a more detailed description can be found in [71–73].

Laser cooling relies on the momentum transfer between photons and atoms. More precisely, the absorption of a photon leads to a change in momentum of the atom by

$$\Delta \mathbf{p}_{atom} = \mathbf{p}_{photon} = \hbar \mathbf{k}_{photon} \quad . \tag{4.1}$$

Following the absorption of a photon the atom emits a photon into a random direction. If such an absorption and emission process happens multiple times, the net momentum transfer of the emission averages to zero as this process is isotropic. However, if the absorption process is directional, this process can be used to lower the velocity of atoms and hence to cool an atomic sample. The averaged spontaneous light force acting on the atoms can thus be written as as function of the scattering rate of photons γ_p

$$\langle \mathbf{F} \rangle = \hbar k \gamma_p \quad . \tag{4.2}$$

The scattering rate itself depends on the laser detuning from resonance $\delta = \omega_0 - \omega_{laser}$ and the intensity I and is given by [72]

$$\gamma_p = \frac{\Gamma}{2} \frac{I/I_{sat}}{1 + I/I_{sat} + \left(\frac{2\delta}{\Gamma}\right)^2} \quad , \tag{4.3}$$

where the natural linewidth Γ for the D_2 transition in lithium is $2\pi \cdot 5.87\,\mathrm{MHz}$ and $2\pi \cdot 9.79\,\mathrm{MHz}$ for sodium. I_{sat} is the saturation intensity, which is $2.54\,\mathrm{mW\,cm^{-2}}$ for lithium and $6.26\,\mathrm{mW\,cm^{-2}}$ for sodium (for the cooling transition and σ polarized light). The maximum deceleration is achieved for a maximum of scattering events ($\delta = 0$, $I \to \infty$) and is therefore given by

$$a_{max} = \frac{\hbar k \Gamma}{2m} \quad . \tag{4.4}$$

To realize this maximal deceleration, laser sources operating ideally on resonance of an atomic transition with high intensities are necessary. How this is addressed in our experiment is presented in the following.

4.2 Laser Systems

Since we are dealing with two atomic species, two laser systems had to be designed, which need to be operating in parallel in order to cool, manipulate and image sodium and lithium atoms simultaneously.

4.2.1 Sodium Laser System

The creation of laser light at a wavelength of 589 nm needed for sodium is achieved by combination of a diode laser, a Raman fiber amplifier and a frequency doubling cavity. Commercial semi-conductor based lasers such as laser diodes are not available at 589 nm and dye lasers weren't an option for us as the dye solution has to be exchanged regularly, which can take a lot of time from the available daily experiment time. The diode laser used is an external cavity diode laser[1] operating at a wavelength of 1 178 nm. The light of the diode laser is coupled into a fiber and sent to a single frequency Raman fiber amplifier[2]. In principle, this amplifier can intensify the power of incoming light (typically 20 mW) up to 8 W. However, for our experiments we only need about 3 W of infrared light. This can be advantageous as operating the amplifier at lower than the maximum possible power extends its lifetime. Besides that, it also leaves the option to cool more atoms in the future.

After having amplified the infrared light the next step is to double its frequency to generate light at 589 nm, which is the resonant wavelength to drive the D_2 transition of sodium. In the following section the design process and functionality of the frequency doubling cavity (SHG cavity) is described. A sketch of the complete laser system for sodium can be found in Figure 4.1.

Frequency Doubling Cavity

In this section the design stages of the SHG (second harmonic generation) cavity is briefly presented, which achieves the goal of generating a high power source at 589 nm. A detailed description of a similar design process can be found in [74], which also covers most of the derivations of formulas used in the following part of this thesis.

---

[1] Toptica, ECDL, DL pro

[2] from MPB Communications Inc.

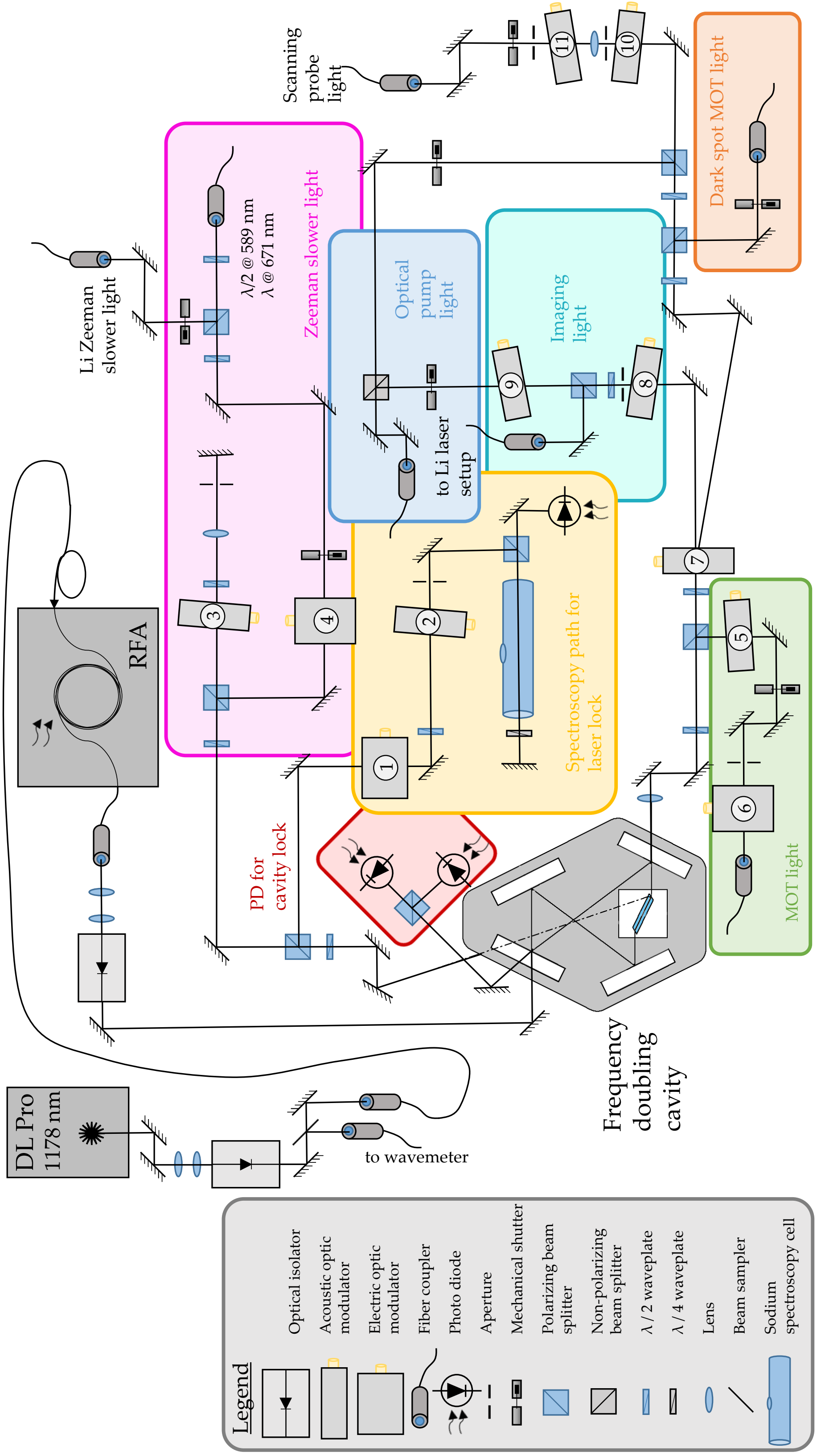

Figure 4.1: Simplified sketch of the laser system for cooling, trapping, imaging and manipulating sodium atoms. AOM and EOM frequencies are listed in Table 4.3. For more details see main text. A picture of the laser system is shown in Figure A.2.

With an incoupling power of 2.5 W of infrared light sent to the cavity we achieve an output power of 1.3 W of yellow light. This high efficiency together with a stable power source serves as a laser light source for the sodium laser system.

Second harmonic generation can be observed in nonlinear materials and it can be pictured as a conversion of two photons with frequency ω into one photon with twice the frequency. Another way to think about this mechanism is to think about the electrons inside the nonlinear material, which are driven by a sinusoidal force coming from the light's electric field. As the electrons sit in an anharmonic potential, their response in motion is nonlinear to the applied light field. Hence, nonlinear effects can happen, one example being the second harmonic generation of light. This effect was first observed by Peter Franken et al. [75] in 1961.

If nonlinear terms of the polarization of the medium are incorporated (in this case up to second order), it can be shown [76] that the efficiency of the second order generation is proportional to L^2P, where L is the length of the medium and P the power. At the same time it is anti proportional to the area of the interaction between light and material. Due to the fact that Gaussian beams diverge more when they are focused more tightly, one has to find a tradeoff between small interaction area and interaction length.

Another aspect to consider is that all generated second harmonic waves should add up constructively. This means that the phase of those waves should be the same at a reference point, independently of the position where they had been generated. This is called the phase matching condition. Following [77], this requirement can be translated into a condition for the refractive index. The condition for the refractive index is equivalent to the requirement in time and space

$$\begin{aligned} n(\lambda_{FM}) &= n(\lambda_{SH}) \quad , \\ 2\omega_{FM} &= \omega_{SH} \quad , \\ 2\mathbf{k}_{FM} &= \mathbf{k}_{SH} \quad , \end{aligned} \tag{4.5}$$

where n is the refractive index, λ the wavelength, FM stands for the fundamental wave, SH for second harmonic, ω is the frequency and k the momentum. The last two equations not only show the condition for energy and momentum conversion but also connect to the above described picture of the second harmonic generation where two photons with the same frequency are converted into one photon with twice the frequency. The phase matching condition is often difficult to achieve because dispersion prohibits it. However, due to birefringence, the refractive index can be different for different polarizations allowing the phase matching condition to be fulfilled.

The nonlinear material used in the experiment is a lithium triborate (LBO) crystal, which is cut (relatively to its crystal symmetry) such that the phase matching condition is fulfilled. In addition, it is Brewster cut to avoid backscattering of the light hitting the first surface of the crystal. The polarization of the second harmonic light is perpendicular to the one of the fundamental. This is because we are using Type I conversion where two photons with ordinary polarization are generating one photon with extraordinary polarization. Therefore, some of the second order harmonic light is reflected by the second surface of the crystal. In our case this is about 170 mW, which is used for the sodium spectroscopy and for the Zeeman slower light, see Figure 4.1.

Moreover, the power of the second harmonic can be calculated using the theory developed by Boyd and Kleinman [78] in 1968. Their ansatz is to divide the crystal into many small slices and then sum up their contribution to the second harmonic. In addition, they consider a focused laser beam and use the slowly varying envelope approximation. With this in mind, the power of the second harmonic can be expressed as

$$\begin{aligned} P_{out}(\sigma, B, \xi) &= \frac{16\pi^2}{\epsilon_0 c n_{FM} n_{SH} \lambda_{FM}^3} \cdot d_{eff}^2 \cdot e^{-\alpha' l} \cdot h(\sigma, B, \kappa, \xi, \mu) \cdot P_{in}^2 \\ &= \kappa_{NL} P_{in}^2 \quad , \end{aligned} \tag{4.6}$$

where ϵ_0 is the vacuum permittivity, c the speed of light, $n_{FM/SH}$ the refractive index of the fundamental and second harmonic respectively, λ_{FM} the wavelength of the fundamental, d_{eff} a crystal specific nonlinear conversion coefficient [3], α' a damping coefficient, l the length of the crystal and $h(\sigma, B, \kappa, \xi, \mu)$ is the Boyd-Kleinman factor. This Boyd-Kleinman factor depends on several parameters, namely σ, which describes the phase matching condition, B the walk-off between the two waves, κ the absorption coefficient of the second harmonic, $\xi = \frac{l}{2z_0}$, where z_0 is the Rayleigh range, and $\mu = \frac{l-2f}{l}$ (f is the distance of the focus from the crystal surface). Knowing the length of the crystal (25 mm) and assuming the walk-off to be zero the absorption of the second harmonic has to be zero as well as $\mu = 0$. The Boyd-Kleinman factor can be optimized resulting in two optimized values $\xi_{opt} = 2.83$ and $\sigma_{opt} = 0.57$. By using the

---

[3] which is in our case $0.8 \cdot 10^{-12}$

relation between ξ_{opt} and the Rayleigh range as well as the relation between Rayleigh range ($z_0 = \pi w_0^2/\lambda$) and waist w_0 the optimal waist in the center of the crystal can be calculated and is 32 µm for our set of parameters.

As resonator design a bow-tie-cavity is used, which is a ring resonator consisting out of four mirrors, two planar and two curved ones. The setup of the mirrors and the crystal is shown in the sketch of the laser system, see Figure 4.1. The way the curved mirrors can be used to compensate for astigmatism caused by the crystal is explained later.

The next step in order to find the optimized cavity parameters is to calculate the distances between the mirrors. This is done by using the ABCD matrix formalism and simulating the round trip of the light inside the cavity. There are two conditions that have to be fulfilled. The first one is the stability condition

$$\frac{A+D}{2} \leq 1 \quad , \tag{4.7}$$

where A and D are the matrix elements of the matrix, which describe one round trip inside the cavity. The second condition is that the $q-$parameters should be the same after one round trip. Using these conditions, equations for the distance the light travels in air between the curved mirror d_{air} and the remaining cavity length L can be derived [74]

$$\begin{aligned} d_{air} &= R\left(1 + \frac{l}{\xi_{opt} R n}\right) - \frac{l}{n} \quad , \\ L &= R\left(1 + \frac{\xi_{opt} R n}{2l}\right) \quad . \end{aligned} \tag{4.8}$$

Here, R is the radius of curvature of the cavity mirrors. For our system the values are d_{air} =64 mm and L =226 mm. In addition, one can calculate the waist between the two planar mirrors, which is needed match the mode of the incoming beam to the cavity mode.

As mentioned earlier, the crystal inside the cavity causes astigmatism since the projection of the circular beam onto the crystal is elliptical. Looking at the tangential and sagittal plane and using the ABCD matrix formalism, a condition for the angle of incidence on the curved mirrors can be found in order to minimize astigmatism

$$\cos(\theta) = \sqrt{1 + \left(\frac{lN}{2R}\right)^2} - \left(\frac{lN}{2R}\right) \quad , \tag{4.9}$$

where

$$N = \frac{\left(n^2 - 1\right)\sqrt{n^2+1}}{n^4} \quad . \tag{4.10}$$

In our case, this angle is 26.6°. Using this angle the waist in the center of the crystal of both planes can be calculated as a function of d_{air}. From this calculation it can be seen that the initial calculated distance d_{air} (Equation 4.8) has to be slightly adjusted in order to make the waists equal to the optimal one.

After having calculated the optimized reflectivity of the incoupling mirror R_1, the expected output power can be calculated [74] as function of the circulating power P_{circ}, the multiplied reflectivities R_{234} of the remaining mirrors and the losses inside the crystal β

$$\begin{aligned} P_{out} &= \kappa_{NL} \cdot P_{circ}^2 \\ &= \kappa_{NL} \left(P_{inc} \frac{1 - R_1}{\left(1 - \sqrt{R_1 R_{234} \left(1 - \kappa_{NL} P_{circ}\right)\left(1 - \beta\right)}\right)^2} \right)^2 \quad . \end{aligned} \tag{4.11}$$

For an input power of 2.5 W the theoretical output power is 1.7 W. The maximum achieved output power in the experiment is 1.3 W. The discrepancy could come from losses from the mirrors or overestimated conversion efficiencies. However, achieving an efficiency of 76% is excellent. The calculated finesse of this cavity is ~ 100. To summarize, the parameters of our frequency doubling cavity are given in Table 4.1.

In order to have a stable cavity, we employ a monolithic design (manufactured from a single piece of aluminum). The mechanical design of the frequency doubling cavity can be seen in Figure 4.2. After the initial alignment and optimization procedure, the cavity mirrors never had to be realigned again. From time to time (every 6 month to one year) the cavity mirrors and crystal surfaces are cleaned very carefully, which reestablishes the optimum output power. The cavity mirrors are mounted using fine thread screws, springs and plates from Radiant Dyes and the crystal is mounted on top of three translation stages allowing the crystal to be moved and rotated in the plane of the beam as well as being tilted. In addition, a temperature sensor and a Peltier element are used to tune the temperature of the crystal. To avoid accumulation of dust on the mirrors and on the crystal surface, the top is covered with a lid and the incoupling and outcoupling ports are covered with an anti reflection (AR) coated window.

Fundamental wavelength	λ_{FM}	1 178 nm
Second harmonic wavelength	λ_{SH}	589 nm
Crystal (LBO) length	l	25 mm
Distance in air between curved mirrors	d_{air}	46 mm
Remaining cavity length	L	226 mm
Angle of incidence on mirrors	θ	26.6°
Optimal waist at the center of the crystal	w_0	32 µm
Optimal waist between planar mirrors	w_{02}	206 µm
Input power	P_{in}	2.5 W
Output power	P_{out}	1.3 W

Table 4.1: Parameters of the frequency doubling cavity, which converts infrared light at 1 178 nm into light at 589 nm. The total output power includes backscattering from the second crystal surface.

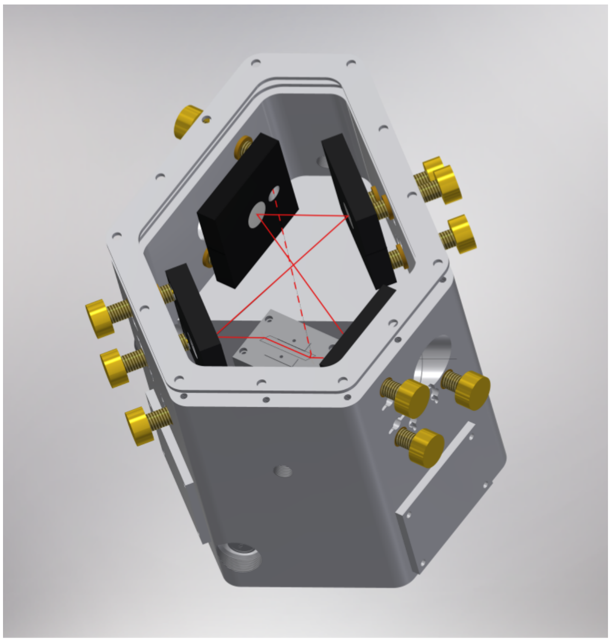

Figure 4.2: Frequency doubling cavity of sodium laser system, which generates light at a wavelength of 589 nm from light at a wavelength of 1 178 nm. The beam path is shown as a red line, the dashed line shows the reflected light from the inner crystal surface. The curved mirrors are placed next to the crystal.

Finally, the cavity length is adjusted to stabilize the output power. For this purpose, a piezo element is mounted behind one of the planar mirrors and the backreflection of the cavity is monitored while the piezo is scanning. For monitoring, we use a slow and a fast photodiode. The slow photodiode is used to optimize the incoupling during the initial alignment procedure, whereas the fast photodiode is used to lock the cavity using the Pound-Drever-Hall technique [79, 80]. This technique is typically either being used to stabilize the laser frequency relative to a reference cavity or vice versa. The latter is implemented in our setup and is achieved in the following way. The laser current is modulated, which induces sidebands onto the laser frequency. The sideband of the reflected light is then phase shifted with respect to the carrier and if the signal is measured with as fast photodiode, a beat signal can be detected. This signal is mixed down with the modulation frequency yielding a dc signal with a monotonic slope and a zero crossing on resonance as shown in Figure 4.3 (a). Together with a PID controller, this error signal is used to stabilize the cavity length, hence a stable source (in terms of power) of light at 589 nm is set up.

Locking the DL Pro Using Frequency Modulation Spectroscopy

In the last section the setup of a stable laser source at 589 nm with respect to power is described. However, for creating ultracold gases the laser source does not only have to be stable with respect to the power but also to its frequency. In particular, the bandwidth of the laser has to be small compared to the natural linewidth (which is $\Gamma/2\pi = 9.8\,\mathrm{MHz}$ for sodium). We use a technique called frequency modulation spectroscopy to stabilize the laser frequency. Since the current modulation is used to create sidebands for the cavity lock (and which are filtered by the cavity), we use an electro optic modulator (EOM) to create sideband for a spectroscopy.

A Doppler-free spectroscopy setup is necessary because the hyperfine structure has to be resolved in order to lock the laser to a specific transition and hence to achieve the desired frequency resolution and stability. The light is frequency shifted by 65 MHz before it is sent through the spectroscopy cell. This serves the purpose that scattered light at the resonance frequency is minimized, which could potentially disturb the atoms. Moreover, the frequency of the light has to be shifted depending on its purpose. In detail, detunings of e.g. 15 MHz are more easily achieved by adding approximately 80 MHz using an acousto optic modulator (AOM) than detuning by 15 MHz as AOMs are usually only available with a center frequency of 50 MHz and higher. The absorption signal is obtained by sending the light trough a homemade cell [81] filled with approximately one gram of sodium and heated up to about 140°C. In order to circumvent the drawback of commercial vapor cells made out of glass, which become opaque when they are heated to high temperatures, we developed our own optimized design. As result, we designed a cell made out of a steel pipe with optical viewports and an attached valve.

The most pronounced signature in the error signal corresponds to the crossover between the F′= $|2\rangle$ and F′= $|3\rangle$ state. The splitting between these two states is 58 MHz. As the laser frequency is shifted by 65 MHz before it is sent through vapour cell and the crossover is used for locking, the laser is locked 94 MHz below the $|3^2S_{1/2}, F = 2\rangle \rightarrow |3^2P_{3/2}, F' = 3\rangle$ transition. The setup of the spectroscopy path is illustrated in Figure 4.1 and the error signal, which serves as an input signal for the PID, is shown in Figure 4.3 (b).

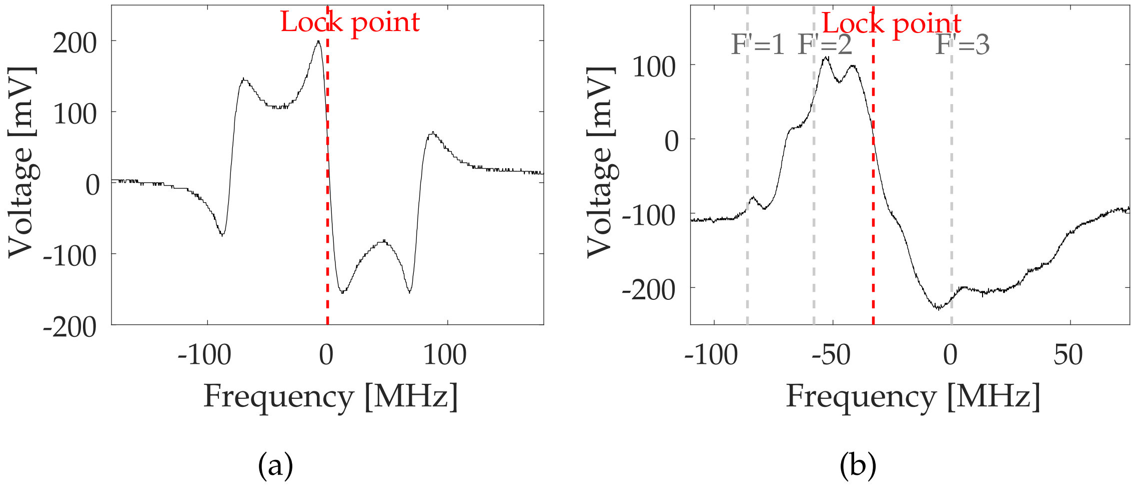

Figure 4.3: (a) Error signal of the doubling frequency cavity lock, which is generated by monitoring the light coupled into the cavity. **(b)** Error signal of the laser lock, which is obtained after performing Doppler-free saturation spectroscopy on sodium vapor and using frequency modulation technique as a locking technique.

Distribution of Laser Light and Power

The laser powers for the different applications, e.g slowing or trapping, are listed in Table 4.2. In addition, the different detunings relative to the $|3^2S_{1/2}, F = 2\rangle \rightarrow |3^2P_{3/2}, F' = 3\rangle$ transition are listed in Table 4.3.

Purpose of laser light	Power [mW]	Beam radius [mm]	Intensity [I_{sat}]
Zeeman slower	65	15	1.5
Magneto-optical trap	$6 \cdot 25$	20	1.8
Dark spot MOT (with dot in the center)	8.0	20	0.1
Optical pumping $\|F=1\rangle \rightarrow \|F'=2\rangle$	1.3	10	0.07
Optical pumping $\|F=2\rangle \rightarrow \|F'=2\rangle$	0.2	10	0.01
Imaging	0.3	5	0.06

Table 4.2: Laser powers used for cooling, trapping, manipulating and imaging ultracold sodium atoms. The intensity is the averaged (not the peak) intensity and the saturation intensity for sodium is 6.26 mW [82].

AOM/ EOM No.	Purpose of laser light	Freq. [MHz]
1	Sidebands for laser lock	67
2	Frequency shift for laser lock	65
3	Zeeman slower	$-2 \cdot 205$
4	Zeeman slower repumper	1713
5	Magneto-optical trap (MOT)	72
6	Repumper for optical molasse	1713
7	Repumper for dark spot MOT and optical pumping	1783
8	Optical pumping AOM 1	88
9	Optical pumping AOM 2 $\|F = 2\rangle \rightarrow \|F' = 2\rangle$	-68
10	Scanning Probe 1	200
11	Scanning Probe 2	-200
12	Imaging	$2 \cdot 47$

Table 4.3: Frequencies of acousto and electro optic modulators (AOMs and EOMs) of the sodium laser system shown in Figure 4.1.

Purpose of laser light	Detuning from $\vert F=2\rangle \rightarrow \vert F'=3\rangle$ [MHz]
Laser lock	-94
Zeeman slower	-504
Magneto-optical trap	-22

Table 4.4: Laser light detuning relative to the cycling transition in the sodium laser setup.

4.2.2 Lithium Laser System

In this section our setup for a stable laser source for cooling, trapping and imaging lithium atoms is described. Two homemade external cavity diode laser with laser diodes from Eagleyard[4] are used as a laser source. The first one is frequency locked to a lithium vapor cell using the frequency modulation spectroscopy as explained in section 4.2.1, whereas the second one is offset locked to the first one. This opens up the opportunity to change the frequency of the second laser by more than 1 GHz, which allows imaging lithium atoms at high magnetic field where the resonant frequency is shifted due to the Zeeman shift. This is a necessary tool as most of the experiments are carried out in the proximity of the Feshbach resonance at $\sim$ 834 G. The light of both lasers is amplified using tapered amplifiers[5] and it is frequency shifted depending on its purpose. A sketch of the laser frequencies can be seen in Figure 4.4 and the AOM/EOM frequencies can be found in Table 4.6.

Locking Setup of he Lithium Laser System

As mentioned above, the first laser is locked to an atomic transition, obtained by a Doppler-free spectroscopy of lithium vapor and by using frequency modulation as a locking technique. The current of the laser is modulated, which creates sidebands on the laser frequency before the light is sent through a homemade vapor cell filled with $\sim$ 2 g lithium. This vapor cell consists of a long steel tube with optical viewports attached to either end. In addition, apertures inside the cell prevent lithium from traveling towards the windows and condensing on the windows. The cell is heated up to 340°C at the center and to 180°C at the windows providing a vapor pressure suitable for performing spectroscopy in the center and avoiding condensation at the windows.

---

[4] EYP-RWE-670-00702-100-SOT02-0000

[5] EYP-TPA-670-00500-2003-CMT02-0000

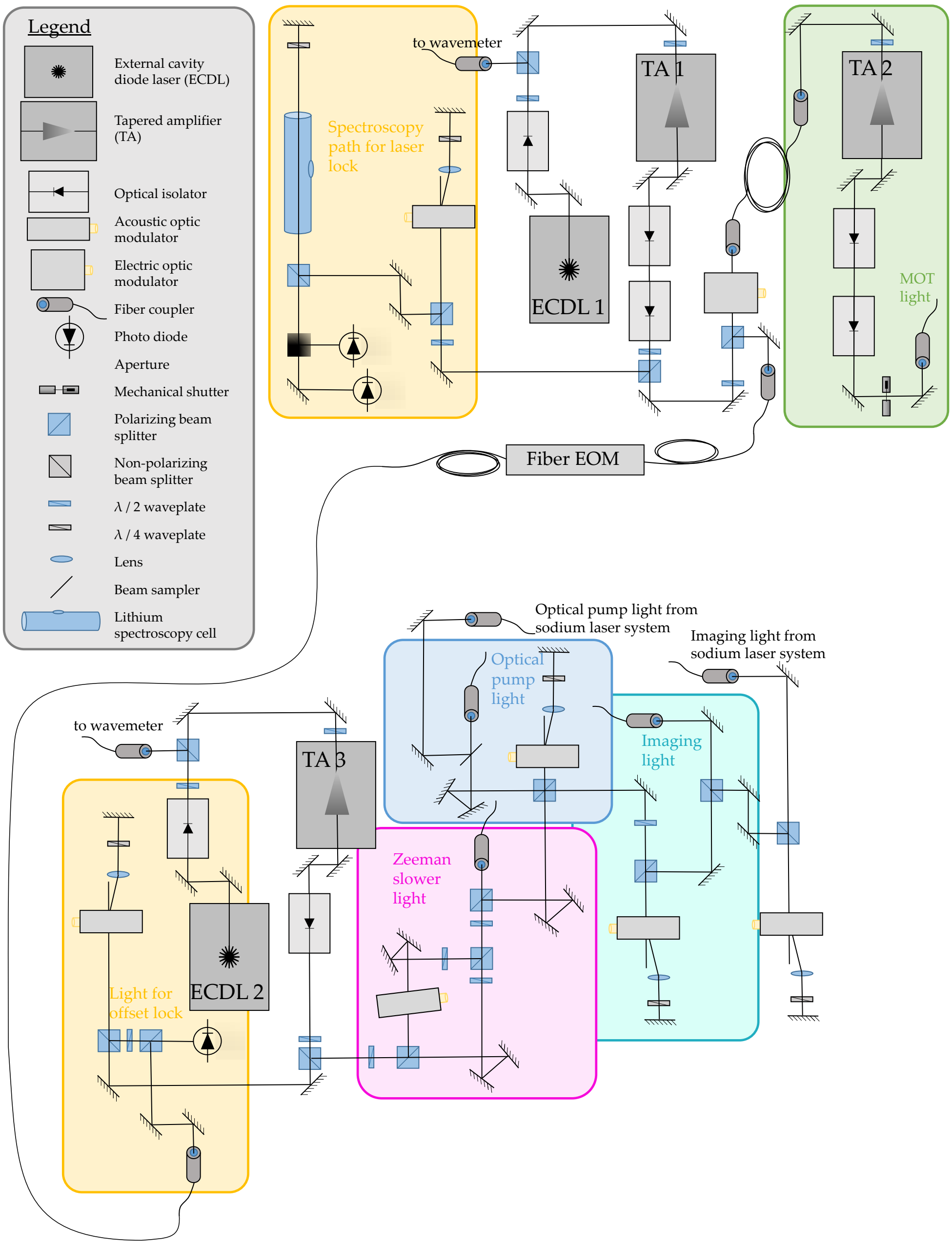

Figure 4.4: Simplified sketch of the laser system for cooling, trapping, imaging and manipulating lithium atoms. Frequencies of AOMs and EOMs can be found in Table 4.6. For more details see main text.

Purpose of laser light	Power [mW]	Beam radius mW	Intensity [I$_{\text{sat}}$]
Zeeman slower cooler	24	15	1.3
Zeeman slower repump	4	15	0.2
Magneto-optical trap	$6 \cdot 12$	11	7.5
Optical pumping $\left\|F = \frac{3}{2}\right\rangle \to \left\|F'\right\rangle$	1.5	11	0.2
Optical pumping $\left\|F = \frac{1}{2}\right\rangle \to \left\|F'\right\rangle$	1.5	11	0.2
Imaging	0.2	4	0.2

Table 4.5: Laser powers used for cooling, trapping, manipulating and imaging ultracold lithium atoms. The intensity is the averaged (not the peak) intensity and the saturation intensity for lithium is 2.54 mW [83]. $|F'\rangle$ denotes the excited state of which the hyperfine states are not resolved relatively to the linewidth and hence not further specified.

AOM/ EOM No	Purpose of laser light	Freq. [MHz]
1	Frequency shift of laser lock	2×70
2	Sidebands/ Repumper for MOT light	228
3	Frequency shift for offset lock	-2×250
4	Repumper for Zeeman slower	-228
5	Optical pump	2×230
6	Imaging	2×100

Table 4.6: Frequencies of acousto and electro optic modulators (AOMs and EOMs) of the lithium laser setup shown in Figure 4.4.

The setup of the cell is described in more detail in [84]. After being sent through the vapor cell, the signal is monitored with a fast photodiode. The signal is mixed down yielding an error signal, which can be used to stabilize the frequency of the first laser. The first laser is locked 26 MHz below the $\left|F = \frac{3}{2}\right\rangle \to |F'\rangle$ transition ($|F'\rangle$ denotes the excited state of which the hyperfine states are not resolved relatively to the linewidth and hence not further specified).

As the first laser produces the light for trapping the atoms in the magneto-optical trap (MOT), the second laser generates the light for slowing, optical pumping and imaging. In order to be able to image the atoms over a wide range of magnetic fields, a frequency offset lock technique is implemented, which accounts for the Zeeman shift. This technique allows changing the frequency by about 1 GHz. The working principle is as described in [85]. The beat signal ($\Delta\nu = \nu_1 - \nu_2$) after filtering the high frequency component of the two lasers is monitored by a photodiode, amplified and subsequently mixed with the output of a local oscillator (VCO). Afterwards, the signal ($|\Delta\nu - \nu_{VCO}|$) is split into two parts. One is sent through a delay line and then combined with the other one on a phase detector. A low pass filter blocks the frequency at twice the frequency yielding a voltage signal proportional to $\cos(\phi)$, where $\phi = 2\pi\left(\Delta\nu - \nu_{VCO}\right)\tau$. In combination with a servo loop this signal is fed back to the piezo moving the grating of the second laser, stabilizing its frequency. The frequency resolution is given by the slope of the error signal at the zero crossing, which is used as a lock point. A longer delay line increases the resolution but decreases the capture range of the lock. A sketch of such an offset lock can be found in section A.5.

If the frequency of the local oscillator is changed, the lock point of the second laser is changed accordingly. A tunable RF signal generator[6] is used as a local oscillator, which can be swept over a broad range. This RF signal is sent to a fiber EOM[7], which can be phase modulated by 10 to 20 GHz, hence the necessary sidebands on the beat signal are created.

One additional requirement of sweeping the laser frequency and imaging at different fields has been neglected so far. This is that the laser has to stay in lock while changing its frequency. A sufficiently broad mode free hopping range is necessary for this purpose. The error signal for the two lock signals are shown in Figure 4.5.

---

[6] Windfreak Technologies, SynthNV 34.4 MHz to 4.4 GHz

[7] Photoline, MPX800

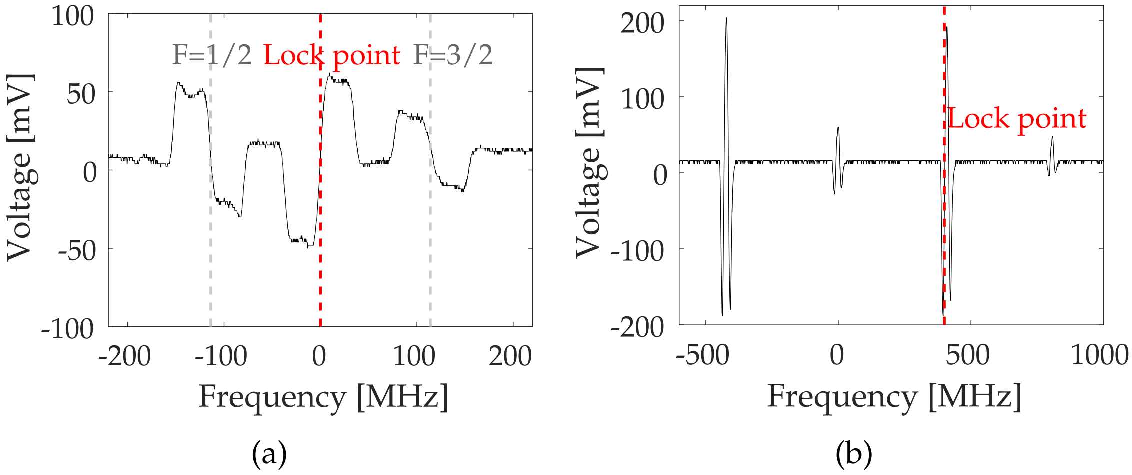

Figure 4.5: **(a)** Error signal of the laser lock, which is obtained by Doppler-free saturation spectroscopy of lithium and by using frequency modulation technique as a locking technique. This signal is used to lock the first laser of the lithium laser system generating the MOT light. **(b)** Error signal of the laser offset lock, which is used to lock the second laser with a frequency offset relative to the first laser. The feature at zero MHz is the carrier and the two bigger features to each side are the red and blue sideband respectively. The second laser generates the light for slowing, optical pumping and imaging.

4.2.3 Combining Sodium and Lithium Laser Light

As sodium and lithium share the same Zeeman slower and as they are trapped at nearly the same position, their cooling, trapping and imaging light has to share the same optical path. In case of the Zeeman slower for example, the light is coupled into the same fiber and sent to the experiment table. In order to do so, the beams are overlapped on a polarizing beamsplitter. Due to the requirement that they have the same polarization (as the atoms experience the same magnetic field inside the Zeeman slower), a special waveplate from Casix is placed before the fiber. This waveplate does not change the polarization for sodium light but acts a $\lambda/2$ waveplate for lithium light, resulting in the same polarization for both wavelengths.

The MOT light for both species is coupled separately into a fiber and sent to a fiber splitter[8], which divides the light into six MOT beams with equal power (up to $\pm 5\%$). The beam for sodium and lithium are overlapped on the experiment table in the same way as for the Zeeman slower but separately for every spatial direction.

For debugging the system and for example for aligning the plug and optical dipole beams it is helpful to have an imaging system along three perpendicular axes. For

---

[8] 1×6 polarization maintaining Coupler Array from Evanescent Optics Inc.

this purpose, the imaging beam is sent to a fiber switch[9], which allows switching between eight different fiber outputs and therefore granting the possibility to switch the imaging direction.

4.3 Zeeman Slower

The Zeeman slower is the first instance to slow the atoms leaving the oven. At first, this section describes the working principles of a Zeeman slower, and discusses different design options. A variable pitch spin-flip Zeeman slower is chosen and its construction is explained afterwards. Finally, the magnetic field is tested and perfect agreement with the desired field is shown, a perfect starting point to slow sodium and lithium atoms.

4.3.1 Working Principle of a Zeeman Slower and Design Considerations

The sodium and lithium atoms leaving the oven have a peak velocity of $750\,\mathrm{m\,s^{-1}}$ and $1500\,\mathrm{m\,s^{-1}}$ respectively and need to be slowed down to a velocity smaller than the capture velocity of the MOT, which is $70\,\mathrm{m\,s^{-1}}$ for sodium and $50\,\mathrm{m\,s^{-1}}$ for lithium. The capture velocity is the velocity corresponding to the maximum spontaneous force and is given by Equation 4.25. The deceleration is achieved by the implementation of a Zeeman slower, which is described in this section.

As the atoms leave the oven and travel along the Zeeman slower towards the MOT they absorb photons from a counter propagating laser beam. Due to their velocity, the atomic resonance frequency is shifted by the Doppler shift, namely by an amount equal to $\delta_v = -kv$, where k is the wavenumber of the laser and v the velocity of the atoms. As the atoms scatter photons and their velocity changes, also the atomic resonance frequency changes. This has to be accounted for and the easiest way is to make use of the Zeeman shift. The shape of the magnetic field of the slower is chosen in such a way that the atomic resonance frequency remains resonant with the slowing light during the whole deceleration process.

The counter propagating laser light is usually circularly polarized, therefore driving either $\Delta m_F = -1$ or $\Delta m_F = +1$ transitions depending on the handedness of the

---

[9] Leoni, model eol $1x8$, FC/APC, $PM630$

polarization. Note that depending on the field range these driving transitions are closed, hence no transition to a dark state is possible. A closer look at the frequency dependence of the $\Delta m_F = +1$ (σ^+-polarization) shows that the resonance frequency decreases with decreasing magnetic field. Hence, this enables the implementation of a decreasing magnetic field slower, as the Doppler shift decreases with decreasing velocity is possible. On the contrary, using the $\Delta m_F = -1$ transition (σ^--polarization) permits the realization of an increasing magnetic field slower as the resonance frequency decreases with increasing magnetic field. Besides these two possible magnetic field configurations there is a third option, namely the spin-flip Zeeman slower, which consists of a decreasing and an increasing field section with a zero crossing of the magnetic field in between. In the lab frame the spin of the atoms does not change but the sign of the magnetic field changes.

The advantages and disadvantages of the above mentioned design options are as follows. First of all, in case of a decreasing magnetic field slower the field is zero at the end of the slower, where the magneto-optical trap (MOT) is located. This means that the atoms in the MOT are still resonant with the slower photons, which can disturb the atoms unintentionally. On the other hand, the MOT can be placed very close to the end of the Zeeman slower and hence reduce the divergence of the atomic beam leading to a higher atomic flux available for the MOT.

Secondly, in case of an increasing field slower the abrupt change in magnetic field at the end of the slower helps the atoms to quickly leave the resonance condition. Therefore, the detuning of the atoms in the MOT relative to the slower light can be big enough such that they are not disturbed by the slower light.

A disadvantage of both mentioned configurations is the relatively high peak magnetic field, which is necessary to slow down the atoms. This brings us to the third option, the spin-flip Zeeman slower. It has a considerably lower peak magnetic field and therefore less current and less cooling of the coil is needed to generate the field. In addition, the finite magnetic field at the end of the slower leads to a sharp velocity distribution as the atoms quickly fall out of resonance. For these reasons, we decided in favor of a spin-flip Zeeman slower.

Another aspect to consider is whether the cooling transition is closed in the magnetic field region chosen for the operation of a Zeeman slower. The cooling transition used for sodium is the $|3^2S_{1/2}, F = 2\rangle \rightarrow |3^2P_{3/2}, F' = 3\rangle$ transition and for lithium it is the $|2^2S_{1/2}, F = 3/2\rangle \rightarrow |2^2P_{3/2}, F'\rangle$ transition. In case of lithium the intermediate regime where neither F (at low field) nor I and J (at high field) are good quantum numbers reaches from approximately 3 Gauss to 100 Gauss. In this magnetic field region the allowed transitions are difficult to predict and transition to other states can occur. For instance, at zero field the m_F levels are degenerate and atoms can additionally fall into the $|F = 1/2\rangle$ ground state. Hence, additional light is needed to repump the atoms into the desired state used for cooling. Likewise, it is necessary to pump the atoms into the desired state when the atoms come out of the oven as they are initially in their electronic ground state. Repump light is used for same reasons for sodium as well.

Our Zeeman slower design is optimized for sodium as the goal was to maximize the cold cloud of bosonic sodium atoms, which serves as a coolant for the fermionic species. If the detuning of the slowing light for lithium is chosen accordingly, lithium is slowed to a good degree as well. However, a smaller total fraction of the atoms coming out of the oven is slowed as its peak velocity is higher (by a factor of two approximately due to their difference in mass). As winding pattern we chose a single-layer variable pitch coil pattern for the decreasing field coil presented in [86] and a two-layer variable pitch design for the increasing field coil. This has several advantages over the common way of using a solenoid with a variable number of layers. First of all, there are no steps in the magnetic field due to a change in the number of layers when going from high fields to low fields as the distance between the windings is adjusted continuously and smoothly. Secondly, the desired winding pattern can be calculated analytically and if the coil is wound precisely according to the calculations, later adjustments and improvements are unnecessary. Indeed, we didn't have to adjust the winding pattern at all. The staff members of our mechanical workshop did a great job in machining a groove into the outside of a tube according to the calculated pattern, which then was used to wind the coils. The measured magnetic field of these coils (see Figure 4.7) agrees very well to the calculated and simulated field.

4.3.2 Construction of a Variable Pitch Spin-Flip Zeeman Slower

The design process of our Zeeman slower closely follows other well performing Zeeman slowers [66, 87] and is now described in more detail. The magnetic field as a function of position desired to keep the atoms resonant with the slower light is given by [72]

$$B(z) = \frac{\hbar\delta}{\mu'} - \frac{\hbar k}{\mu'}\sqrt{v_c^2 - 2a_\eta z} \quad , \tag{4.12}$$

where δ is the detuning and $\mu' = \mu_B \left(g_e m_e - g_g m_g\right)$. Here, μ_B is the Bohr magneton and $g_{e,g}$ are the Landé factors of the excited and ground state respectively, k is the wavevector of the slowing light. The capture velocity v_c describes the highest velocity of the atomic velocity distribution, which are still slowed down. The maximum deceleration a_{max} is given by $a_{max} = \hbar k\Gamma/2m$, where Γ is the natural linewidth. The reduced deceleration $a_\eta = \eta \cdot a_{max}$ accounts for imperfections in the design and realization of for example the magnetic field and typically a value between 0.4 and 0.8 is chosen. We use $\eta = 0.55$ for our slower. From (Equation 4.12) it can be seen that by changing the detuning of the slowing light the initial offset field can be adjusted. This detuning is chosen such that the detuning at the end of the Zeeman slower is high enough to not disturb the atoms in the MOT. In addition, in case of a spin-flip slower it is optimized in a way that the peak magnetic field is minimized. Last but not least, the desired shift in frequency should be achievable by means of commercial available acousto optic modulators (AOM).

After having calculated the magnetic field of the Zeeman slower the next step is to consider the flux of atoms. The flux of slow atoms as a function of the slower length can be calculated accordingly to [87]

$$Q_{\text{slow}}\left(L_{\text{ZS}}\right) \propto \frac{A_{\text{oven nozzle}}}{\left(L_{\text{ZS}} + L_{\text{OZS}}\right)^2}\left[1 - \left(1 + \frac{mL_{\text{ZS}}a_\eta}{k_B T}\right)\exp\left(-\frac{mL_{\text{ZS}}a_\eta}{k_B T}\right)\right] \quad . \tag{4.13}$$

Here, $A_{\text{oven nozzle}}$ is the oven nozzle area, L_{ZS} the Zeeman slower length, L_{OZS} is the distance between oven nozzle and entrance of the Zeeman slower and m the mass of an atom. In the experimental setup, L_{OZS} is nonzero as some space for the collimator plate and atomic beam shutter is needed. In our setup, L_{OZS} is 45 cm. With an eta η of 1 this function has a peak at about 45 cm. However, as mentioned before the slower length is almost doubled (or equivalently η is set to ≈ 0.5) to account for imperfections. The choice of the capture velocity v_c and the design parameter η yields the length of the Zeeman slower [87]

$$L_{\text{ZS}} = \frac{1}{2}\frac{v_c^2}{a_\eta} \quad . \tag{4.14}$$

The oven temperature sets the velocity distribution of the atoms arriving at the entrance of the Zeeman slower. The highest velocity v_c should be set slightly higher than the peak velocity of the Maxwell-Boltzmann distribution to ensure that a large fraction of atoms is slowed. In our case the temperatures of the oven are 390°C for lithium and 330°C for sodium. As mentioned earlier, the slower is optimized for sodium and with the above given oven temperature the peak velocity is equal to $v_{\text{peak}} = 750\,\text{m}\,\text{s}^{-1}$. The capture velocity is set to $v_c = 950\,\text{m}\,\text{s}^{-1}$, $\eta = 0.55$ and the detuning is set to $\delta = -2\pi \cdot 500\,\text{MHz}$, which also sets the relative length of the two parts of the spin-flip Zeeman slower (see Equation 4.12). This also determines the detuning for the lithium slower light to be $\delta = -2\pi \cdot 420\,\text{MHz}$. Given this choice of parameters the ideal magnetic field can be calculated and is shown in Figure 4.7.

Variable Pitch Coil Winding Pattern

The next step is to calculate the desired coil pattern to generate the ideal magnetic field. This is done very similar to the technique described in [86]. As mentioned before, we chose a variable pitch pattern. The helical coil can be parametrized using the following equations

$$\begin{aligned}
\mathbf{r}(p) &= [x(p), y(p), z(p)] \quad , \\
x(p) &= R\cos\left(\theta(p)\right) \quad , \\
y(p) &= R\sin\left(\theta(p)\right) \quad , \\
z(p) &= c_7 p + c_8 \quad , \\
\theta(p) &= \sum_{m=0\cdots 6} c_m p^m \quad ,
\end{aligned} \tag{4.15}$$

where $p \in [0, 2\pi]$ and z is the distance along the coil and x and y are the transverse axes relative to the z-axis and R is the fixed radius of the coil. The angle θ describes the relative position along the helix relatively to the starting point.

The magnetic field for such a coil at a position $\mathbf{r'} = \mathbf{r} + (0, 0, z')$ is given by (Biot-Savart law)

$$\mathbf{B}_{helix}(z') = \frac{\mu I}{4\pi} \int_0^{2\pi} \frac{(d\mathbf{r'}/dp) \times \mathbf{r'}}{r'^3} dp \quad , \tag{4.16}$$

where z' is a position on the coil axis, μ is the magnetic permeability and I is the current. Integrating gives

$$dB_z = \frac{(dx(p)/dp) \cdot y(p) - (dy(p)/dp) \cdot x(p)}{\left(x(p)^2 + y(p)^2 + (z(p) - z)^2\right)^{3/2}} \tag{4.17}$$

and fitting the result to the ideal magnetic field along the symmetry axis along the coil (while fixing the radius of the coil and leaving the coefficients c_i as free parameters) gives the desired winding pattern shown in Figure 4.7. Two coils creating the decreasing and increasing field are pictured. The small size of the increasing field coil allows this coil to be placed very close to the location of the MOT (only 4.5 cm away) ensuring a high flux of atoms to the MOT.

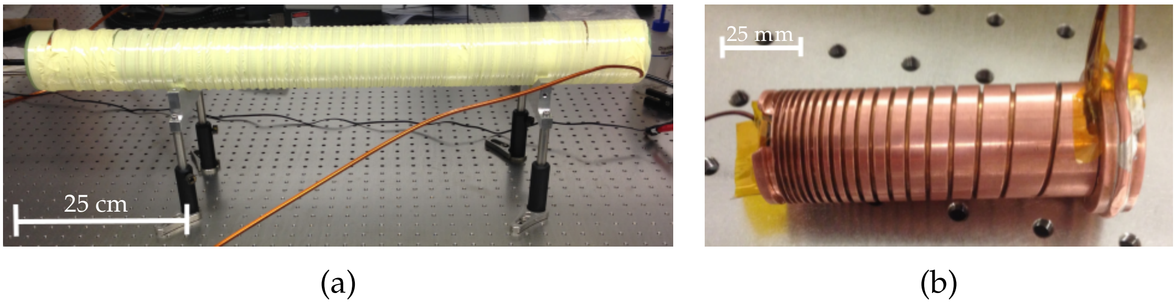

(a) (b)

Figure 4.6: Pictures of the variable pitch coils for creating the Zeeman slower field: **(a)** Decreasing field coil: a single layer with variable pitch creates the magnetic field for the first part of the Zeeman slower. The entrance of the Zeeman slower is shown on the right hand side where the windings lie closest to each other and therefore create the highest magnetic field along the symmetry axis. The outer dimensions of the copper wire are 4 mm x 4 mm. It is electrically insulated with Kapton and with a 2.5 mm wide hole in the center for water cooling. **(b)** Increasing field coil: a variable pitch coil with two layers. The small size of the coil allows this coil to be placed very close to the location of the MOT ensuring a high flux of atoms to the MOT.

4.3.3 *Testing the Magnetic Field of the Zeeman Slower*

The magnetic field of the two Zeeman slower coils is measured with a Hall-probe sensor and compared to the predicted values in order to ensure a high performance of the slower. The tests are performed at lower current (25 A instead of 400 A, which is used in the experiment for the decreasing field coil and 10 A instead of 30 A for the increasing field coil) and no water cooling had to be attached. As the field is proportional to the current, this gives an accurate description of the field. The results can be seen in Figure 4.7. The measured fields agree very well with the predicted fields such that no adjustments or improvements of the coils were necessary afterwards. Note, the field of the decreasing field coil was measured on the symmetry axis, whereas the field of the increasing field coil was measured off-axis as the Hall-probe sensor was too big for an on-axis measurement. Hence, the measured field is compared to the predicted offset field.

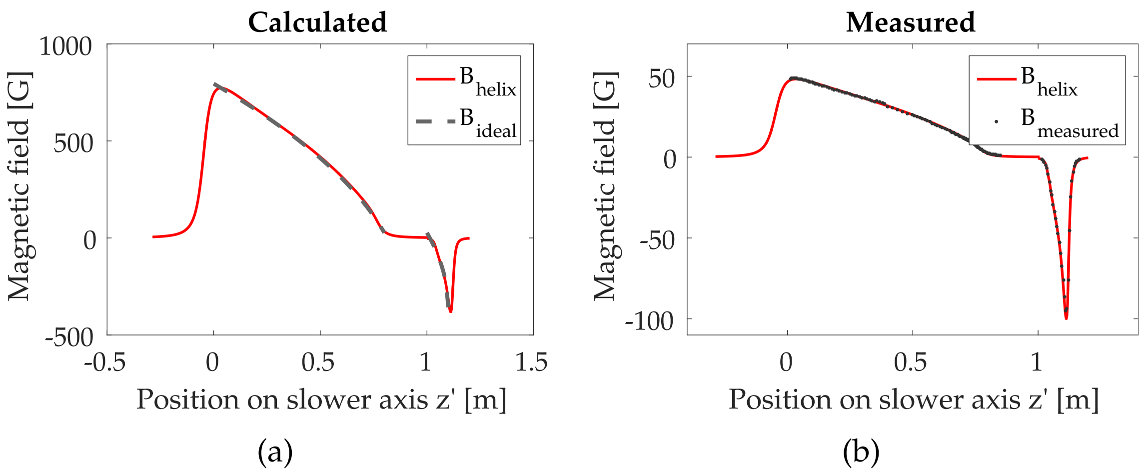

Figure 4.7: Comparison of the ideal magnetic field of the Zeeman slower to the measured magnetic field: **(a)** Dashed line: ideal magnetic field given by Equation 4.12 for the following parameters: detuning $\delta_{Na} = -2\pi \cdot 500\,\mathrm{MHz}$, capture velocity $v_{c\,Na} = 950\,\mathrm{m\,s^{-1}}$ and slower length L =0.9 m. Solid line: Calculated magnetic field produced by a helical coil, which best fits the ideal field. **(b)** Comparison between calculated field produced by the helical coils and measured field after construction. Testing was done at lower current. Shown are the calculated field of the helical coil for 25 A (decreasing field coil) and for 10 A (increasing field coil). Error bars of field measurement are smaller than the dot size. The measured fields agree well with the predicted fields. No adjustments or improvements of the coil were necessary after winding them.

4.3.4 Simultaneous Slowing of Sodium and Lithium

As mentioned above, our slower is optimized for sodium but also used to slow lithium atoms. The question to be answered here is how well this actually works [88]. The capture velocity of the Zeeman slower is given by

$$v_c = \frac{\mu_B B(0)}{\hbar k} \propto \frac{1}{k} \tag{4.18}$$

and the most probable velocity of the atoms coming out of the oven is

$$v_{\text{peak}} = \sqrt{\frac{2k_B T}{m}} \quad . \tag{4.19}$$

Therefore, the capture velocities of sodium and lithium are comparable in contrast to the peak velocities. This is due to the difference in mass. This means that a much smaller fraction of the thermal distribution of the lithium atoms is slowed down compared to the sodium atoms. Furthermore, one can compare the deceleration of both species achieved with the same slower, namely the same magnetic field. The deceleration of atoms in the slower is given by (recall Equation 4.14)

$$a = \frac{1}{2}\frac{v_c^2}{L_{\mathrm{ZS}}} \propto \frac{1}{k^2} \quad . \tag{4.20}$$

This leads to a comparable deceleration of both species in the same slower (recall Equation 4.20)

$$\frac{a_{\mathrm{Li}}}{a_{\mathrm{Na}}} = \left(\frac{671}{589}\right)^2 \approx 1.3 \quad . \tag{4.21}$$

However, as mentioned before, the maximum deceleration at maximum light intensity is given by $a_{\max} = \hbar k \Gamma / 2m$, which is $190\,\mathrm{cm\,s^{-2}}$ for lithium and $90\,\mathrm{cm\,s^{-2}}$ for sodium. This means that a slower optimized for sodium slows lithium atoms at a smaller fraction of the maximum deceleration. Nevertheless, this is not a problem as we achieve to trap more than 10^9 lithium atoms in the MOT as described in the following section.

4.4 Magneto-Optical Trap (MOT)

After the atoms have been slowed by the Zeeman slower they are trapped and cooled in the magneto-optical trap. With the aim to sympathetically cool fermionic lithium atoms with bosonic sodium atoms we can derive an optimum trapped atom number ratio between the two species. The sodium atoms are evaporatively cooled using a radio frequency sweep in the magnetic trap. If a sample of atoms is efficiently cooled using evaporation, the phase-space density can be increased by a factor of about 10^6 while the atom number is reduced by a factor of about 100 [89]. This means that for sympathetic cooling, the initial atom number of the bosonic species has to be higher by a factor of 100. We therefore maximize the sodium atom number in the magneto-optical trap (MOT) and minimize their temperature while keeping the lithium atom number lower by a factor of about $50 - 100$. Before giving the experimental details of the two-species MOT, a brief introduction of the trapping principles of a MOT is given in the next section.

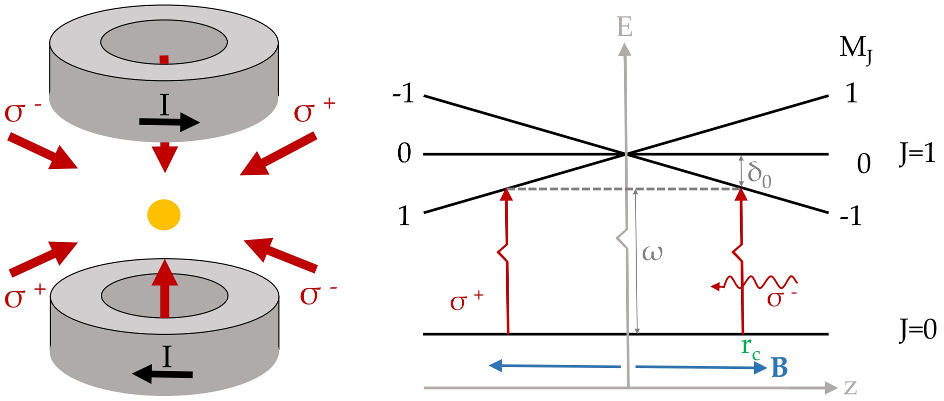

(a) (b)

Figure 4.8: Working principle of the magneto-optical trap (MOT): **(a)** Coil and laser beam setup for creating the magnetic gradient field and the counter-propagating laser beams, which lead to a velocity dependent force trapping and cooling the atoms. **(b)** Illustration of the mechanism of a MOT for the case where the atom is initially in the ground state with total angular momentum $J = 0$. By absorbing a photon it is transferred to the excited state with $J = 1$. The presence of the magnetic gradient field leads to a position depend shift of the energy levels of the excited state due to the Zeeman shift. Two counter propagating laser beams with circular polarization illuminate the atom. Their frequency is lower than the atomic resonance frequency at zero magnetic field (red detuned). Because of the selection rules, atoms moving to the right absorb photons of the σ^--polarized light, whereas atoms moving in the opposite direction absorb photons from the σ^+-polarized beam. Hence, if the atoms try to leave the trap, they are pushed back to the center as a result of the scattering force.

4.4.1 Trapping Principle of a Magneto-Optical Trap (MOT)

After the Zeeman slower the atoms arrive at the position of the MOT, our first stage of trapping. A MOT is a trap, which cools the atoms further and confines them spatially. In more detail, three pairs of counter propagating laser beams and a magnetic gradient field are used. The latter causes an imbalance in the scattering force of the laser beams and confines the atoms due to the radiation force. This idea was first suggested by Jean Dalibard and successfully demonstrated at the Bell Laboratories in cooperation with MIT in 1987 [90].

Figure 4.8 illustrates the mechanism of a MOT for the simple case of an atom in a ground state with a total angular momentum $J = 0$ and an excited state characterized by $J = 1$ where the atom is initially in the ground state with total angular momentum $J = 0$. By absorbing a photon it is transferred to the excited state with $J = 1$. The presence of the magnetic gradient field leads to a position depend shift of the energy levels of the excited state due to the Zeeman shift. Two counter-propagating laser beams with circular polarization illuminate the atom. The laser frequency is lower than the atomic resonance frequency at zero magnetic field (red detuned). Because of the selection rules, atoms moving to the right absorb photons of the σ^--polarized light, whereas atoms moving in the opposite direction absorb photons from the σ^+-polarized beam. Hence, if the atoms try to leave the trap, they are pushed back to the center as a result of the scattering force. This mechanism even holds true in three dimensions and for atoms with much more complicated level structures. Theoretical proof is nontrivial but many experiments have shown that it works very well and that the realization of a MOT is a powerful tool to create a cold atom source for more sophisticate experiments.

The theory of Doppler cooling for two level atoms predicts a minimum temperature of atoms in a MOT [72]

$$T_D = \frac{1}{2}\frac{\hbar\Gamma}{k_B} \quad , \tag{4.22}$$

which is 240 µK for sodium ^{23}Na and 140 µK for lithium ^{6}Li. Lower temperatures can be achieved by applying sub-Doppler cooling methods, such as polarization gradient cooling. One example of polarization gradient cooling is optical molasses (see subsection 4.4.6), which is applied after keeping the molasses beams on before transferring them into the magnetic trap. As the hyperfine states of the excited states of lithium are unresolved, polarization gradient methods are inefficient for this species. That is why we perform optical molasses for sodium only.

One design goal of this experimental setup was to achieve a large cloud of cold bosonic sodium atoms, which are later used to sympathetically cool fermionic lithium atoms. The first stage in order to do so was to ensure a high flux of cold atoms, which can be trapped in the MOT see section 4.3. The maximized flux then needs to be trapped as efficient as possible.

While loading the MOT from a slowed beam of atoms, the number of atoms in the MOT as a function of time can be described by [91]

$$N(t) = R\tau\left(1 - e^{-t/\tau}\right) \quad , \tag{4.23}$$

where R is the loading rate of the MOT and τ describes the lifetime due to collisions with atoms from the background gas and due to light induced losses. Two-body loss rates are neglected here, which is valid at low densities (the main two boy loss rates in a MOT are losses due to spin changing collisions and radiative escape). On the other hand, the capture radius of a MOT is given by [91]

$$r_c = \frac{\hbar\delta}{\mu' \frac{\partial B}{\partial z}} \quad , \tag{4.24}$$

where δ is the detuning and μ' is given by $\mu' = \mu_B \left(g_e m_e - g_g m_g \right)$. This relation can be read off from Figure 4.8. From this equation it is clear that the bigger the detuning, the bigger the capture range is. On the other hand, the temperature of the optical molasse decreases if one increases the detuning [92] and the scattering rate goes down as it is maximum on resonance. A greater gradient compresses the MOT, which might be in favor of loading into a magnetic trap (to mode match the two traps) but also enhances two-body losses. In addition, the capture velocity of the MOT can be found using the expression of the capture radius r_c and kinematic relations [91]

$$v_c^{\mathrm{MOT}} < \sqrt{\frac{2 r_c F_{\mathrm{spont}}}{m}} \quad , \tag{4.25}$$

where F_{spont} is the spontaneous light force. The higher the capture velocity of the MOT, the more atoms can be trapped from the slowed beam (it essentially increases the acceptable capture velocity of the Zeeman slower). Typically values for the capture velocity of a MOT are $70\,\mathrm{m\,s^{-1}}$ for sodium and $50\,\mathrm{m\,s^{-1}}$ for lithium compared to the capture velocity of pure molasses ($v_c^{\mathrm{molasses}} = \Gamma/k$), which are approximately $6\,\mathrm{m\,s^{-1}}$ for sodium and $4\,\mathrm{m\,s^{-1}}$ for lithium.

Besides the above mentioned criteria, the beam diameter of the counter-propagating laser beams has to be big enough such that capture radius r_c is not limited by the size of the laser beams.

Regarding the maximum density in a MOT there are two limitations. First of all, during collisions of atoms in the ground and the excited state, the excitation energy can be transformed into kinetic energy and the atoms are lost from the trap. Secondly, scattered photons can be reabsorbed leading to a repulsive force between the atoms. This mechanism is called radiation trapping. At a certain atomic density this radiation pressure balances the confining forces of the laser beams. Hence, an increase of atom number leads to an increase in size of the MOT but not to an increase in density. One solution to this problem is the implementation of a so-called dark-SPOT, which is described in subsection 4.4.3.

4.4.2 Alignment of the MOT

To ensure a stable MOT operation and a MOT containing a large number of atoms, several laser beams have to be overlapped with the center of the magnetic gradient coils; six beams for the lithium MOT, six cooling beams and one repumper beam for the sodium dark-SPOT MOT. Furthermore, these beams have to be collimated well, they have to have the correct polarization and the counter-propagating beams should be power balanced to ensure high efficiency sub-Doppler cooling while performing optical molasses. The cooling light is split into six separate beams using a fiber splitter[10]. The fiber ends are connected cage systems containing a telescope (to enlarge the beam size to a diameter of 30 mm for sodium and 22 mm for lithium), a polarizing beam splitter (to overlap the light of the lithium MOT with the cooling light of the sodium MOT), a half-waveplate (which rotates the polarization of the sodium light and leaves the lithium light unaffected) and a quater-waveplate (with a design wavelength of 633 nm, which creates the circularly polarized light necessary for both MOTs), see Figure 4.9. The cage systems are mounted vertically onto the optical table to save space for dipole trap, plug and imaging optics. We designed the cage system, which was manufactured by Radiant Dyes with bigger 45° mirrors, which enable the use of 30 mm wide beams. After collimating the large beams using a shear plate collimator, the beams are aligned through the vacuum chamber. The procedure for aligning is as followed. The zero position of the magnetic gradient field is known from the relative position of the coils and the CAD file of the experiment can be used to find the trajectories of the beams relative to some vacuum components. We printed transparencies of the vacuum windows indicating the MOT beam positions. This allowed a straight forward and easy alignment of the counter propagating laser beams. The polarization of each beam in front of the vacuum chamber was checked and optimized using a polarization analyzer from Schäfter+Kirchhoff.

Balancing the power of counter-propagating laser beams was achieved by comparing the power measured with large area photodiodes and using a half-waveplate and a polarizing beam splitter to adjust the power set to the atoms, see Figure 4.9. Finer adjustments were achieved by looking at the increase of the cloud size while performing optical molasses and optimizing the growth for isotropic expansion.

Besides aligning the laser beams, earth and stray magnetic fields have to be compensated. This is achieved by running the MOT coils at much higher current leading to

---

[10] Evanescent Optics Inc., 1 × 6 polarization maintaining Coupler Array

a higher gradient and therefore confining the atoms to a much smaller region, which is less influenced by stray fields. The position of the atoms on two cameras, which are orthogonal to each other, is marked. Afterwards at again low magnetic fields, compensation fields are applied in such a way that the position of the MOT coincides with the position at high magnetic fields. These compensation field coils surround the main vacuum windows, see Figure 3.5.

Furthermore, when turning off the Zeeman slower coil the position of the MOT should not change. For this purpose, a compensation coil at the opposite side of the main chamber was installed, which cancels the Zeeman slower field at the position of the MOT and, which is ramped down together with the Zeeman slower field.

Aligning the lithium MOT while having the sodium MOT as a reference proofed to be much easier as the magnetic fields were already correct and as the beams only had to be overlapped with the prealigned sodium MOT beams.

4.4.3 Sodium dark-SPOT

The realization of dark-SPOT for sodium was first demonstrated in 1993 by [93] and the name is an abbreviation for dark spontaneous-force optical trap. It circumvents the problem of radiation trapping as most of the atoms are in a dark state and therefore allows an increase of density by a factor of about 100 compared to a bright MOT. It is nowadays used in most ultracold sodium machines. The implementation is simple and it is explained in the following.

In case of a bright MOT, repumper beams ($|3^2S_{1/2}, F = 1\rangle \rightarrow |3^2P_{3/2}, F' = 2\rangle$) and cooling beams ($|3^2S_{1/2}, F = 2\rangle \rightarrow |3^2P_{3/2}, F' = 3\rangle$) are overlapped. Usually, the repumper frequency is created with the help of an EOM, which creates sidebands at the desired frequency. In contrast, a dark-SPOT MOT uses repumper light only at the outer region of the MOT allowing the atoms in the center to fall into the ground state. Therefore, the atoms in the center are not resonant to the trapping light allowing higher densities to be reached as the radiation pressure is minimized. This is usually achieved by using one (or more) repumper beams, which are hollow in the center. In our setup we overlap the repumper beam with one of the cooling beams on a beam splitter. The hollow beam is created by imaging a black dot (a dot non-transparent epoxy resin (Stycast) on an AR coated window) onto the center of the MOT (see Figure 4.9). It is important to make sure that the center of the repumper beam does not contain any repumper light due to diffraction effects as this limits the achievable density. The

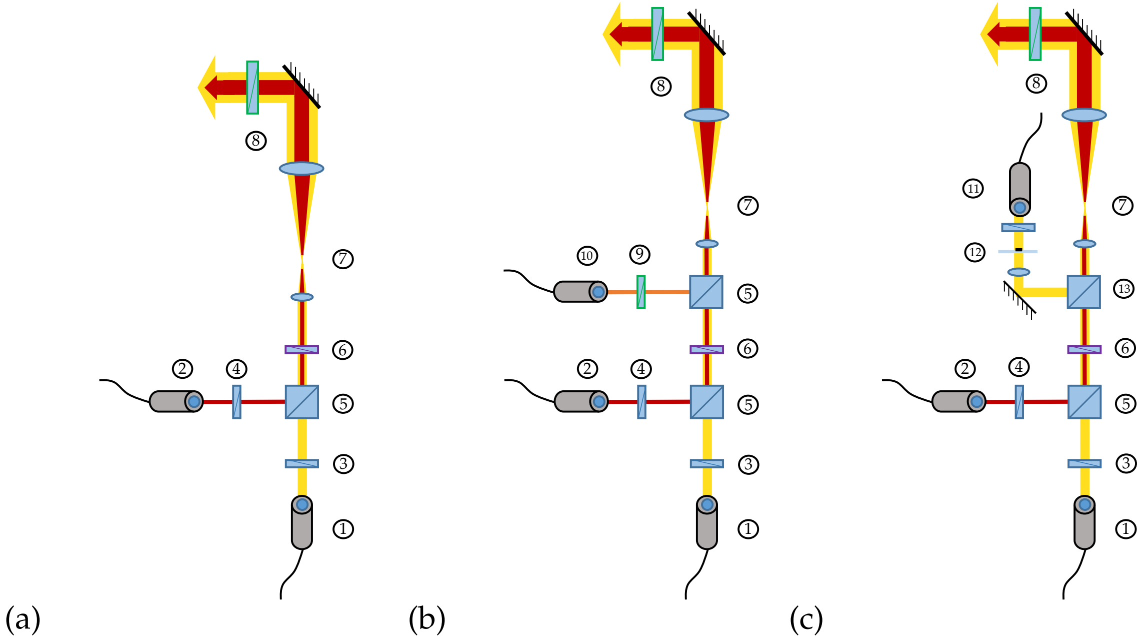

Figure 4.9: Combining the MOT light on experiment table: **(a)** Optics for overlapping sodium and lithium cooling light, **(b)** optics for overlapping MOT light with optical pump light and **(c)** optics for adding the (repumper) dark-SPOT light for sodium. **(1)** Sodium cooling light, **(2)** Lithium cooling and repumper light, **(3)** $\lambda/2$ waveplate for 589 nm, **(4)** $\lambda/2$ waveplate for 671 nm, **(5)** Polarizing beam splitter, **(6)** $\lambda/2$ waveplate for 589 nm and λ waveplater for 671 nm, **(7)** Telescope for enlarging beam diameters, **(8)** $\lambda/4$ waveplate for 633 nm, **(9)** $\lambda/2$ waveplate for 633 nm, **(10)** Optical pump light, **(11)** Dark-SPOT light for sodium MOT, **(12)** Dark-SPOT on AR coated window, which is imaged onto the atom, **(13)** Non-polarizing beam splitter. The optics are mounted in cage systems, which are positioned vertically onto the optical table to save space for other optics. A home made design of a cage system is used manufactured by Radiant Dyes.

diameter of the dark region at the position of the trap is approximately 10 mm. The radius of the MOT beams is about 15 mm and the beam power for the cooling light is 25 mW per beam corresponding to $3.3\,\mathrm{I}_{\mathrm{sat}}$, whereas we use 8 mW for the repumper beam corresponding to $0.2\,\mathrm{I}_{\mathrm{sat}}$. The frequency of the repumper light is generated by an AOM[11] with a center frequency of 1.8 GHz. The maximum efficiency of this high frequency AOM is 10 to 20%. Compared to a bright MOT, the dark-SPOT MOT looks much dimmer with a central dense region and a halo surrounding it.

After having set up the MOT for sodium for the first time, we compared the density with the densities presented in [93]. For this purpose we used a beam, which probes the absorption and thus the density while scanning the frequency over a broad range

---

[11] from Brimrose

($\approx \pm 100\,\mathrm{MHz}$). This can be achieved with the help of two AOMs. The first one is used to shift the frequency by $+200\,\mathrm{MHz} + \delta$, the second one shifts the frequency by $-(200\,\mathrm{MHz} - \delta)$ resulting in a net shift of 2δ. Placing a lens in between the two AOMs, this setup can be aligned in such a way that the beam does not stir and the fiber coupling efficiency can be maintained while changing the frequency. While during the bright MOT the hyperfine structure can be resolved, the optical density of the dark-SPOT MOT is so high that all the probe light gets absorb and the hyperfine structure can not be resolved anymore. From these measurements we concluded that we reach equivalent or even higher optical densities compared to [93]. The atom number in the MOT was later calibrated using the fluorescence light during optical molasses to be about $(2 \pm 2) \times 10^{10}$. Nowadays, the atom number is recorded in every experiment cycle by taking a fluorescence picture of the MOT with a CCD camera[12] during optical molasses.

A picture of the MOT is shown in Figure 4.10. The temperature of the atoms is $(125 \pm 8)\,\mu\mathrm{K}$ as described in subsection 4.4.7. The MOT is fully loaded after 3 s, which can be seen from the loading curves illustrated in Figure 4.11.

4.4.4 Compressed Lithium Magneto-Optical Trap (CMOT)

For the lithium MOT, a standard bright MOT configuration with six counter-propagating laser beams is used for loading, which is compressed at the end. Each of these beams contains the cooling frequency, which drives the $|2^2S_{1/2}, F = 3/2\rangle \rightarrow |2^2P_{3/2}, F'\rangle$ transition and the repumper frequency, which addresses the $|2^2S_{1/2}, F = 1/2\rangle \rightarrow |2^2P_{3/2}, F'\rangle$ transition. This repumper light is of special importance as the excited state is not resolved and hence many atoms can accumulate in the ground state through spontaneous emission and need to be pumped into a state resonant with the cooling light. For this reason, the repumper light for lithium is much stronger than the one for the sodium MOT (in units of $\mathrm{I}_{\mathrm{sat}}$). The total cooling light power is 72 mW, which corresponds to $7.6\,\mathrm{I}_{\mathrm{sat}}$. The beam radius for lithium is slightly smaller than for the sodium MOT (11 mm instead of 15 mm), which results in higher intensities.

In order to increase the density of the lithium atoms in the MOT and to reduce the temperature, we ramp the power of the MOT beams down to approximately $0.04\,\mathrm{I}_{\mathrm{sat}}$ and we reduce the detuning by approximately 10 MHz over a time scale of 25 ms. We

---

[12] Basler acA1300-60gm

keep the gradient constant as we do not want to compress the sodium MOT. Smaller detunings reduce the capture range but decrease the temperature.

A picture of the MOT is shown in Figure 4.10. The temperature of the atoms is measured using the time-of-flight expansion, see subsection 4.4.7 and at the end of the CMOT the temperature is estimated to be $(290 \pm 30)\,\mu\mathrm{K}$.

4.4.5 Coexisting Sodium and Lithium MOT

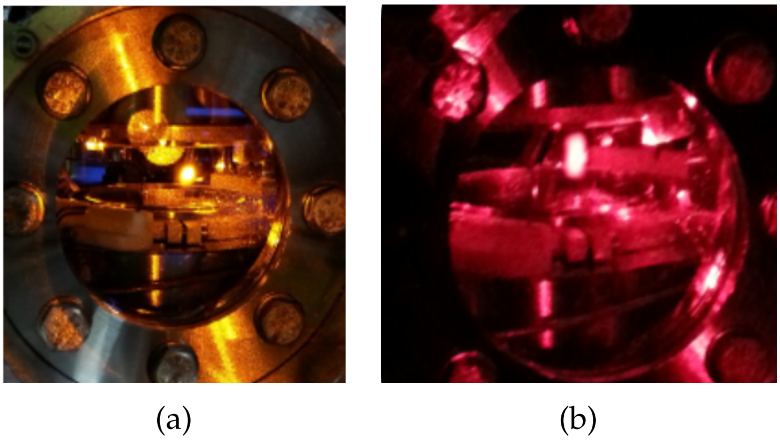

(a) (b)

Figure 4.10: Picture of a **(a)** sodium and **(b)** lithium MOT containing 10^{10} and 10^{9} atoms respectively.

The cooling and repumper light of both MOTs share the same optical path and the same magnetic field is used to produce the position and velocity dependent spontaneous light force to trap the two species in a MOT. Therefore, the two MOTs overlap. This gives rise to the question whether they influence each other and the coexistence leads to a smaller atom number. Indeed, the presence of the sodium atoms reduces the number of lithium atoms by 30%. However, the comparably dilute lithium cloud does not affect the loading of the sodium MOT. This is advantageous as our minimum temperature at maximum atom number of the molecular lithium BEC is mainly limited by the initial sodium atom number, which reflects our cooling capacity. The lithium atoms in the MOT are reduced on purpose to have an optimum ratio between atom number for evaporative cooling of sodium in the magnetic trap and sympathetic cooling of lithium.

In principle, the two MOTs can be slightly displaced relatively to each other by adjusting the power balance between two counter-propagating laser beams and therefore shifting the MOT from the zero magnetic field of the anti-Helmholtz field. However, there are two disadvantages of this method. First of all, this can lead to heating of the cloud when transferring the atoms from the MOT to the magnetic trap as the center positions do not coincide. And second, optical molasses is not as efficient as the power balance has been changed.

Figure 4.11 shows typical loading curves of the double species MOT before creating a molecular BEC out of lithium atoms. The loading of the sodium MOT starts 1 s before the loading of the lithium MOT. At the end of the MOT the lithium MOT is compressed and optical molasses is performed on sodium. From these loading curves one can extract the loading rate of the MOT. While atoms are still slowed with the Zeeman slower, the atom number in the MOT follows

$$N(t) \approx \frac{L}{R_{\text{1-body}}} \left(1 - e^{R_{\text{1-body}} t}\right) \quad , \tag{4.26}$$

where L is the loading rate of the MOT and $R_{\text{1-body}}$ is the one-body loss rate due to collisions with atoms from the background gas. Other loss mechanisms, e.g. many-body collisions are neglected here. The loading rates for the two MOTs are 10^{10} atoms per second for sodium and 10^9 atoms per second for lithium, which shows that the flux of slowed atoms from the Zeeman slower is high.

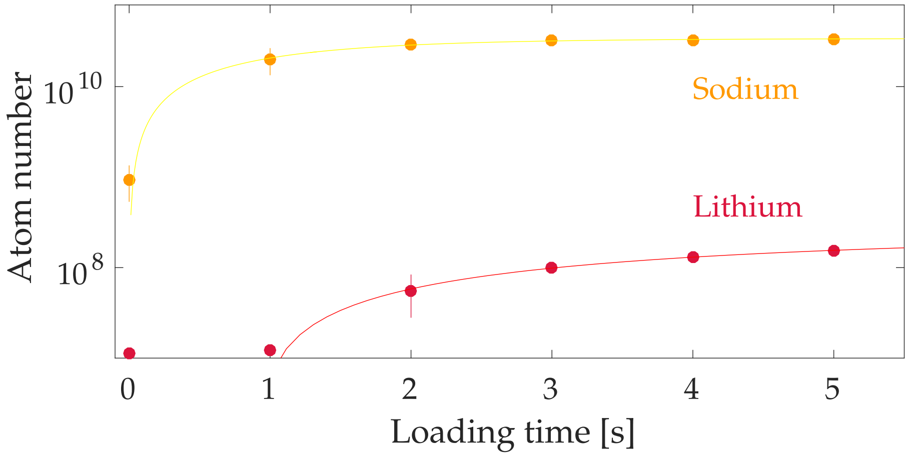

Figure 4.11: Typical loading curves of the double species MOT before creating a molecular BEC out of lithium atoms. The loading of the sodium MOT starts 1 s before the loading of the lithium MOT. At the end of MOT the lithium MOT is compressed and optical molasses is performed on sodium (not shown). The error bars denote the standard error of approximately three measurements. The atom number is calibrated within a factor of two. The solid lines are fits to the data following Equation 4.26.

4.4.6 Optical Molasses

Before loading both species into the magnetic trap, sodium is further cooled by optical molasses, which relies on the principle of polarization gradient cooling [92, 94]. As the hyperfine structure of the excited level of lithium is not resolved, this technique does not work for lithium. However, it is exploited for sodium.

For optical molasses, the gradient fields are turned off and cooler and repumper light for sodium are applied for 2 ms. This time was optimized for achieving the lowest temperature with the highest atom number in the molecular BEC of lithium atoms. Longer molasses times decrease the temperature of sodium but also decrease the atom number of lithium in the magnetic trap due to the longer expansion times.

4.4.7 Temperature of Atoms Confined in the MOT

The temperature of the atoms trapped in the magneto-optical trap was extracted from measurements monitoring the expansion of the cloud after switching off the trap. From the evolution of the cloud size, one can deduce the temperature by using the following relation of ballistic expansion [95]

$$\sigma(t) = \sqrt{\sigma_0^2 + \frac{k_B T}{m} t^2} \quad , \tag{4.27}$$

where σ describes the width of the Gaussian fitted to the cloud size. The data and fitted function can be seen in Figure 4.12. From this measurement the temperature of the atoms in the sodium and lithium MOT (after sodium molasses and at the end of the CMOT for lithium) are estimated to be (125 ± 8)µK and (290 ± 30)µK respectively. The temperature of the atoms in the sodium MOT can be further reduced by optimizing the molasses.

4.4.8 Conclusion

To summarize, chapter 4 describes the successful creation of a double species MOT containing laser cooled sodium and lithium atoms. The atom numbers achieved are comparable and higher than similar experiments (Na-Li experiments at MIT and in Heidelberg) and give an excellent starting point for further cooling in a magnetic trap

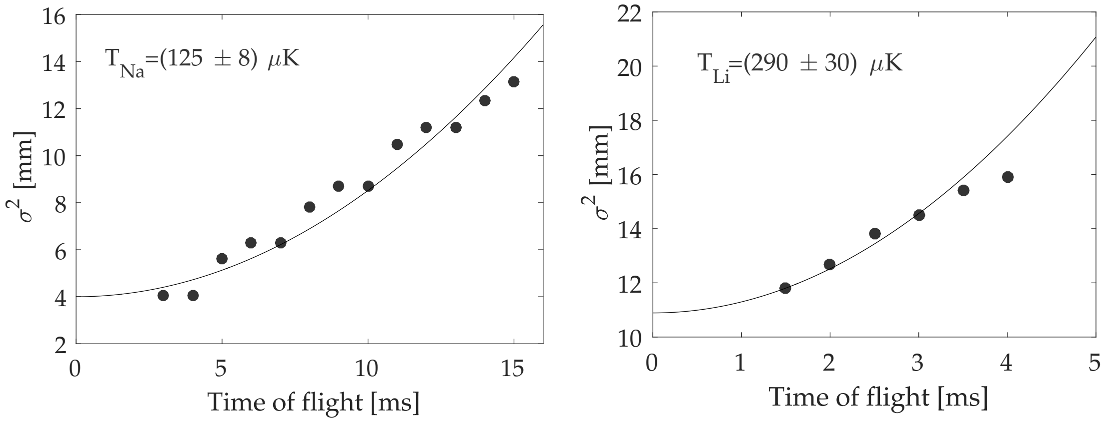

(a) (b)

Figure 4.12: Size of the cloud after releasing the atoms from the MOT /CMOT (and performing molasses for sodium) as a function of time for **(a)** sodium and **(b)** lithium. Solid lines show the fits (Equation 4.27) to data, which are used to extract the temperature. The temperature of the atoms in the sodium MOT can be further reduced by optimizing the molasses.

and dipole trap. A summary of the experimental sequence of the MOT loading and the molasses technique is sketched in Figure 4.13.

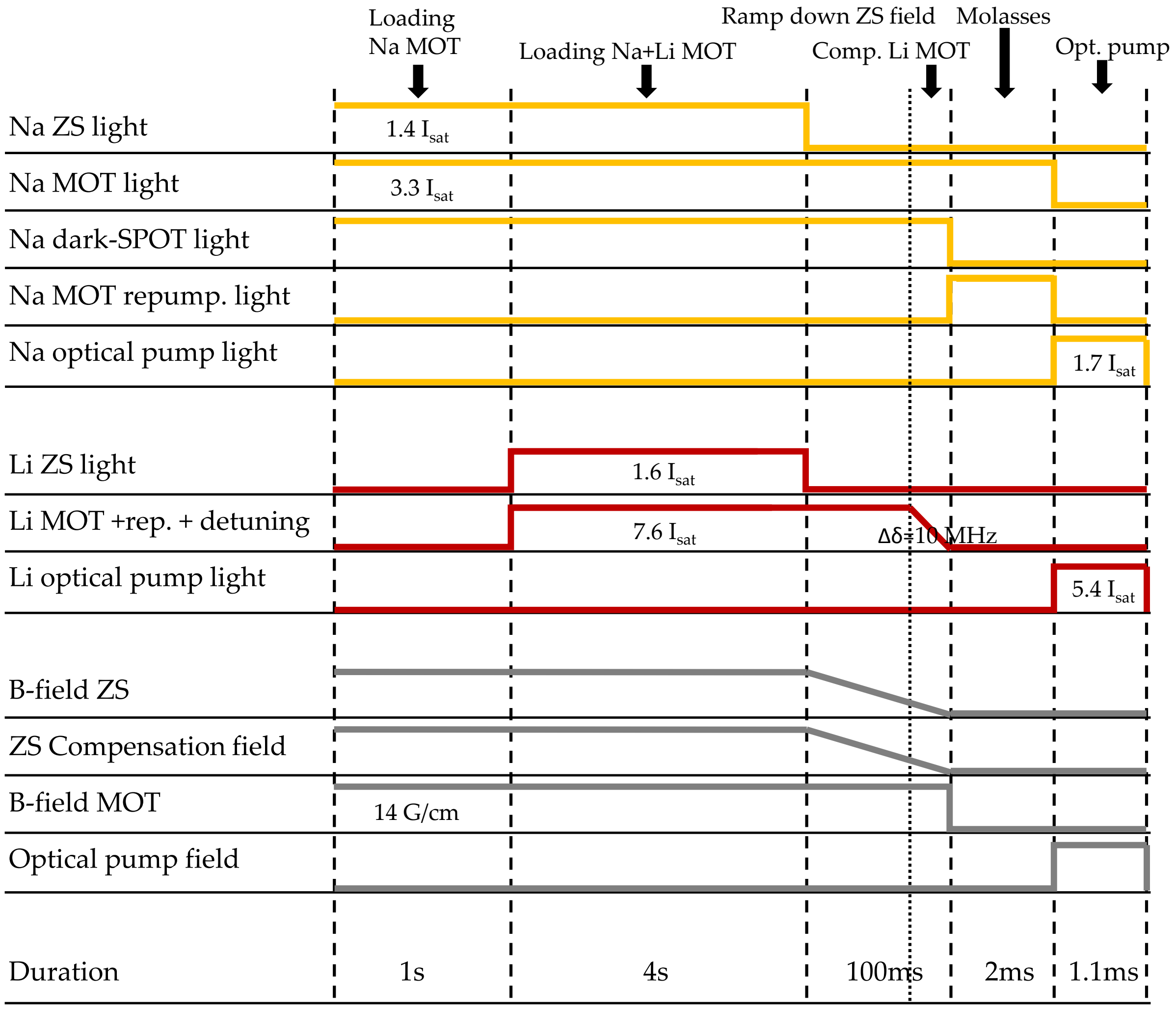

Figure 4.13: The experimental sequence of the MOT loading, molasses and optical pumping to the stretched state, which is loaded into the magnetic trap later on. For more details see text. The Zeeman slower (ZS) compensation field makes sure that when the Zeeman slower is turned off, the MOT position does not change. Time steps and powers as indicated are not to scale.

CHAPTER 5

Trapping and Cooling Neutral Atoms in an Optical Plugged Magnetic Trap

The creation of a quantum degenerate gas requires cooling methods, which go beyond the limit of laser cooling. One possible method to achieve this goal is the radio frequency (rf) evaporation of a precooled gas confined in a magnetic trap. This is done after the atoms have been trapped and laser cooled in the magneto-optical trap (MOT) and transferred to a magnetic trap. While sodium is cooled by means of rf evaporation, it thermalizes with lithium and therefore reduces the temperature of the lithium cloud. This is called sympathetic cooling. A magnetic trap is necessary to keep the atoms tightly confined ensuring a high collision rate guaranteeing efficient evaporation. The atoms are initially trapped by the magnetic gradient field of the MOT coils and are then transferred to the final magnetic trap by switching off the MOT gradient and turning on the final magnetic field coils. Both coil pairs, which generate the magnetic field for the magnetic trap, consist of two coils in anti-Helmholtz configuration generating a magnetic field gradient. We decided in favor of this simple quadrupole coil configuration as this leaves more space for optical access and as this one needs fewer coils than configurations such as the Ioffe-Pritchard or Cloverleaf trap. In addition, magnetic quadrupole traps provide a large trap volume and confine the atoms tightly due to the linearity of the potential, which is advantageous for efficient evaporation as it ensures high collision rates [96].

Nevertheless, there is one drawback of this simple magnetic trapping scheme. Close to the center of the magnetic trap where the magnetic field goes to zero non-adiabatic spin transitions to untrapped states can happen, which not only causes atom loss but also results in heating. This mechanism limits the maximum achievable phase-space density. To prevent this atom loss several different techniques have been realized, such as an early transfer into an optical dipole trap [97], introducing a time-orbital bias field [98] or by applying an optical repulsive potential [96, 99, 100]. We circumvent this so-called Majorana loss by applying the latter method. For this purpose, a blue detuned laser beam is focused to the center of the quadrupole trap creating the desired repulsive potential. The laser is focused to the center of the final magnetic trap position as it only becomes important at the end of the evaporation when the atoms get colder and accumulate at the bottom of the trap. This trapping configuration is called optical plugged magnetic trap. In the following, I will often refer to this trap as magnetic trap (MT) for simplicity.

When the atoms have reached their final position (given by the magnetic gradient field of the Feshbach coils, which is 3 mm below the window) radio frequency transfers the high energetic sodium atoms to an untrappable state. If they carry away more energy than the average energy of the trapped atoms, the temperature of the whole cloud is reduced. A prerequisite that this process happens efficiently is that the elastic collision rate is high such that the rethermalization happens on a time scale faster than any other loss processes, for example losses due to collisions with the background gas. If the density and the number of elastic collisions are kept high, this process can lead to an increase of the phase-space density, which is the requirement to achieve quantum degeneracy. While sodium is cooled by evaporation, favorable collision properties between sodium and lithium lead to sympathetic cooling of lithium.

This chapter first describes the principles of magnetic trapping, then continues with the properties of the optically plugged magnetic trap and finally demonstrates highly efficient radio frequency evaporation of sodium within only 5 s and simultaneous cooling of lithium. High loading and cooling rates enable increased rates for data acquisition while reducing errors due to drifts of example laser frequencies and magnetic fields yielding a perfect starting point for experiments with ultracold atoms.

5.1 Magnetic Trapping

Magnetic trapping relies on the interaction of the atom's magnetic moment $\boldsymbol{\mu}$ with an external magnetic field $\mathbf{B}$, which leads to a shift of the atomic energy [73, 101]. Classic electromagnetism predicts this energy to be

$$E = -\boldsymbol{\mu} \cdot \mathbf{B} \quad . \tag{5.1}$$

Quantum mechanically this interactions leads to a splitting of the energy levels into different Zeeman levels. At low magnetic field the energy of an atom in the hyperfine state $|F, m_\mathrm{F}\rangle$ is given by [62]

$$E(\mathbf{r}) = g_F m_F \mu_B \, |\mathbf{B}(\mathbf{r})| \quad . \tag{5.2}$$

Here, g_F is the g-factor for an atom with total atomic angular momentum $F = I + J$, μ_B the Bohr magneton and $\mathbf{B}(\mathbf{r})$ the magnetic field at position $\mathbf{r}$. This magnetic field dependence of the different hyperfine states (^{23}Na and ^{6}Li) is plotted in Figure 5.1. One distinguishes between two different set of states: States with lower energy at high magnetic field (so-called high field seeking states, where $g_\mathrm{F} m_\mathrm{F} < 0$) and states with lower energy at small magnetic field values (so-called low field seeking states, where $g_\mathrm{F} m_\mathrm{F} > 0$). Due to Maxwell's equations, only a magnetic field minimum in free space is allowed, not a maximum. Therefore, only low field seeking states can be trapped in pure magnetic traps. This trapping method for ultracold neutral atoms was first purposed by David Pritchard in 1983 [102] and first demonstrated by the group of William D. Phillips in 1985 [101]. Magnetic traps are the workhorse in most Bose-Einstein experiments and led to the first realization of a Bose-Einstein condensate in ultracold atoms in the group of E.Wieman and E. A. Cornell in 1995 [98] and shortly after in the group of W. Ketterle [96]. Cornell, Wieman, and Ketterle received the Nobel Prize in 2001 for their discovery.

In case of sodium the low field seeking states are $|2, 2\rangle$, $|2, 1\rangle$ and $|1, -1\rangle$. Mixtures of these states and pure $|2, 1\rangle$ samples can undergo spin exchange collisions leaving the two states $|2, 2\rangle$,$|1, -1\rangle$ as the only option for magnetic trapping. Lithium on the other hand can be magnetically trapped being in either the $|3/2, 3/2\rangle$ or the $|1/2, -1/2\rangle$ state (when not considering state, which can under go spin exchange collisions). At low temperatures only s-wave collisions are allowed and therefore ensures that spin

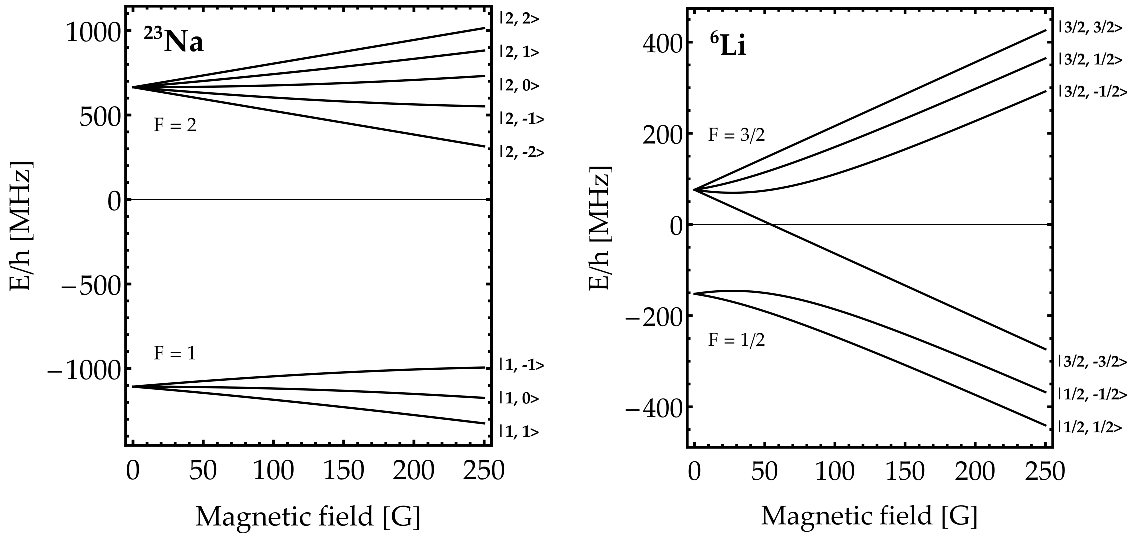

(a) (b)

Figure 5.1: Magnetic field dependence of **(a)** ^{23}Na sodium $3^2S_{1/2}$ and **(b)** ^{6}Li lithium $2^2S_{1/2}$ ground level hyperfine structure. Here, $|F, m_F\rangle$ denotes the quantum numbers at low field. In later chapter the hyperfine states of the lithium ground state are denoted with $|1\rangle$ (lowest state) up to $|6\rangle$ (upper most state).

polarized samples are stable as they do not interact. However, a mixture of different spin states would lead to inelastic collisions. The question is which combination of lithium and sodium is stable and suitable for evaporative cooling of sodium and sympathetic cooling of lithium in a magnetic trap. Two combination of states are safe in order to prevent spin exchange collisions between the two different species

$$\begin{aligned} \text{Na} : |1, -1\rangle \text{ and Li} : |1/2, -1/2\rangle \\ \text{Na} : |2, 2\rangle \text{ and Li} : |3/2, 3/2\rangle \end{aligned} \tag{5.3}$$

Historically, sodium was first condensed in the lower $|1, -1\rangle$ state (see for example [88]) as essentially all the atoms are in the $F = 1$ state (distributed equally among the three m_{F} levels) when they are trapped in the dark-SPOT. In addition, the measured three-body loss rate in the $F = 2$ state is approximately an order of magnitude higher than in the $F = 1$ state [103] making evaporation in the higher upper hyperfine state less favorable. However, the $|1/2, -1/2\rangle$ state is a low field seeking state only for moderate field strength as shown in Figure 5.1, which makes this state not suitable for magnetic trapping and sympathetic cooling. That evaporation of sodium to quantum degeneracy in the stretched $|2, 2\rangle$ state is nevertheless possible as well as simultaneously cooling of lithium in the stretched $|3/2, 3/2\rangle$ state was first shown by the MIT group [104] and is also shown in this chapter.

5.1.1 Optical Pumping and Loading of the Magnetic Trap

Before the atoms can be loaded into the magnetic trap they need to be prepared in the stretched state. About two thirds of the atoms in the lithium MOT are in the $F = 3/2$ state, whereas most of the sodium atoms are in the $F = 1$ state. The transfer into the $|2, 2\rangle$ state for sodium and $|3/2, 3/2\rangle$ state for lithium respectively is achieved by optical pumping: After the gradient fields of the MOT have been turned off and optical molasses has been preformed on sodium, a homogenous bias field of a few Gauss is turned on and σ^+-light transfers the atoms into the stretched states within 2 ms. The intensities of the optical pump light can be found for sodium in Table 4.2 and in Table 4.5 for lithium. To maximize the atom transfer and to prevent atom loss, it is important that the optical pumping field is switched on very fast. This is achieved by charging the capacitors of the power supply before the MOSFET is opened.

Subsequently, the gradient field of the MOT coils is turned on providing a confining gradient field of 70 $\mathrm{G cm^{-1}}$ in the strongest confined direction. This value is optimized to maximize the transfer of atoms from the MOT to the magnetic trap. In order to do so, the trap volumes have to be mode matched and the trap depth needs to be big enough to confine all atoms. The trap depth of this initial magnetic trap is approximately 2.5 mK. After a wait time of 100 ms the gradient field is exponentially ramped up to the maximum value of 220 $\mathrm{G cm^{-1}}$, which compresses the trap adiabatically. Directly afterwards, the transfer to the final magnetic trap begins. This is done by sinusoidally lowering the current running through the MOT coils and increasing the current of the final magnetic trap such that the cloud is moved smoothly to its final position. The transfer over a distance of 30 mm is completed within 500 ms. The final position of the atoms is 3 mm below the top window as sketched in Figure 3.5. This short distance to the window is needed to perform high resolution imaging with a high numerical aperture objective in the future. The trap depth of the final magnetic trap due to the presence of the window is approximately 2 mK.

We measure a long lifetime of both sodium and lithium in the optical plugged magnetic trap indicating a low background pressure in the vacuum system. Before evaporative cooling we measured a lifetime of about 30 s for lithium (with sodium present) and 50 s for sodium (after a hold time of about 60 s). After evaporation the lifetime of sodium is about $15 - 20$ s.

The trapping potential at the final position is a combination of the potential given by the magnetic trap and the repulsive potential created by the blue detuned laser beam, which is focused to the trap center in order to avoid Majorana losses. Calculations of this trapping potential are presented in the next section.

5.1.2 Potential of the Optical Plugged Magnetic Trap

As mentioned above, the potential at the final optical plugged magnetic trap is a combination of the potential given by the magnetic trap and the repulsive potential created by the blue detuned laser beam covering the zero magnetic field region [100]

$$V(\mathbf{r}) = V_{\mathrm{MT}}(\mathbf{r}) + V_{\mathrm{Plug}}(\mathbf{r}) + V_{\mathrm{Gravity}}(\mathbf{r}) \quad , \tag{5.4}$$

where $V_{\mathrm{MT}}(\mathbf{r})$ is the potential of the magnetic trap of an anti-Helmholtz configuration given by

$$V_{\mathrm{MT}}(\mathbf{r}) = \mu_B \, g_F \, m_F \, B' \sqrt{x^2 + y^2 + (2z)^2} \quad . \tag{5.5}$$

Here, μ_{B} is the Bohr magneton, g_{F} the g-factor for an atom with total atomic angular momentum $F = I + J$, B' is the magnetic field gradient in the weak confining direction and $\mathbf{r} = \sqrt{x^2 + y^2 + z^2}$ denotes the position in the magnetic trap. $V_{\mathrm{Plug}}(\mathbf{r})$ is the repulsive potential of the blue detuned laser beam that plugs the zero magnetic field region and which is given by Equation 6.3. V_{Gravity} is the potential arising from the gravitation given by $V_{\mathrm{Gravity}} = -mgz$ (assuming gravity acts along the z-direction).

As $g_{\mathrm{F}} \cdot m_{\mathrm{F}}$ is equal to unity for both sodium and lithium in the $|2,2\rangle$ and $|3/2,3/2\rangle$ state respectively, both species feel the same magnetic field potential. Figure 5.2 shows the potential of the plugged magnetic trap after the magnetic transport has been completed for which the experimental trapping parameters are as follows. The magnetic gradient field in the strongest confined direction (z-direction) is $220\,\mathrm{G\,cm}^{-1}$ and the plug beam travels along the x-direction. At the position of the atoms it is focused to a beam waist of 23 µm and with a power of about 5 W it creates a repulsive barrier of $U_p \approx k_B \times$ 400 µK for lithium and $U_p \approx k_B \times$ 1 000 µK for sodium. The right plot shows the potential along the strongest confined direction. The potential along the x-direction (along the plug) is a pure linear potential with an offset from zero due to the plug potential (not shown).

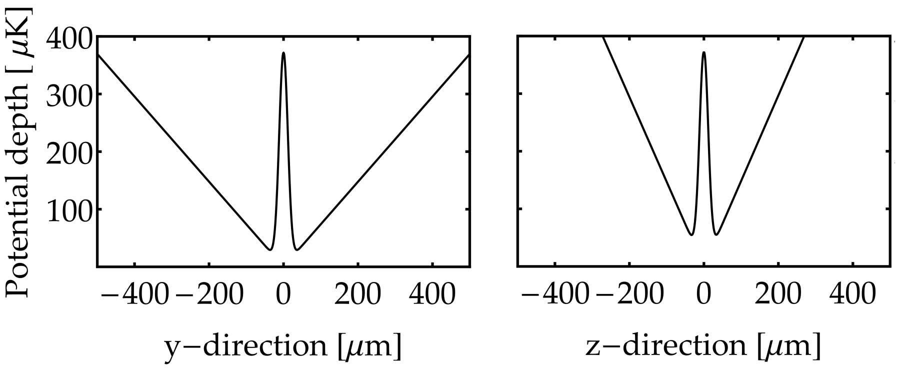

Figure 5.2: Potential of plugged magnetic trap for lithium. Trap parameters are as follows: magnetic gradient field in the strongest confined direction (z-direction) 220 Gcm^{-1} and the plug beam travels along the x-direction. At the position of the atoms it is focused to a beam waist of 23 µm and with a power of about 5 W it creates a repulsive barrier of $U_p \approx k_B \times$ 400 µK for lithium and $U_p \approx k_B \times$ 1 000 µK for sodium. The right plot shows the potential along the strongest confined direction (compare to the left plot). The potential along the x-direction (along the plug) is a pure linear potential with an offset from zero due to the plug potential (not shown).

The following section describes the setup of the blue detuned laser and the alignment procedure of this so-called plug.

5.2 Setup of the Plug Laser

The laser creating the repulsive barrier at the zero magnetic field region is a diode pumped solid state laser from Lighthouse Photonics (Sprout-G Laser) with an emission wavelength of 532 nm and a maximum output power of 15 W. A setup of the laser system can be found in Figure 5.3. The beam after the laser head is collimated and sent through an AOM[1] in order to stabilize and to adjust the beam power. A mechanical shutter blocks the residual beam whenever the beam is not used during the experimental cycle. The light is then coupled into a 2 m long photonic crystal fiber[2] and sent to the experiment. These photonic crystal fibers are able to confine light in hollow cores and are therefore well suited for high power applications. In addition,

---

[1] Gooch & Housego, Quartz AOM for 532 nm active aperture 2.5 mm, 97-03118-02, diffraction efficiency of first order: $>$ 85%

[2] NKT Photonics, Photonic Crystal Fiber Patch Cable LMA-PM-15-S/A, 2m, SMA905/FC APC

they maintain the polarization and output a single mode. Beam dumps along the beam path allow dumping power while aligning optics and coupling the light into the fiber. As the coupling at high laser powers is a very delicate process and the fiber can easily be damaged, an additional home made cooling body is attached to the incoupling side. It is clamped to the table, which acts as a heat sink and a Peltier element in between provides active cooling. To further protect the fiber, the temperature of the fiber is measured close to the incoupling side and an interlock is connected, which turns the laser off if the temperature goes above 40°C (which is still much below the damage threshold).

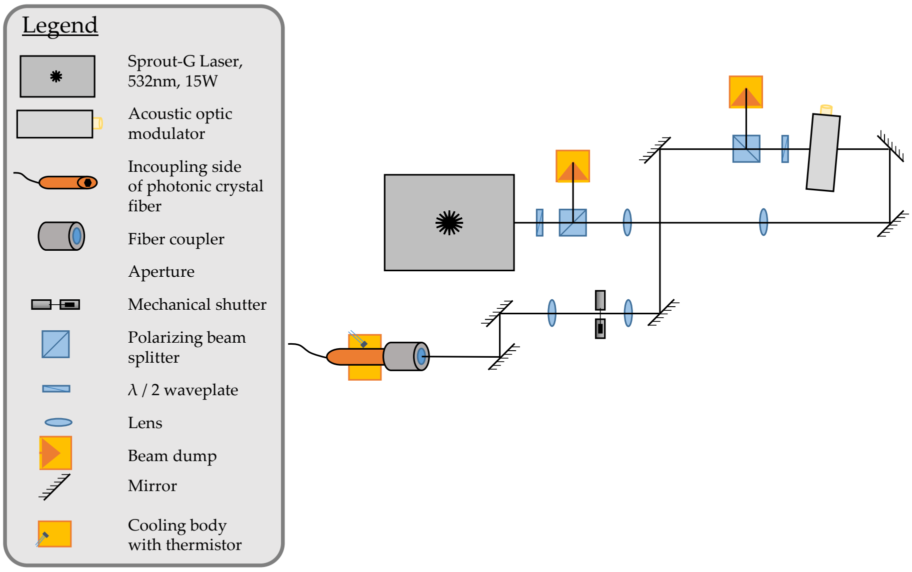

Figure 5.3: Sketch of the optics setup of the plug laser. The beam after the laser is collimated and sent through an AOM in order to stabilize and adjust the beam power. A mechanical shutter blocks the beam whenever the beam is not used during the experimental cycle. The light is then coupled into a photonic crystal fiber. Beam dumps along the beam path allow dumping power while aligning optics and coupling the light into the fiber. As the coupling at high laser powers is a very delicate process and the fiber can easily be damaged, an additional home made cooling body is attached to the incoupling side. It is clamped to the table acting as a heat sink and a Peltier element provides additional cooling. To further protect the fiber, the temperature of the fiber is measured close to the incoupling side and an interlock is connected, which turns the laser off if the temperature goes above 40°C (which is still much below the damage threshold).

When we set up the laser for the first time we did not use a fiber but instead sent the beam directly to the atoms. However, we had problems with atom number fluctuations and therefore decided to use a fiber in order to improve the beam pointing stability.

A small fraction of the light is split off behind the photonic crystal fiber and sent to a fast photodiode[3] for power stabilization. The maximum power achieved after the fiber at maximum laser power is 9.3 W. So far this high power is not needed as we cannot load all atoms from the magnetic trap into the dipole trap. This is due to the current depth of the dipole trap given by the maximum laser power of the fiber laser. We are therefore able to operate the plug laser at lower power and still obtain the same number of atoms in the lithium BEC. Typically, we operate at 11 W output power and about 6.5 W after the fiber. Lower operation of the laser should extend its lifetime and also damage the photonic crystal fiber less likely.

The plug beam is focused down to a size of $(22 \pm 2)\,\mu\mathrm{m}$ (beam waist radius) at the position of the atoms using an achromatic lens with a focal length of 160 mm directly in front of the chamber. The size of the beam focus is measured by placing a small mirror after the achromat and measuring the size as a function of distance by using a CCD camera mounted onto a translation stage. With this method we obtained the desired beam waist, but could not prove the correct position of the focus at the atoms. The alignment procedure to ensure this correct position is described in the next section.

5.2.1 Alignment Routine

This section gives an overview of the alignment procedure of the plug beam relative to the atoms. It starts with a very rough alignment procedure of the beam position and then concludes with a more precise positioning to make sure that for example the focus of the beam coincides with the center position of the magnetic trap.

To begin with, an in trap picture of the atoms is taken with a camera sitting on the axis of the plug beam. Then, the plug is sent through the chamber and a fraction of the light is imaged onto the camera. Afterwards, the position of the plug is adjusted such that it overlaps with the position of the atoms on the camera. For positioning the plug a motorized mirror[4] is used, which makes the alignment procedure quicker, more repeatable and more precise. The next step is to image the cloud with the hole created by the repulsive potential of the plug beam and align the hole to the center of the cloud. This is initially done with a hot sample and repeated for colder clouds until two separate clouds are visible, which makes the positioning even more precise, see Figure 5.4.

---

[3] Thorlabs, PDA10CS-Switchable Gain Amplified InGaAs Photo detector

[4] Newport, 2-Axis Picomotor Piezo Mirror Mount (model No. 8821 and -L)

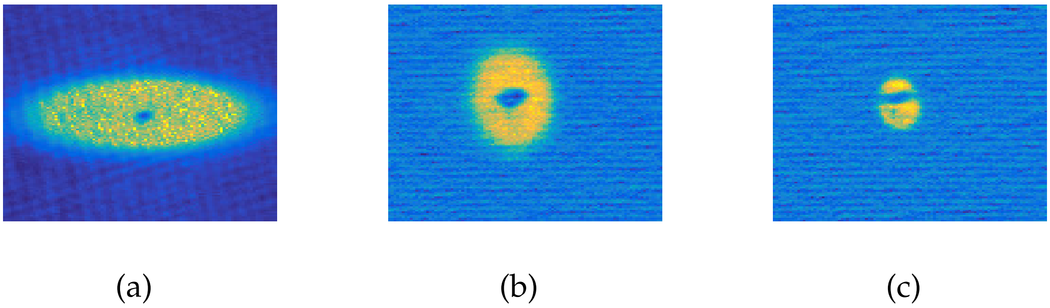

Figure 5.4: In trap density distribution of lithium in the magnetic trap for different evaporation times. The hole in the center is created by the repulsive potential of the plug beam. These images were taken for aligning the plug to the center of the trap center. The temperature decreases from left **(a)** to right **(c)**. The position of the beam is correct when it is centered relative to the atoms.

The last step is to make sure that the focus of the beam lies at the center of the trap and to fine tune the position. This is done by monitoring the atom number after 10 ms time-of-flight as a function of laser power for different focus positions. If the beam is not focused at the trap center, the atom number saturates slowly as a function of laser power at a low level. In contrast, if the focus position is correct, the atom number saturates quickly at a much higher level. In order to get a good signal to noise ratio, this alignment procedure has to be performed with a cold cloud as the atom number is then most sensitive to misalignment as the atoms reside mainly in the center of the trap. As the repulsive barrier created by the plug is approximately a factor of 2 higher for sodium than for lithium (see Equation 6.8), lithium is more sensitive to misalignment.

So far, the trapping mechanism, which we use to trap both species in a tightly confined trap ensuring high elastic collision rates, has been explained resulting in a perfect starting point to start radio frequency evaporative cooling of sodium. The next section continues with the demonstration of the cooling process.

5.3 Radio Frequency Evaporation of Sodium and Sympathetic Cooling of Lithium

Evaporation in general describes the process of atoms leaving the surface of a liquid and being transformed into a gaseous phase. In cold gases we speak of evaporation if particles of the high energy tail of a thermal (Maxwell-Boltzmann) distribution are forced to leave the trap. This process leads to a lower average temperature of the sample if the particles leaving the sample carry more energy per particle away than the average energy of a trapped atom. This cooling method is a very powerful tool to reach quantum degeneracy as it can increase the phase-space density by typically six orders of magnitudes. There is one main requirement, which has to be fulfilled to make this mechanism work well and sustainable. The thermalization time of the remaining atoms has to be fast compared to their lifetime to ensure that the cooling process can be completed before losses, such as background gas collisions, become important. In a more general way of expressing this condition, the ratio of elastic collisions (often refereed to as "good" collision) to inelastic collisions (often refereed to as "bad" collision) has to be high. In addition, it is important to keep the elastic collision rate (or equivalent the density) high while lowering the temperature, such that the phase-space density is increased and eventually quantum degeneracy is achieved. The phase-space density is defined as

$$D = n\,\lambda_{\mathrm{dB}}^{3} \quad , \tag{5.6}$$

where n is the density and λ_{dB} the de-Broglie wavelength given by $\lambda_{\mathrm{dB}} = \sqrt{\frac{2\,\pi\,\hbar^2}{m\,k_{\mathrm{B}}T}}$. Bose-Einstein condensation for bosonic atoms occurs if the phase-space density reaches approximately 2.612 [105]. If the elastic collision rate is kept constant or if it is increased during the process of evaporation, the process is called runaway evaporation.

The disadvantage of cooling the cloud by means of evaporation is that atoms are lost from the trap. However, as the efficiency is very high (the increase in phase-space density is high), the atom loss can be accounted for by high initial atom numbers. In addition, only sodium is evaporated in our experiment and the number of lithium atoms is not affected. As we aim for large cold lithium clouds, this is an ideal cooling process. The whole process of loading the magnetic trap and subsequent evaporative cooling of sodium is illustrated in Figure 5.5.

Removing the high energy atoms from the trap can be achieved by lowering the effective trapping potential. In the magnetic trap the effective trapping potential of the sodium atoms is lowered by applying a radio frequency field transferring atoms with high energy from the $|F = 2, m_{\mathrm{F}} = 2\rangle$ state into an untrappable state, namely the $|F = 1, m_{\mathrm{F}} = 1\rangle$ state. Radio frequency transitions are typically magnetic dipole transitions and they act as a spin operator. Depending on the magnetic field range they either flip the nuclear spin (Paschen-Back regime) or the electronic spin. So by applying the correct frequency these states are transferred as desired. Suddenly after the flip the atoms feel a repulsive potential and are expelled from the trap.

The fact that this process indeed addresses only the hottest atoms can be understood in the following way. Particles at high temperature have a high velocity and therefore reside mainly at the outer regions of the trap where the magnetic field strength is higher. This results in a larger Zeeman splitting of the energy levels compared to the cold atoms sitting in the trap center and encountering a smaller Zeeman shift. If the detuning of the radio frequency is chosen such that it addresses the outermost, the hottest particles of the system are removed. The radio frequency used is between 1.900 to 1.7774 GHz (see Figure 5.5), which is completely invisible for lithium, hence does not affect the lithium cloud at all. This means that the trapping potential of lithium is kept the same but due to thermalization with sodium its temperature is lowered and its phase-space density is increased.

As mentioned above, it is important to keep the elastic collision rate high during evaporation. For this reason, the gradient field of the magnetic trap is increased before the evaporation is started. In more detail, the initial gradient field of 70 $\mathrm{Gcm^{-1}}$ (in the strongest confined direction) is exponentially increased to 220 $\mathrm{Gcm^{-1}}$ over 50 ms (see Figure 5.5). Assuming the compression of the trap is adiabatic, it conserves atom number and phase-space density, while increasing the density and hence the collision rate. Following the adiabatic compression, the magnetic transport to the final position is started and completed after 500 ms as illustrated in Figure 5.5. When the gradient field of the magnetic trap is changed, care has to be taken that the zero field position does not shift in space. This would lead to an effective misalignment of the plug beam.

After 5 s of evaporation the density of the sodium atoms has increased to around $10^{14}\,\mathrm{cm^{-3}}$ such that three-body collisions become important and lead to trap losses and heating effects [103]. In order to avoid this, the magnetic trap is decompressed before further evaporation is performed (see Figure 5.5).

The cloud size is bigger than 6 mm when they are transferred to the final magnetic trap position. As the atoms are transported to a position 3 mm below the optical viewport, the hottest atoms are effectively evaporated on to this window. The highest radio frequency is determined experimentally by the frequency when atom loss sets in. The radio frequency is linearly swept from 1900 to 1777 MHz within 5 s. After a decompression of the magnetic trap to 100 $\mathrm{Gcm^{-1}}$ over 100 ms, the last part of the evaporation is performed by sweeping the frequency from 1777.5 MHz to 1777.4 MHz

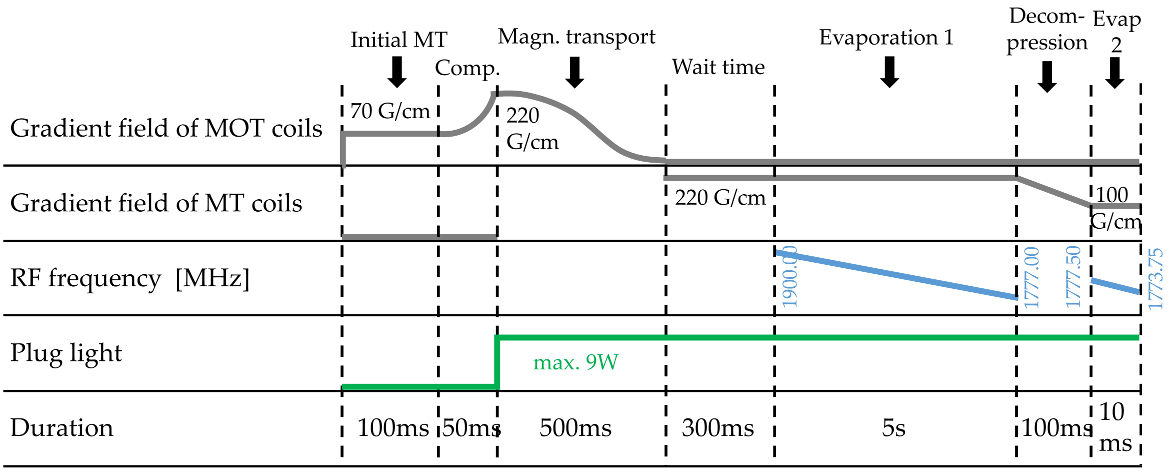

Figure 5.5: Loading of the magnetic trap (MT), transport to final position and radio frequency (RF) sweep during evaporation in an optically plugged magnetic trap.

within 10 ms. With lithium present essentially all sodium is evaporated resulting in a pure cold lithium cloud. Evaporation to lower temperatures after decompression can of course be extended, for example when sodium is evaporated without lithium and the goal is to achieve a Bose-Einstein condensate of sodium atoms. The above described sequence is however optimized to obtain the largest molecular lithium Bose-Einstein condensate.

The radio frequency field is generated by a coil mounted onto the top viewport. It consists of an U-shaped 1 mm thick silver foil with the dimensions of 7.5 mm × 41 mm and it is connected to a 12 W amplifier[5].

Figure 5.6 shows the time evolution of the atom number and temperature during rf evaporation. The reduction of the sodium atom number and the associated decrease of temperature is clearly visible and shows efficient evaporative cooling of sodium. Atom number (accurate to a factor of two) and temperature are measured after the longest possible time-of-flight, being limited by the field of view of the imaging system, to minimize the error in temperature. The latter is the reason why no data points are shown for short evaporation times where the cloud is still relatively hot and too big to be imaged by the current imaging setup. The error bars denote the standard deviation of approximately three measurements. When lithium is present the additional heat load results in a reduced atom number for sodium, which can be seen in the plot.

---

[5] microwave amps, AM38A-1.7-2.1-40-40

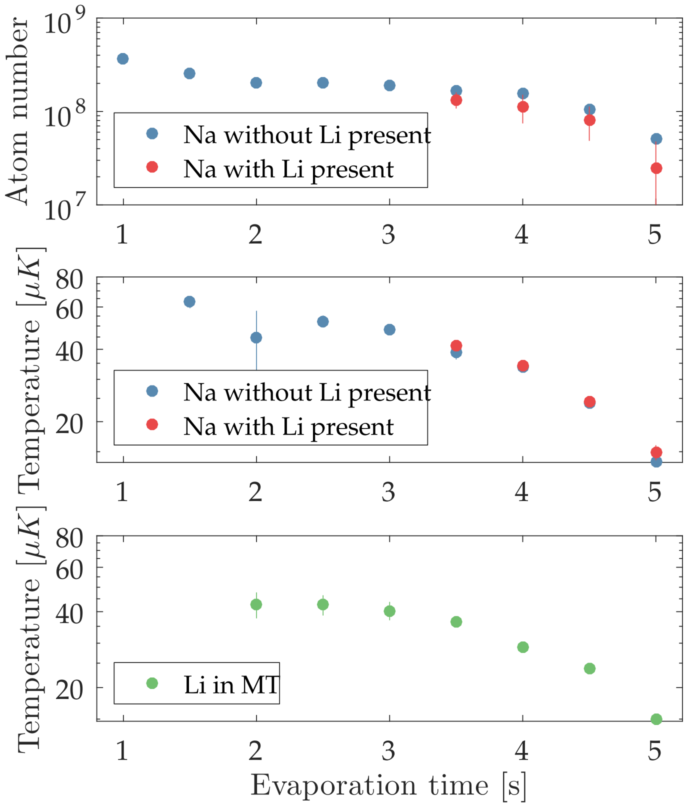

Figure 5.6: Time evolution of the atom number and temperature during radio frequency evaporation in the magnetic trap. (**Top**) Sodium atom number during rf evaporation. (**Center**) The temperature of the atoms at a certain evaporation time is given by the radio frequency, therefore explaining the same temperature whether or not lithium is present. However, when lithium is present the additional heat load results in a reduced atom number for sodium, which can be seen in the (**Top**) plot. The number of lithium atoms stays constant during the evaporation (not shown) but due to thermalization with sodium its temperature changes accordingly (**Bottom**). The lithium temperature especially at the early stages of the evaporation is underestimated as the expansion time can not be extended to higher values as the field of view is limited by the imaging system.

The temperature of the atoms at a certain evaporation time is given by the applied radio frequency, therefore explaining the same temperature whether or not lithium is present. The number of lithium atoms stays constant during the evaporation (not shown) but due to its high elastic collision rate with sodium, it thermalizes quickly with sodium (see bottom plot in Figure 5.6). An increase in density and a decrease in temperature of lithium can be seen from the absorption pictures after time-of-flight depicted in Figure 5.8. Combining the two first subplots of Figure 5.6 results in Figure 5.7, which shows the temperature as a function of the sodium atom number.

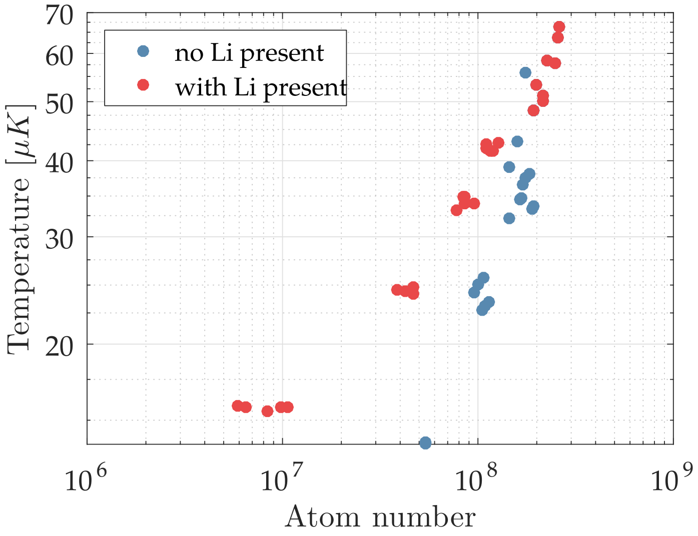

Figure 5.7: Sodium temperature versus sodium atom number during radio frequency evaporation. This plot combines the first two subplots of Figure 5.6. It shows how the system gets colder on the expense of atom number. If lithium is present, it adds an additional heat load to the system and the same temperature can only be reached with a lower atom number.

The minimum achievable temperature at maximum atom number of the lithium cloud is set by the cooling capacity of the sodium cloud. As a rule of thumb, 100 times more sodium than lithium atoms are needed before evaporation to efficiently cool lithium. This is the reason why we do not fill the lithium MOT completely but we restrict the atom number of lithium to 10^8 in the MOT.

At the early stage of the experiment the evaporation was optimized for sodium only. The goal was to achieve the highest atom number at the lowest possible temperature. Adding lithium to the magnetic trap and evaporating sodium immediately showed sympathetic cooling of lithium. Nevertheless, lithium adds a heat load to the sodium cloud such that there was room to optimize the combined cooling scheme. This was

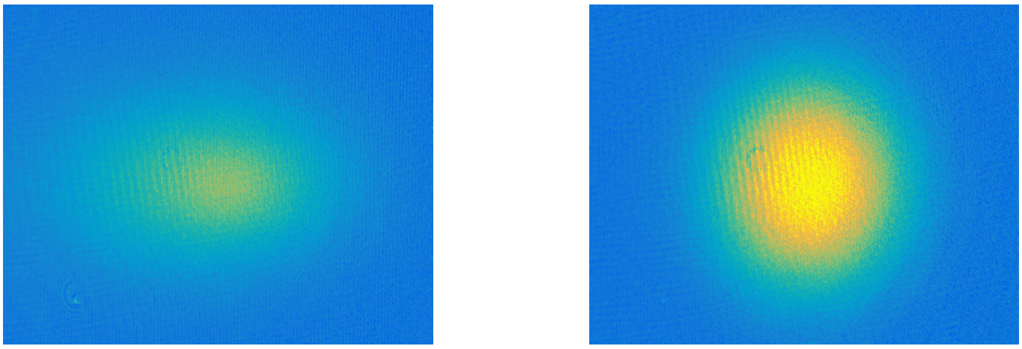

(a) (b)

Figure 5.8: Density distribution of lithium after time-of-flight **(a)** before (0.5 ms expansion) and **(b)** after (3 ms expansion) sodium evaporation in the magnetic trap. An increase in density and a decrease in temperature is clearly visible.

initially achieved by monitoring the atom number and temperature of both species independently on two cameras allowing different time-of-flights for the different species. As later the number and temperature of lithium is critical, the current scheme is optimized for a high lithium number at the lowest possible temperature.

The achieved atom number and temperature of lithium result in an excellent starting point for further cooling in a dipole trap, where a spin mixture of the lowest two hyperfine states is created allowing for thermalization via s-wave collisions. Subsequent lowering of the dipole trap beam powers reduces the potential height and releases hot atoms from the trap. The preparation of the spin mixture in the dipole trap and the evaporation of lithium is presented in chapter 6.

CHAPTER 6

The Formation of a Molecular Bose-Einstein Condensate

For the investigation of the Higgs mode and the quench dynamics of a strongly interacting superfluid, which are presented in chapter 9-chapter 11, an interacting fermionic superfluid is required. This is achieved in an optical dipole trap. Interactions are introduced by the preparation of a spin mixture of two hyperfine states. This allows interaction via s-wave collisions and opens up the way for evaporative cooling. As the interaction between lithium atoms can be greatly enhanced by means of a Feshbach resonance, a trapping mechanism is needed that is independent of the magnetic field. A solution offers the optical dipole trap. Evaporation is then started by lowering the trapping potential (see section 6.4) in a way that the cloud has time to thermalize and the phase-space density is increased (similar to sodium evaporation in the magnetic trap). If this process is done on the BEC side close to a Feshbach resonance, this cooling technique is extremely efficient as the scattering length is very large and molecules can form. If the phase-space density reaches the critical value, the molecules undergo Bose-Einstein condensation. We show that we can prepare a molecular Bose-Einstein condensate within only 1 s of evaporation in the dipole trap containing more than $4 \cdot 10^6$ molecules in the lowest two hyperfine states at a temperature of $T/T_F = 0.07 \pm 0.02$, where T_F is the Fermi temperature.

The first part of this chapter describes the trapping mechanism of neutral atoms in an optical dipole trap and continues with the characterization of our dipole trap setup.

Afterwards, the loading of the dipole trap and the preparation of the spin mixtures is explained. Following that the evaporation in the dipole trap is demonstrated resulting in one of the largest reported molecular Bose-Einstein condensates of lithium.

6.1 Optical Dipole Trap

The mechanism that allows atoms to be confined in optical dipole traps arises from the interplay between far off-resonant light fields and induced dipole moments of the atoms (AC Stark effect). The resulting trapping potential, which is derived in the following section, depends on the polarizability of the atoms and on the intensity distribution of the light field.

Besides having a trapping mechanism, which is independent of the magnetic field, another advantage of this trapping mechanism is the many different possible trapping configurations one can set up. Depending on the shape of the laser beams and the number of overlapped beams different potentials can be created. For example, the constructive interference of standing waves can be used to create two dimensional light sheets or optical lattices. In the following, a brief introduction to the trapping mechanism generated by far detuned light is given. Afterwards, a description of our dipole trap follows.

6.1.1 Theory of Confining Atoms Using Light Fields

If an atom is placed inside a spatially inhomogeneous light field, the presence of the electric field $\mathbf{E}(\mathbf{r},t) = \hat{e}E_0(\mathbf{r})\exp(-i\omega t)$ results in an induced oscillating dipole moment $\mathbf{p} = \alpha(\omega)\mathbf{E}(\mathbf{r},t)$ of the atom, where $\alpha(\omega)$ describes the atomic polarizability. The following interaction of the dipole moment with the electric field leads to a shift in the ground state energy and can be expressed in second-order perturbation theory [62]

$$\Delta E_g = -\frac{1}{2}\alpha(\omega)\left\langle \mathbf{E}(\mathbf{r},t)^2 \right\rangle \quad , \tag{6.1}$$

where $\langle ... \rangle$ denotes the time average. The polarizability is given by

$$\alpha(\omega) = \sum_e |\langle e\,|\mathbf{p}\cdot\hat{e}|\,g\rangle|^2 \left(\frac{1}{E_e - i\hbar\Gamma_e/2 - E_g - \hbar\omega} + \frac{1}{E_e - i\hbar\Gamma_e/2 - E_g + \hbar\omega} \right) \tag{6.2}$$

and the summation takes place over all possible excited states. g and e label the ground end excited state respectively and $1/\Gamma_e$ describes the lifetime of the excited state. This term includes the spontaneous emission from the excited state in a phenomenological way.

In order to understand the density distribution in a dipole trap, its potential has to be derived. The interaction potential of the induced dipole moment is given by [106]

$$U_{\text{dip}}(\mathbf{r}) = -\frac{1}{2}\langle \mathbf{p}\cdot\mathbf{E}\rangle = -\frac{1}{2\epsilon_0 c}\text{Re}(\alpha(\omega))I(\mathbf{r}) \quad , \tag{6.3}$$

where ϵ_0 is the dielectric constant, c the speed of light, $\text{Re}(\alpha(\omega))$ the real part of the polarizability and $I(\mathbf{r})$ the field intensity given by $I(\mathbf{r}) = 2\epsilon_0 c\left|\mathbf{E}^*(\mathbf{r},t)\cdot\mathbf{E}(\mathbf{r},t)\right|^2$. The factor $\frac{1}{2}$ in the above equation takes into account that the dipole moment is not permanent but an induced dipole moment. Thus, the potential of an atom in an electric field is proportional to the intensity and the real part of the polarizability. On the other hand, the light field induces scattering, which is described by the rate

$$\Gamma_{\text{sc}}(\mathbf{r}) = \frac{P_{\text{abs}}}{\hbar\omega} = \frac{\langle\dot{\mathbf{p}}\cdot\mathbf{E}\rangle}{\hbar\omega} = \frac{1}{\epsilon_0 c\hbar}\text{Im}(\alpha)I(\mathbf{r}) \quad , \tag{6.4}$$

where P_{abs} is the power of the light field absorbed by the atom.

The dipole matrix element $\mu_{ij} = \left\langle e_i\left|\mu\right|g_j\right\rangle$ in Equation 6.2 can be decomposed [107] into a product of the Clebsch-Gordan coefficients C_{ij} and a reduced matrix element $||\mu||$ (Wigner-Eckart theorem). For a specific hyperfine transition between the two states $|g\rangle = |F, m_F\rangle$ and $|e\rangle = \left|F', m_{F'}\right\rangle$ the dipole matrix element can be written as

$$\begin{aligned}\left\langle F, m_F\left|er_q\right|F', m_{F'}\right\rangle &= \left\langle J\left\|e\mathbf{r}\right\|J'\right\rangle\cdot(-1)^{2F'+J+I+m_F}\cdot\sqrt{(2F'+1)(2F+1)(2J+1)}\\ &\cdot\begin{Bmatrix} J & J' & 1\\ F' & F & I\end{Bmatrix}\cdot\begin{pmatrix} F & 1 & F'\\ m_F & q & -m_{F'}\end{pmatrix} \quad .\end{aligned} \tag{6.5}$$

Here, $\{...\}$ and $(...)$ are the Wigner 6-j and 3-j symbols, q specifies the polarization and equals to 0 for $\pi-$polarized light and ±1 for $\sigma^{\pm}-$ polarized light. J is the total angular momentum, which is the sum of the orbital angular momentum L and the spin angular momentum S. The quantity missing to calculate potentials created by light fields is the reduced matrix element $\left\langle J \left\| e\mathbf{r} \right\| J' \right\rangle$, which can be expressed via the measurable decay rate $\Gamma_{J\to J'}$ [108]

$$\Gamma_{J\to J'} = \frac{\omega^3_{J\to J'}}{3\pi\epsilon_0\hbar c^3}\frac{2J'+1}{2J+1}\left|\left\langle J \left\| e\mathbf{r} \right\| J' \right\rangle\right|^2 \quad . \tag{6.6}$$

The above given formulas are used to calculate our trapping potential for multi-level atoms (such as sodium and lithium) further below. Moreover, a simplification of the above formulas (Equation 6.3 and Equation 6.4) shows two important relations. First, the sign of the detuning determines the sign of the potential. And second, the potential depth depends on the scattering rate.

In case of a two-level system large detunings and a negligible saturation, the dipole potential and the scattering rate simplifies to [106]

$$\begin{aligned} U_{\mathrm{dip}}(\mathbf{r}) &= -\frac{3\pi c^2}{2\omega_0^3}\left(\frac{\Gamma}{\omega_0-\omega}+\frac{\Gamma}{\omega_0+\omega}\right) I(\mathbf{r}) \quad , \\ \Gamma_{\mathrm{sc}}(\mathbf{r}) &= \frac{3\pi c^2}{2\hbar\omega_0^3}\left(\frac{\omega}{\omega_0}\right)^3\left(\frac{\Gamma}{\omega_0-\omega}+\frac{\Gamma}{\omega_0+\omega}\right)^2 I(\mathbf{r}) \quad , \end{aligned} \tag{6.7}$$

where ω_0 is the resonance frequency between the ground and the excited state and ω is the driving frequency of the electric field. If the detuning $\Delta = \omega - \omega_0$ fulfills the condition $|\Delta| \ll \omega_0$, namely the frequency of the driving laser is relatively close to the resonance frequency ω_0, the rotating-wave approximation can be applied and results in the equations

$$\begin{aligned} U_{\mathrm{dip}}(\mathbf{r}) &= \frac{3\pi c^2}{2\omega_0^3}\frac{\Gamma}{\Delta} I(\mathbf{r}) \quad , \\ \Gamma_{\mathrm{sc}}(\mathbf{r}) &= \frac{3\pi c^2}{2\hbar\omega_0^3}\left(\frac{\Gamma}{\Delta}\right)^2 I(\mathbf{r}) \quad . \end{aligned} \tag{6.8}$$

From Equation 6.8 we can see that for laser frequencies below the atomic resonance ($\Delta < 0$, so-called red detuned), the dipole potential is negative and therefore attracts atoms into the light field. The opposite is true for laser frequencies above the atomic resonance ($\Delta > 0$, so-called blue detuned). In the latter case atoms are repelled from the light field. The above equations lead to a simple relation between the dipole potential and the scattering rate, namely

$$\hbar\Gamma_{\mathrm{sc}} = \frac{\Gamma}{\Delta} U_{\mathrm{dip}} \quad . \tag{6.9}$$

Due to this scaling mainly far-detuned traps at high intensity are used in experiments to reduce the heating due to scattering and to produce deep traps.

So far all quantities necessary to calculate the dipole potential have been derived with exception of the intensity distribution $I(\mathbf{r})$ leading to the spatial dependence of the trapping potential. This follows in the upcoming section.

6.1.2 Intensity Distribution of Laser Beams

In a more general context, the spatial dependence of electromagnetic waves is described by the Helmholtz equation, which is the time-independent form of the wave equation. Moreover, in the paraxial approximation the complex field amplitude is expressed as a plane wave multiplied with a complex amplitude, which is modulated by a sinusoidal plane wave. Assuming that this complex amplitude is slowly varying along the propagation direction (z-direction), the slowly varying envelope approximation can be applied and results in the equation [76]

$$\nabla_{\perp}^{2} \psi - 2ik \frac{\partial \psi}{\partial z} = 0 \quad , \tag{6.10}$$

where ψ is the complex field amplitude and $\nabla_{\perp}^{2} = \partial^2/\partial x^2 + \partial^2/\partial y^2$ is the transverse Laplace operator. One solution of this equation is the fundamental Gaussian mode (also called TEM_{00} mode). Most laser outputs can be described by Gaussian beams. Their field distribution of a beam propagating along the z-direction is given by

$$\mathbf{E}(r,z) = E_0\, \hat{\mathbf{x}} \frac{w_0}{w(z)} \exp\left(\frac{-r^2}{w(z)^2}\right) \exp\left(-i\left(kz + k\frac{r^2}{2R(z)} - \phi(z)\right)\right) \quad , \tag{6.11}$$

where r is the radial distance from the beam center and E_0 is the amplitude. $w(z)$ describes the radius of the field where its amplitude has fallen to $1/e$ of their maximum value at the center and $w_0 = w(0)$. $R(z)$ is the radius of curvature and $\phi(z)$ the Gouy phase given by $\phi(z) = \arctan(z/z_R)$ and $z_R = \pi w_0^2/\lambda$ is called the Rayleigh range. The waist $w(z)$ and the radius of curvature $R(z)$ have the following $z-$dependence

$$\begin{aligned} w(z) &= w_o\sqrt{1+\left(\frac{z}{z_R}\right)^2} \quad , \\ R(z) &= z\left[1+\left(\frac{z_R}{z}\right)^2\right] \quad . \end{aligned} \tag{6.12}$$

From Equation 6.11 the intensity distribution $I(\mathbf{r}) = 2\epsilon_0 c \left|\mathbf{E}^*(\mathbf{r},t)\cdot\mathbf{E}(\mathbf{r},t)\right|^2$ can be calculated and results in

$$I(r,z) = I_0\left(\frac{w_0}{w(z)}\right)^2 \exp\left(\frac{-2r^2}{w(z)^2}\right) \quad , \tag{6.13}$$

where I_0 is the intensity at the center of the beam. With the intensity distribution being specified, the full dipole potential can be constructed.

For distances smaller than the beam waist $r < w_0$, the potential can be approximated by a harmonic potential of the form $U(\mathbf{r}) = 1/2(\omega_x^2 x^2 + \omega_y^2 y^2 + \omega_z^2 z^2)$ as shown in the following section and in Figure 6.1. The frequencies $\omega_x, \omega_y, \omega_z$ are called trap frequencies. The measurement of the trap frequencies is demonstrated in subsection 6.1.6. The following section describes the beam configuration of our dipole trap.

6.1.3 Potential of the Dipole Trap

The beam configuration is a cross beam dipole trap with one horizontal beam and one vertical beam. The horizontal beam is shaped elliptically and it is focused to a waist of 110 µm in the horizontal plane and to a waist of 50 µm in the z-(gravity-)direction. In contrast, the vertical beam is circular and its waist is 120 µm. It is sent into the main chamber from the bottom and backreflected from the top viewport (UKAEA window). In addition, the Rayleigh range is approximately 40 mm and the distance to the window is 3 mm meaning that the size of the beam does not increase considerably over a range of 6 mm. Hence, the atoms feel twice the laser power. The coherence length of the laser is very short (0.2 mm compared to a distance of 3 mm to the window) such that no standing wave is created, which is not intended for a dipole trap. Figure 6.1 shows the dipole potential calculated with Equation 6.3 including gravity (solid line) for the following beam powers: 160 mW in the horizontal beam and $2 \cdot 175$ mW in the vertical beam. The dashed line indicates a harmonic fit to the trap center from which the theoretical harmonic trapping frequencies can be deduced. They are approximated to be $w_i \simeq 95, 150, 240$ Hz ($i = x, y, z$). The lowest trap depth is along the gravity direction and is 0.6 µK. This trapping configuration is used for the measurements presented in chapter 9.

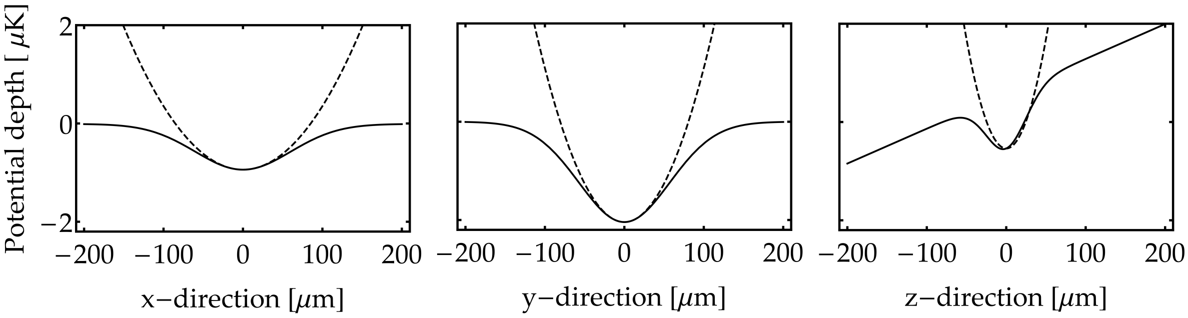

Figure 6.1: Dipole potential (solid line) including gravity for the following beam powers: 160 mW in the horizontal beam (x- and y-direction) and $2 \cdot 175$ mW in the vertical beam along gravity (z-direction). The dashed line indicates a harmonic fit to the trap center from which the theoretical harmonic trapping frequencies can be deduced. They are approximated to be $w_i \simeq 95, 150, 240$ Hz ($i = x, y, z$). The lowest trap depth is along the gravity direction and is 0.6 µK.

6.1.4 Generation of the Dipole Trap Beams

The light of the two laser beams forming the potential of the crossed dipole trap is produced by a diode-pumped continuous wave ytterbium fiber laser[1] with an output power of 55 W at a wavelength of 1 070 nm. This light is sent through an optical isolator and divided into two main parts, one for the horizontal and one for the vertical dipole beam as illustrated in Figure 6.2. Both beams are sent through acousto-optic modulators[2], which are used for power regulation and for intentionally decreasing the power for evaporation. Mechanical shutter, which are water cooled, ensure that if the beams are not needed during the experimental cycle, absolutely no light reaches the atoms in the vacuum chamber. In order to improve the beam pointing stability as well as the beam profile, the light is sent to the experiment table through optical fibers. For the

---

[1] IPG Photonics, model YLR-50-Y12

[2] Gooch & Hausego LLC, 23080-2-1.06-LTD, center frequency 80 MHz

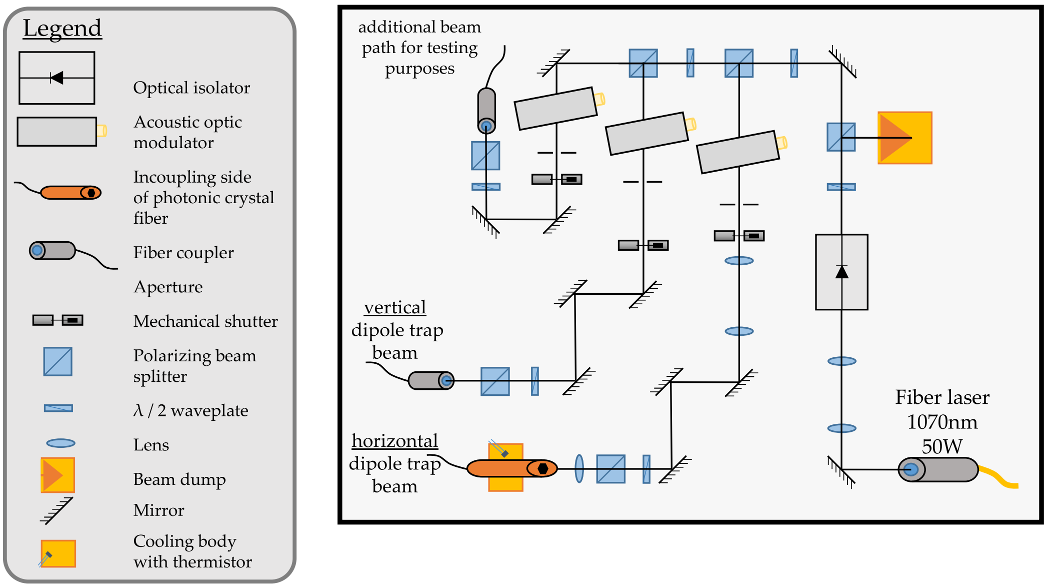

Figure 6.2: Sketch of the setup of the dipole trap optics before the fiber on the laser optics table. The light for the crossed dipole beams is generated from a diode-pumped continuous wave ytterbium fiber laser. It light is sent through an optical isolator and is divided into two main parts, one for the horizontal and one for the vertical dipole beam. Both beams are sent through acousto-optic modulator, which are used for power regulation. Mechanical shutter ensure that if the beams are not needed during the experimental sequence, absolutely no light reaches the atoms in the vacuum chamber. In order to improve the beam pointing stability as well as the beam profile, the light is sent through optical fibers to the experiment table.

horizontal path we use a 10 m long photonic crystal fiber[3] and a standard optical fiber[4] for the vertical beam path. Surprisingly, these standard fibers still work very well with an incoupling power of 20 W but are about five times cheaper than the photonic crystal fibers. In the beginning we intended to send more power through the horizontal path and decided in favor of a fiber suitable for high power. However, in the current setup we use about equal power in both beams.

The beam dump shown in Figure 6.2 is an important part of the optics setup. As the beam profile of the laser can change with power and the optical isolator can introduce variation of the beam shape due to optical lensing occurring at high power, it is important to align all the optics at maximum laser power. To be able to reduce the power for fiber coupling for example, most of the power can be dumped in this water

---

[3] NKT Photonics, Photonic Crystal Fiber Cable LMA-PM-15, 10m

[4] Thorlabs, P3-1064PM-FC-10

cooled beam dump. This can be achieved by changing the polarization in front of the polarizing beam splitter next to the beam dump.

The incoupling side of the photonic crystal fiber is cooled in the same way as the photonic crystal fiber of the plug beam (see section 5.2) and a temperature sensor is attached such that the laser turns off if the fiber end gets too hot.

6.1.5 Alignment of the Dipole Trap

The initial rough alignment of the dipole trap is completed in two steps. At first the horizontal beam along the direction of the plug is aligned. Afterwards, the alignment of the vertical beam along the direction of gravity follows. The positioning of the horizontal beam makes use of the aligned plug beam, which takes essentially the same beam path. We put a mirror directly before the chamber and sent both beams to a place, where the overlapping foci positions could be checked. In addition, the size of the atomic cloud is analyzed depending on the lens position, which defines the location of the focus. The beam is focused onto the atoms if the trapped atomic cloud is smallest.

For rough positioning of the vertical dipole beam a vertical blaster beam is implemented. This beam is resonant with the atoms and destroys the cloud if the beam hits the atoms. After having aligned this beam, the vertical beam is simply overlapped with the blaster beam.

Finer alignment is achieved by looking at the atomic cloud during the transfer from three perpendicular directions. Similar to the plug beam setup, motorized mirrors[5] are used for precise alignment. An example picture during alignment is shown in Figure 6.3. The horizontal and the vertical beam are roughly aligned and the untrapped hotter atoms fall down under gravity. Even more precise alignment is realized by maximizing the transferred atom number after some hold time. Offset fields are used to keep the atoms in place while ramping down the magnetic field.

During the optimization procedure of the evaporation in the dipole trap we noticed some strange dynamics of the cloud while holding the atoms in the trap. It turned out that the dipole trap was not centered relatively to the magnetic Helmholtz field of the Feshbach coils. Due to its curvature the Helmholtz field introduces a harmonic trapping potential with a trapping frequency of $w_i = 16\,\mathrm{Hz}$ at $800\,\mathrm{G}$ along the x-direction, which was responsible for the dynamics in the trap. From the ob-

---

[5] Newport, 2-Axis Picomotor Piezo Mirror Mount model No. 8821 and -L

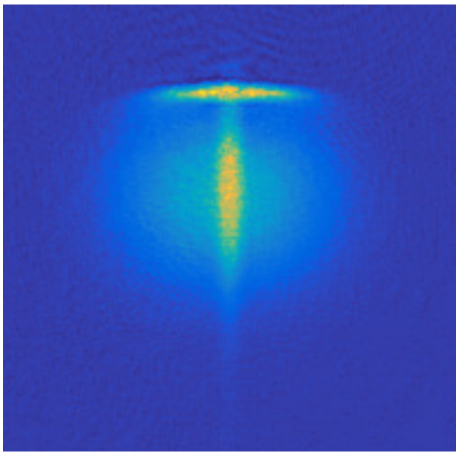

Figure 6.3: Horizontal and vertical dipole trap beam alignment with a relatively hot cloud: The horizontal and the vertical beam are roughly aligned and the untrapped hotter atoms fall down under gravity.

served dynamics it was possible to deduce the center point of the Helmholtz field and the dipole trap was aligned to this new reference position. Unfortunately, this lead to a decrease of efficiency of the evaporation in the dipole trap as the atoms were not removed as efficiently from the trap as before. Initially, the Helmholtz field acted as a gradient field across the cloud and the atoms were preferably removed in the direction of the gradient. We therefore decided to implement an artificial gradient, which can be used during evaporation. The coil setup for this gradient is described in more detail in chapter 7 and the evaporation procedure in the dipole trap in section 6.4.

We measured the lifetime for different trap depths. The $1/e$ lifetime of lithium after evaporation in the dipole trap was measured to be about 3 s. With the same power in the horizontal beam but no vertical beam the lifetime is about 9 s, which is more than long enough for experiments with ultracold gases.

6.1.6 Measurement of the Trapping Frequencies

For later experiments and analysis of the data, it is crucial to know the exact trapping frequencies of the system. As an example, the trapping frequencies define, together with the atom number, the Fermi energy E_F of a harmonically confined Fermi gas (see Equation 2.2). Together with the scattering length they characterize the dimensionless interaction parameter $1/k_F a$. This is an important parameter to characterize the physics in the BEC-BCS crossover as it becomes clear later. In addition, the measured frequencies can be compared to the theoretical predicted value and possible errors in assumed beam waists can be found.

There are different methods for measuring the trapping frequencies with high reliability. The principle of all measurements is similar: Following the preparation of a thermalized sample in the trap, the cloud is excited by modulating the trapping potential or displacing the cloud relatively to its initial position. After this excitation the atoms are released into the initial trap where they start to oscillate according to the underlying harmonic trapping potential. From the change in size or position the trapping frequencies can be deduced.

One method is to excite **center-of-mass oscillations** by displacing the cloud letting it move in the trap and record the position after a variable hold time. The change in position is directly related to the trapping frequency and it is independent of interactions and other internal parameters. We use the this method to measure the trapping frequencies of our system and displace the cloud by applying a magnetic field gradient. (In x- and y- direction a simple wire on top of the UKAEA viewport adds a gradient across the trap, whereas along the gravity axis the cloud is displaced by the gradient of an offset coil depicted in Figure 7.3). A typical measurement is given in Figure 6.4, which shows the center position of an oscillating lithium cloud in a dipole trap. Fitting (decaying) sine-functions to the data yields the trapping frequencies.

Another option is to use the method of **parametric heating** [109], where the power of a dipole trap beam is modulated with a variable frequency over a fixed time. This modulation results in the excitation of a breathing mode, which leads to an increase of temperature at a certain driving frequency. For a non-interacting gas this increase occurs at twice the trap frequency ($w_{\text{breath, non-int}} = 2 \cdot w_{\text{trap}}$), whereas on resonance the peak appears at $w_{\text{breath, res}} = \sqrt{3} \cdot w_{\text{trap}}$ [110]. In between these two cases the relation between trapping frequency and breathing mode is more difficult to predict making this method less reliable. Besides that, the higher trapping frequency may dominate the atom loss spectrummaking it difficult to measure the lower trapping frequency at the same time.

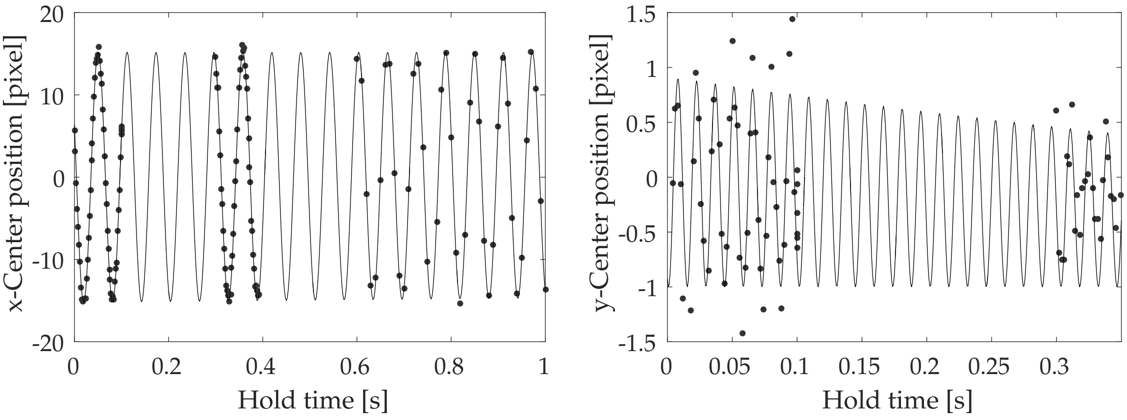

(a) (b)

Figure 6.4: Measurement of dipole trap frequencies by exciting a center-of-mass oscillation of lithium atoms and recording the center position as a function of hold time. Shown are measurements of the trap frequency at the end of evaporation. **(a)** Center-of-mass oscillation in x-direction. Fitting a sine-function yields a frequency of 16.3 Hz, which is determined by the magnetic field curvature of the homogeneous Feshbach field at 810 G as the power of the vertical beam is ramped down to zero. **(b)** Center-of-mass oscillation in y-direction. Fitting a decaying sine-function yields a frequency of 69.4 Hz.

6.2 Loading of the Dipole Trap

Following the cooling in the magnetic trap, the atoms need to be transferred into the dipole trap for further cooling. Close to the end of the rf evaporation in the magnetic trap both dipole beams are ramped up over 50 ms such that the cold enough atoms can be loaded into the dipole trap. Full transfer is achieved by ramping down the gradient field of the magnetic trap after the rf evaporation is finished. At the same time the plug beam power is ramped down, while making sure that the central trap position does not change. This is achieved by adjusting the offset fields accordingly. As mentioned above, we cannot transfer all atoms from the magnetic trap into the dipole trap as the dipole trap cannot confine the hot energy tail. More laser power would allow even bigger and hotter samples, which could be cooled to lower temperatures by evaporative cooling. However, our achieved atom numbers and temperature are more than sufficient for the experiments described in this thesis. The loading procedure is sketched in Figure 6.5.

The initial power of the horizontal dipole beam is 13 W, whereas the initial power of the vertical dipole beam is 7 W (×2 as the beam is reflected at the top viewport). This gives rise to a potential depth of 40 µK. We noticed that it actually helps to load some remaining sodium atoms to the dipole trap as well. The reason might be that with sodium present during the transfer, thermalization of the spin polarized lithium cloud is still possible. The sodium atoms can be removed afterwards for example through resonant light.

6.3 Preparation of an Interacting Spin Mixture

After the dipole trap is loaded, the next step is to prepare a spin mixture to allow collisions between the two different states such that evaporation can be performed. The experimental sequence to do so is outlined in this section. Atoms in the magnetic trap are in the upper hyperfine state denoted as $|6\rangle$ as explained in section 5.1. For evaporation in the dipole trap the atoms are prepared in a spin mixture of the lowest two hyperfine states, labeled as $|1\rangle$ and $|2\rangle$ (or any other two-component mixture of the lowest three hyperfine states), which is stable against spin changing collisions but allows elastic collisions to thermalize. In addition, a Feshbach resonance located at 834 G allows tuning the scattering length to values as high as several thousands Bohr radii making the evaporation process close to the resonance extremely efficient.

The first spin-flip in the dipole trap from the stretched state $|6\rangle$ to the lowest hyperfine state $|1\rangle$ is achieved by an adiabatic Landau-Zener sweep across the single photon rf transition at around 228 MHz. In our case this is performed at an offset field of approximately 5 G to lift the degeneracy of the hyperfine states and which leads to a Zeeman shift such that the resonance frequency for this transition is shifted to 240 MHz. The source of this radio frequency is a signal generator[6] and its power and frequency are optimized to obtain maximum transfer. The amplifier, which enhances the signal, is a 8 W amplifier (ZHL-03-5WF) from Mini-Circuits. While the frequency is kept fix, the magnetic field is swept through the rf resonance and the atoms are adiabatically transferred from the $|6\rangle$ state to the $|1\rangle$ state. The efficiency of this process is about (98%).

In general, the Landau-Zener probability for transferring atoms from an initial $|i\rangle$ to a final $|f\rangle$ state is given by [46]

$$P_{|6\rangle\rightarrow|1\rangle} = 1 - \exp\left(-2\pi\frac{\Omega_{\mathrm{R}}^2}{\dot{\omega}}\right) \quad , \tag{6.14}$$

---

[6] Windfreak Technologies, SynthNV: 34 MHz − 4.4 GHz RF Signal Generator w/ Power Detector

where Ω_R is the Rabi frequency depending on the radio frequency and $\dot{\omega}$ denotes the sweep rate. For the creation of a spin mixture the offset field is increased to 100 G and while keeping the field fixed, the radio frequency is swept through the single photon resonance situated at around 60 MHz. By adjusting the sweep rate or power, the amount of atoms transferred to the final state can be adjusted such that a 50 : 50 mixture is prepared. However, this spin transfer is a coherent process such that a superposition of atoms in the $|1\rangle$ and $|2\rangle$ state is prepared. For the creation of a true spin mixture a decoherence mechanism is required. This is for example imposed by the inhomogeneity of the magnetic field, which mixes the relative phase of atoms taking different paths in the trap. For this reason a wait time of 100 ms is added before the evaporation in the dipole trap is started. The field sweeps and the application of radio frequencies necessary for performing these spin transfers are sketched in Figure 6.5.

Following the creation of an interacting spin mixture, the magnetic field is increased to 795 G where the scattering length is on the order of several thousands Bohr radii ($\sim 900 a_B$) allowing fast thermalization, hence efficient evaporation. This is explained in more detail in the next section.

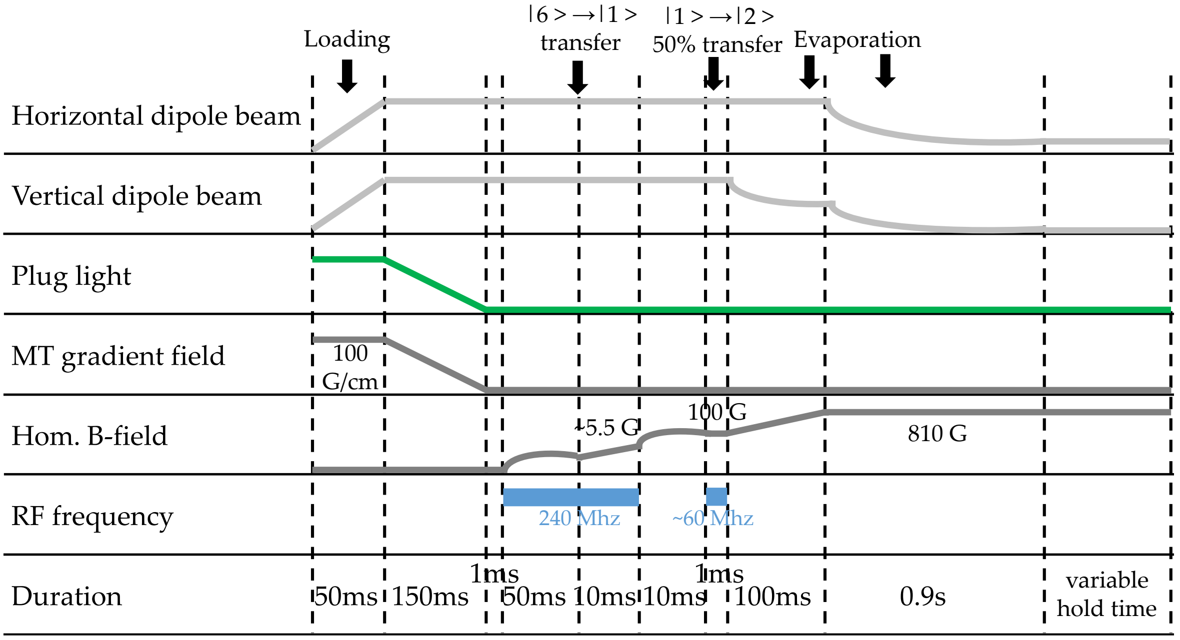

Figure 6.5: Sketch of the experimental sequence to load the dipole trap, prepare the spin mixture in the lowest two hyperfine states and evaporate to obtain a molecular Bose-Einstein condensate of fermionic lithium atoms.

6.4 Evaporation in the Dipole Trap and Formation of a Molecular Bose-Einstein Condensate

Evaporation in the dipole trap is performed on the BEC side of a Feshbach resonance. Historically, the first Feshbach resonances in bosonic gases were studied by monitoring the atom losses from the trap [111, 112]. The observed loss mechanism was predicted to happen due to the formation of molecules of two bosons, which are short-lived ($\approx$100 µs). In fermionic samples however, the gas close to resonance was found to be stable and in case of ^{6}Li, the lifetime of the molecules was measured to be 10 s [113–115]. This finding allows to evaporatively cool the gas close to and on the BEC side of the Feshbach resonance and to populate the molecular branch [113–115]. To be more precise, the molecules are formed by three-body collisions. Close to the resonance, where the binding energy of the molecules is similar to $k_B T$, the released energy of the third atom does not considerably heat the sample. A decay to more a deeply bound molecule requires three fermions close to each other. However, this is suppressed by the Pauli principle, which in turn leads to the formation of a stable sample.

As the polarizability of molecules is twice as high as for atoms, molecules are more deeply trapped by the optical dipole trap. Keeping this in mind it is clear why evaporation removes dominantly atoms. The process of converting atoms to molecules becomes more probable at lower temperatures as the inter particle distance is decreased. The molecular cloud can be cooled analogously to a bosonic cloud and the formation of a molecular Bose-Einstein condensate can be achieved. For this purpose the power of the dipole beams is exponentially lowered over 1 s as depicted in Figure 6.5. The vertical beam is fully ramped down such that the confinement along the horizontal beam is solely given by the curvature of the Feshbach field, which leads to a trapping frequency of $2\pi \cdot 16\,\mathrm{Hz}$ along this direction. The trapping frequency in the y- and z-direction (gravity) are $2\pi \cdot 68\,\mathrm{Hz}$ and $2\pi \cdot 157\,\mathrm{Hz}$ respectively. The decrease in temperature while atoms are evaporating from the trap can be seen from Figure 6.6. The temperature and atom number are deduced from absorption pictures after a time-of-flight measurement. As the optical density especially at the end of evaporation is quite high (OD=3-5), the fits to the density distribution underestimate the atom number and the atom number is only accurate to a factor of two. However, this measurement quantitatively shows the efficiency of the evaporation. The temperature is extracted from the expansion of the tightest confined direction.

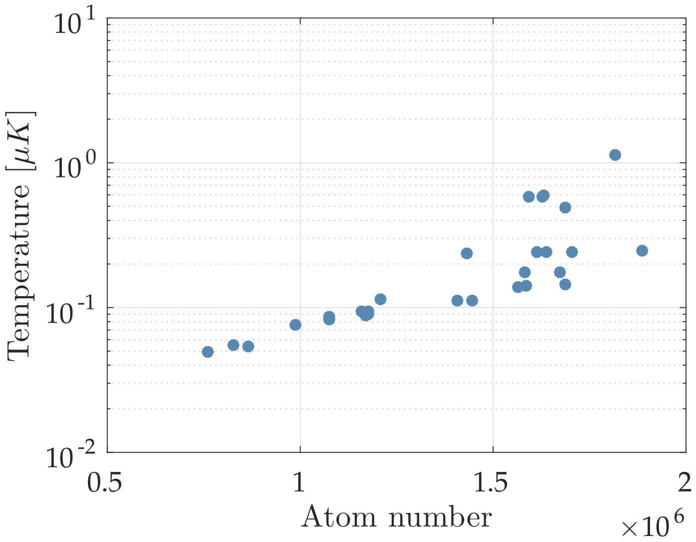

Figure 6.6: Trajectory of evaporation of lithium in the dipole trap. The temperature is plotted as a function of atom number per spin state. While the hottest atoms are evaporating from the trap, the temperature of the remaining atoms is clearly reduced and a molecular Bose-Einstein condensate is obtained at the end of evaporation, see Figure 6.7.

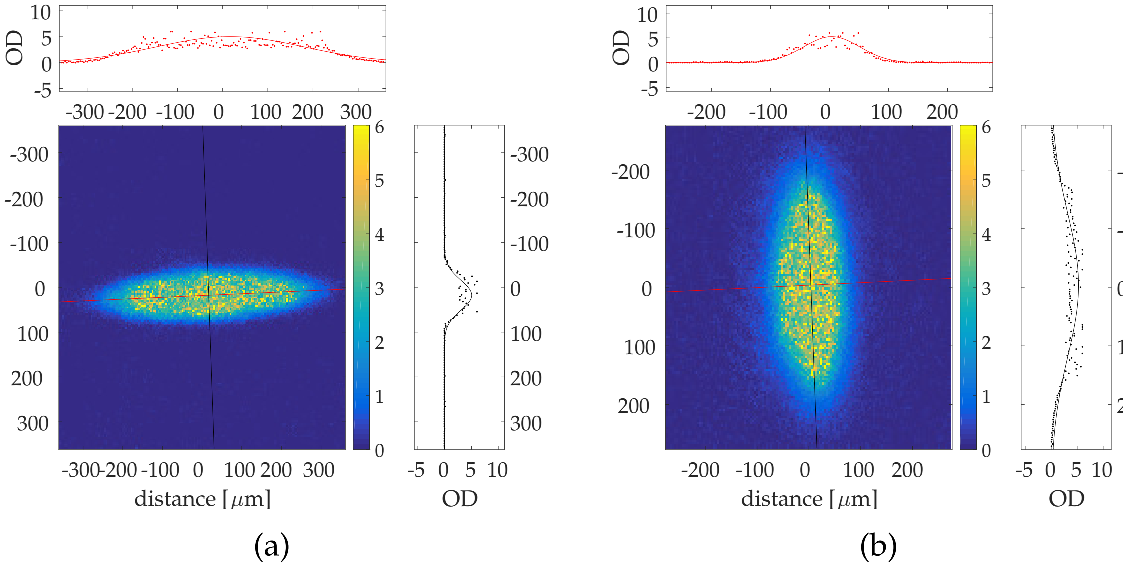

(a) (b)

Figure 6.7: (a) Picture of the optical density (OD) obtained by resonant absorption imaging of the molecular lithium Bose-Einstein condensate in the dipole trap. **(b)** Typical picture of a molecular lithium Bose-Einstein condensate after 15 ms time-of-flight. The solid lines show cuts through the clouds and 2D Gaussian fits to the density distribution are shown on the side. This condensate contains about $(5 \pm 2) \times 10^6$ atoms. The anisotropic free expansion from the trap is visible, which is typical for existence of a Bose-Einstein condensate.

Figure 6.7 shows a typical absorption picture of a molecular lithium Bose-Einstein condensate in the dipole trap and after time-of-flight. Imaging was performed on the BEC side of the Feshbach resonance. The anisotropic free expansion from the trap is visible, which is typical for a Bose-Einstein condensate.

CHAPTER 7

Magnetic Field and Radio Frequency Coils

The precise application of magnetic fields is an important requirement in order to perform experiments with ultracold atoms. In our case, the following fields are necessary to perform the experiments presented in this thesis. The first magnetic field during the experimental cycle is the Zeeman slower field, which keeps the atoms resonant with the slowing beam. Afterwards, the magnetic field of the magneto-optical trap (MOT) is a key ingredient to build up a confining force and to trap the atoms after the oven. Moreover, a compensation coil (ZS compensation coil in Table 7.1) ensures that the position of the MOT does not change when the Zeeman slower field is turned off. Further cooling of the atoms is achieved in a magnetic trap (MT) where the atomic density is increased to ensure high collision rates during evaporative cooling. The same coils later generate a homogeneous magnetic field in order to tune the s-wave scattering length by means of a Feshbach resonance. During the different experimental stages of the experiment, the earth magnetic field and stray fields have to be canceled. In addition, fields are required to define quantization axes for example for optical pumping and imaging. This is the reason why compensation coils in Helmholtz and anti-Helmholtz configuration are placed along all three axes of the experiment.

Another important aspect is the application of microwave and radio frequency fields. With the help of these fields the hyperfine states of atoms can be manipulated. This is used for example during radio frequency evaporation of sodium in the magnetic trap and for creating spin mixtures of lithium in the dipole trap.

Coil	Windings	[GcA^{-1}]	[GA^{-1}]	Current [A]
ZS comp.	2×3 $+2 \times 8$	not measured	not measured	20
MOT	6×2	0.70	not needed	20 (MOT) 105 (MT)
MT and Feshbach	3×5	0.41	1.89	535
Three layers on top of Feshbach coils	5	~ 0.1	~ 0.4	depends on purpose
Comp. along x and y	2 coils *à* 2×4	0.02	0.14	depends on purpose

Table 7.1: Overview of the properties of the magnetic field coils: Zeeman slower compensation coil (ZS comp., red), magneto-optical trap (MOT, orange), magnetic trap (MT, black), three layers on top of the Feshbach coil (black) and the compensation coils along the x- and y-direction (green). The colors refer to Figure 7.1 andFigure 7.4. The field values are given for the strongest confining direction. The number of winding are to the number of layers times the number of windings and refer to a single coil of coil pairs.

Due to this importance of the magnetic and rf coils, this chapter gives an overview of all of them and specifies important experimental parameters. A summary of important details can be found in Table 7.1 for the magnetic field coils and in Table 7.2 for the radio frequency coils and an illustration of the magnetic field coils in Figure 7.1.

7.1 Coils for Laser Cooling

Two sets of coils are used during the process of laser cooling: the Zeeman slower and the MOT coils. The Zeeman slower including its field has been extensively described in section 4.3 and is not reviewed again. One of the MOT coils however is displayed in Figure 7.2. It consists of 6×2 windings glued to a water cooled body made out of copper. Both MOT coils are mounted to the main chamber and leave space for a MOT beam with a diameter of approximately 22 mm. These coils produce a magnetic field gradient of 0.7 Gcm^{-1} A^{-1}. The gradient for the MOT is approximately 14 Gcm^{-1}.

After the MOT coils have been used for the magneto-optical trap, the fields are ramped up for the initial magnetic trap with a gradient field of 70 $\mathrm{G\,cm^{-1}}$ as explained in chapter 5. The bare winding pattern of the Zeeman slower and MOT coils are illustrated in Figure 7.1.

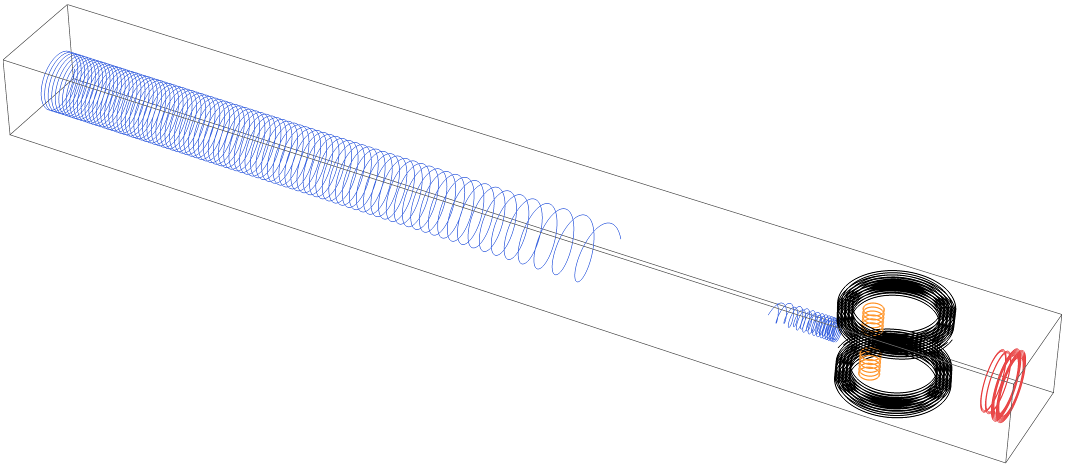

Figure 7.1: Illustration of the following magnetic field coils: Zeeman slower (blue), compensation coil to cancel Zeeman slower field at MOT position (red), MOT coils (orange) and final magnetic trap coils/ Feshbach coils (black).

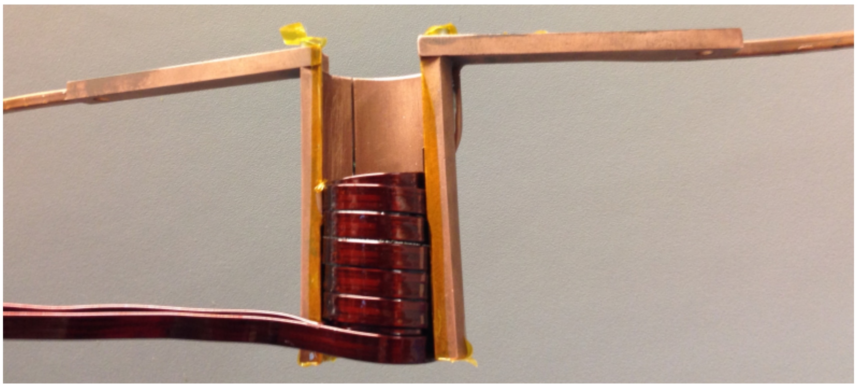

Figure 7.2: This image shows one of the MOT coils. It consists of 6 × 2 windings glued to a cooling body made out of copper. Both MOT coils are mounted to the main chamber and leave space for a MOT beam with a diameter of approximately 22 mm. After the MOT coils have been used for the magneto-optical trap, the fields are ramped up for the initial magnetic trap as explained in chapter 5. A more detailed drawing of the coils surrounding the chamber can be found in Figure 7.4.

7.2 Magnetic Trap and Feshbach Coils

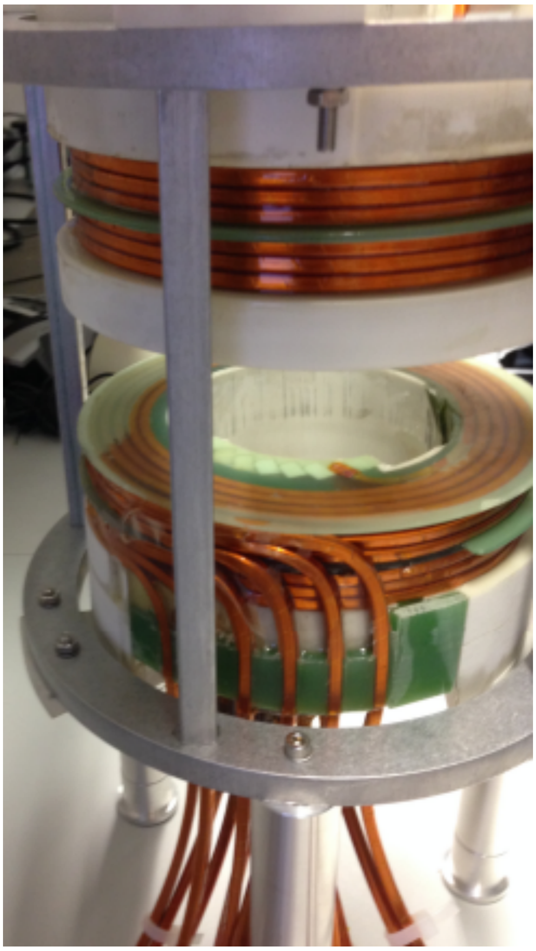

Figure 7.3: Magnetic field coils for the final magnetic trap and for applying a homogenous magnetic field as well as for offset and gradient fields along the gravity direction. This picture shows a test setup for measuring the magnetic field before the coils were mounted onto the experimental chamber.

The final magnetic trap and Feshbach coils are shown in Figure 7.3. This picture shows a test setup for measuring the magnetic field before the coils were mounted onto the experimental chamber. The coil consists of six different layers grouped into two stacks. Each layer consists of five windings. The stack closest to the center is used in anti-Helmholtz configuration for the final magnetic trap. These layers together induce a magnetic field gradient of $0.413\,\mathrm{G\,cm^{-1}\,A^{-1}}$ in the strongest confining (z-) direction. Later during the experimental cycle, the coils are used in Helmholtz configuration in order to apply a homogeneous magnetic field in order to tune the s-wave scattering length by means of a Feshbach resonance. In this case the coils generate a magnetic field of 1.895 GA^{-1}. The outer layers are needed to apply offset fields and to compensate the earth magnetic field. Each layer can be addressed independently in order to increase the homogeneity of the Feshbach field if needed. The coils are usually operated at currents of up to 550 A. Therefore, efficient cooling of the coils is necessary, which is the reason why each of the layer is water cooled from the inside.

These Feshbach coils are mounted directly onto the main vacuum chamber with the hope to increase the relative stability of the vertical lattice and magnetic field position. To be more specific, the coils can slightly move due to thermal expansion or while switching from anti-Helmholtz to Helmholtz configuration (as a repulsive force between the coils is changed to an attractive force). The lattice beam, which will create two dimensional trapping potentials will be reflected by the top vacuum window. Having the coils mounted onto the chamber should increase the stability of the relative alignment of the two dimensional pancakes and the magnetic field. This should make the addressing of single layers by radio frequency more reliable.

As the bottom coil configuration touches the steel chamber, a spacer is inserted for the top one. This off-centers the final magnetic trap position from the center of the vacuum chamber and brings the zero magnetic field position of the magnetic trap and hence the atoms 3 mm below the vacuum window. This small distance is needed for high resolution imaging with an objective, which will be placed directly onto the vacuum window.

The coils were designed in a way that the curvature of the magnetic field in Helmholtz configuration is minimized and at the same time only reasonable currents are needed. They were manufactured by the mechanical workshop of the physics institute. First, a winding body was made out of TECADUR PBT GF30, which is a special kind of polyester reinforced with glass fiber. It is non-magnetic, hence inductive currents inside the mount are suppressed. All layers were wound at the same time while the winding body was rotating on a lathe. The wire has a cross section of $(4 \times 4)\,\mathrm{mm}^2$ and a hole in the center with a diameter of 2.5 mm for water cooling. Electric insulation is given by two layers of Kapton surrounding the outside of the wire.

7.2.1 Magnetic Field Stability

In order to measure long term field stability at a certain point during the sequence, for example when an radio frequency flip is performed, the current sent to the Feshbach coils was measured with a current transducer[1]. The average of four measurements, which are 300 µs apart, give one data point. After several hours of measurement time this results in a measured standard deviation divided by the mean value of $2 \cdot 10^{-5}$. This shows a high magnetic field stability.

In addition, such a current transducer monitors the current during the sequence and is used to regulate the magnetic field as described in the next section.

7.2.2 PID Control for Magnetic Field and 50 Hz Synchronization

An additional regulation of the magnetic field is implemented for long term stability of the fast rf flips. The regulation of the power supply is not reliable enough. For this purpose a PID circuit is installed, which compares the set voltage to the measured voltage of the current transducer. There are two current transducers in operation: one for monitoring purposes and a second one for regulation.

Moreover, a synchronization of the experimental sequence to the 50 Hz AC power line is implemented. This 50 Hz shows up on the current sent to the Feshbach coils. The synchronization is done shortly before a fast RF flip is performed. To be more specific, the experimental sequence pauses and waits until a peak of the 50 Hz noise is reached and continues afterwards. This ensures that the magnetic field during the RF flips is not influenced by 50 Hz noise.

7.2.3 Fast Turn Off of Magnetic Fields

For the rapid ramp technique described in section 8.2 the magnetic field has to be turned off quickly. Switching off currents can be done fast (within nano seconds) with the help of IGBTs or MOSFETS. However, these fast turn-offs induce a voltage, which can easily exceed 1 000 V and which can cause damage to the Kapton insulation leading to short between the coils. This has to be avoided by any means. We therefore built snubber circuits consisting of high power resistors to damp the power and more importantly varistors across the coils, which lower their resistance above a certain clamping voltage (50 V). More details on this snubber circuit can be found in [116].

---

[1] LEM, ITN 600-S ULTRASTAB

7.2.4 Calibration of Magnetic Fields

The first calibration of the magnetic field coils was performed before installing them in the experiment. The magnetic field dependence on the current and position was recorded with a Hall probe sensor. A more precise measurement was later achieved with the atoms in the experiment by finding the imaging resonances, which can be theoretically predicted with the Breit-Rabi formula. The magnetic field accuracy of this calibration technique is set by the linewidth of the imaging, which is about 6 MHz. This technique was also used for measuring the decay of the magnetic field during the rapid ramp technique (section 8.2). Even better accuracy can be achieved by using radio frequency induced spin-flips as their linewidth is on the order of 100 Hz, which results in an accuracy of approximately 16mG (for the rf transition used, we have 6.3Hz/mG).

7.3 Compensation Coils

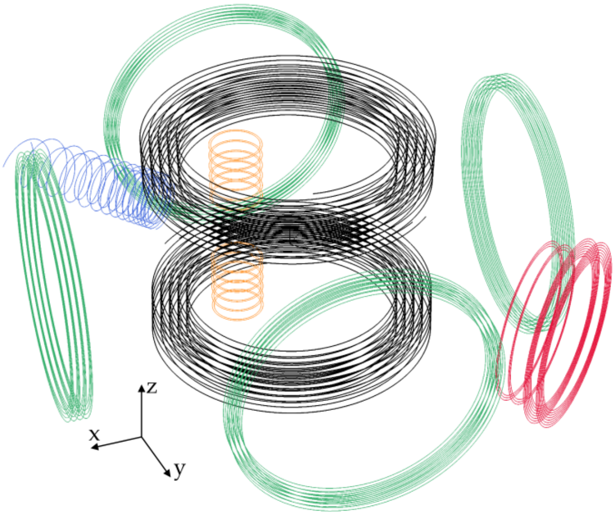

Figure 7.4: Illustration of all magnetic field coils surrounding the main vacuum chamber: Zeeman slower (blue), compensation coil to cancel the Zeeman slower field at the position of the MOT (red), MOT coils (orange), Feshbach coils (black) and compensation coils along x- and y-direction (green).

The magnetic field of the Zeeman slower is switched on while loading the magneto-optical trap. After enough atoms have been loaded, the slower beam is turned off and the magnetic field of the Zeeman slower is ramped down. As the magnetic field of the slower is not zero at the magneto-optical trap (MOT), it contributes to the MOT magnetic field. In order to ensure that the zero field position of the MOT does not change when the slower is turned off, a compensation field is applied, which cancels the contribution of the magnetic field of the Zeeman slower at the position of the MOT. This ensures loading of the magnetic trap without any sloshing of the cloud and subsequent heating. The Zeeman slower compensation field is simultaneously ramped down with the slower field. The coil creating this field sits opposite of the Zeeman slower on the other side of the main chamber (as shown in Figure 7.4).

Similarly, stray fields can for example change the position of the MOT relative to the zero position at high gradients. Hence, offset fields are applied to force the MOT at low gradients into the same position as for high gradients. This ensures that the position of the MOT is the same as the position of the initial magnetic trap, which is generated by the MOT coils. These compensation coils surround the main optical viewports in the x-y-plane and are located in the outer layers of the Feshbach fields for fields in the z-direction to apply offset and gradient fields. Typically two sets of compensation coils are designed for each axis, one for generating offset fields and one for canceling gradient fields. All compensation field coils are illustrated in Figure 7.4.

7.4 Microwave and Radio Frequency Sources

The evaporation scheme of sodium in the magnetic trap utilizes microwave transitions to transfer atoms into magnetically untrapped hyperfine states as described in section 5.3. For this purpose microwave fields between $1.7 - 1.9\,\mathrm{GHz}$ are necessary. This frequency range is obtained by mixing a fixed frequency of 2.2 GHz generated by a signal generator[2] with a variable frequency generated by an FPGA controlled feed-back system [117]. The signal is amplified by a 10 W amplifier from microwave amps[3] and sent to an U-shaped coil (with following dimensions: 1 mm thick silver foil, 7.5 mm $\times$41 mm wide bended to a radius of 10 mm).

Besides this microwave coil, we use two radio frequency coils to drive Landau-Zener sweeps and to perform fast spin-flips between the three lowest lying hyperfine ground states in lithium. For this purpose a single loop rectangular coil with the dimensions of 20 mm $\times$ 50 mm is built and a 100 W amplifier[4] enhances the signal. As a source

---

[2] Marconi Instruments, AM/FM Signal Generator 2024 (9kHz-2.4GHz)

[3] AM38A-1.7-2.1-40-40

[4] Kuhne electronic, KU PA BB 003055-100 A

for the frequency for the $|6\rangle \rightarrow |1\rangle$ transfer at 240 MHz, a signal generator[5] is used. In contrast, for creating the spin mixture the magnetic field is kept constant and the frequency is ramped across the resonance. Here, the signal is again generated by a home made FPGA system and can be swept across the resonance at 60.5 MHz at 103 G.

For the experiments described in chapter 9 to chapter 11 an essential requirement is to perform fast rf transfers between the lowest three hyperfine states at high fields. For this reason another rectangular coil (15 mm × 15 mm wide and two windings) is made and mounted close to the atoms. The frequency is produced by a signal generator[6] and amplified by a 100 W amplifier[7]. The spin-flip can be completed within 22 µs.

In addition to the above mentioned coils we have another microwave coil, which can be used to transfer atoms from the $|1\rangle$ state into the $|6\rangle$ state at high magnetic field. Similar to the other microwave coil, this coil is U-shaped with a radius of 8 mm made out of a 6 mm × 2 mm thick copper wire. It is connected to an 80 W amplifier[8].

All rf coils are mounted onto the top viewport, such that they are less than one centimeter away from the atoms. The radio frequency coils are slightly tilted in order to drive sigma transitions as the magnetic field direction is perpendicular to the viewport. A summary of the radio frequency and microwave coils is given in Table 7.2.

---

[5] Windfreak TechnologiesSynthNV: 34 MHz $-$ 4.4 GHz RF Signal Generator w/ Power Detector

[6] Agilent, N5183A MXG Microwave Analog Signal Generator

[7] Kuhne electronic, KU PA BB 003055-100 A

[8] Kuhne electronic, KU PA BB 070270-80 A

Purpose of coil	Shape	Frequency range	Amplifier
Evaporation of ^{23}Na in MT	U-shaped coil, radius of 11 mm	$1.7 - 1.9$ GHz	10 W, AM38A-1.7-2.1-40-40, microwave amps
Landau-Zener sweeps in ^{6}Li	rectangular coil, $20\,\text{mm} \times 50\,\text{mm}$	$60 - 240$ MHz	100 W KU PA BB 003055-100 A, Kuhne electronic
Fast RF flips in ^{6}Li	rectangular coil, $15\,\text{mm} \times 15\,\text{mm}$, two windings	$70 - 85$ MHz	100 W, KU PA BB 003055-100 A, Kuhne electronic
$\lvert 1\rangle \rightarrow \lvert 6\rangle$ transfer at high fields	U-shaped coil, radius 8 mm	$2.0 - 2.7$ GHz	80 W, KU PA BB 070270-80 A, Kuhne electronic

Table 7.2: Overview of microwave and radio frequency (rf) coils.

CHAPTER 8

Techniques for Characterizing Ultracold Gases

8.1 Imaging Technique

Sophisticated imaging techniques are required to extract properties of the atomic cloud, which then permit conclusions about the state and dynamics of the cloud. Resonant absorption imaging is the most important technique used in our experiment to extract information about the temperature, atom number, condensate fraction and its dynamical evolution. Resonant light gets absorbed by the atoms resulting in a shadow on the camera from which the atomic density, atom number, temperature and condensate fraction can be reconstructed. A general introduction to resonant absorption imaging can be found elsewhere [64]. This section specifies details of our imaging systems, the calibration for high intensity imaging and high field imaging of lithium.

8.1.1 Overview of Imaging Systems

In total we use five different cameras for monitoring atom numbers, aligning beams and taking the data presented in this thesis. Two CMOS cameras[1] monitor continuously the sodium and lithium atom number respectively in the magneto-optical trap. For this purpose, they collect the fluorescence of the atoms from which the atom number can

---

[1] Basler, acA1300-60gm

be calculated. For lithium, the picture is taken at the end of the MOT with an exposure time of 3 ms. As most of the sodium atoms occupy the dark state in the dark SPOT, the sodium picture is taken during molasses with an exposure time of 150 µs. Each camera is covered with a laser line filter to make sure that only the desired wavelength reaches the sensor. These cameras were used to compare the MOT position at low and high fields and to adjust the offset fields to maintain a fixed position while loading the magnetic trap.

Three CCD and EMCCD cameras are placed along each coordinate axis (see Figure A.6 and Figure A.7). One CCD camera[2] sits along the axis of the plug and the horizontal dipole beam (along the x-axis) and is used for aligning both beams relative to the atoms. In addition, this imaging axis is used for imaging sodium and lithium in the magnetic trap. The magnification of this system is 1, whereas the resolution is approximately 5 µm.

Perpendicular to this camera (along the y-axis) we have another EMCCD camera[3]. With a magnification of 4.25 and a resolution of approximately 5 µm it is mainly used for debugging the systems performance.

The main imaging system is set up vertically along the magnetic field direction of the Feshbach fields (z-axis). It contains an EMCCD camera[4], a first lens (focal length: f =120 mm, diameter: 30 mm, from lens optics, AR coated for 589 nm, 671 nm, 1 064 nm after the atoms, which collimates the image beam from the atoms and a second lens focuses the beam onto the camera. The magnification of this system is 6.25 and the resolution is $\lesssim$ 3.3 µm. We typically use a 2 µs long pulse to image lithium. Two pictures are taken within one experimental run, the first one C_{atoms} with the atoms present and the second one C_{bright} 30 ms later without the atoms but only with the imaging light. By dividing the counts of these two pictures we account for fringes imprinted by the imaging path and non-homogenous light distribution of the imaging beam. In principle, this camera can be operated in a so-called fast kinetics mode, which allows taking subsequent images within a much smaller time window. This is achieved by storing the electrons in a sub region of the chip while taking the next picture. The sub region for storage is covered with a razor blade to hide from the imaging light while taking further pictures. After all pictures are taken, the readout starts. In addition, we took several dark pictures C_{dark} with the camera shutter closed

---

[2] Apogee, Alta U1

[3] Andor, ixon-ultra 897

[4] Andor, ixon-ultra 897, 512px × 512px, pixel size: 16 µm × 16 µm

and average them. Subtracting C_{dark} from C_{atoms} and C_{bright} allows removing dark counts from the pictures.

8.1.2 High Field Imaging of ^{6}Li

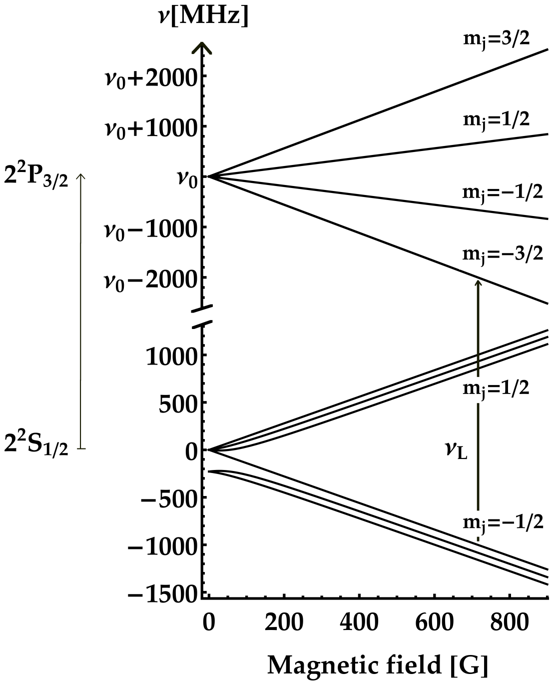

Figure 8.1: High field imaging of the three lowest hyperfine levels of the $2^2S_{1/2}$ ground state to the $2^2P_{3/2}$ state of ^{6}Li using the optical D2 transition. ν_0 denotes the $|F = 3/2\rangle \rightarrow |F'\rangle$ transition at zero field and ν_L is the laser frequency.

The experiments in this thesis are performed for different interaction strengths, which are adjusted by means of a Feshbach resonance. This resonance is located at 690 G for $|13\rangle$, 811 G for $|23\rangle$ and 834 G for $|12\rangle$. The field region used for the experiments goes up to 1000 G. As the resonance condition for imaging changes with the magnetic field, an imaging system is needed where the imaging frequency can be adjusted over a wide range of frequencies. The magnetic field dependence of the energy levels of ^{6}Li for the optical D2 transition is shown in Figure 8.1. Here, ν_0 denotes the $|F = 3/2\rangle \rightarrow \left|F'\right\rangle$ transition at zero field and ν_L is the laser frequency. The six hyperfine levels of the ground state are named $|1\rangle, |2\rangle \ldots |6\rangle$ (not shown in picture).

To calculate the precise imaging frequency, the Breit-Rabi problem has to be solved and the result is plotted in Figure 8.1. However, for high fields ($> 350\,\mathrm{G}$) and within the precision of the natural linewidth a simplified formula for the transition frequency can be given [88]

$$\begin{aligned} \nu_{|1\rangle\rightarrow m_j=-3/2} &= \nu_0 - 1.4\,\mathrm{Mhz/G}\cdot\mathrm{B} + 158\,\mathrm{MHz} \quad , \\ \nu_{|2\rangle\rightarrow m_j=-3/2} &= \nu_0 - 1.4\,\mathrm{Mhz/G}\cdot\mathrm{B} + 82\,\mathrm{MHz} \quad , \\ \nu_{|3\rangle\rightarrow m_j=-3/2} &= \nu_0 - 1.4\,\mathrm{Mhz/G}\cdot\mathrm{B} \quad . \end{aligned} \tag{8.1}$$

These are the frequencies we use to image either one of the three lowest hyperfine states of lithium at high field. At high fields states with different m_I within the same m_J are not resolved due to the small hyperfine constant of lithium (they are only about 1 MHz apart).

This known frequency dependence of the energy levels on the magnetic field is used to calibrate the magnetic field coarsely. For example, the measurement of the imaging detuning during the rapid magnetic field ramp, which converts pairs into tightly bound molecules, is used to measure the change in the magnetic field as shown in Figure 8.4. Likewise, radio frequency transitions between different hyperfine states have been used for more precise calibration of the magnetic field.

As explained in subsection 4.2.2 we use a second laser, which is offset locked to the main laser allowing to tune its frequency by a variable amount. During the first part of the experimental sequence this laser is used to generate the light for Zeeman slowing and optical pumping. At the end of the sequence, where this light is not needed for this purpose anymore, its frequency is automatically shifted to the desired resonance frequency at the imaging field. This change in frequency is achieved by ramping the frequency of a signal generator[5] acting as a local oscillator in the locking scheme.

In addition, we placed a motorized waveplate in the imaging path of our main imaging axis allowing to switch between different imaging polarizations depending whether imaging is performed at high or at low field.

---

[5] Windfreak Technologies, SynthNV 34.4MHz to 4.4 GHz

8.1.3 High Intensity Absorption Imaging

For an accurate calibration of our atom number from pictures with a high optical density, we need to perform high intensity absorption imaging. We follow a technique adapted from [118–120]. While the atoms are imaged during time-of-flight, they experience a force given by the transferred momentum $\hbar k_L$ (where k_L is the wavenumber of the laser) times the scattering rate γ given by Equation 6.4. This results in an average acceleration of the atoms, namely

$$\bar{a} = \frac{\hbar k_L}{m} \frac{\Gamma}{2} \frac{I}{I + I_s} \quad . \tag{8.2}$$

Here, Γ is the natural linewidth, I the intensity, m the atomic mass and I_s the saturation intensity. During an imaging pulse of length τ, the atoms gain an averaged velocity $v_\tau = \bar{a}\tau$ and travel a distance $d_\tau = \bar{a}\tau^2/2$. As a result of the change in velocity during the imaging process also the resonant imaging frequency changes due to the Doppler shift. To make sure that the maximum Doppler shift $k_L v_\tau$ is smaller than the intensity broadened line width the first imaging constraint reads

$$k_L v_\tau < f_{Doppler} \Gamma \sqrt{1 + s} \quad , \tag{8.3}$$

where $f_{Doppler}$ is a specified factor and s is the saturation parameter given by $s = I/I_s$. Together with Equation 8.2, the latter condition on the imaging pulse length can be written as

$$\tau < f_{Doppler} \frac{2m}{\hbar k_L^2} \sqrt{s \left(\frac{1}{s} + 1 \right)^3} \quad . \tag{8.4}$$

Another requirement on the imaging pulse length can be derived from the fact that the atoms should stay within the depth of field $d_{dof} = \lambda_L / \mathrm{NA}^2$ (NA is the numerical aperture). Or equivalent, they should travel less than the depth of field times a factor f_{displ}

$$d_\tau < f_{displ} d_{dof} \quad . \tag{8.5}$$

Similar to above this condition can be translated to a condition on the imaging pulse length τ

$$\tau < \frac{2}{\Gamma} \sqrt{\frac{f_{displ} d_{dof} \Gamma m}{\hbar k_L} \left(\frac{1}{s} + 1 \right)^3} \quad . \tag{8.6}$$

These two conditions (Equation 8.4 and Equation 8.6) arising from the Doppler shift and the displacement are plotted in Figure 8.2.

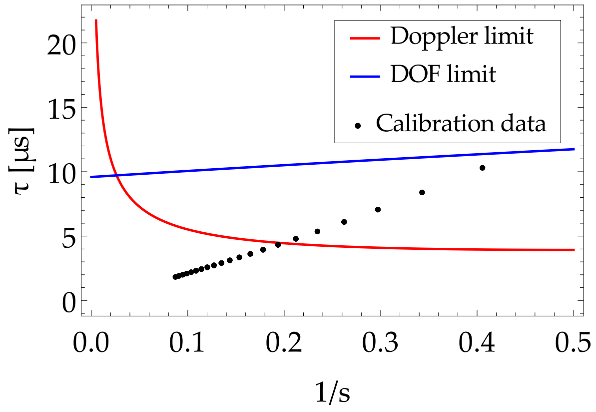

Figure 8.2: This figures shows the imaging constraints on the pulse length due to the Doppler shift (Equation 8.6) and displacement out of the depth of view (DOF) (Equation 8.4). The Doppler and displacement factors are set to be $f_{Doppler} = 0.7$ and $f_{displ} = 1.8$. The calibration data lying below the two limits is used to determine the α-parameter, see text. We can see that an imaging pulse time of 2 µs lies well below the two limits.

The modified Beer-Lambert law has to be applied [121] as we perform high intensity imaging in order to image clouds with high optical density

$$\rho\sigma_0 = -\alpha \log\left(\frac{I_f}{I_i}\right) + \frac{I_i - I_f}{I_{0,sat}} \quad . \tag{8.7}$$

The left hand side denotes the optical density given by the atomic density ρ times the bare atomic cross section $\sigma_0 = 3\lambda_L^2/(2\pi)$. Before the imaging light gets absorbed by the atoms, its initial intensity is given by I_i, whereas afterwards it is described by I_f. The parameter α relates the effective saturation intensity I_s to the ideal saturation intensity $I_{0,sat}$, which can be different due to imperfect imaging polarization, Doppler shift or off-resonant probe light etc. . The first term on the right hand side of Equation 8.7 describes the low intensity limit and corresponds to the Beer-Lambert law. However, the second term needs to be included when the intensity of the imaging pulse is comparable and higher than I_s. The intensities before and after the atoms are proportional to the counts $C_{i/f}$ of the bright and atom picture

$$I_{i/f} = \frac{\hbar\omega_L}{\eta\tau A_{px,obj}} C_{i/f} \quad , \tag{8.8}$$

where $C_i = (C_{bright} - C_{dark})$ and $C_f = (C_{atoms} - C_{dark})$. The area of a pixel in the object plane is described by $A_{px,obj} = d^2_{px,img}/M^2$, where $d_{px,img}$ is the pixel size and M the magnification. The total photon-to-count conversion efficiency is given by η. This parameter also contains the quantum efficiency of the camera and the transmission through the optical path. With these definitions, we can write Equation 8.7 as

$$\rho\sigma_0 = -\alpha \log\left(\frac{C_f}{C_i}\right) + \frac{C_i - C_f}{C_{0,sat}\tau/\tau_0} \quad . \tag{8.9}$$

Here, $C_{0,sat} = \eta\tau_0 A_{px,obj}/(\hbar\omega_L)$ and τ_0 corresponds to the pulse time used in the experiment, which is 2 µs in our case. The main task is to calibrate $C_{0,sat}$ and α. We calibrate the proportionality factor $\eta A_{px,obj}/(\hbar\omega_L)$ between the counts on the camera and the intensity of the imaging beam (Equation 8.8) by measuring the power with a power meter and comparing it to the counts on the camera. The α-calibration is performed by repeatably taking pictures of the atoms, which are always prepared the same way. However, the pulse time is varied but the number of counts are kept constant by varying the light power instead. This is done by accordingly changing the attenuation voltage of the imaging AOM. Due to the fact that the cloud is always prepared the same way, $\rho\sigma_0$ (left hand side of Equation 8.9) is assumed to be the same each time. Rearranging Equation 8.9 and considering regions with equal optical density $\rho^{(b)}\sigma_0$ then leads to the linear relation between $\frac{C_i - C_f}{\tau/\tau_0}$ and $\log\left(\frac{C_f}{C_i}\right)$ with a slope given by $-C^{(b)}_{0,sat}$

$$\frac{C_i^{(b)} - C_f^{(b)}}{\tau/\tau_0} = C^{(b)}_{0,sat} \log\left(\frac{C_f^{(b)}}{C_i^{(b)}}\right) + C_{0,sat}\rho^{(b)}\sigma_0 \quad . \tag{8.10}$$

Here, (b) stands for the bin index and $C^{(b)}_{0,sat} = \alpha^{(b)} C_{0,sat}$. The bins (pixel regions of the camera) with equal density are grouped by defining rings of equal optical density. From linear fits to bins with the same optical density but imaged with different pulse times (hence different C_i) we can deduce α as a function of optical density, see Figure 8.3.

After the calibration of all parameters of Equation 8.9, the atom number can be deduced by solving Equation 8.9 for the atomic density ρ. Integrating over all pixels and multiplying by the imaged area per pixel gives the atom number.

The temperature can either be extracted from the shape of the thermal wings after time-of-flight, or by adiabatically ramping to the field to a value where Cooper pairs

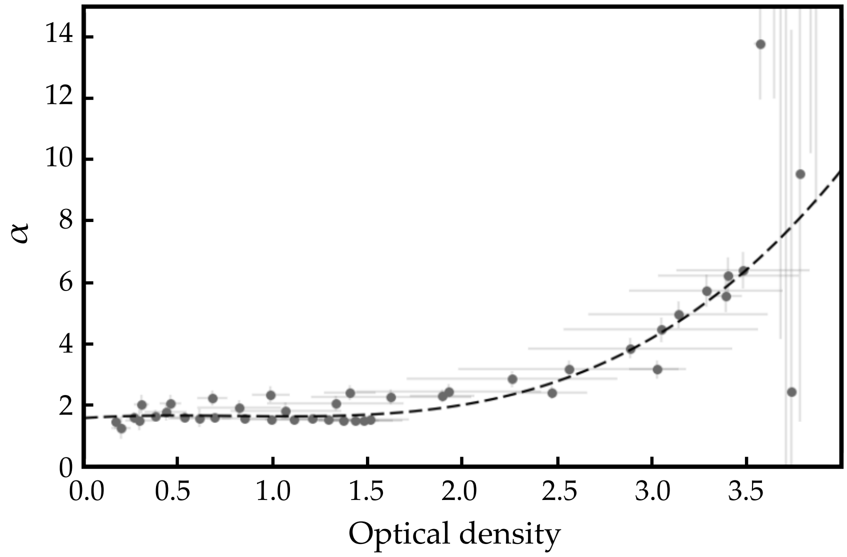

Figure 8.3: Calibrated α-parameter for high intensity imaging.

start to form. Then the temperature is given by $T = 0.28T_{c,BCS}$ (called the Gor'kov-Melik-Barkhudarov correction; $T_{c,BCS}$ is given by Equation 2.15).

8.2 Rapid Ramp Technique

To the degree of superfluidity and pairing on the BCS-side a different technique as the simple time-of-flight technique is needed as Cooper pairs break during release and subsequent expansion from the trap. Molecular Bose-Einstein condensates show the characteristic bimodal distribution after expansion, which is the smoking gun of Bose-Einstein condensation. On the BCS-side however, the pairs of fermions are very fragile and the binding energy of the pairs can drop below $k_B T$ during expansion meaning that the pairs can break when the gas becomes more dilute after the release of the trap. A technique, which circumvents this problem and allows imaging of the Cooper pairs was first introduced at JILA [55] and later adapted for ^{6}Li at MIT [122]. This technique relies on a magnetic field sweep starting on the BCS-side and rapidly ramping the field to the BEC-side of the resonance converting the fragile pairs into stable molecules. If this conversion efficiency is very high, no molecules are formed during the ramp on the molecular side and collisions can be neglected, the momentum information of the initial pair is preserved. After time-of-flight the imaged momentum distribution reveals the momentum distribution of the pairs on the BCS-side. This technique results in a measure of the degree of coherence on the BCS-side.

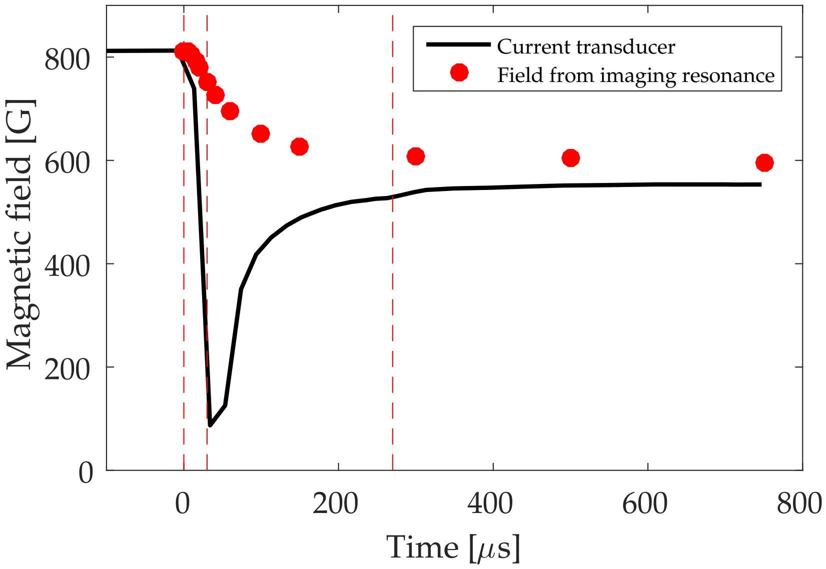

Figure 8.4: Example of a fast magnetic field ramp. The field is rapidly ramped to a value where the scattering length is close to zero, such that the sample is mostly non-interacting during the expansion and interactions do not change the momentum distribution. The first dashed line indicates when the MOSFET connected to the power supply is turned off meaning the coils are rapidly disconnected. In addition, the discharge of the power supplies is started. The second dashed line indicates when the MOSFET is turned on and the last dashed line marks the point where the discharge of the power supply is turned off.

An example of a fast magnetic field ramp is shown in Figure 8.4. The field is rapidly ramped to a value where the scattering length is close to zero such that the sample is mostly non-interacting and interactions do not change the momentum distribution during the expansion. Following this expansion the field is ramped up for imaging to a field where the molecular binding energy is small enough such that the molecules can be imaged with the same light as for free atoms. The solid line in Figure 8.4 shows the field converted from the measured current of the coils[6]. Compared to that, the dots show the real field value at the position of the atoms measured by finding the resonant imaging frequency and converting the frequency into a field value with the help of the Breit-Rabi formulas (see subsection 8.1.2). Due to induced currents in the steel chamber and gaskets, the field value does not follow the field measured with the transducer. Fitting the first data points up to 40 µs shows that the field changes by 114 G within

---

[6] current transducer, LEM, TN 600-S ULTRASTAB

50 µs. This ramp starts near resonance on the BEC-side of the Feshbach resonance, however similar ramps can be implemented all over the BEC-BCS crossover regime.

CHAPTER 9

Observation of the Higgs Mode in a Strongly Interacting Superfluid

We report on the first observation of the Higgs mode in a strongly interacting Fermi gas in the crossover from a weakly interacting BCS superfluid to a Bose-Einstein condensate. By modulating the amplitude of the superconducting order parameter Δ, we spectroscopically observe a resonance behavior at twice the gap frequency $2\Delta/h$. This resonance behavior broadens if the interactions are increased signaling the disappearance of the mode when Cooper pairs turn into strongly bound dimers. In addition, we show that our novel excitation scheme couples directly to the Higgs mode and does not create single-particle excitations or phase fluctuations.

9.1 Introduction to the Higgs Mode

The Higgs mode is a collective mode of the order parameter, which arises after the symmetry is spontaneously broken. The typical picture illustrating the spontaneous symmetry breaking uses the Mexican hat potential, shown in Figure 9.1 (a). If the system resides in a state corresponding to the center of the hat, the system is symmetric with respect to rotations around the center axis. However, if the system spontaneously picks a point along the minimum of the Mexican hat potential, which is an equilibrium state, the symmetry is broken as the new state exhibits a lower symmetry. Starting from this equilibrium state, two possible modes arise due to the new landscape, the gapless

Goldstone mode and the orthogonal gapped Higgs mode. The Goldstone mode describes long-wavelength variations of the phase of the order parameter corresponding to fluctuations along the minimum of the potential. In contrast, the Higgs mode alters the amplitude of the order parameter, which equals radial excitations in the Mexican hat potential.

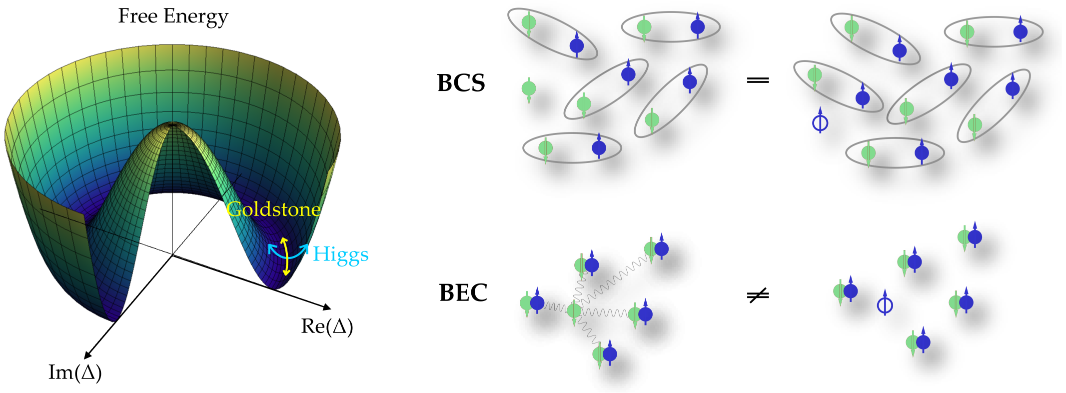

(a)

(b)

Figure 9.1: (a) Mexican hat potential of the free energy as a function of real and imaginary part of the complex order parameter Δ. The equilibrium state order parameter spontaneously takes one of the values at the energy minimum. From this, two collective modes arise: a Goldstone mode (yellow curve) varying the phase of the order parameter and a Higgs mode (blue curve) altering its amplitude. **(b)** Illustration of the (absence of) particle–hole symmetry in the BEC-BCS crossover. In the BCS limit the addition of an extra quasiparticle is equal to having a hole in the opposite spin state in a configuration with an extra Cooper pair. Since the number of Cooper pairs is not fixed in BCS theory, particle-hole symmetry is fulfilled. In the BEC limit an additional quasiparticle can interact with the bosons and acquires an effective mass. A hole does not interact with the bosons and hence has different properties.

While Goldstone modes, such as phonons, appear necessarily when continuous symmetries are broken, stable Higgs modes are rare. The Higgs mode requires an additional symmetry to prevent its direct decay to lower lying modes such as the Goldstone mode. The probably best known example of the Higgs mode appears in the Standard Model of particle physics in which it gives elementary particles their mass [15]. After a decade-long search the Higgs boson was found [16, 17], which completes the electro-weak theory of the Standard Model. The stability of the Higgs mode in particle and high energy physics is ensured by Lorentz invariance. In the context of condensed-matter physics, the stability can be ensured by particle-hole symmetry [18]. An example of a particle-hole symmetric system hosting a stable Higgs mode is the Bardeen-Cooper-Schrieffer (BCS) Hamiltonian, which describes weakly interacting superconductors [18, 19]. Figure 9.1 (b) illustrates particle-hole symmetry in a BCS superfluid and its absence in a molecular Bose-Einstein condensate. In the BCS limit the addition of an extra quasiparticle is equal to having a hole in the opposite spin state in a configuration with an extra Cooper pair. Since the number of Cooper pairs is not fixed in BCS theory, particle-hole symmetry is fulfilled. In the BEC limit an additional quaisparticle can interact with the bosons and acquires an effective mass. A hole does not interact with the bosons and hence has different properties.

Indeed, the existence of the Higgs mode in weakly interacting superconductors and conventional BCS superconductors has been proven experimentally [20–22]. However, the excitation mechanisms have only been indirect since the Higgs mode does not couple directly to the electromagnetic field used to excite the mode. This is due to the gauge invariance required for its existence. By exciting other modes such as the charge density wave (CDW) mode in a superconductor [23] weight is transferred to the Higgs mode, which then can be detected by Raman scattering afterwards.

Moreover, the Higgs mode has been observed in systems such as antiferromagnets [28], liquid ^{3}He [29], ultracold bosonic atoms near the superfluid/Mott-insulator transition [30, 31], spinor gases [32] and Bose gases coupled strongly to optical fields [33]. However, weakly interacting Bose-Einstein condensates do not show a Higgs mode as particle-hole symmetry is not fulfilled (see Figure 9.1 (b)).

The situation changes in the realm of strongly correlated superconductors, which require a description beyond the conventional BCS description. Recent research has focused in this context on advanced materials such as cuprates, pnictides and the unitary Fermi gas. The question whether a stable Higgs mode exists in such systems has been subject of numerous discussions [1, 5, 24–27] and experimental signatures have been missing. Our results following in this chapter are the first sign of its existence.

9.2 Coupling to the Modulus of the Order Parameter: The Method

Excitation of the Higgs mode requires a scheme, which couples to the modulus of the order parameter rather than creating phase fluctuations or strong single-particle excitations. Previous theoretical proposals [1, 39, 123] for exciting the Higgs mode in ultracold Fermi gases have focused on a modulation of the interaction parameter $1/(k_F a)$ by changing the magnetic field in vicinity of a Feshbach resonance. However, in the experiment only single-particle excitations have been observed from such a modulation [124].

We have developed a novel excitation scheme employing a radio frequency (rf) field dressing the second lowest hyperfine state $|2\rangle$ of lithium with the initially unoccupied hyperfine state $|3\rangle$. Previous experiments investigating ultracold gases with rf spectroscopy [46, 59, 125, 126] have focused on studying single-particle excitations. To this end, the duration of the rf pulse τ was chosen shorter than the inverse of the Rabi frequency Ω_R such that the spectra could be interpreted in the weak-excitation limit using Fermi's golden rule. Here, we employ a rf drive in the far red-detuned regime and long-pulse limit $\Omega_R \tau \gg 1$ in order to couple to the amplitude of the order parameter. For simplicity, consider the isolated two-level system of the $|2\rangle$ and the $|3\rangle$ state coupled by a Rabi frequency Ω_R with detuning δ from the resonance. The occupation probability of the atoms in the $|2\rangle$ state is $p_{|2\rangle} = 1 - 2\Omega_R^2/\Omega_R'^2 \sin^2(\Omega_R' t/2)$, i.e. the continuous rf drive leads to a time-periodic modulation of the occupation with the effective Rabi frequency $\Omega_R' = \sqrt{\Omega_R^2 + \delta^2}$.

In the many-body problem of the BEC-BCS crossover, the situation is complicated by the dispersion of the (quasi-)particles and the presence of interactions. In particular, a continuum of excitations typically occurs above the energy of the lowest single-particle excitation to state $|3\rangle$ (see Figure 9.2). Deep in the BCS regime, the continuum of excitations is related to the different momentum states. Here, the excitation scheme can be approximated by coupling each occupied momentum state of the BCS quasiparticles in level $|2\rangle$ to the corresponding momentum state in state $|3\rangle$ since the rf dressing transfers negligible momentum. The effective Rabi frequency $\Omega_{R,k}' = \sqrt{\Omega_R^2 + \delta_k^2}$ connecting these two states and the excitation probability become momentum dependent by the detuning $\delta_k = \delta - E_{-k}/h - \xi_k/h$. Here, ξ_k is the single-particle dispersion, $E_k = \sqrt{\xi_k^2 + |\Delta|^2}$ is the quasiparticle dispersion and Δ is the superconducting order parameter. As a consequence, only a blue-detuned (with respect to the atomic level spacing) rf drive couples resonantly to the single-particle continuum. In contrast, a red-detuned rf drive avoids resonant coupling to the single-particle excitations. However, the rf still modulates offresonantly the occupation of the excited states. In Figure 9.3 (a) we illustrate this for three different values of the momentum.

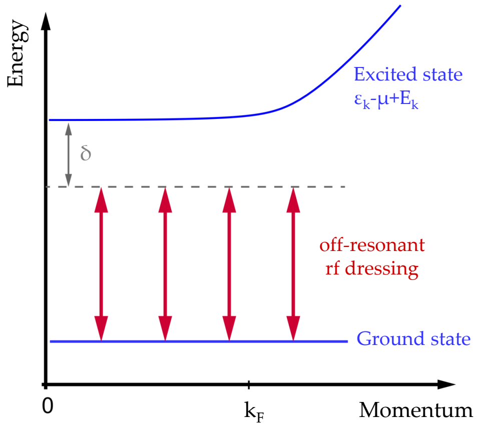

Figure 9.2: Illustration of the excitation scheme. The radio frequency field is red-detuned from the single-particle excitation. It creates an off-resonant excitation to the state $|3\rangle$ with a detuning dependent on the momentum.

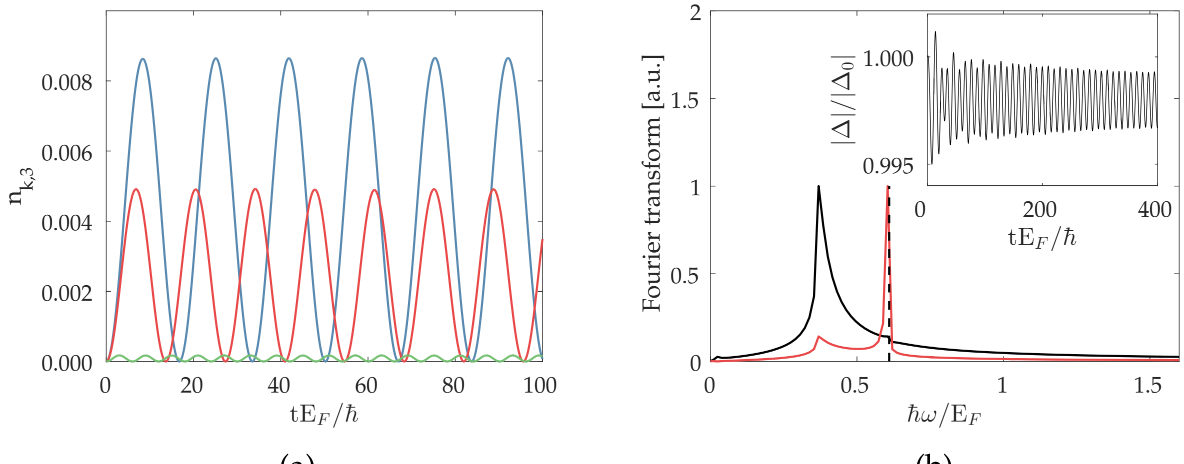

(a)

(b)

Figure 9.3: (a) Time evolution of the momentum-resolved occupation of the $|3\rangle$ state for a fixed value of $1/(k_F a) = -0,67$, a Rabi frequency of $\hbar\Omega_R/E_F = 0.035$, and a detuning $\delta = -0.3247\, E_F/\hbar$. Blue: $k/k_F = 0$, red: $k/k_F = 0.8$, green: $k/k_F = 1.1$. **(b)** Fourier spectra of the occupation of the $|3\rangle$ state (black) and of the amplitude of the order parameter $|\Delta|$ (red). The dashed line is the expected location of the Higgs mode at $2\,|\Delta_0|$. The inset shows the time dependence of Δ.

9.3 Theoretical Modeling

Theoretically, we find that the periodic modulation of the occupation of the state $|2\rangle$ with controllable frequency $\Omega'_{R,k}$ induces a modulation of the amplitude of the order parameter Δ and hence couples to the Higgs mode. To be more precise, the experimental system can be described taking the three different fermionic levels into account. Initially, the system is prepared in a balanced mixture of the states $|1\rangle$ and $|2\rangle$. Since we are mainly interested in the excitation mechanism and the number of excited atoms in the $|3\rangle$ state is very low, we take only the interaction between these two states into account. The BCS Hamiltonian for a spin mixture in the states $|1\rangle$ and $|2\rangle$ is given by

$$H_{BCS} = \sum_{k,\sigma} \epsilon_k c^\dagger_{k,\sigma} c_{k,\sigma} + \frac{g}{V} \sum_{k,q} c^\dagger_{q,1} c^\dagger_{-q,2} c_{-k,2} c_{k,1} \quad , \tag{9.1}$$

where $\epsilon_k = \hbar^2 k^2 / (2m)$ is the single-particle dispersion, g the interaction strength and V the volume. The operator $c^\dagger_{k,\sigma}$ ($c_{k,\sigma}$) creates (annihilates) a fermion with spin σ and momentum k. Introducing a mean field decoupling with an order parameter $\Delta = g/V \sum_k \langle c_{-k,2} c_{k,1} \rangle$ leads to the simplified Hamiltonian

$$H^{mf}_{BCS} = \sum_k \epsilon_k \left(n_{k,1} + n_{k,2} \right) + \sum_k \left\{ \Delta^\star c_{-k,2} c_{k,1} + \Delta c^\dagger_{k,1} c^\dagger_{-k,2} \right\} \quad . \tag{9.2}$$

The first term describes the free energy of atoms in state $|1\rangle$ and $|2\rangle$ and the second term describes the pairing with opposite momentum and spin. The next step to simulate our experiment is to introduce the periodic modulation of the occupation of the state $|2\rangle$. As the wavelength of the radio frequency is on the order of a meter, $p = h/\lambda \ll 1$, we can neglect the momentum transfer. Thus the modulation can be modeled by $\hbar\Omega_R \cos(\omega_{rf} t) \sum_k \left(c^\dagger_{k,3} c_{k,2} + h.c. \right)$ with the Rabi-frequency Ω_R of the drive. Using the rotating wave approximation for the coupling between the states $|2\rangle$ and $|3\rangle$, we obtain the Hamiltonian

$$H = H^{mf}_{BCS} + \sum_k \left(\epsilon_k - \hbar\delta \right) n_{k,3} + \frac{\hbar\Omega_R}{2} \sum_k \left(c^\dagger_{k,3} c_{k,2} + c^\dagger_{k,2} c_{k,3} \right) \quad . \tag{9.3}$$

Here, $\hbar\delta = \hbar\omega_{rf} - \left(\epsilon^0_3 - \epsilon^0_2 \right)$ is the momentum independent detuning, where ϵ^0_n is the bare energy for the state $n = 2, 3$.

In order to determine the time evolution of the order parameter, we derive a closed set of equations for the expectation values

$$\begin{aligned}
\hbar\frac{\partial}{\partial t}\left\langle c_{-k,2}c_{k,1}\right\rangle &= i\left\{-2\epsilon_k\left\langle c_{-k,2}c_{k,1}\right\rangle - \frac{\hbar\Omega_R}{2}\left\langle c_{-k,3}c_{k,1}\right\rangle + \Delta\left(n_{k,1}+n_{-k,2}-1\right)\right\}\\
\hbar\frac{\partial}{\partial t}\left\langle c_{-k,3}c_{k,1}\right\rangle &= i\left\{-\frac{\hbar\Omega_R}{2}\left\langle c_{-k,2}c_{k,1}\right\rangle - \left(2\epsilon_k-\hbar\delta\right)\left\langle c_{-k,3}c_{k,1}\right\rangle + \Delta\left\langle c^{\dagger}_{-k,2}c_{-k,3}\right\rangle\right\}\\
\hbar\frac{\partial}{\partial t}\left\langle c^{\dagger}_{-k,2}c_{-k,3}\right\rangle &= i\left\{\Delta^{\star}\left\langle c_{-k,3}c_{k,1}\right\rangle + \hbar\delta\left\langle c^{\dagger}_{-k,2}c_{-k,3}\right\rangle - \frac{\hbar\Omega_R}{2}\left(n_{-k,2}-n_{-k,3}\right)\right\}\\
\hbar\frac{\partial}{\partial t}n_{k,1} &= -2\mathrm{Im}\left(\Delta^{\star}\left\langle c_{-\mathbf{k},2}c_{\mathbf{k},1}\right\rangle\right)\\
\hbar\frac{\partial}{\partial t}n_{-k,2} &= -2\mathrm{Im}\left(\Delta^{\star}\left\langle c_{-\mathbf{k},2}c_{\mathbf{k},1}\right\rangle\right) + \hbar\Omega_R\mathrm{Im}\left(\left\langle c^{\dagger}_{-\mathbf{k},2}c_{-\mathbf{k},3}\right\rangle\right)\\
\hbar\frac{\partial}{\partial t}n_{-k,3} &= -\hbar\Omega_R\mathrm{Im}\left(\left\langle c^{\dagger}_{-\mathbf{k},2}c_{-\mathbf{k},3}\right\rangle\right) \quad ,
\end{aligned} \tag{9.4}$$

where the number densities are defined as $n_{k,m} = \left\langle c^{\dagger}_{k,m}c_{k,m}\right\rangle$ with $m = 1,2,3$. Note the following appearing terms. The term $\left\langle c_{-k,2}c_{k,1}\right\rangle$ describes the coherence between particles in the states $|1\rangle$ and $|2\rangle$. The application of the radio frequency introduces a coherent transfer of atoms from state $|2\rangle$ into state $|3\rangle$, which is modeled by the term $\left\langle c^{\dagger}_{-k,2}c_{-k,3}\right\rangle$ in the above equations. This leads to the therm $\left\langle c_{-k,3}c_{k,1}\right\rangle$, which similarly to the first term describes the coherence between particles in the states $|1\rangle$ and $|3\rangle$.

An important conclusion follows from the first of these six equations, namely

$$\hbar\frac{\partial}{\partial t}\left\langle c_{-k,2}c_{k,1}\right\rangle \sim \Delta n_{-k,2} \quad . \tag{9.5}$$

Recall, the order parameter is defined as $\Delta = g/V\sum_k\left\langle c_{-k,2}c_{k,1}\right\rangle$. Equation 9.5 shows that a variation of the occupancy of state $|2\rangle$, namely $n_{-k,2}$, introduces a variation of $\left\langle c_{-k,2}c_{k,1}\right\rangle$, which is so to say the k-(momentum-)resolved order parameter.

We solve these six equations numerically discretizing both time t and momentum k and using the self-consistency condition $\Delta = g/V\sum_k\left\langle c_{-k,2}c_{k,1}\right\rangle$ at each time step. This ensures both the convergence for the time step δt and the momentum spacing. Typical values taken are $dk/k_F = 10^{-4}$, $dt = 5\times10^{-4}\hbar/E_F$ and the cutoff for the momentum sum is $E_c = 100E_F$, with E_F the Fermi energy.

To illustrate that the mechanism described above couples to the modulus of the order parameter, we numerically solve the minimal set of coupled equations of motion describing the evolution of the order parameter in presence of an rf coupling to state

$|3\rangle$. In Figure 9.3 (b) we show both the time evolution of $|\Delta|$ and its Fourier transform. Aside from the response corresponding to the modulation frequencies $\Omega'_{R,k}$, we see that the Fourier spectrum displays a sharp peak at twice the initial gap value $2\,|\Delta_0|$. The amplitude of the Fourier spectrum is maximum when $\hbar\Omega'_{R,k} \approx 2\,|\Delta|$.

Figure 9.4 shows the momentum-resolved spectral weight of the gap computed as

$$A_{\mathbf{k}}(\omega) = \left| \mathcal{F}\left\{ \left|\langle c_{\textbf{-k},2} c_{\mathbf{k},1}\rangle\right| - \frac{1}{T}\int_0^T dt\, \left|\langle c_{\textbf{-k},2} c_{\mathbf{k},1}\rangle\right| \right\} \right| \quad . \tag{9.6}$$

The circles indicate the Higgs mode, the stars mark the response to the modulation frequency and the crosses indicate the quasiparticle excitations at $2E_k$. The important result of this theoretical model is that we see this clear resonance at twice the initial gap, which is the signature of the Higgs mode.

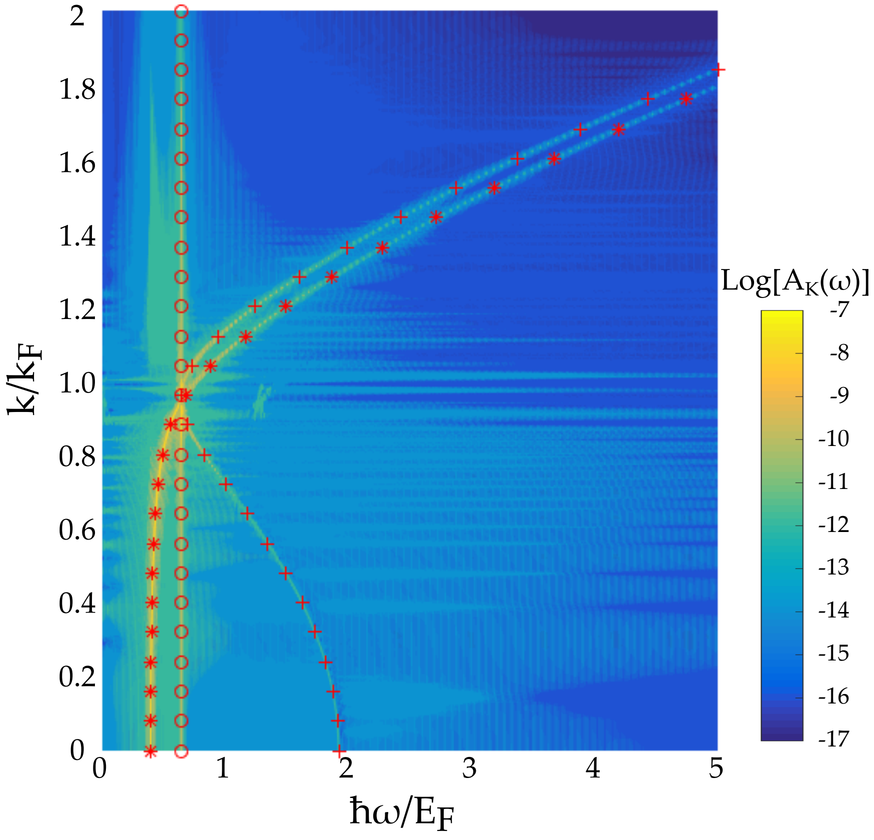

Figure 9.4: Momentum-resolved spectral weight $A_{\mathbf{k}}(\omega)$ of the gap. The circles indicate the Higgs mode, the stars mark the response to the modulation frequency and the crosses indicate the quasiparticle excitations at $2E_k$.

9.4 Preparation of a Strongly Interacting Superfluid

Using standard techniques of laser cooling and sympathetic cooling in a mixture with sodium atoms in a magnetic trap (see chapter 5), we start with a cloud of $\sim 5 \times 10^7$ cold fermionic lithium atoms in a crossed beam optical dipole trap (see chapter 6). An equal mixture of the two lowest hyperfine states $|1\rangle$ and $|2\rangle$ is prepared herein. Using subsequent evaporative cooling in a homogeneous magnetic field of 795 G in immediate vicinity of the Feshbach resonance at 834 G, we produce a condensate in the BEC-BCS crossover regime with a temperature of $T/T_F = 0.07 \pm 0.02$, see section 6.4.

Our measurements are conducted in a gas of approximately 4×10^6 ^{6}Li atoms prepared in a balanced mixture of $|1\rangle$ and $|2\rangle$. The trapping frequencies of the harmonic dipole potential are $(\omega_x, \omega_y, \omega_z) = 2\pi(91, 151, 235)$ Hz. The Fermi energy in the center of the gas is $E_F \backsimeq h \times 34\,\text{kHz}$ and sets the Fermi wave vector $k_F = \sqrt{8\pi^2 m E_F / h^2}$, where m denotes the mass of the atom and h is Planck's constant. After preparation of the fermionic superfluid the magnetic offset field is adiabatically adjusted in the range between 740 G and 1000 G in order to control the interaction parameter $1/(k_F a)$ in the range of $-0.8 < 1/(k_F a) < 1$, i.e. across the whole BEC-BCS crossover region.

9.5 Experimental Calibration and Results

We measure the energy absorption spectrum of the fermionic superfluid in the $|12\rangle$ state for different interaction strengths. Using the Rabi frequency Ω_R and the detuning δ as adjustable parameters, we drive periodic excitations into the $|3\rangle$ state with adjustable modulation frequency.

We experimentally calibrate the modulation frequency and amplitude to take into account energy shifts owing to interaction effects of the initial and final states and the efficiency of the rf antenna setup. To this end, we drive Rabi oscillations with a set value of detuning δ and power and measure the population of state $|3\rangle$ $p_{|3\rangle}$ as a function of time. The population during the rf drive can be then described by $p_{|3\rangle} = \alpha \sin(\Omega_{mod} t)$. This provides us with a direct measurement of the modulation frequency and amplitude. In order to model the data, we assume a Lorentzian line shape $\alpha = \frac{\Omega_R^2}{\Omega_R^2 + (\delta - \delta_0)^2}$. However, we allow for a frequency shift $\delta_0(k_F a)$ by which the detuning δ is corrected as compared to the Zeeman energy resonance of the free atom. The fit parameter δ_0 absorbs the effects of interactions in the final state of the spectroscopy, the condensation energy of the initial state, and the averaging of different momentum states and densities in the trap. Experimentally, the calibration is performed at a value of $\alpha = 4\%$ for which we obtain agreement with the Lorentzian model to a few percent. Figure 9.5 shows an example of the oscillations during the modulation of atoms in the $|3\rangle$ state. The frequency is calibrated well if the amplitude and frequency for red and blue detuning are equal. We then use this calibration to infer the driving parameters for $\alpha = 0.5\%$, which is too small an occupation of the $|3\rangle$ state to be directly measurable.

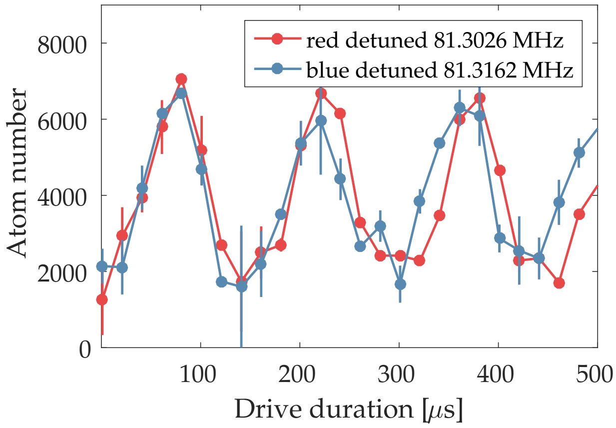

Figure 9.5: Calibration of the detuning: Example of Rabi oscillations during the modulation of atoms in the $|3\rangle$ state. The frequency is calibrated well if the amplitude and frequency for red and blue detuning are equal.

The modulation is applied for a fixed period of 30 ms. We search for the Higgs mode red-detuned from the bare atomic transition to avoid single–particle excitations. Following the excitation we conduct a rapid magnetic field sweep (section 8.2) onto the molecular side of the Feshbach resonance and convert Cooper pairs into dimers. After that, we measure the condensate fraction of the molecular condensate in time-of-flight imaging. The change in the condensate fraction provides us with a sensitive measure of the excitation of modes in the quantum gas.

In Figure 9.6 we plot the measured condensate fraction as a function of the modulation frequency for different values of $1/(k_F a)$. On the BCS-side of the Feshbach resonance up to unitarity, $1/(kFa) < 0$, we observe clear resonances for which the condensate fraction reduces significantly signaling the excitation of a well defined mode. For $1/(k_F a) > 0$, the energy absorption peak is gradually washed out and broadened significantly. Far on the BEC side, for $1/(k_F a) \backsimeq 1$, we cannot observe a resonance on the red-detuned side of the spectrum and conclude that the Higgs mode is absent. The resonances generally exhibit an asymmetric line shape, which we fit with a Gaussian to the high-frequency side in order to extract the peak position and width. The asymmetric peak shape is a result of the momentum-dependence of the effective Rabi frequencies $\Omega'_{R,k}$. As indicated in Figure 9.2, the detuning (and hence the modulation frequency) varies with increasing momentum k. Therefore, a resonant excitation at the Higgs mode frequency $\Omega'_{R,k} = 2\,|\Delta|$ can be achieved for high momenta k even though for low momenta the modulation frequency is below the resonant excitation.

In Figure 9.7 (a) we plot the position of the peak of the energy absorption spectra versus the interaction parameter $1/(k_F a)$ evaluated at the center of the sample. The Higgs mode is a collective mode of the system and hence has one unique value irrespective of the density variation of the trapped gas. Numerical studies in the BCS limit have shown that in harmonically trapped systems, the Higgs mode is expected to occur at twice the superconducting gap evaluated at the peak density of the gas [1, 127, 128]. We compare the measured peak frequency with twice the superconducting gap evaluated by different theoretical models [129–132]. We find that the measured mode frequencies are consistently below the result from mean-field theory (brown dashed line), which is known to overestimate the superconducting gap. Furthermore, we compare it with quantum Monte-Carlo (QMC) simulations [129–131] and generally find very good agreement with twice the gap value despite the intrinsic variations between the different theoretical results. In particular at unitarity, $1/(k_F a) = 0$, some QMC calculations of $2\,|\Delta|$ and our measurements agree within error. It has been suggested [1] that the Higgs mode frequency could be a precise measure of the superconducting gap in the BEC-BCS crossover. Especially at unitarity, $1/(k_F a) = 0$, the exact value of Δ was unknown and a previous gap measurement [133, 134] yielded a smaller gap value than predicted by the QMC calculations shown here.

Within the BCS mean field approach, we find that the width of the spectroscopic feature should be on the order of the gap parameter Δ. Hence, we cannot directly interpret the linewidth of our spectra as the inverse lifetime of the Higgs mode, but only as its lower limit. In Figure 9.7 (b) we plot the width of the Gaussian fits to the energy absorption peaks and compare them with the above prediction. We find reasonable agreement on the BCS side of the resonance. However, towards the BEC side the measured width far exceeds the prediction. This could indicate that the Higgs mode becomes strongly broadened, for example due to the violation of particle-hole

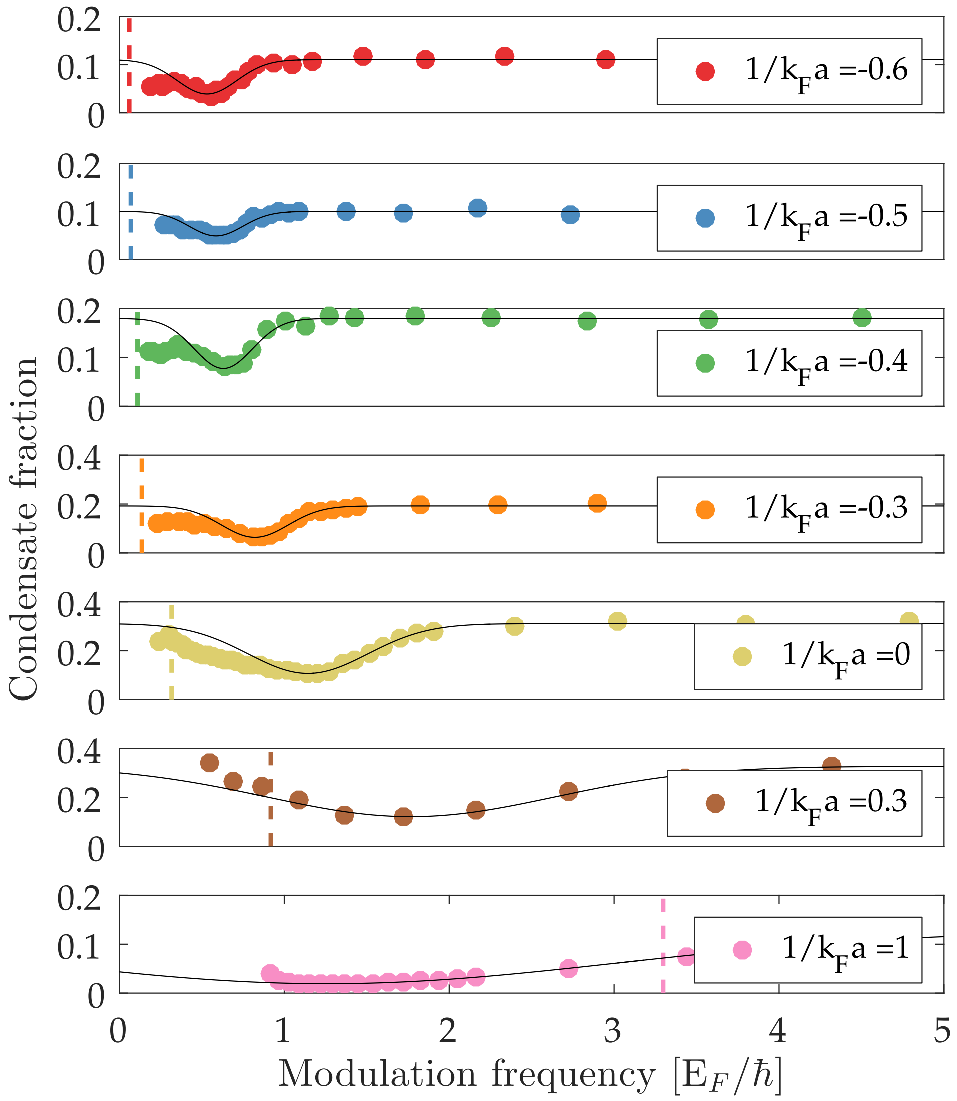

Figure 9.6: Excitation spectra of the Higgs mode for different interaction strengths $1/(k_F a)$. The vertical dashed lines indicate where the rf frequency used for the modulation crosses the atomic Zeeman transition. RF frequencies used for the modulations to the right of the dashed line are red-detuned; blue-detuned to the left of the dashed line. The different levels of background condensate fraction are due to the different $1/(k_F a)$. The solid lines shows the Gaussian fit to the high frequency side of the spectra. Each data point is averaged over approximately four measurements. The error bars of the standard deviation are smaller than the dot size indicating the measurements.

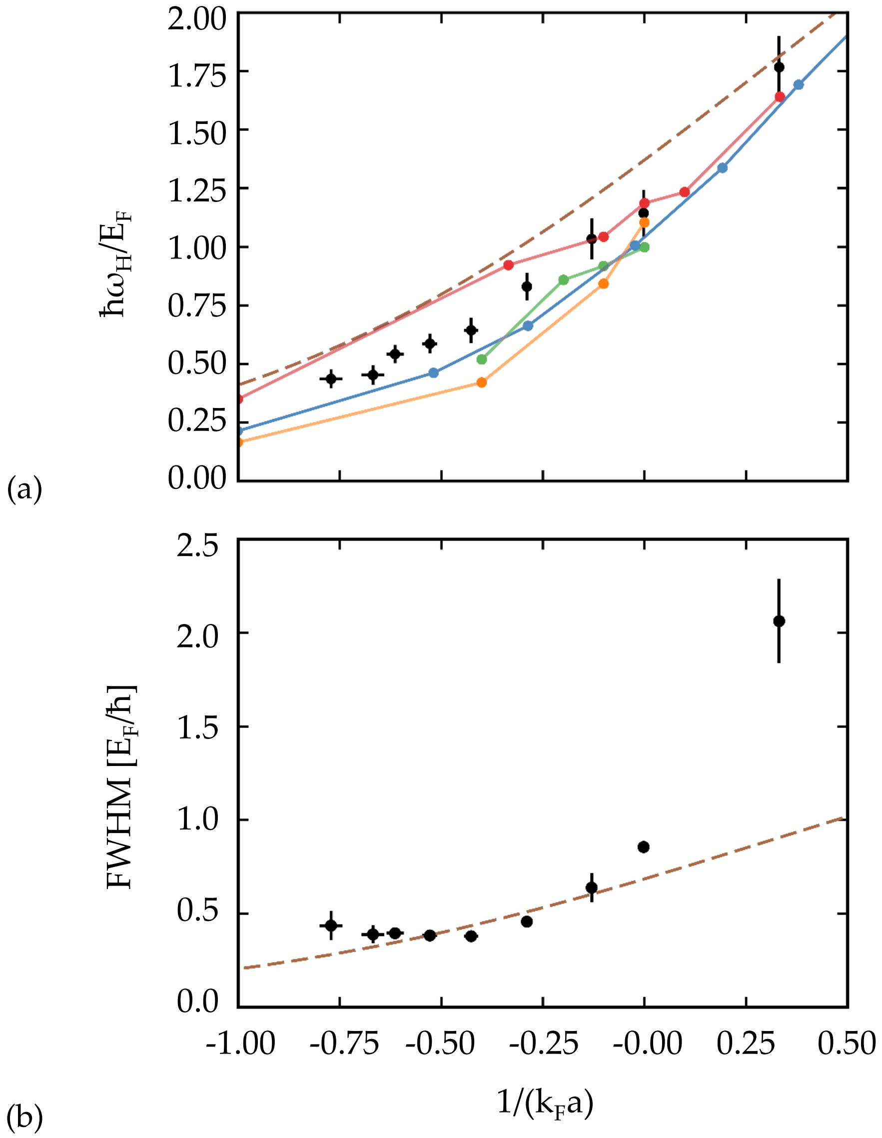

Figure 9.7: (a) Measured peak positions of the energy absorption spectra (black dots), which mark the Higgs mode frequency ω_H. For comparison we show numerical simulations of the gap parameter multiplied by 2: BCS mean field theory (brown dashed line), Quantum Monte Carlo simulations (red [129], green [130], orange [131]) and particle-hole channel analysis (blue [132]). **(b)** Measured fullwidth at half maximum (FWHM) of the absorption peaks (black dots). For comparison, the BCS mean field theory gap is also shown (brown dashed line). The error bars in (a) and (b) represent the standard errors.

symmetry. Hence, this results in a decay into Goldstone modes [5, 26, 27] indicating the breakdown of BCS theory.

In Figure 9.8 we compare width of the energy absorption spectrum (shown in Figure 9.6) to the integrated area under the Higgs component of the Fourier spectra shown in Figure 9.3 for two different interaction parameters (a) $1/(k_F a) = -0.63$ with an order parameter of $\Delta = 0.3/E_F$ and (b) $1/(k_F a) = -0.43$ with an order parameter of $\Delta = 0.4/E_F$. The data is rescaled with Δ resulting in the same width for different interaction values. The FWHM$= 2\Gamma \approx \Delta$ is as expected. Only very close to the unitary regime this relation does not hold anymore.

9.5.1 Demonstration of Robustness of Method

We confirm the robustness of our measurement method by varying the modulation amplitude α, checking for single-particle excitations and changing the duration of the modulation τ. We confirm that the resonance position is independent of α, τ and that we do not excite single-particle excitations.

In more detail, we measure the dependence of the excitation spectra on the modulation amplitude and duration. A change in amplitude in the range of $0.001 < \alpha < 0.02$ does not change the resonance frequency, see Figure 9.9. The amplitude and duration of the modulation for the measurements shown in Figure 9.6 is chosen to minimize the ratio of the width to the amplitude of the signal. We also measured that the total atom number is conserved during the excitation.

We check for unpaired atoms in the $|2\rangle$ state for red and blue detuned radio frequencies with $|2\rangle$ respect to δ_0 as a result of the modulation. This has been achieved by rapidly ramping the field to $450\,\mathrm{G}$ with approximately $4\,\mathrm{G}/\mu\mathrm{s}$ allowing to detect free atoms rather than paired atoms. In case of a red-detuned modulation frequency, no enhancement of the signal of unpaired atoms could be observed over the whole range of modulation frequencies. However, a blue detuned radio frequency modulation increases the number of unpaired atoms due to single-particle excitations to the continuum, see Figure 9.10.

We also measure the dependence of the condensate fraction on the duration of the modulation for different modulation amplitudes α as shown in Figure 9.11 (a). We then fit the initial linear slope and plot the gradient versus the amplitude α as illustrated in Figure 9.11 (b), which shows a linear dependence. For the spectra in Figure 9.6, the

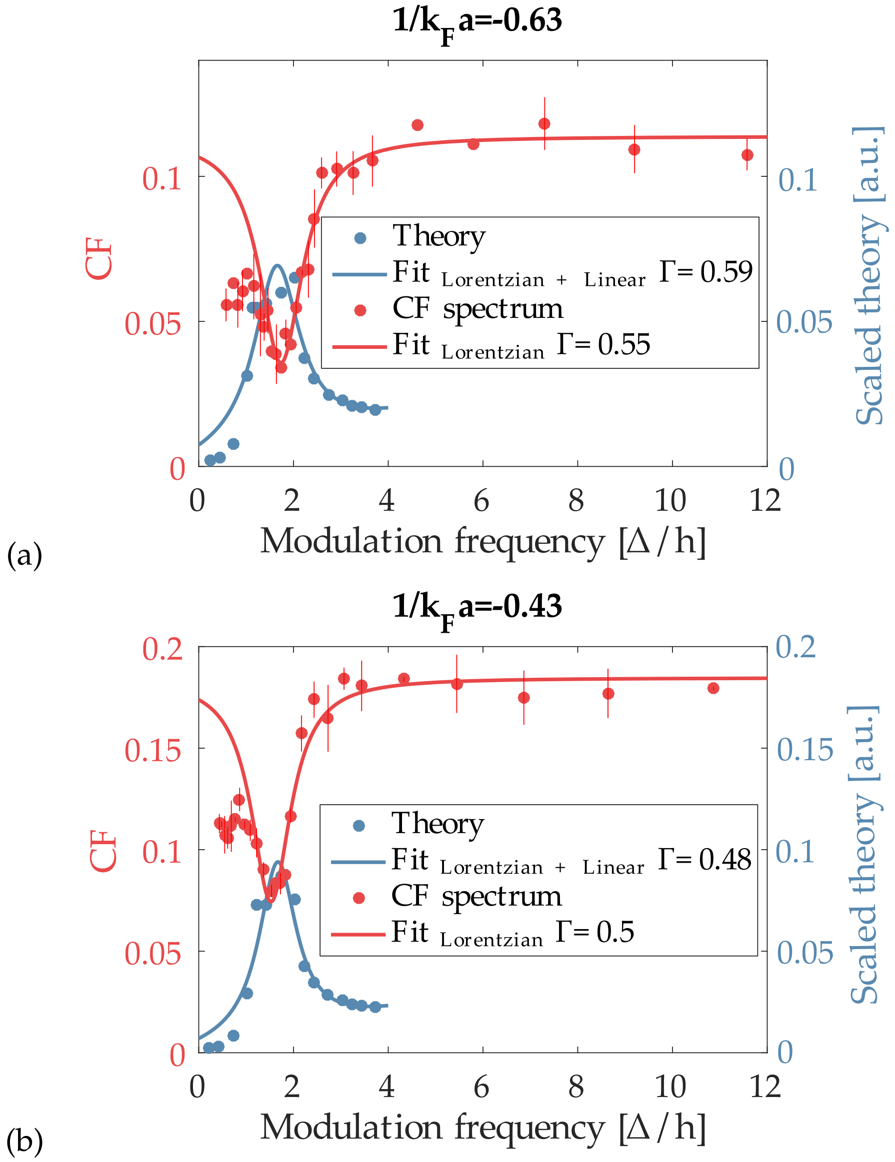

Figure 9.8: Comparison of the half width at half maximum between theory and data (condensate fraction (CF)) for two different interaction parameters **(a)** $1/(k_F a) = -0.63$ with an order parameter of $\Delta = 0.3/E_F$ and **(b)** $1/(k_F a) = -0.43$ with an order parameter of $\Delta = 0.4/E_F$. The data is the same as shown in Figure 9.6 but rescaled in units of Δ. The theory represents the integrated area under the Fourier spectra shown in Figure 9.3. The full width half maximum of the above fits is FWHM$= 2\Gamma$. From the fits we can deduce $\Gamma \approx 0.55 \cdot \Delta$ leading to $2\Gamma \approx \Delta$ or FWHM$\approx \Delta$. Only very close to the unitary regime this relation does not hold anymore (not shown).

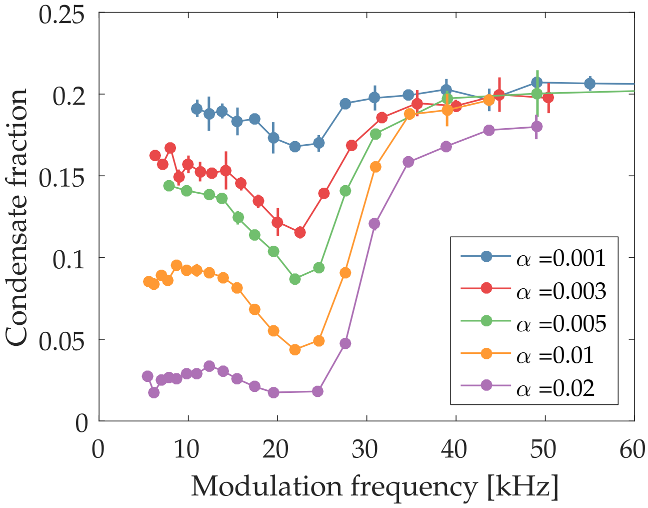

Figure 9.9: Excitation spectra of the Higgs mode for different modulation amplitudes showing no change in the resonance frequency. Data is taken for $1/(k_F a) = -0.4$. The error bars show the standard deviation of three measurements.

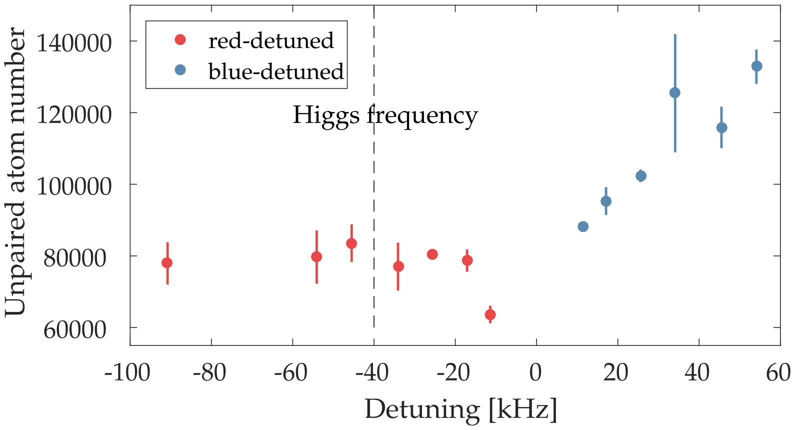

Figure 9.10: Single-particle excitations. There are no visible single-particle excitations on the red-detuned side of the spectrum. The background level on the red-detuned side corresponds to an unpaired atom fraction of approximately 5%, which is the same as for the case without any modulation. On the blue-detuned side we observe excitations of unpaired atoms. Data was taken at $1/(k_F a = -0.1)$. The vertical dashed line indicates the position of the Higgs mode.

modulation amplitude is set to $\alpha = 0.005$ and the duration to 30 ms. From that we can infer that we are in the linear response regime.

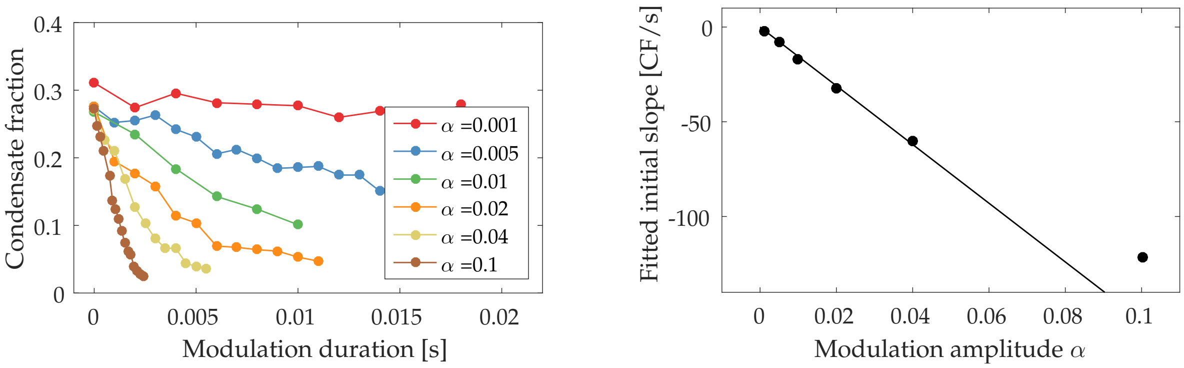

(a) (b)

Figure 9.11: (a) Dependence of the condensate fraction on modulation time for different modulation amplitudes α. **(b)** Fitted initial slope of data shown in **(a)**, which shows a linear dependence. The solid line is a linear fit to the first five data points. For the spectra in Figure 9.6, the modulation amplitude is set to $\alpha = 0.005$ and the duration to 30 ms. From that we can infer, that we are in the linear response regime.

In addition, we check the momentum-dependence of the resonance. After the modulation we perform a time-of-flight expansion for a period of 15 ms, which is approximately a quarter period of the residual harmonic potential during ballistic expansion. This procedure maps the initial momentum states to positions in the absorption image. We analyze the detected condensate density in momentum intervals of $0.02\,k_F$ and find that the excitation resonance is at the same frequency for all momentum intervals. This strongly indicates the collective behavior of the observed mode.

9.6 Conclusion and Outlook

In conclusion, we observed the collective Higgs mode for a strongly interacting fermionic superfluid for the first time. Our work indicates that the Higgs mode exists as a collective excitation of the superfluid even when particle-hole symmetry is not strictly fulfilled near unitarity. Our results open the path for searches of the Higgs mode in strongly correlated driven superconductors and, more generally, for tests of relativistic field theories in table-top experiments.

The method of exciting the Higgs mode introduced here is the first presented direct excitation scheme in a fermionic superfluid. Methods such as Raman scattering in superconductors [20, 23] couple to charge density waves, which require transfer of spectral weight to the Higgs mode. Besides that, no one has observed the Higgs mode in a strongly interacting superconductor before. The spectrum can be taken within only 500 µs as shown in Figure 9.12. This opens up possible investigations of dynamics of strongly interacting Fermi systems.

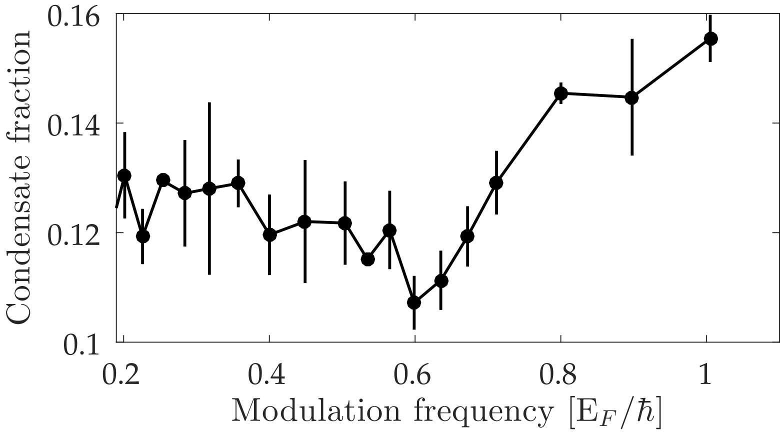

Figure 9.12: Higgs mode spectrum taken for a modulation amplitude of 0.1 and a modulation time of only 500 µs. This short modulation time opens up the possibility to study dynamical properties of strongly interacting fermi gases.

CHAPTER 10

Collapse and Revival of Order in a Quenched Superfluid

Another advantage of cold atomic gases is that the characteristic energies are small while the coherence times are long. This leads to the possibility of studying intrinsic time dynamics. One field of investigation, which so far has mostly drawn theoretical interest, are the non-equilibrium dynamics in a superfluid Fermi gas and addresses questions arising in the BCS pairing problem. The non-equilibrium dynamics studied in this and the following chapter are induced by an abrupt change in the interaction strength. In the following, the BCS state is characterized by a coupling constant g and an order parameter Δ.

We investigate the regime of rapid changes of the interaction strength and subsequent dynamics. In more detail, we perform rapid variations of the dimensionless interaction parameter $g = 1/(k_F a)$ (here, k_F is the Fermi wavevector and a the scattering length) and vary both the initial interaction strength g_i and the amplitude of the quench $\Delta g = g_i - g_f$ (g_f characterizes the final interaction strength). We employ radio frequency transitions between two hyperfine states to transfer one spin component of a spin mixture to a different hyperfine state. The scattering length between the spin components after the transfer differs from the one before the transfer, hence the interaction is rapidly changed. In general, quantum mechanical quenches of the order parameter provide insight to the energy spectrum of the systems Hamiltonian and the time scale in which the systems responds to the change (thermalization and decoherence). In addition, time-dependent amplitudes of the quantum state can interfere during the evolution. If the coherence time is longer enough, interference can lead to a revival of order.

In the experiment we observe a fast relaxation to a zero order parameter for large quenches, whereas for small quenches we observe, after a sudden drop, a revival of the order parameter and equilibration to a long-term superfluid steady state. This revival of the order can be connected with a critical quench parameter possibly signalizing the appearance of a dynamical phase transition.

In this chapter we introduce the quench phase diagram predicted by [6] for integrable systems and compare our findings to the theoretical predictions. However, for strong interactions, which is the case in the BEC-BCS crossover, the system is non-integrable and direct comparisons are not applicable. In the first section, the theory of [6] and [39] are reviewed. The consecutive section contains a description of the experimental setup and parameters and concludes with a presentation of the observations.

10.1 Theory

In the following, an introduction to required theory is given. In more detail, subsection 10.1.1 gives an introduction to the quench phase diagram [6, 135] and subsection 10.1.2 explains the theory about the dynamical vanishing of the order parameter [39].

10.1.1 General Phase Diagram of Interaction Quenches

Volkov and Kogan [36] showed in 1973 that the order parameter of a BCS superconductor can exhibit oscillations after small perturbations of the order parameter. These oscillations are attenuated by a power law decay. More theoretical studies were motivated by experiments with ultracold gases. For example, Barankov et al. [37] investigated the non-adiabatic regime of the BCS state formation. They discovered large periodic oscillations between the superfluid and the normal state. Furthermore, Yuzbashyan et al. [38] extended Volkov and Kogan's work to larger deviations from equilibrium using an analytic method. They showed that the frequency of the oscillation of the order parameter is twice the gap parameter $2\Delta(t \rightarrow \infty)$.

A later paper by Barankov and Levitov [135] describes three distinct regimes depending on the coupling strength, which are explained below. Yuzbashyan et al. [6] com-

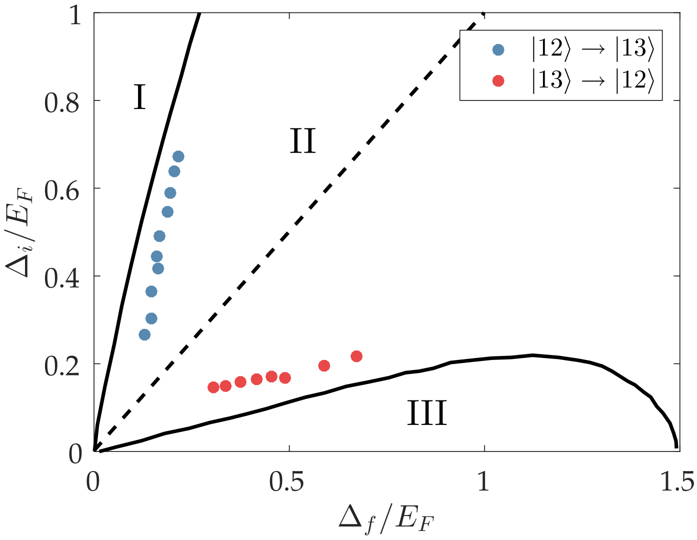

Figure 10.1: Interaction quench phase diagram. The solid lines are the predicted [6] transition lines between region I, II and III. Δ_i denotes the order parameter before the quench, whereas Δ_f denotes the order parameter of system prepared at equilibrium with otherwise the same parameters as the system after the quench. In region I the amplitude of the order parameter approaches zero, while following a power law decay. In contrast, in region II damped oscillations to a nonzero value occur. In region III these oscillations are persistent in time. These distinct regions are non-equilibrium phases. The dashed diagonal line separates the region where $\Delta_i > \Delta_f$ (upper half) from the the region where $\Delta_i < \Delta_f$ (lower half). This figure also shows also gap parameter of the interaction quenches presented in this thesis, blue points in this chapter, red points in chapter 11.

pleted the picture of integrable models by describing all possible interaction quenches in the BEC-BCS crossover. To be more precise, they include BEC to BCS, BCS to BEC and BEC to BEC quenches. They study the dynamic response of a condensate interacting via s-wave interactions by using a two-channel model and extending their studies beyond the weak-coupling limit. Each of these quenches can be characterized by an initial order parameter Δ_i and an order parameter Δ_f of the system at equilibrium with the same interaction strength as the system after the quench. The behavior of the order parameter at long times after the quench is described by $\Delta(t \to \infty) = \Delta_\infty$.

Barankov and Levitov [135] analyze the BCS problem using the pseudospin formulation and solving the time evolution, which is induced by a change of interaction characterized by $\lambda(t)$. Cooper pairs are described in this formulation by spin 1/2 operators $s^{\pm}_{\mathbf{p}} = s^x_{\mathbf{p}} \pm i s^y_{\mathbf{p}}$ and the Hamiltonian takes the form

$$H = -\sum_{\mathbf{p}} 2\epsilon_{\mathbf{p}} s^z_{\mathbf{p}} - \lambda(t) \sum_{\mathbf{p},\mathbf{q}} s^-_{\mathbf{p}} s^+_{\mathbf{q}} \quad , \tag{10.1}$$

where $\epsilon_{\mathbf{p}} = \mathbf{p}^2/2m - \mu$ is the free particle spectrum and μ is the Fermi energy. The interaction parameter $\lambda(t)$ is changed at time zero accordingly to a step function.

Three different regions can be distinguished as illustrated in Figure 10.1. In region I the amplitude of the order parameter approaches zero, while following a power law decay. During the evolution no oscillation occur and the order parameter in the limit when the coupling is almost turned off completely is described by [135]

$$\Delta(t \gg \Delta_i^{-1}) \propto (\Delta_i t)^{-1/2} \exp(-2\Delta_i t) \quad . \tag{10.2}$$

In contrast, in region II damped oscillations to a nonzero value occur and the order parameter can be written as [135]

$$\Delta(t) = \Delta_\infty + A(t) \sin(2\Delta_\infty t + \alpha) \quad , \quad A(t) \propto t^{-1/2} \quad . \tag{10.3}$$

In region III these oscillations are persistent in time and the order parameter oscillates between two values Δ_+ and Δ_-. These distinct regions are non-equilibrium phases. The main result of Yuzbashyan et al. [6] is summarized and shown in Figure 10.1. The dashed diagonal line separates the region where $\Delta_i > \Delta_f$ (upper half) from the the region where $\Delta_i < \Delta_f$ (lower half).

This figure also shows the gap parameter of the interaction quenches presented in this thesis. Due to the fixed relative positions of the Feshbach resonance between the three lowest hyperfine states, we cannot probe the whole phase diagram. However, a small region around the data points can be accessed by changing parameters, which change the Fermi energy E_F (and therefore Δ) such as the atom number and the trap frequencies. In addition, the transition lines between the different regions might be shifted relatively to our data points due to deviations from mean-field theory, finite temperature effects and more important due to strong interactions and non-integrable system effects.

10.1.2 Dynamical Vanishing of the Order Parameter

In their paper about the dynamical vanishing of the order parameter in a fermionic condensate [39] E. Yuzbashyan and M. Dzero study the evolution of a fermionic condensate after a sudden change of the interaction strength. Before the quench is performed, the gas is in equilibrium at zero temperature in the superfluid BCS regime. It is described by an initial coupling constant $g_i > 0$ and a corresponding BSC gap value Δ_i. At $t = 0$, the pairing strength is changed and the systems is then described by a new coupling constant $g_f > 0$ and BCS gap value Δ_f (at equilibrium). The initial gap value is assumed to be bigger or equal to the final gap value (as a starting condition). This means experimentally that the quench is performed from a value close to the Feshbach resonance to a value further away from the resonance (see Figure 10.3). Related to the phase diagram Figure 10.1, these quenches are performed in the upper half of the diagram. One way to perform these quenches in the experiment is to change the magnetic field close to a Feshbach resonance abruptly. However, this method suffers from experimental difficulties and we employed a better method described in section section 10.2.

At long times the gas reaches a non-stationary steady state and the superfluid order parameter Δ approaches a constant value Δ_∞, which is in general not equal to Δ_f. The time it takes to approach this constant value Δ_∞ is on the scale of $\tau_\Delta = \frac{\hbar}{\Delta_i}$. Only if the system is cooled, the BCS ground state can be reached after the quench described by the gap parameter Δ_f.

If the ratio of the final and the initial gap values undergoes a critical value ($\Delta_f/\Delta_i \leq 0.21$ [39]), the gap Δ_∞ in the steady state vanishes. This situation is different from a normal state as it combines properties of the normal and the superfluid state. In more detail, when the gap goes to zero the superfluid density as shown in [39] is finite. From an experimental point of view, if the gap goes to zero also the measured condensate fraction is zero. Recall, the condensate fraction is measured after a rapid magnetic field quench, which converts Cooper pairs into tightly bound dimers. After expansion from the trap, a bimodal density distribution (a function consisting of Gaussian plus parabola) is fitted to the density distribution from which the condensate fraction (fraction underneath the parabola) is extracted.

Figure 10.2 illustrates the predicted theoretical evolution of the gap and shows the time dependent gap for two different value of Δ_f/Δ_i [39]. The solid line shows the situation above the critical pairing strength, where the gap approaches a finite value.

In comparison, the dashed line demonstrates how the gap vanishes if the ratio is below the critical pairing strength ratio. In addition, they [39] show that the decay law of $\Delta(t)$ changes from an exponential decay in the region where the long term gap vanishes ($\Delta_\infty = 0$) to a power law decay in the region with finite long term gap Δ_∞.

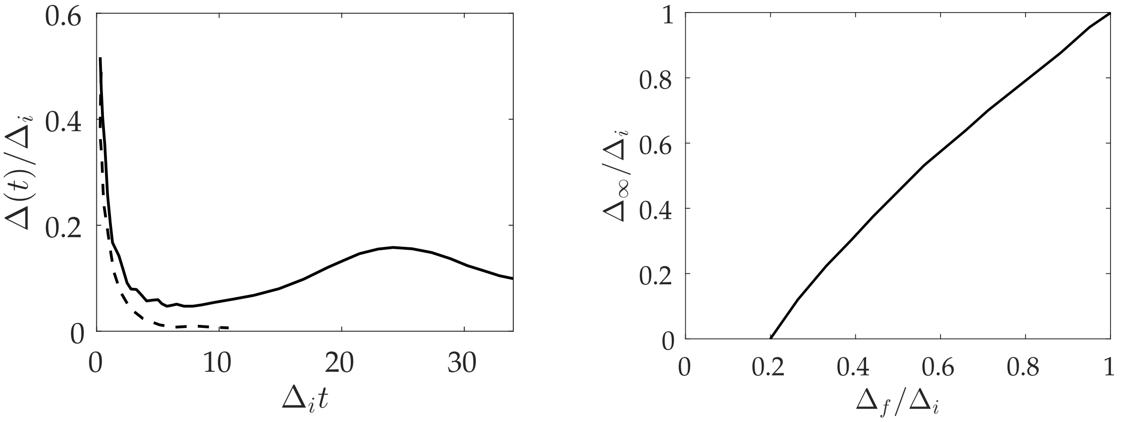

(a) (b)

Figure 10.2: **(a)** Theoretical time dependence of the gap for two different value of Δ_f/Δ_i. The solid one shows the situation above the critical pairing strength ($\Delta_f/\Delta_i = 0.25$), where the gap approaches a finite value. In comparison, the dashed line demonstrates that the gap vanishes if the ratio is below the critical pairing strength ratio ($\Delta_f/\Delta_i = 0.19$). **(b)** Predicted long term gap parameter (for times bigger than τ_Δ) as a function of Δ_f/Δ_i. The maximum of Δ_∞ is reached when $\Delta_f/\Delta = 1$. Below a value of $\Delta_f/\Delta_i \approx 0.21$, the gap vanishes $\Delta_\infty = 0$. Figures adapted from [39].

Figure 10.2 (b) displays the predicted long term gap parameter Δ_∞ (for times bigger than τ_Δ) as a function of Δ_f/Δ_i. It can be seen that the maximum of Δ_∞ is reached when $\Delta_f/\Delta_i = 1$. The critical pairing strength is reached below a value of $\Delta_f/\Delta_i \approx 0.21$, where the gap vanishes $\Delta_\infty = 0$.

E. Yuzbashyan and M. Dzero calculated the evolution of the order parameter within the BCS model assuming the thermodynamic limit and using the BCS mean field approach in the weak coupling limit. From that it is clear that their prediction does not include strong interactions close to the unitary regime. This means that their prediction can only be seen as a first approximation to our experiments as we study a strongly interacting, finite system close to unitarity at finite temperature.

10.2 Experimental Setup and Measurement Technique

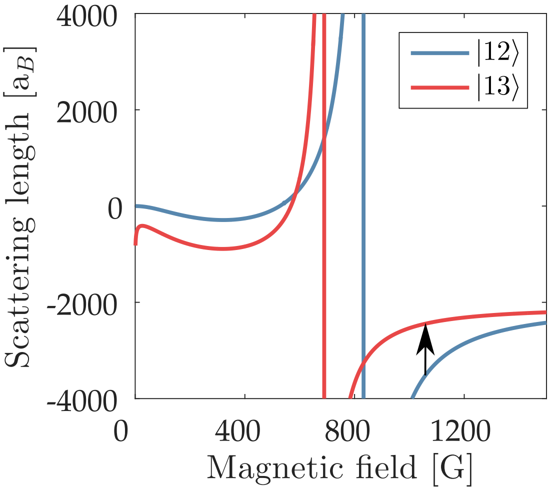

Figure 10.3: Illustration of experimental technique for performing interaction quenches. Scattering length of different spin mixtures of the three lowest hyperfine states of ^{6}Li as a function of an external magnetic field. The Feshbach resonance is located at 690 G for $|13\rangle$, 811 G for $|23\rangle$ and 834 G for $|12\rangle$. The black arrow illustrates the population transfer and shows how the scattering changes when performing such a spin-flip. The data is taken from [34].

As mentioned before, one way to suddenly change the interaction strength is to change the magnetic field in proximity of a Feshbach resonance. This technique however, suffers from experimental difficulties. The current through the magnetic field coils can be turned off abruptly with the help of MOSFETs or IGBTs. However, the magnetic field falls off much slower. This is due to the fact that the change in field induces eddy currents in the steel chamber and vacuum gaskets leading to a slower decay of the magnetic field. The relevant time scale at unitarity is the Fermi time, which is 30 µs. In order to be faster than the Fermi time, we employed a different technique. Instead of changing the magnetic field, a fast transfer from a mixture of two spin states to a different spin mixture is performed. As the Feshbach resonance of a spin mixture of the states $|1\rangle$ and $|2\rangle$ is located at a different magnetic field than the one of a spin mixture of the sates $|1\rangle$ and $|3\rangle$, a fast transfer from $|12\rangle$ to $|13\rangle$ induces an abrupt change of the interaction strength in the sample, see Figure 10.3. Due to the different locations of the Feshbach resonances, the equilibrium BCS gap value of the $|12\rangle$ mixture is bigger than the one of the

$|13\rangle$ mixture. Indeed, this transfer satisfies the condition $\Delta_i > \Delta_f$, or in our case $\Delta_{12} > \Delta_{13}$.

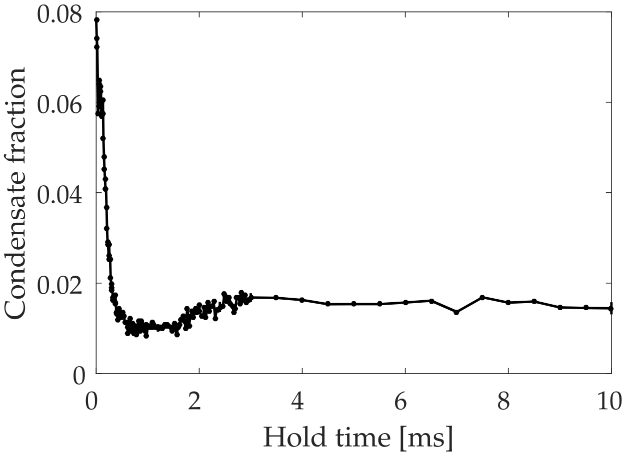

Figure 10.4: Evolution of the condensate fraction after a fast transfer from a $|12\rangle$ spin mixture into a $|13\rangle$ mixture, which leads to an abrupt change in the coupling strength. The transfer is completed after 50 µs. This measurement was performed at 910 G ($1/(k_F a_{12}) = -0.4$), where the equilibrium BCS gap parameter changes from $\Delta_i = 19$ kHz for a $|12\rangle$ mixture to $\Delta_f = 7$ kHz for a $|13\rangle$ mixture. This means $\Delta_f/\Delta_i = 0.4$. In accordance with [39], a revival of the condensate fraction occurs as the pairing strength ratio is bigger than the critical one. The condensate fraction decays within 90 µs to its minimum value and recovers on the time scale of milliseconds. Note, the observed condensate fraction is not equal to the equilibrium condensate fraction of a $|13\rangle$ mixture at 910 G but is instead determined by Δ_∞

We study the evolution of the condensate fraction after such a quench is completed. For this purpose we start with a molecular Bose-Einstein condensate of a $|12\rangle$ spin mixture and adiabatically ramp within 200 ms to the magnetic field where the transfer is performed. The transfer is conducted with a π-pulse of 50 µs at approximately 81 MHz. With an optimized setup the transfer can be performed within only 22 µs.

Figure 10.4 shows the evolution of the condensate fraction after a fast transfer from an initial $|12\rangle$ spin mixture into a $|13\rangle$ mixture. This measurement was performed at 910 G (or $1/k_F a = -0.42$), where the equilibrium BCS gap parameter changes from $\Delta_i = 0.42\,\mathrm{E}_F$ for a $|12\rangle$ mixture to $\Delta_f = 0.17\,\mathrm{E}_F$ for a $|13\rangle$ mixture. In accordance with [39], a revival of the condensate fraction occurs as the pairing strength ratio is bigger than the critical one. The condensate fraction decays within 90 µs to its minimum value and recovers on the time scale of milliseconds. Note, the observed condensate fraction at long times the condensate fraction CF_∞ is not equal to the equilibrium condensate fraction of a $|13\rangle$ mixture at 910 G. Instead, it is related to the order parameter Δ_∞ when the evolution time approaches infinity. In the following section, we study the sudden initial drop. The section afterwards describes the revival of the condensate fraction in more detail at later times.

10.3 Fast Dynamics of the Condensate Fraction: The Initial Decay

The initial fast decay of the condensate fraction after the quench is related to the partial projection of the initial state to the finial state when the initial spin mixture is transferred to the final spin mixture. This projection of Cooper pairs depends on the overlap of their wavefunctions. Besides the fact that the order parameter is changed, also quasiparticles are created, which influence the dynamic on a time scale of the quasiparticle relaxation time $t_\epsilon = hE_F/\Delta_i^2$. In addition, the dynamics of the order parameter should be driven by its fundamental modes, the Higgs mode and the Goldstone mode. The associated time scale of the Higgs mode is related to the gap by the relation $t_\Delta = h/\Delta_i$. Goldstone modes are linked to excitations at the velocity of sound. Interesting dynamics can be observed when the time-dependent amplitudes of the quantum state interfere during the evolution. If the coherence time is longer than the relaxation time, interference can lead to a revival of the order.

In order to compare the above mentioned times scales to the observed ones, Figure 10.5 shows this fast initial decay for different initial interaction strengths. From these measurements, we extract the time constant of the decay by fitting an exponentially decaying function to the data. The obtained time constants are plotted in Figure 10.6.

For large quenches, i.e. when the amplitude of the quench $g_i - g_f = 1/(k_F a_{12}) - 1/(k_F a_{13})$ is big, the decay follows the time constant t_Δ set by the frequency of the Higgs mode. This is the case for quenches from the unitary regime with $g_i = 1/(k_F a_{12}) \approx 0$ to the BCS regime. For small quenches the dynamics follow the quasiparticle relaxation time t_ϵ. This is eventually related to the amount of quasiparticles created by the quench. However, close to the unitary regime the quasiparticle relaxation time approaches the gap time $t_\epsilon \to t_\Delta$ such that a clear distinction is not possible.

Our measurements give insights to the different dynamics occurring in an interacting Fermi gas after an abrupt change of the pairing strength.

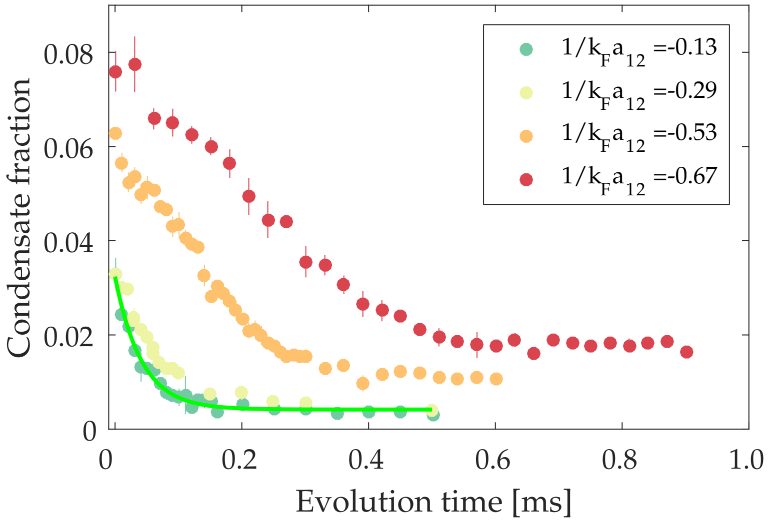

Figure 10.5: Fast initial decay of the condensate fraction for different $1/(k_F a_{12})$ values following from the abrupt change in interaction strength by transferring a $|12\rangle$ mixture into a $|13\rangle$ mixture. The solid line shows an exponential fit from which the time constant is extracted and plotted in Figure 10.6. The initial condensate fraction decreases the further the sample is in the BCS regime in accordance with a decreasing gap parameter.

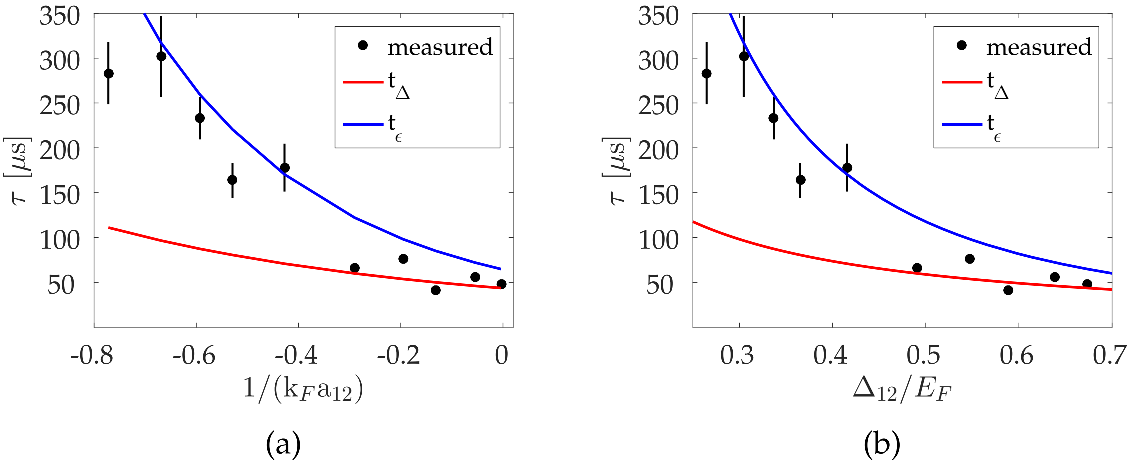

Figure 10.6: Time constant of fast initial decay of the condensate fraction, as a function of **(a)** $1/(k_F a_{12})$ and **(b)** gap parameter Δ_{12}, extracted from plots such as shown in Figure 10.5. The error bars show the standard deviation from different fitting conditions. For large quenches, i.e. from the unitary regime with $g_i = 1/(k_F a_{12}) \approx 0$ to the BCS regime, the decay follows the time constant t_Δ. For small quenches, the dynamics follow the quasiparticle relaxation time t_ϵ. The solid line denote the gap time $t_\Delta = h/\Delta_i$ and the quasiparticle relaxation time $t_\epsilon = hE_F/\Delta_i^2$.

10.4 Slow Dynamics of the Condensate Fraction: The Revival

As a next step, we measure the condensate fraction at long times CF_∞ for different magnetic fields, or equivalently for different ratios of the final and the initial gap Δ_f/Δ_i. We compare the observed signal to the predicted gap Δ_∞ in Figure 10.2 (b). An important fact is that the measured condensate fraction gives an estimation whether the order parameter (or gap value) is different from zero and a bigger condensate fraction indicates a bigger gap value. However, a precise relation between the two is difficult to derive and has not yet been done. Therefore, we are mainly interested in the tendency of the condensate fraction at long times CF_∞ as a function of the ratio Δ_f/Δ_i. For comparison Figure 10.7 shows the condensate fraction before the transfer is performed. The condensate fraction decreases for higher magnetic fields as the gap parameter decreases the further the system is in the BCS regime.

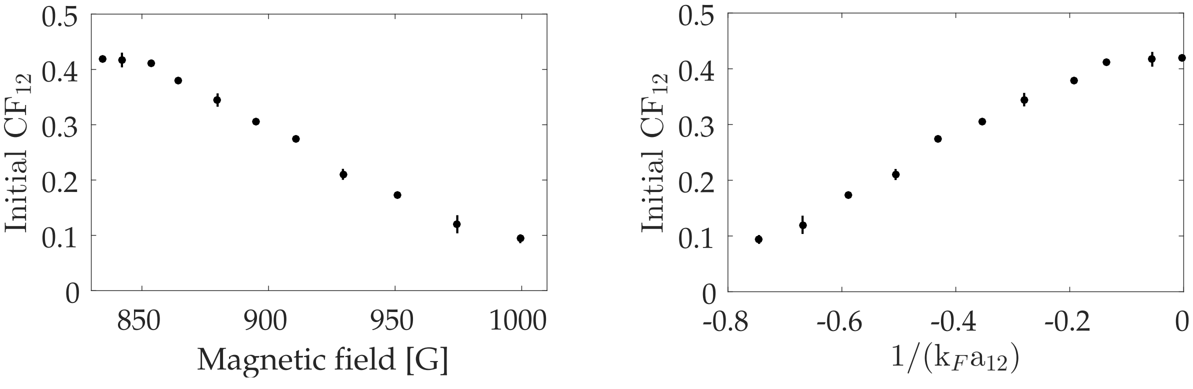

(a) (b)

Figure 10.7: Initial condensate fraction of a $|12\rangle$ mixture without performing any transfer as a function of **(a)** the magnetic field and **(b)** the interaction parameter $1/k_F a_{12}$.

Figure 10.4 indicates that after an evolution time of 3 ms, a new steady state is reached. The condensate fraction of this new non-stationary steady state is shown in Figure 10.8 after 4 ms evolution time as a function of the magnetic field and $1/(k_F a_{12})$ values. This time is chosen such that the observed dynamics are finished, but before any evaporation or atom loss has occurred. For large quenches, the condensate fraction CF_∞ remains zero. However, for weak quenches there appears to be a critical value after which a revival of order is visible, see Figure 10.9. This threshold behavior motivates

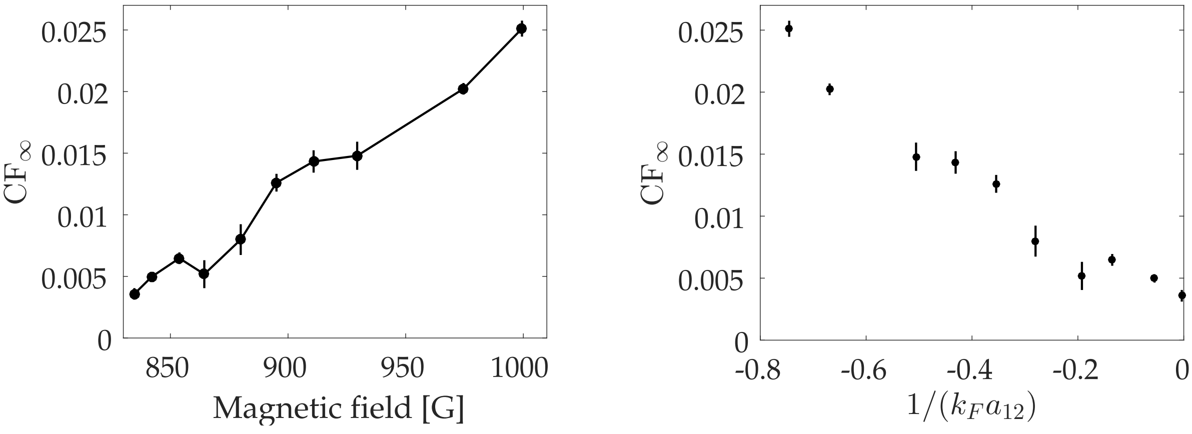

(a) (b)

Figure 10.8: Condensate fraction CF_∞ of the $|13\rangle$ as a function of **(a)** magnetic fields and **(b)** $1/(k_F a_{12})$ values after 4 ms evolution time after the transfer was completed. This measures the recovered condensate fraction of the new non-stationary steady state. If the magnetic field is increased, the sample is brought further away from unitary and further into the BCS regime and the measured condensate fraction CF_∞ increases. This might be counter-intuitive as at the same time the equilibrium ground state gap value Δ_{13} decreases and one would expect naively that this method gives a measure of Δ_{13}. However, the sample is not continuously cooled such that the ground state cannot be reached. Hence, our experiment does not give a measure of Δ_{13}. Nevertheless, this increase of the condensate shows the same tendency as predicted by [39] (compare to Figure 10.2(b)). The error bars show the standard deviation of four measurements.

the possible interpretation of a dynamical phase transition [40]. A dynamical phase transition indicates a non-analytical behavior at a critical point in time similar to a temperature driven phase transition, where this behavior occurs in the free energy density at a critical temperature. If the magnetic field is increased, the sample is brought further away from unitary and further into the BCS regime and the measured condensate fraction CF_∞ increases. This might be counter intuitive as the equilibrium ground state gap value Δ_{13} decreases and one would expect naively that this method gives a measure of Δ_{13}. However, the sample is not continuously cooled such that the ground state cannot be reached. Hence, our experiment does not give a measure of Δ_{13}. This highlights that the system is far from equilibrium. Nevertheless, the increase of the condensate shows the same tendency as predicted by [39] (compare to Figure 10.2 (b)). In order to better compare the measured value to theory, the condensate fraction CF_∞ is plotted as a function of Δ_{13}/Δ_{12} in Figure 10.9. Here, Δ_{ij} is the BCS ground state gap of a $|ij\rangle$ spin mixture. As the explicit relation between the measured condensate fraction and the gap value of the gas is not known, the theory curve is rescaled with

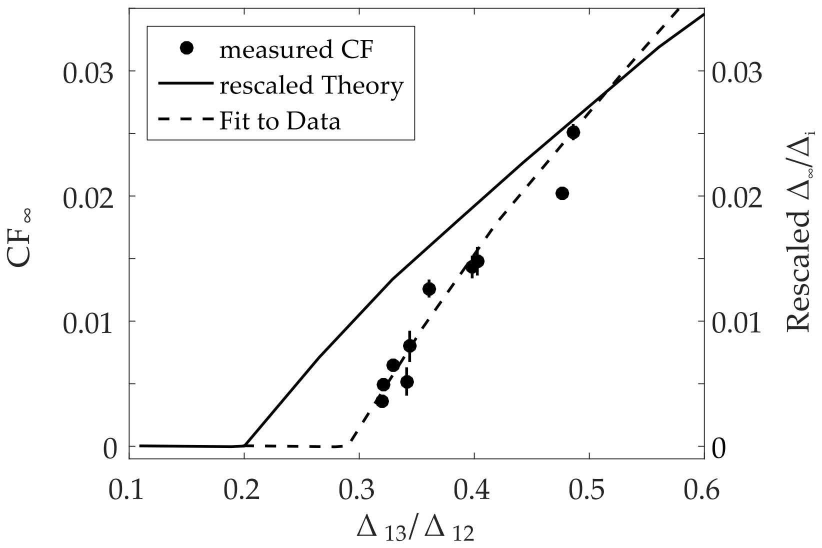

Figure 10.9: Measured condensate fraction CF_∞ (dots) of Figure 10.8 as a function of Δ_{13}/Δ_{12}, where Δ_{ij} is the BCS ground state gap of a $|ij\rangle$ spin mixture. The solid line shows the rescaled theory curve from [39] (compare to Figure 10.2 (b)). As the explicit relation between the measured condensate fraction and the gap value of the gas is not known, the theory curve is rescaled with a factor $c = 0.06$ to match the measured values. The dashed line is a guide to the eye.

a factor $c = 0.06$ to match the magnitude of the measured values. The theoretical prediction might be shifted relatively to our data points due to deviations from mean-field theory, finite temperature effects and more importantly due to strong interactions and non-integrable system effects.

10.5 Conclusion and Outlook

In our experiment, we observe a fast relaxation of the initially finite order parameter to zero for large quenches, whereas for small quenches we observe, after a sudden drop, a revival of the order parameter and equilibration to a long-term superfluid steady state. This revival of the order parameter can be connected with a critical quench parameter signalizing the possible interpretation of a dynamical phase transition. Our measurement provides the first evidence of a collapse and subsequent revival of order in a strongly interacting fermionic system. In addition, we observe that the time scale of the initial sudden drop depends on the amplitude of the quench. For large quenches the decay follows h/Δ, whereas for small quenches the decay follows the quasiparticle relaxation time. Hence, our experiments provide insight into the intrinsic mechanisms occuring after a sudden interaction quench.

CHAPTER 11

Formation of a Condensate after an Abrupt Increase of the Pairing Strength

In contrast to the previous chapter, the quenches studied here start with an initial gap value, which is smaller than the final ground state gap, $\Delta_i < \Delta_f$. The experiment starts with no measurable condensate fraction before the quench and studies the appearance and growth of a condensate fraction. In other words, quenches from the normal state to the superfluid state are performed and the formation of a superfluid phase is observed. However, the interpretation is not easy as evaporation occurs on the same time scale. Similar to before, these quenches are realized by transferring a spin mixture with an initial coupling constant g_i to a different spin mixture with a higher coupling constant g_f.

This chapter is organized as follows. At the beginning, an overview of existing theory is given and the experimental setup and the measurement are explained afterwards. In the end, a summary and conclusion are given.

11.1 Theory

From a theoretical point of view, quench dynamics from a normal to a superfluid state of Fermi gases have been studied, see for example Warner et al. [136]. Similarly, Barankov et al. [137] studied the BCS state formation after the interactions are turned on, and Yuzbashyan et al. [138] looked at the dynamics following an abrupt increase in the BCS coupling constant at finite temperature.

Warner and Barankov start from semi classical equations of motion and study the time evolution of the order parameter, while neglecting certain possible responses of the individual pseudo spins and dephasing of the spins with time. They show that for quenches outside the Ginzburg-Landau regime ($1/\tau_\epsilon \neq \Delta/\hbar$) quantum fluctuations drive the system to a new steady state, which is characterized by a gap parameter $\tilde{\Delta}_\infty = \epsilon_c / \sqrt{\exp{(2/N(0)\lambda)} - 1}$, where ϵ_c is the the BCS cutoff, $N(0)$ the Fermi surface density of states and $\lambda > 0$ the interaction parameter. They point out that this gap parameter is half the BCS gap in the weak coupling limit. This reduction of the order parameter is due to the residual motion of the pairs. We show that our observed condensate fraction shows a similar trend as a function of interaction, see section 11.2. However, they also claim that this new steady state is approached faster, the bigger the quenches are, namely the more the interaction parameter is changed. This is in contradiction to our observation (section 11.2). Yuzbashyan and co-authors demonstrate that if the gas is initially in the normal phase and the interaction parameter is suddenly increased, the time averaged gap $\langle|\Delta(t)|\rangle$ exhibits exponentially damped oscillations with a time constant depending on the final gap parameter Δ_f: $t_0 = \ln(4\Delta_f^2/T\delta)$. Here, Δ_f is the steady state gap at equilibrium (no quench), which the system would have under otherwise identical conditions. The temperature is given by T and the single particle-level spacing by δ. This equation suggests that if the final gap value is increased, the time it takes to reach the constant value gets longer. Indeed, we observe a similar tendency in Figure 11.4. However, in our experiment we cannot be sure that the temperature T and the single particle-level spacing δ stay constant. Furthermore, the theory presented here leaves several questions unanswered and more detailed studies are needed to complete the picture at finite temperature and strong interactions.

11.2 Emergence of a Condensate Fraction

In the experiment the interaction quench is performed by transferring the $|3\rangle$ state atoms of a $|13\rangle$ spin mixture into the $|2\rangle$ state. As the Feshbach resonance of the $|12\rangle$ mixture is located at higher magnetic field than the one of a $|13\rangle$ mixture, this transfer results in an increase of the interaction parameter (opposite to the transfer conducted in chapter 10). The preparation of the spin mixture follows the routine described below.

We start with a spin mixture of the lowest two hyperfine states of lithium as described in section 6.2. The magnetic field is kept fix at $\sim 100\,\mathrm{G}$ and after a decoherence time of 10 ms a Landau-Zener sweep transfers all atoms of the $|2\rangle$ state into the $|3\rangle$ state. This transfer is conducted within 1 ms while the frequency is swept from 120.65 MHz to 121.15 MHz. During the time the atoms decohere, the magnetic field is ramped to $\sim 670\,\mathrm{G}$ within 100 ms and the evaporation of the spin mixture in the dipole trap is started. The final trapping potential is reached after 1 s and it is described by trapping frequencies of $2\pi \times (94, 151, 242)$ Hz in the x-,y-, and z-direction respectively. The next step is to adiabatically adjust the magnetic field to the value where the interaction quench is performed. This sets the interactions before and after the quench, g_i and g_f. The field ramp is completed after 200 ms and an additional wait time of 400 ms ensures that the cloud is thermalized. Then, the quench is performed by a π-pulse at a fixed frequency transferring the atoms in the $|3\rangle$ state into the $|2\rangle$ state within 50 µs. After a variable hold time the rapid ramp technique (see section 8.2) converts Cooper pairs into molecules, which can undergo condensation. After 15 ms time-of-flight the density distribution is imaged. Applying a bimodal fit to the observed density distribution gives the condensate fraction plotted in Figure 11.1 as a function of hold time after an interaction quench at different magnetic fields.

Naively, one could expect that the stronger the interactions are (the closer the sample is to unitarity) the faster the new steady state with the maximum condensate is reached. However, Figure 11.1 shows that the opposite case is true. The closer the field value is to unitarity (834 G, which is the location of the Feshbach resonance of a $|12\rangle$ spin mixture), the longer it takes to reach the maximum condensate fraction. Figure 11.2 shows optical density pictures of the condensate growth for different hold times and two different magnetic field values. Far away from unitarity (975 G) the sample has approached a new steady state after about 10 ms, whereas close to unitarity (834 G) it takes several hundreds milliseconds to settle into a new steady-state. Time scales, which could be of importance are the quasiparticle relaxation time t_ϵ, the time scale related with the gap parameter t_Δ and the time scale on which evaporation occurs. Indeed, evaporation does happen, see Figure 11.3. However, this only influences the growth at unitarity. The growth further away from unitarity happens within 50 ms, whereas evaporation sets in afterwards. This is illustrated in Figure 11.3. The particle number decreases during the course of the measurement due to evaporation of atoms from the trap. The biggest loss and fastest evaporation is happening at low fields where the interaction is strongest.

Figure 11.4 displays the fitted exponential time constant of the condensate growth shown in Figure 11.1 as a function of the magnetic field and $1/k_F a$ values. The plot illustrates that at unitarity the evolution to a constant condensate fraction takes longest.

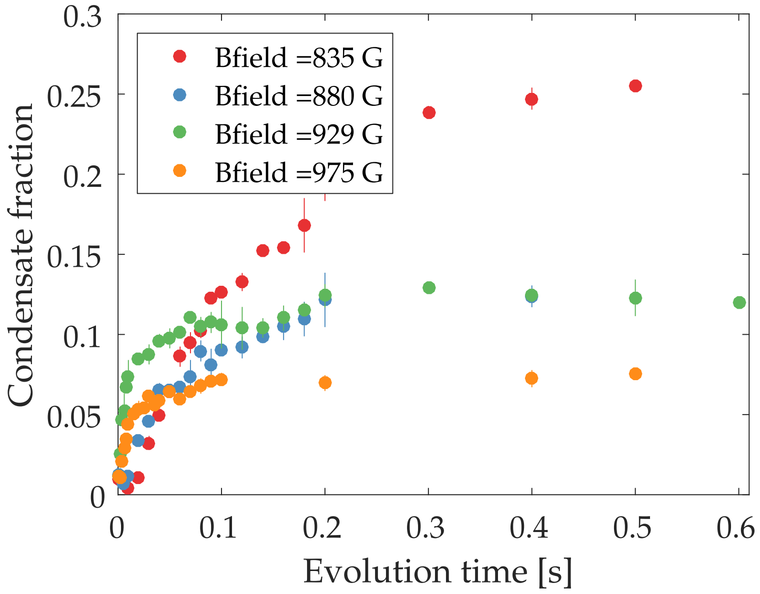

Figure 11.1: Time evolution of the condensate fraction after a fast transfer from a $|13\rangle$ mixture to a $|12\rangle$ mixture at different magnetic fields. For these quenches the initial interaction strength and the corresponding gap value is smaller than the final interaction strength and the final ground state gap value, $\Delta_i < \Delta_f$. Shown is the condensate fraction of the $|12\rangle$ mixture. The closer the field value is to unitarity (834 G, which is the location of the Feshbach resonance of a $|12\rangle$ spin mixture), the longer it takes to reach the maximum condensate fraction. In addition, the condensate fraction reaches its highest background value close to unitarity.

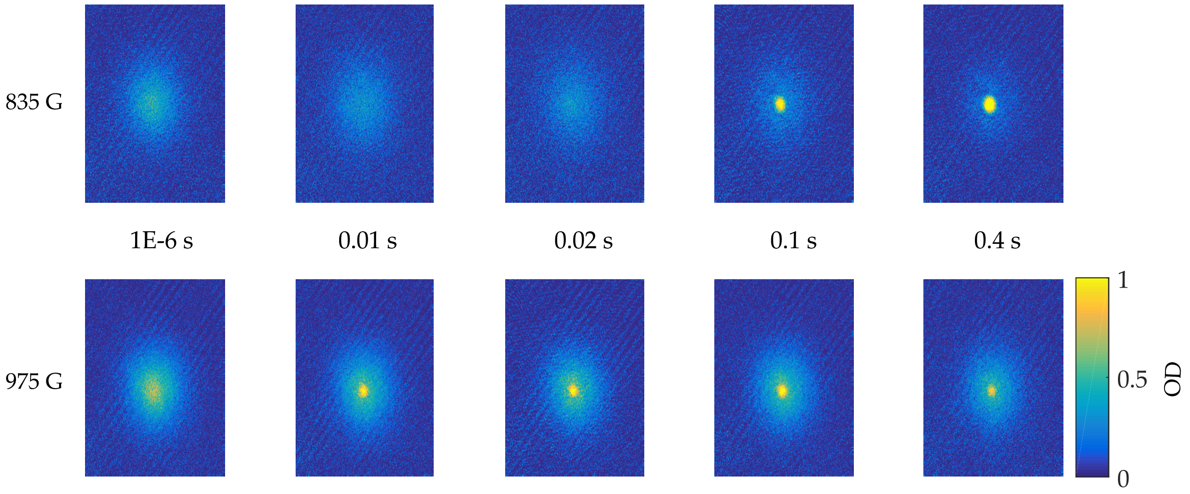

Figure 11.2: Optical density pictures after rapid ramp and time-of-flight of the condensate growth for different hold times after the quench has been performed. The time evolution is shown for two different magnetic field values. The growth of the central dense peak, the condensate, takes longer at unitarity (smaller magnetic field) than in the BCS regime.

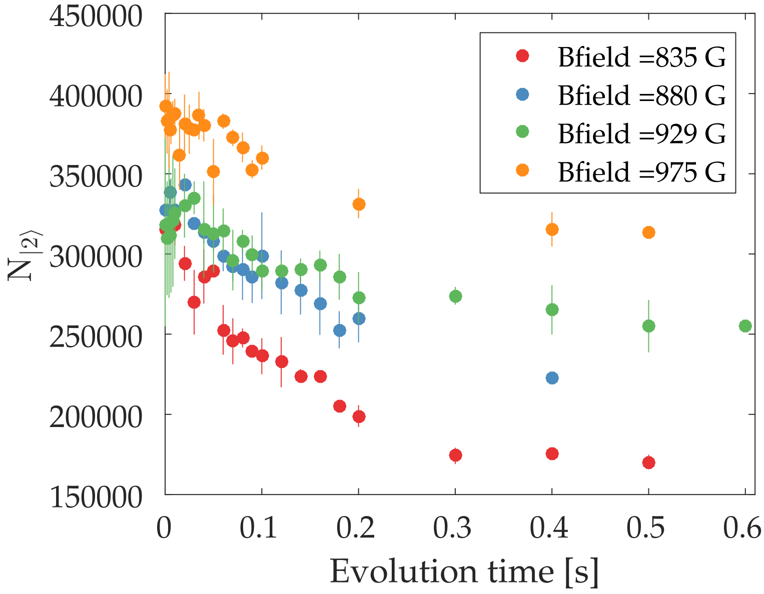

Figure 11.3: Total atom number N in the $|2\rangle$ state of the measurement shown in Figure 11.1. The particle number decreases during the course of the measurement due to evaporation of atoms from the trap. The biggest loss and fastest evaporation is happening at lower fields where the interaction is strongest.

Indeed, this observed tendency agrees with the prediction of Yuzbashyan et al. [138]. However, effects such as evaporation are not taken into account. Further away from unitarity the time constant of the growth is constant.

As described in the theory section section 11.1 and also visible in Figure 11.1 at long time scales a new steady state is reached. This new state differs from the ground state of the system. The new gap value is predicted to be smaller than the one of a system prepared at equilibrium at otherwise identical conditions. This is due to persistent motions of the pairs after the quench. In the weak coupling the gap at long times is predicted to be half the BCS gap value. In the experiment, by measuring the condensate fraction we do not measure the gap parameter directly. Nevertheless, the condensate fraction indicates a relative size of the gap between different measurements. Figure 11.5 presents the condensate fraction after the evolution has reached a constant value as a function of different interaction values. For comparison, the inset shows the condensate fraction when the spin mixture is prepared in equilibrium. It is clearly visible that the condensate fraction after the quench is smaller than the condensate fraction of the sample prepared at equilibrium. Far on the BCS side, the condensate fraction after the quench is roughly half of the value at equilibrium. The solid line refers to one possible

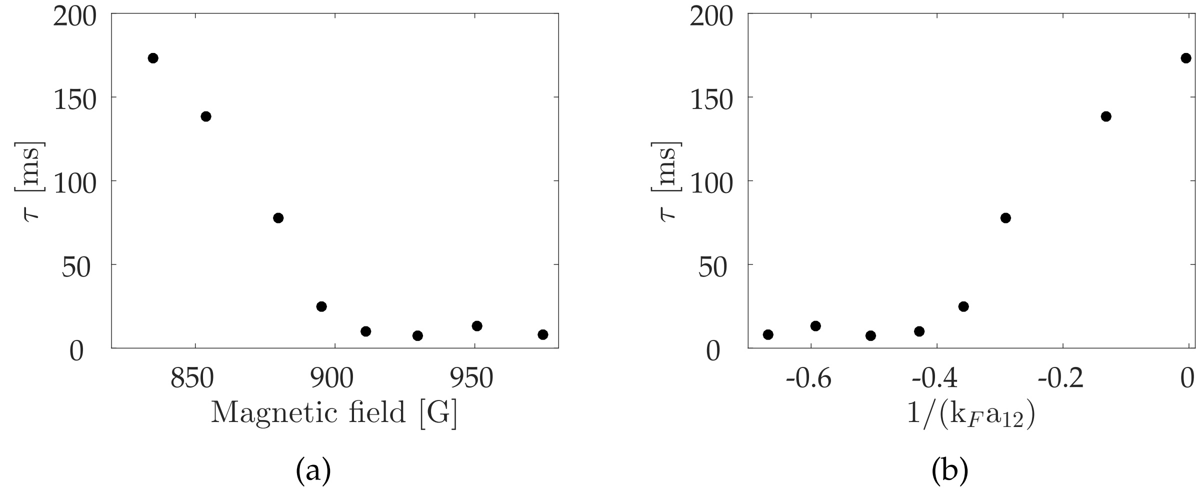

Figure 11.4: Fitted exponential time constant of the condensate growth shown in Figure 11.1; **(a)** for different magnetic field values. **(b)** and for different interaction parameters $1/(k_F a_{12})$. At unitarity, the evolution to a constant condensate fraction takes longest.

fitting solution [136], which studies the dynamics of a quench from the normal to the superfluid state of a Fermi gas. They predict a gap at long times after the quench of $\Delta_\infty = \epsilon_c / \sqrt{\exp{(2/N(0)\lambda)} - 1}$.

11.3 Conclusion and Outlook

We studied the evolution of a Fermi gas after the interaction strength was increased abruptly and observed the growth of a condensate fraction. Depending on the increase of the interaction strength, this evolution takes 10 to 200ms. The more the interaction strength is increased, the longer it takes to reach a steady state.

At long times after the quench, the system settles and is characterized by a new gap value. We compare the condensate fraction at long times with the condensate fraction of a spin mixture prepared at equilibrium with otherwise identical conditions. As predicted by theory, the condensate fraction after the quench is smaller than the condensate fraction of a spin mixture prepared at equilibrium. Nevertheless, for the exact time dependence and understanding of the growth mechanism further experimental and theoretical studies are necessary.

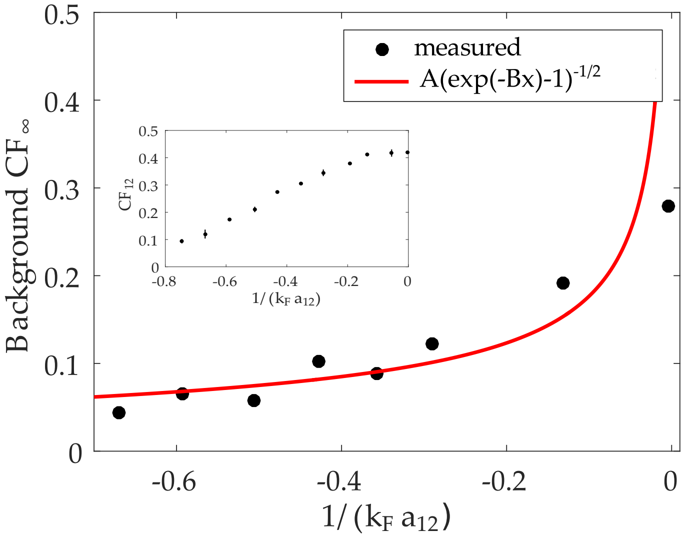

Figure 11.5: Condensate fraction CF_∞ after the evolution reached a constant (background) value as a function of interaction values. For comparison, the inset shows the condensate fraction CF_{12} when the spin mixture is prepared in equilibrium. It is clearly visible that the condensate fraction CF_∞ after the quench is smaller than the condensate fraction CF_{12} of the sample prepared at equilibrium. Far on the BCS side ($1/(k_F a_{12}) = -0.7$), the condensate fraction CF_∞ after the quench is roughly half of the value at equilibrium. The solid line refers to one possible fitting solution [136], which studies the dynamics of a quench from the normal to the superfluid state of a Fermi gas. They predict a gap of $\Delta_\infty = \epsilon_c / \sqrt{\exp(2/N(0)\lambda) - 1}$ at long times after the quench, which is not equal to the ground state BCS gap value Δ. Δ_∞ is smaller than the ground state BCS gap value due to residual collective motion of the pairs.

CHAPTER 12

Conclusion and Outlook

Within the scope of this thesis, we present a novel apparatus built from scratch to study ultracold, strongly interacting fermionic lithium atoms confined in a three-dimensional harmonic trap with tunable interactions. We produce a fermionic superfluid of 4×10^6 lithium ^{6}Li atoms at a temperature of $T/T_F = 0.07 \pm 0.02$. This is achieved within 23 s by a combination of laser cooling, radio frequency evaporation of ^{23}Na and simultaneous sympathetic cooling of ^{6}Li in an optical plugged magnetic trap and subsequent evaporative cooling of ^{6}Li in a dipole trap.

We investigate the response of the system to perturbation of the order parameter and the interaction strength. For the first time, we observe the Higgs mode in a strongly interacting fermionic system. Our excitation method is the first one, which couples directly to the Higgs mode in a strongly interacting Fermi gas. It has been suggested [1] that the Higgs mode is a precise measure of the superconducting gap in the BEC-BCS crossover where the exact value of the amplitude of the gap is yet unknown and numerical calculations are challenging. Previous gap measurements [133, 134] have yielded smaller gap values than predicted by different Quantum Monte Carlo (QMC) calculations. Our result agrees well with QMC calculations at unitarity and provides a lower bound for the gap parameter throughout the BEC-BCS crossover. An upper bound is provided by the theoretical result of mean-field theory, which is known to overestimate the superconducting gap.

Moreover, we present the first observation of collapse and revival of order in a quenched strongly interacting superfluid of ultracold fermions. In our experiment we observe a fast relaxation to a zero order parameter for large quenches, whereas for small quenches we observe, after a sudden drop, a revival of the order parameter and equilibration to a long-term superfluid steady state. This revival of the order can be connected to a critical quench parameter indicating a potential dynamical phase transition. In addition, we observe that the time scale of the initial sudden drop depends on the amplitude of the quench. For large quenches the decay follows the gap time, whereas for small quenches the decay follows the quasiparticle relaxation time. Hence, our experiments provide insight into the intrinsic mechanisms occurring after a sudden interaction quench. We can perform the quenches in half the Fermi time, which is experimentally very close to a sudden change and faster than any other group performing interaction quenches with ultra cold gases.

In two dimensional systems with continuous symmetry true long range order does not exist as it is prohibited by thermal fluctuations [139, 140]. Fluctuations such as the Goldstone mode destroy long range order resulting in the absence of Bose-Einstein condensation below a critical temperature in two dimension. However, below a finite temperature the system can still undergo a second order phase transition and become superfluid. This quantum phase transition is called Berezinskii-Kosterlitz-Thouless transition (BKT) [141, 142]. Kosterlitz and Thouless were recently (2016) awarded with the Nobel prize for their work on this topological phase transition. The emergence of topological order below the phase transition results from the pairing of vortices. However, no symmetry is spontaneously broken and no spatially uniform order parameter exists. Instead, the correlation length diverges at the critical point [141, 142]. The BKT transition has been observed in helium film [143], Josephson junctions [144] and Bose gases [145]. The question arising is whether in a two dimensional superfluid, a system which does not exhibit spontaneous symmetry breaking, a stable Higgs mode exists [146–148].

The ability to create lower dimensional systems in ultracold gas systems using the interference of laser beams as trapping potential provides an ideal system to study the Higgs mode in lower dimensions. Together with our novel detection method presented in this thesis, this is a really exciting way to go forward.

The novel technique of measuring the superconducting gap paves the way to investigate the behavior of the gap in different systems. One interesting question is the dependence of the gap on increasing spin imbalance compared to the disappearance of the superfluid behavior of the gas. The critical imbalance destroying superfluidity in a fermionic gas has been measured Ì[149, 150]. However, it is not known if the superconducting gap goes to zero at the same time. With the novel technique of measuring the superconducting gap, this question could be answered. Setting up a homogenous potential [151, 152] instead of the current harmonic confinement will circumvent difficulties arising from phase separation in the trap.

With this new apparatus at hand, the prospects of gaining deeper insight into many aspects of strongly interacting Fermi gases are excellent.

APPENDIX A

Appendix

A.1 Pictures of the Experiment

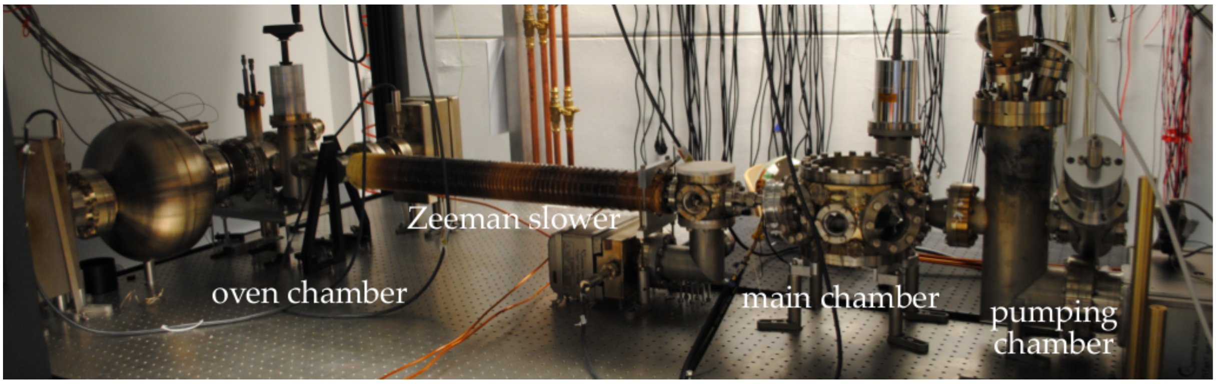

Figure A.1: Picture of the vacuum system sketched in Figure 3.1 including the oven, the Zeeman slower, the main chamber and the pumping chamber.

The vacuum system drawn in Figure 3.1 including the oven, the Zeeman slower, the main chamber and the pumping chamber is shown in Figure A.1. This picture was taken before all optics was installed next to it. The sodium and lithium laser systems are set up on a separate table connected to the main experiment by glass fibers. The sodium laser system as sketched in Figure 4.1 can be seen in Figure A.2.

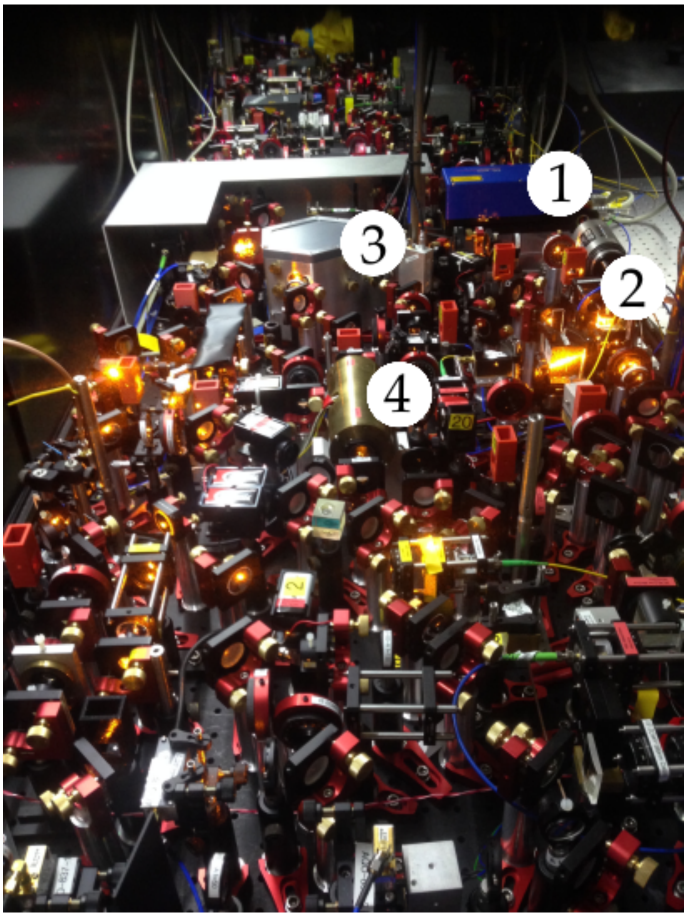

Figure A.2: Picture of the sodium laser system sketched in Figure 4.1. **(1)** Master laser (ECDL from Toptica), wavelength 1 078 nm, output power 30 mW **(2)** Output of Raman fiber amplifier,**(3)** Frequency doubling cavity with an output power of 1.3 W at 589 nm **(4)** Sodium spectroscopy cell. A part of the lithium laser system can be seen in the background.

A.2 Relative Pressure Inside the Vacuum System

As mentioned in chapter 3, the separation between the high pressure region (oven) and the ultra high vacuum (UHV) region (main chamber) has to be performed carefully. This is achieved by placing a long tube with low conductance between the two parts (see section 3.2). If the conductance is low enough and the pumping speed of the vacuum pumps high enough the desired pressure difference can be maintain. The pressure difference can be calculated in the following way [66, 70].

The base pressure P of the vacuum system can be expressed in terms of the throughput Q and the pumping speed S

$$Q = P \cdot S \quad . \tag{A.1}$$

This relation can be understood by relating it to Ohm's law $U = I \cdot R$, where now the current is given by the system throughput $I = Q$, the voltage is the base pressure $U = P$, an the resistance is given by the inverse pumping speed $R = 1/S$. Each vacuum component can be characterized by a certain conductance. If they are arranged in series, the total conductance is given by $1/C_{eff} = 1/C_1 + 1/C_2 + \ldots$. And if they are placed in parallel the conductance adds up like $C_{eff} = C_1 + C_2 + \ldots$. The throughput of the n^{th} element can be written like

$$Q_n = R_n + (P_{n-1} - P_n) \cdot C_{n-1,n} + (P_{n+1,n} - P_n) \cdot C_{n+1,n} - V_n P_n \quad . \tag{A.2}$$

Here, R_n describes the outgassing of the n^{th} element. For simplicity we set all terms to zero except the first one, which describes the pressure in the oven. We assume that during bake-out all vacuum elements were baked out carefully such that the outgassing over time can be neglected. The conductance between vacuum element n and $n+1$ is given by $C_{n,n+1}$ and the effective pumping speed V_n is calculated via the relation $1/V = 1/S + 1/C$. Equation A.2 can be translated into a matrix equation $(\mathbf{C} + \mathbf{V}) \cdot \mathbf{P} = \mathbf{R}$ as the total mass flow is conserved ($\sum_n Q_n = 0$). Following that, the pressure can be calculated by $\mathbf{P} = (\mathbf{C} + \mathbf{V})^{-1} \cdot \mathbf{R}$.

In order to apply these considerations to a real vacuum system, the conductance of each vacuum component has to be calculated [70]. In our case, we had to calculate the conductance of tubes, apertures and conical adapters. The conductance of such elements are listed in Table A.1. We applied these relations to the vacuum system shown in Figure 3.1and Figure A.1 and verified that the desired pressure difference between oven and main chamber can be maintained with the chosen vacuum pumps. We use the following ion pumps in our setup. One pump with a pumping speed of $100\,\mathrm{l\,s^{-1}}$ is connected to the vacuum chamber containing the cold cup, another one ($75\,\mathrm{l\,s^{-1}}$) is mounted between two differential pumping tubes, one ($45\,\mathrm{l\,s^{-1}}$) is connected to the small vacuum chamber between the two Zeeman slower parts and the last one ($100\,\mathrm{l\,s^{-1}}$) is set up close to the main chamber. Besides that, we use titanium sublimation pumps and SAES getter pumps to maintain high pressure. The simplified calculations

Vacuum element	Conductance $[\frac{m^3}{s}]$
Aperture	$\frac{v}{4}\pi\left(\frac{d}{2}\right)^2$
Tube	$\frac{\pi}{12}v\frac{d^3}{l}$
Short tube	$\left(\frac{1}{C_{tube}}+\frac{1}{C_{aperture}}\right)^{-1}$
Conical adapter	$\int_{d_{min}}^{d_{max}} C_{aperture}\mathrm{d}d$

Table A.1: Different types of conductance of vacuum parts [70]. These equations can be used to calculate $C_{n,n+1}$ in Equation A.2.

presented in this paragraph have to be taken with care. Different gas components are pumped with different efficiencies, outgassing might reduce the vacuum pressure and conductances can be underestimated for example.

A.3 Oven Refill

After typically 1.5 to 2.5 years of operation the sodium reservoir gets empty and has to be refilled. During operation most of the sodium condenses on the cold cup (see Figure 3.2 and Figure A.3). To avoid clogging of the cold cup and deposition of sodium around the atomic beam shutter[1] it is favorable to clean or simply change the cold cup whenever the sodium reservoir is refilled. For this purpose we can close the gate valve between oven chamber and main chamber and remove the baffel for cleaning the cold cup. The reservoir cups can be dismounted, refilled and attached to the vacuum system. Following that, a roughing pump is connected to the oven chamber as well as an argon reservoir. Argon is used to avoid unnecessary contamination of the chamber as well as to protect the remaining lithium in the lithium reservoir from oxidation. Nitrogen should not be used instead as it reacts with lithium to lithium nitrite.

Care has to be taken while cleaning the oven as sodium reacts heavily with water (also with the water in the air) and it is easily flammable. Sodium can be directly purchased from Strem Chemicals and is delivered in a glass ampoule packed under

---

[1] A future oven design will have a sodium collecting cup at the bottom and the shutter feedthrough will be mounted to the top of the oven chamber.

argon atmosphere. In contrast, lithium cannot be purchased in a glass ampoule packed under argon. Therefore, we buy enriched lithium from Sigma Aldrich and get it cleaned from oil and oxide layers and packed under argon atmosphere from a lab called Ames Lab in the US. We typically refill the sodium reservoir with $25-50$g of sodium. The first amount of lithium we put into the lithium reservoir was around 10g. Pictures of the oven champer and the deposition of sodium herein, are shown in Figure A.3.

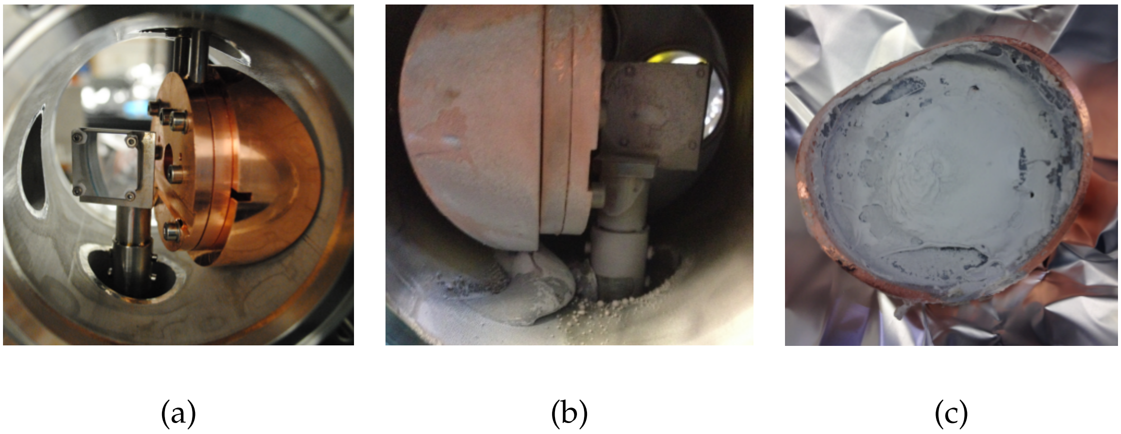
(a) (b) (c)

Figure A.3: Pictures of the oven. **(a)** Vacuum chamber containing cold cup and atomic beam shutter before closing the vacuum system for the first time. **(b)** After $1.5-2.5$ years of operation the sodium reservoir is empty and has to be refilled. During operation most of the sodium condenses on the cold cup. The condensed sodium on the cold cup can be clearly seen in **(c)**. Here, no hole in the cold cup is visible as we heated up the cold cup with a high power laser to remove sodium from the cold cup. However, this was not the problem, the reason of no atoms in the MOT chamber was that there was simply no sodium left in the reservoir.

A.4 Optical Viewports

A special feature of our vacuum system is the sealing method of the main optical viewports surrounding the main chamber. The design of those homemade viewports follows the idea by Scott Crane and Christopher Ekstrom [68]. Their sealing method relies on crushing thin copper knife-edges between a glass and steel chamber sealing the vacuum up to UHV. The principle is illustrated in Figure A.4. Even though this procedure might sound complicated and not easy to apply, it has several advantages, the first one being larger optical access. Many standard optical viewports have reduced optical access due to the method they are sealed to the flange. The second one being the free choice of glass material and coating. In addition, the glass can be coated before

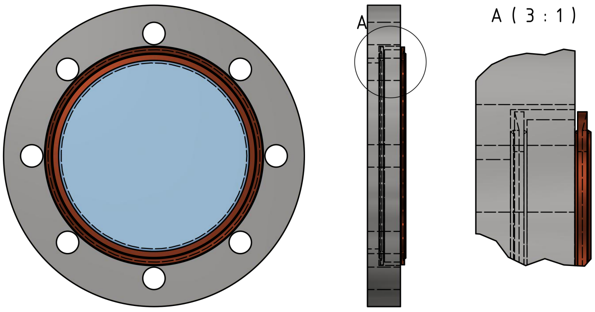

Figure A.4: Drawing of the optical viewports used around the main chamber. The design principle of those homemade viewports follows the idea by Scott Crane and Christopher Ekstrom [68]. Their sealing method relies on crushing thin copper knife-edges (brown) between glass and steel chamber. A close-up is shown on the right hand side of the drawing.

attaching it to the flange guaranteeing a coated area up to the steel flange. In contrast, this is not the case for standard viewports, which are coated after being sealed to the flange and therefore have an uncoated ring on the edge. The choice of the glass material is also important. A material with low birefringence is favorable for all applications related to optical trapping of ultracold atoms.

A.5 Laser Offset Lock

A sketch of a laser offset lock is shown in Figure A.5. This method is used for creating the error signal, which allows stabilizing the frequency of a second laser relative to the first laser with a defined offset frequency. This technique is used to stabilize the second laser generating for example the Zeeman slower light but also for a third laser, which can be used to image the hyperfine state $|6\rangle$ at high fields.

A.6 Combining Light on the Experiment Table

An important task while planing and setting up such an experiment is to make sure that the optical access is optimized to get all beams aligned to the atoms. In more detail, six MOT beams, two dipole beams, three beams for resonant absorption imaging, optical access for detecting the fluorescence of the MOT and eventually three counter

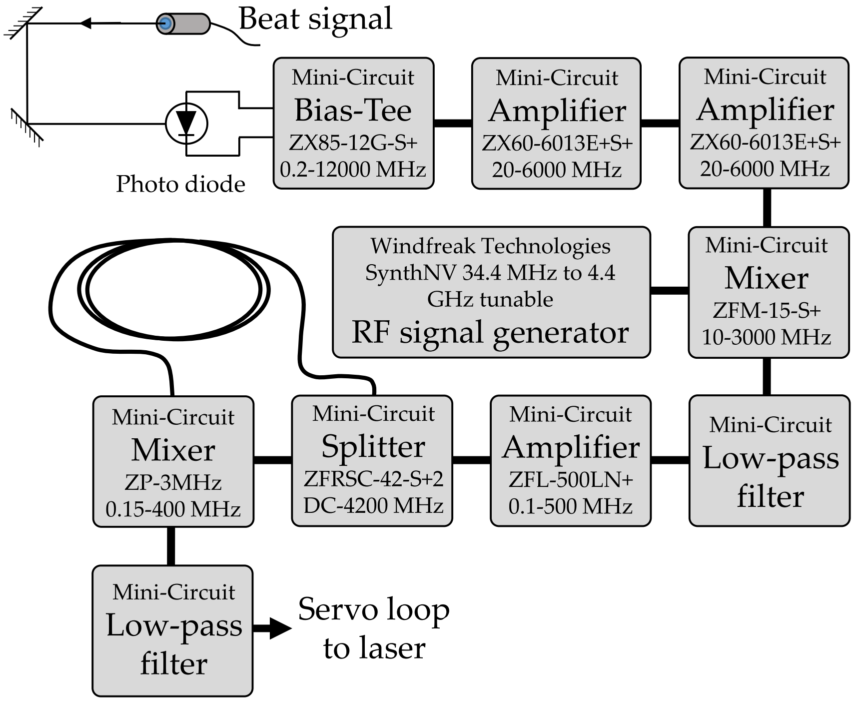

Figure A.5: Lithium offset lock: Sketch of the RF components used for creating the error signal, which allows stabilizing the frequency of another laser relative to the first laser with a defined offset frequency. This technique is used to stabilize a third laser, which can be used to image the hyperfine state $|6\rangle$ at high magnetic fields.

propagating lattice beams have to find their space. Our arrangement of beams and imaging systems is sketched in Figure A.6 and Figure A.7.

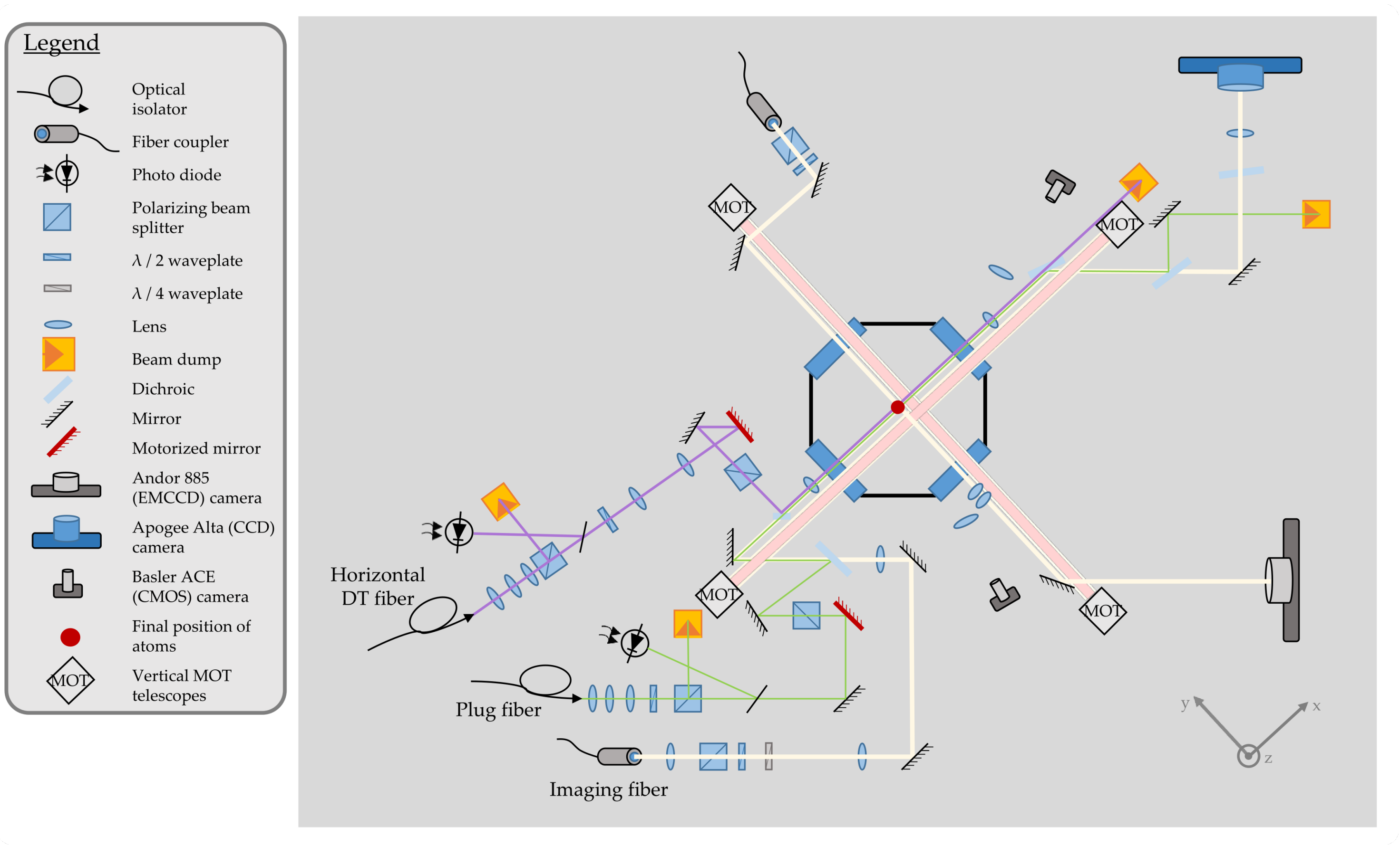

Figure A.6: Sketch of the vertical dipole trap setup and main imaging axis.

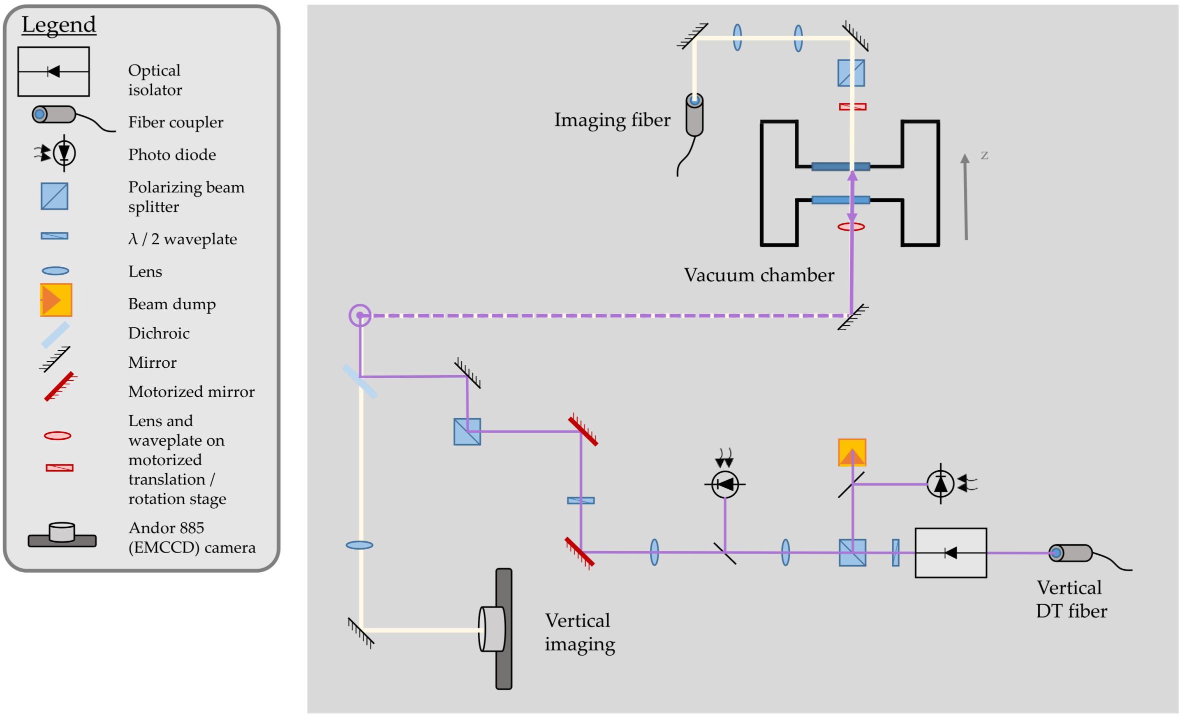

Figure A.7: Sketch of MOT, plug, horizontal dipole trap and imaging optics.

List of Figures

List of Tables

Bibliography

[1] R. G. Scott et al.,
Rapid ramps across the BEC-BCS crossover: A route to measuring the superfluid gap,
Physical Review A - Atomic, Molecular, and Optical Physics **86** (2012) 053604
(cit. on pp. v, 5, 20, 127, 135, 165).

[2] J. E. Thomas and M. E. Gehm, *Optically Trapped Fermi Gases*,
American Scientist **92** (2004) 238 (cit. on pp. 1, 2).

[3] J. E. Thomas and N. Carolina, *Ultracold Fermi gas on a chip*,
Nature Physics **2** (2006) 377 (cit. on p. 1).

[4] J. E. Thomas, *Superfluidity in the picture*, Nature **442** (2006) 32 (cit. on p. 1).

[5] D. Pekker and C. M. Varma,
Amplitude / Higgs Modes in Condensed Matter Physics,
Annual Review of Condensed Matter Physics **6** (2015) 269
(cit. on pp. 1, 4, 5, 127, 138).

[6] E. A. Yuzbashyan et al.,
Quantum quench phase diagrams of an s-wave BCS-BEC condensate,
Physical Review A - Atomic, Molecular, and Optical Physics **91** (2015)
(cit. on pp. 1, 7, 144–146).

[7] C. A. R. Sá de Melo, M. Randeria and J. R. Engelbrecht,
Crossover from BCS to Bose Superconductivity: Transition Temperature and Time-Dependent Ginzburg-Landau Theory, Physical Review Letters **71** (1993) 3202
(cit. on pp. 2, 18).

[8] M. Randeria and E. Taylor, *Crossover from Bardeen-Cooper-Schrieffer to Bose-Einstein Condensation and the Unitary Fermi Gas*,
Annual Review of Condensed Matter Physics **5** (2014) 209 (cit. on pp. 2, 18).

[9] J. Bardeen, L. N. Cooper and J. R. Schrieffer, *Theory of Superconductivity*, Physical Review **108** (1957) 1175 (cit. on pp. 2, 17).

[10] J. Bardeen, L. N. Cooper and J. R. Schrieffer, *Microscopic Theory of Superconductivity*, Physica Status Solidi (B) **106** (1957) 162 (cit. on p. 2).

[11] S. Bose, *Plancks Gesetz und Lichtquantenhypothese*, Z. Phys **26** (1924) 178 (cit. on p. 2).

[12] A. Einstein, *Sitzungsberichte der Preussischen Akademie der Wissenschaften, Physikalisch-mathematische Klasse*, tech. rep., 1924 261 (cit. on p. 2).

[13] A. Einstein, *Sitzungsberichte der Preussischen Akademie der Wissenschaften, Physikalisch-mathematische Klasse*, tech. rep., 1925 3 (cit. on p. 2).

[14] M. Tinkham, *Introduction to superconductivity*, Second Edi, McGraw-Hill, Inc., 2004 (cit. on pp. 2, 3, 18–21).

[15] P. W. Higgs, *Broken Symmetries and the Masses of Gauge Bosons*, Physical Review Letters **13** (1964) 508 (cit. on pp. 5, 126).

[16] A. Collaboration, *Observation of a new particle in the search for the Standard Model Higgs boson with the ATLAS detector at the LHC*, Physics Letters B **716** (2012) 1 (cit. on pp. 5, 126).

[17] C. M. S. Collaboration, *Observation of a new boson at a mass of 125 GeV with the CMS experiment at*, Physics Letters B **716** (2012) 30 (cit. on pp. 5, 126).

[18] P. B. Littlewood and C. M. Varma, *Gauge-Invariant Theory of the Dynamical Interaction of Charge Density Waves and Superconductivity*, Physical Review Letters **47** (1981) 811 (cit. on pp. 5, 126, 127).

[19] P. B. Littlewood and C. M. Varma, *Amplitude collective modes in superconductors and their coupling to charge-density waves*, Physical Review B **26** (1982) 4883 (cit. on pp. 5, 127).

[20] R. Sooryakumar and M. V. Klein, *Raman Scattering by Superconducting-Gap Excitations and their Coupling to Charge-Density Waves*, Physical Review Letters **45** (1980) 660 (cit. on pp. 5, 127, 142).

[21] R. Matsunaga et al., *Higgs amplitude mode in the BCS superconductors Nb1-xTi xN induced by terahertz pulse excitation*, Physical Review Letters **111** (2013) 1 (cit. on pp. 5, 127).

[22] D. Sherman et al., *The Higgs mode in disordered superconductors close to a quantum phase transition*, Nature Physics **11** (2015) 188 (cit. on pp. 5, 127).

[23] M.-A.Méasson et al., *Amplitude Higgs mode in the 2H-NbSe2 superconductor*, Physical Review B **89** (2014) 1 (cit. on pp. 5, 127, 142).

[24] D. Podolsky, A. Auerbach and D. P. Arovas, *Visibility of the amplitude (Higgs) mode in condensed matter*, Physical Review B **84** (2011) 174522 (cit. on pp. 5, 127).

[25] Y. Barlas and C. M. Varma, *Amplitude or Higgs modes in d-wave superconductors*, Physical Review A - Atomic, Molecular, and Optical Physics **87** (2013) 054503 (cit. on pp. 5, 127).

[26] B. Liu, H. Zhai and S. Zhang, *Evolution of the Higgs mode in a fermion superfluid with tunable interactions*, Physical Review A **93** (2016) 033641 (cit. on pp. 5, 127, 138).

[27] X. Han, B. Liu and J. Hu, *Observability of Higgs mode in a system without Lorentz invariance*, Physical Review A **94** (2016) 033608 (cit. on pp. 5, 127, 138).

[28] C. Rüegg et al., *Quantum Magnets under Pressure: Controlling Elementary Excitations in TlCuCl 3*, Physical Review Letters **205701** (2008) 205701 (cit. on pp. 5, 127).

[29] W. Halperin and E. Varoquax, "Order-parameter collective modes in superfluid 3He", *Helium Three*, ed. by W. In Halperin and L. Pitaevskii, Elsevier Science Publisher, 1990 353 (cit. on pp. 5, 127).

[30] U. Bissbort et al., *Detecting the amplitude mode of strongly interacting lattice bosons by Bragg scattering*, Physical Review Letters **106** (2011) 205303 (cit. on pp. 5, 127).

[31] M. Endres et al., *The 'Higgs' amplitude mode at the two-dimensional superfluid/Mott insulator transition*, Nature **487** (2012) 454 (cit. on pp. 5, 127).

[32] T. M. Hoang et al., *Adiabatic quenches and characterization of amplitude excitations in a continuous quantum phase transition*, Proceedings of the National Academy of Sciences **113** (2016) 9475 (cit. on pp. 5, 127).

[33] J. Léonard et al., *Monitoring and manipulating Higgs and Goldstone modes in a supersolid quantum gas*, arxiv (2017), arXiv: `1704.05803v1` (cit. on pp. 5, 127).

[34] G. Zürn et al., *Precise Characterization of 6Li Feshbach Resonances Using Trap-Sideband-Resolved RF Spectroscopy of Weakly Bound Molecules*, Physical Review Letters **110** (2013) 135301 (cit. on pp. 6, 16, 149).

[35] M. Greiner et al., *Collapse and revival of the matter wave field of a Bose–Einstein condensate*, Nature **419** (2002) 51 (cit. on p. 7).

[36] A. F. Volkov and S. M. Kogan, *Collisionless relaxation of the energy gap in superconductors*, Sov. Phys. JETP **38** (1974) 1018 (cit. on pp. 7, 144).

[37] R. A. Barankov, L. S. Levitov and B. Z. Spivak, *Collective Rabi oscillations and solitons in a time-dependent BCS pairing problem*, Physical Review Letters **93** (2004) 160401 (cit. on pp. 7, 144).

[38] E. A. Yuzbashyan, O. Tsyplyatyev and B. L. Altshuler, *Relaxation and Persistent Oscillations of the Order Parameter in Fermionic Condensates*, Physical Review Letters **96** (2006) 097005 (cit. on pp. 7, 144).

[39] E. A. Yuzbashyan and M. Dzero, *Dynamical vanishing of the order parameter in a fermionic condensate*, Physical Review Letters **96** (2006) 230404 (cit. on pp. 7, 127, 144, 147, 148, 150, 154, 155).

[40] M. Heyl, *Dynamical Quantum Phase Transitions in the Transverse-Field Ising Model*, **135704** (2013) 1 (cit. on pp. 8, 154).

[41] C. Kittel and H. Kroemer, *Thermal Physics*, W. H. Freeman and Company, 1980 (cit. on p. 11).

[42] L. Landau and E. Lifschitz, *Statistical Physics Part 2*, Robert Maxwell, M.C., 1981 (cit. on p. 12).

[43] S. Giorgini, L. P. Pitaevskii and S. Stringari, *Theory of ultracold atomic Fermi gases*, Reviews of Modern Physics **80** (2008) 1215, ISSN: 00346861, arXiv: `0706.3360` (cit. on p. 12).

[44] L. D. Landau and E. M. Lifshitz, *Quantum Mechanics; Non-Relativistic Theory*, Third Edit, Pergamon Press, 1991 (cit. on pp. 12, 13).

[45] L. F. Cohen-Tannoudji C., Diu B., *Quantum Mechanics Volume 2*, Wiley-VCH, 2005 (cit. on pp. 12, 13).

[46] W. Ketterle and M. W. Zwierlein, "Making, probing and understanding ultracold Fermi gases", *Ultracold Fermi Gases, Proceedings of the International Scholl of Physics "Enrico Fermi", Course CLXIV*, ed. by M. Inguscio, W Ketterle and C Salomon, IOS Press, 2008 95 (cit. on pp. 12, 13, 15, 18–20, 99, 128).

[47] I. Bloch, J. Dalibard and W. Zwerger, *Many-body physics with ultracold gases*, Reviews of Modern Physics **80** (2008) 885 (cit. on p. 13).

[48] J.-L. Basdevant and J. Dalibard, *BASDEVANT & DALIBARD - Quantum Mechanics*, Second Edi, Springer, 2005 (cit. on p. 13).

[49] D. S. Petrov, C. Salomon and G. V. Shlyapnikov, *Weakly Bound Dimers of Fermionic Atoms*, Physical Review Letters **93** (2004) 090404 (cit. on p. 14).

[50] L. N. Cooper, *Bound Electron Pairs in a Degenerate Fermi Gas*, Physical Review **104** (1956) 1189 (cit. on p. 17).

[51] A. J. Leggett, "Diatomic molecules and Cooper pairs", *Trends in the Theory of Condensed Matter, Proceedings of the XVIth Karpacz Winter School of Theoretical Physics, Karpacz, Poland*, Springer-Verlag, 1980 13 (cit. on p. 18).

[52] V. N. Popov, *Theory of a Bose gas produced by bound states of Fermi particles*, Zh. Eksp. Teor. Fiz. **50** (1968) 1550 (cit. on p. 18).

[53] L. V. Keldysh and A. N. Kozlov, *Collective properties of excitons in semiconductors*, Zh. EKsp. Teor. Fiz. **54** (1968) 978 (cit. on p. 18).

[54] D. M. Eagles, *Possible Pairing without Superconductivity at Low Carrier Concentrations in Bulk and Thin-Film Superconducting Semiconductors*, Physical Review **186** (1969) 456 (cit. on p. 18).

[55] C. A. Regal, M. Greiner and D. S. Jin, *Observation of Resonance Condensation of Fermionic Atom Pairs*, Physical Review Letters **92** (2004) 040403 (cit. on pp. 18, 122).

[56] M. W. Zwierlein et al., *Condensation of pairs of fermionic atoms near a Feshbach resonance*, Physical Review Letters **92** (2004) 120403 (cit. on p. 18).

[57] J. Kinast et al., *Evidence for Superfluidity in a Resonantly Interacting Fermi Gas*, Physical Review Letters **92** (2004) 150402 (cit. on p. 18).

[58] T. Bourdel et al., *Experimental Study of the BEC-BCS Crossover Region in Lithium 6*, Physical Review Letters **93** (2004) 050401 (cit. on p. 18).

[59] C. Chin et al., *Observation of the Pairing Gap in a Strongly Interacting Fermi Gas*, Science **305** (2004) 1128 (cit. on pp. 18, 128).

[60] G. B. Partridge et al., *Molecular Probe of Pairing in the BEC-BCS Crossover*, Physical Review Letters **95** (2005) 020404 (cit. on p. 18).

[61] M. W. Zwierlein et al., *Vortices and superfluidity in a strongly interacting Fermi gas*, Nature **435** (2005) 1047 (cit. on p. 18).

[62] C. J. Pethick and H Smith, *Bose-Einstein Condensation in Dilute Gases*, Cambridge University Press, 2008 (cit. on pp. 18, 73, 88).

[63] P. Nozières and S. Schmitt-Rink, *Bose Condensation in an Attractive Fermion Gas: From Weak to Strong Coupling Superconductivity*, Journal of Low Temperature Physics **59** (1985) 195 (cit. on pp. 18, 19).

[64] W. Ketterle, S. Durfee and D. M. Stamper-Kurn, "Making, probing and understanding Bose-Einstein condensates", *Bose-Einstein condensation in atomic gases, Proceedings of the International School of Physics Enrico Fermi, Course CXL*, ed. by M. Inguscio, S. Stringari and C. E. Wieman, IOS Press, 1996 67 (cit. on pp. 23, 27, 115).

[65] C. A. Stan and W. Ketterle, *Multiple species atom source for laser-cooling experiments*, Rev. Sci. Instrum. **76** (2005) 063113 (cit. on p. 24).

[66] D. S. Naik, *Bose-Einstein Condensation: Building the Testbeds to Study Superfluidity*, PhD thesis: Georgia Institute of Technology, 2006 (cit. on pp. 27, 52, 170).

[67] T. Leuteritz, *High Resolution Imaging of an Ultracold Fermi Gas*, Master thesis: Rheinischen Friedrich-Wilhelms-Universität Bonn, 2016 (cit. on p. 28).

[68] S. Crane and C. R. Ekstrom, "Nonmagnetic UHV Optical Viewports", *Frequency Control Symposium and Exposition, 2005. Proceedings of the 2005 IEEE International*, 2005 (cit. on pp. 29, 173, 174).

[69] R. Calder and G. Lewin, *Reduction of stainless-steel outgassing in ultra-high vacuum*, Brit. J. Appl. Phys. **18** (1967) 1459 (cit. on p. 30).

[70] J. F. O. Hanion, *A User's Guide to Vacuum Technology Third Edition*, Second Edi, John Wiley & Sons, Inc, 1989 (cit. on pp. 30, 170–172).

[71] W. D. Phillips, *Laser cooling and trapping of neutral atoms*, Review of Scientific Instruments **70** (1998) 721 (cit. on p. 34).

[72] C. J. Foot, *Atomic Physics*, Oxford University Press, 2005 (cit. on pp. 34, 52, 59).

[73] H. J. Metcalf and P. van der Straten, *Laser Cooling and Trapping*, Springer, 1999 (cit. on pp. 34, 73).

[74] H.-M. Meyer, *A Laser System for Trapping and Cooling of Ytterbium-Ions*, Diploma thesis: University of Heidelberg, 2010 (cit. on pp. 35, 39, 40).

[75] A. Franken, *Generation of optical harmonics*, Physical Review Letters **7** (1961) 118 (cit. on p. 37).

[76] B. E. A. Saleh and M. C. Teich, *Fundamentals of Photonics*, vol. 5, John Wiley & Sons, Inc, 1991 (cit. on pp. 37, 91).

[77] W. P. Risk, T. R. Gosnell and A. V. Nurmikko, *Compact Blue-Green Lasers*, Cambridge University Press, 2003 (cit. on p. 37).

[78] G. D. Boyd and G. D. Kleinman, *Parametric Interaction of Focused Gaussian Light Beams*, Journal of Applied Physics **39** (1968) 3597 (cit. on p. 38).

[79] R. W. P. Drever, *Laser Phase and Frequency Stabilization Using an Optical Resonator*, Applied Physics B **31** (1983) 97 (cit. on p. 42).

[80] E. D. Black, *An introduction to Pound – Drever – Hall laser frequency stabilization*, American Journal of Physics **69** (2001) 79 (cit. on p. 42).

[81] M. J. Zawierucha, *Design and Construction of a Sodium Spectroscopy Cell and a Lock-in Amplifier for Frequency Locking a Laser*, Bachelor Thesis: Rheinische Friedrich-Wilhelms-Universität Bonn, 2015 (cit. on p. 43).

[82] D. A. Steck, *Sodium D Line Data*, tech. rep., URL: `http://steck.us/alkalidata` (cit. on p. 44).

[83] M. E. Gehm, *Properties of 6Li*, tech. rep., 2003, URL: `http://steck.us/alkalidata` (cit. on p. 47).

[84] C. Linse, *Construction of a 6Li spectroscopy cell and Doppler-free spectroscopy*, Bachelor thesis: Rheinische Friedrich-Wilhelms-Universität Bonn, 2014 (cit. on p. 48).

[85] U. Schünemann et al., *Simple scheme for tunable frequency offset locking of two lasers*, Review of Scientific Instruments **70** (1999) 242 (cit. on p. 48).

[86] S. C. Bell et al., *A slow atom source using a collimated effusive oven and a single-layer variable pitch coil Zeeman slower.*, The Review of Scientific Instruments **81** (2010) 013105 (cit. on pp. 52, 54).

[87] D. S. Durfee, *Dynamic Properties of Dilute Bose-Einstein Condensates*, PhD thesis: Massachusetts Institute of Technology, 1999 (cit. on pp. 52, 53).

[88] Z. Hadzibabic, *Studies of a Quantum Degenerate Fermionic Lithium Gas*, PhD thesis: MIT, 2003 (cit. on pp. 56, 74, 118).

[89] W. Ketterle and N. J. Van Druten, *Evaporative Cooling of Trapped Atoms*, Advances in atomic, molecular, and atomic physics **37** (1996) 181, ed. by B. Bederson and H. Walther (cit. on p. 57).

[90] E. L. Raab et al., *Trapping of Neutral Sodium Atoms with Radiation Pressure*, Physical Review Letters **59** (1987) 2631 (cit. on p. 58).

[91] F. Serwane, *The setup of a Magneto Optical Trap for the preparation of a mesoscopic degenerate Fermi gas*, Diploma thesis: University of Heidelberg, 2007 (cit. on pp. 59, 60).

[92] J. Dalibard and C. Cohen-Tannoudji, *Laser cooling below the Doppler limit by polarization gradients: simple theoretical models*, J. Opt. Soc. Am. B **6** (1989) 2023 (cit. on pp. 60, 67).

[93] W. Ketterle et al., *High Densities of Cold Atoms in a Dark Spontaneous-Force Optical Trap*, Physical Review Letters **70** (1993) 2253 (cit. on pp. 62–64).

[94] P. D. Lett et al., *Observation of Atoms Laser Cooled below the Doppler Limit*, Physical Review Letters **61** (1988) 169 (cit. on p. 67).

[95] T. M. Brzozowski et al., *Time-of-flight measurement of the temperature of cold atoms for short trap - probe beam distances*, J.Opt. B: Quantum Semiclass. Opt. **4** (2002) 62 (cit. on p. 67).

[96] K. B. Davis et al., *Bose-Einstein Condensation in a Gas of Sodium Atoms*, Physical Review Letters **75** (1995) 3969 (cit. on pp. 71–73).

[97] Y.-J. Lin et al., *Rapid production of Rb87 Bose-Einstein condensates in a combined magnetic and optical potential*, Physical Review A **79** (2009) 063631 (cit. on p. 72).

[98] M. H. Anderson et al., *Observation of Bose-Einstein Condensation in a Dilute Atomic Vapor*, Science **269** (1995) 198 (cit. on pp. 72, 73).

[99] D. S. Naik and C. Raman, *Optically plugged quadrupole trap for Bose-Einstein condensates*, Physical Review A **71** (2005) 033617 (cit. on p. 72).

[100] M. Heo, J. Choi and Y. Shin, *Fast production of large 23Na Bose-Einstein condensates in an optically plugged magnetic quadrupole trap*, Physical Review A **83** (2011) 013622 (cit. on pp. 72, 76).

[101] A. L. Migdall et al., *First Observation of Magnetically Trapped Neutral Atoms*, Physical Review Letters **54** (1985) 2596 (cit. on p. 73).

[102] D. E. Pritchard, *Cooling Neutral Atoms in a Magnetic Trap for Precision Spectroscopy*, Physical Review Letters **51** (1983) 1336 (cit. on p. 73).

[103] A. Goerlitz et al.,
Sodium Bose-Einstein Condensates in the F = 2 State in a Large-Volume Optical Trap,
Physical Review Letters **90** (2003) 090401 (cit. on pp. 74, 82).

[104] Z. Hadzibabic et al.,
Fiftyfold Improvement in the Number of Quantum Degenerate Fermionic Atoms,
Physical Review Letters **91** (2003) 160401 (cit. on p. 75).

[105] K. Huang, *Statistical Mechanics*, Second Edi, John Wiley & Sons, 1987
(cit. on p. 81).

[106] R. Grimm, M. Weidemüller and Y. Ovchinnikov,
Optical dipole trap for neutral atoms, Adv. At. Mol. Opt. Phys. **42** (2000) 95
(cit. on pp. 89, 90).

[107] J.-L. Meunier, *A simple demonstration of the Wigner-Eckart theorem*,
European Journal of Physics **8** (1987) 114 (cit. on p. 89).

[108] R. Loudon, *The Quantum Theory of Light*, Third Edit,
Oxford University Press, 2000 (cit. on p. 90).

[109] T. A. Savard and J. E. Thomas,
Laser-noise-induced heating in far-off resonance optical traps,
Physical Review A **56** (1997) 1095 (cit. on p. 97).

[110] H. Heiselberg, *Collective Modes of Trapped Gases at the BEC-BCS Crossover*,
Physical Review Letters **93** (2004) 040402 (cit. on p. 97).

[111] S. Inouye et al., *Observation of Feshbach resonances in a Bose-Einstein condensate*,
Nature **392** (1998) 151 (cit. on p. 101).

[112] J. Stenger et al., *Strongly Enhanced Inelastic Collisions in a Bose-Einstein Condensate near Feshbach Resonances*, Physical Review Letters **82** (1999) 2422 (cit. on p. 101).

[113] J. Cubizolles et al.,
Production of Long-Lived Ultracold Li2 Molecules from a Fermi Gas Magnetic Field,
Physical Review Letters **91** (2003) 240401 (cit. on p. 101).

[114] K. E. Strecker, G. B. Partridge and R. G. Hulet,
Conversion of an Atomic Fermi Gas to a Long-Lived Molecular Bose Gas,
Physical Review Letters **91** (2003) 080406 (cit. on p. 101).

[115] S. Jochim et al.,
Pure Gas of Optically Trapped Molecules Created from Fermionic Atoms,
Physical Review Letters **91** (2003) 240402 (cit. on p. 101).

[116] T. Harrison,
Measuring the Gap and Investigating Non-equilibrium in the BEC-BCS Crossover,
PhD thesis: Rheinische Friedrich-Wilhelms-Universität Bonn, 2017
(cit. on p. 110).

[117] C. Zipkes, *A Trapped Single Ion Inside a Bose-Einstein Condensate*,
PhD thesis: University of Cambridge, 2011 (cit. on p. 112).

[118] E. Cocchi, *Analogue antum Simulation of the Two-Dimensional Hubbard Model with Ultracold Fermions by Eugenio Cocchi*, PhD thesis: University of Cambridge, 2016 (cit. on p. 119).

[119] L. A. Miller, *Ultracold Fermions in Two-Dimensional Optical Lattices : Quantum Simulation of the Hubbard Model*, PhD thesis: University of Cambridge, 2016 (cit. on p. 119).

[120] L. Chomaz, *Coherence and superfluidity of Bose gases in reduced dimensions: from harmonic traps to uniform fluids Lauriane Chomaz*,
PhD thesis: École Normale Supérieure, 2015 (cit. on p. 119).

[121] G. Reinaudi, T. Lahaye and Z. Wang,
Strong saturation absorption imaging of dense clouds of ultracold atoms,
Optics Letters **32** (2007) 3143 (cit. on p. 120).

[122] M. W. Zwierlein et al.,
Condensation of Pairs of Fermionic Atoms near a Feshbach Resonance,
Physical Review Letters **92** (2004) 120403 (cit. on p. 122).

[123] S. Hannibal et al., *Quench dynamics of an ultracold Fermi gas in the BCS regime: Spectral properties and confinement-induced breakdown of the Higgs mode*,
Physical Review A - Atomic, Molecular, and Optical Physics **91** (2015) 043630 (cit. on p. 127).

[124] M. Greiner, C. A. Regal and D. S. Jin,
Probing the Excitation Spectrum of a Fermi Gas in the BCS-BEC Crossover Regime,
Physical Review Letters **94** (2005) 070403 (cit. on p. 128).

[125] J. T. Stewart, J. P. Gaebler and D. S. Jin,
Using photoemission spectroscopy to probe a strongly interacting Fermi gas,
Nature **454** (2008) 744 (cit. on p. 128).

[126] M. Feld et al., *Observation of a pairing pseudogap in a two-dimensional Fermi gas*,
Nature **480** (2011) 57 (cit. on p. 128).

[127] G. M. Bruun, *Low-Energy Monopole Modes of a Trapped Atomic Fermi Gas*,
Physical Review Letters **89** (2002) 263002 (cit. on p. 135).

[128] J. Tokimoto, S. Tsuchiya and T. Nikuni,
Higgs Mode in a Trapped Superfluid Fermi Gas,
Journal of Low Temperature Physics (2017) 1 (cit. on p. 135).

[129] S. Y. Chang et al., *Quantum Monte Carlo studies of superfluid Fermi gases*,
Physical Review A **70** (2004) 043602 (cit. on pp. 135, 137).

[130] A. Gezerlis and J Carlson, *Strongly paired fermions: Cold atoms and neutron matter*,
Physical Review C **77** (2008) 032801 (cit. on pp. 135, 137).

[131] A. Bulgac and P. Magierski,
Quantum Monte Carlo simulations of the BCS-BEC crossover at finite temperature,
Physical Review A **78** (2008) 023625 (cit. on pp. 135, 137).

[132] Q. Chen, *Effect of the particle-hole channel on BCS – Bose-Einstein condensation crossover in atomic Fermi gases*, Scientific Reports **6** (2016) 25772
(cit. on pp. 135, 137).

[133] A. Schirotzek et al., *Determination of the Superfluid Gap in Atomic Fermi Gases by Quasiparticle Spectroscopy*, Physical Review Letters **101** (2008) 140403
(cit. on pp. 135, 165).

[134] S. Hoinka et al.,
Goldstone mode and pair-breaking excitations in atomic Fermi superfluids, (2017),
arXiv: `1707.00406` (cit. on pp. 135, 165).

[135] R. A. Barankov and L. S. Levitov,
Synchronization in the BCS pairing dynamics as a critical phenomenon,
Physical Review Letters **96** (2006) 1, ISSN: 00319007,
arXiv: `0603317 [cond-mat]` (cit. on pp. 144–146).

[136] G. L. Warner and A. J. Leggett, *Quench dynamics of a superfluid Fermi gas*,
Physical Review B **71** (2005) 134514 (cit. on pp. 157, 162, 163).

[137] R. A. Barankov, L. S. Levitov and B. Z. Spivak,
Collective Rabi Oscillations and Solitons in a Time-Dependent BCS Pairing Problem,
Physical Review Letters **93** (2004) 160401 (cit. on p. 157).

[138] E. A. Yuzbashyan and O. Tsyplyatyev,
Dynamics of emerent Cooper pairing at finite temperature,
Physical Review A **79** (2009) 132504 (cit. on pp. 157, 161).

[139] N. D. Mermin and H. Wagner, *Absence of ferromagnetism or antiferromagnetism in one- or two-dimensional isotropic Heisenberg models*,
Physical Review Letters **17** (1966) 1133 (cit. on p. 166).

[140] P. C. Hohenberg, *Existence of Long-Range Order in One and Two Dimensions*,
Physical Review **158** (1967) 158 (cit. on p. 166).

[141] V. L Berezinskii,
Destruction of long-range order in one-dimensional and two-dimensional systems possessing a continuous symmetry group. II. Quantum systems,
Soviet Physics JETP **34** (1972) 610 (cit. on p. 166).

[142] J. M. Kosterlitz and D. J. Thouless,
Ordering, metastability and phase-transitions in 2 dimensional systems,
J. Phys. C **6** (1973) (cit. on p. 166).

[143] D. J. Bishop and J. D Reppy,
Study of the superfluid transition in two-dimensional 4 He films,
Physical Review Letters **40** (1978) 1727 (cit. on p. 166).

[144] D. J. Resnick et al.,
Kosterlitz-Thouless transition in proximity-coupled superconducting arrays,
Physical Review Letters **47** (1981) 1542 (cit. on p. 166).

[145] Z. Hadzibabic et al.,
Berezinskii – Kosterlitz – Thouless crossover in a trapped atomic gas,
Nature **441** (2006) 1118 (cit. on p. 166).

[146] L. Salasnich, *Goldstone and Higgs Hydrodynamics in the BCS–BEC Crossover*,
Condensed Matter **2** (2017) 22 (cit. on p. 166).

[147] S. A. Weidinger and W Zwerger, *Higgs Mode and Magnon Interactions in 2D Quantum Antiferromagnets from Raman Scattering*, Eur. Phys. J. B **88** (2015) 237 (cit. on p. 166).

[148] T. Hong et al., *Higgs amplitude mode in a two-dimensional quantum antiferromagnet near the quantum critical point*, Nature Physics **13** (2017) 638 (cit. on p. 166).

[149] M. W. Zwierlein et al., *Fermionic Superfluidity with Imbalanced Spin Populations*, Scence **311** (2006) 492 (cit. on p. 166).

[150] Y.-i. Shin et al.,
Phase diagram of a two-component Fermi gas with resonant interactions,
Nature **451** (2008) 689 (cit. on p. 166).

[151] A. L. Gaunt et al., *Bose-Einstein Condensation of Atoms in a Uniform Potential*, Physical Review Letters **200406** (2013) 1 (cit. on p. 167).

[152] B. Mukherjee et al., *Homogeneous Atomic Fermi Gases*,
Physical Review Letters **118** (2017) 123401 (cit. on p. 167).

Acknowledgements

Als allererstes möchte ich mich bei Professor Dr. Michael Köhl bedanken, dass ich dieses wunderbare Experiment aufbauen konnte. Danke dafür, dass ich viel freie Hand hatte, das Design und deren Umsetzung selbstständig realisieren zu könnten. Danke für die vielen anregenden Diskussionsrunden und die Hilfe beim Aufbau des Vakuum- und Lasersystems.

Als nächstes möchte ich mich beim "Humphryteam" bedanken, bei Timothy Harrison für das gemeinsame Aufbauen und Debuggen des Systems, bei Dr. Kuiyi Gao, der technische Expertise und sehr viel gute Laune mitgebracht hat und bei unserem neuen Doktoranden Martin Link, der mit Sicherheit das Experiment erfolgreich in die Zukunft führen wird. Außerdem haben einige Bachelor-, Master-, und Hilfsstudenten mit kleinen aber durchaus wichtigen Projekten unser Experiment voran getrieben, wie Andreas Kell, Till Leuteritz, Justas Andrijauskas, Maximilian Zawierucha und Christoph Linse.

Dem alten und neuen "Fermiteam" von nebenan, das uns immer mit Rat und Tat beiseitestand, mit Dr. Ferdinand Brennecke, Dr. Daniel Perot, Dr. Luke Miller, Dr. Eugenio Cocchi, Jan Drewes, Johanna Bohn, Marcell Gall, Jeffrey Chan und Nicola Wurz möchte ich ebenfalls danken.

Des Weiteren möchte ich mich bei allen "alten" und "neuen" Gruppenmitgliedern bedanken, die für alle möglichen Fragen jeder Zeit offen waren und auch immer mal wieder eine Runde Tischfußball mitgespielt haben wie, Dr. Hendrik Meyer, Dr. Tim Ballance, Dr. Lothar Ratschnacher, Dr. Matthias Steiner, Dr. Leonardo Carcagni, Dr. Jonathan Silver, Kilian Kluge, Thorsten Langerfeld und Pascal Kobel.

Ohne Akos Hoffman hätten einige Elektronikprojekte ewig gedauert. Vielen Dank für die schnelle und kompetente Umsetzung und auch für die Hilfe in manch brenzlichen Situationen (Natriumentsorgung).

Ein ganz besonders großer Dank geht auch an die gute Seele unserer Gruppe, Tina

Naggert, die uns nicht nur den Rücken in organisatorischen Sachen frei hält, sondern auch immer ein offenes Ohr für uns hat.

Auch wäre die Umsetzung dieses Experiments ohne die technische Expertise der Feinmechanik Werkstatt des Physikalischen Instituts unter Leitung von Herrn Christen nicht möglich gewesen. Vielen Dank!

Während meines Studiums und der Doktorarbeit haben mich viele Freunde unterstützt, wie Jojo, Valli, Susanne, Lotte, Thomas, Karla, Maren und noch viele mehr. Danke an euch!

Der größte Dank geht allerdings an meine Eltern, an meinen Vater, der erheblichen Anteil daran hatte, dass ich Physikerin geworden bin und an meine Mutter. Auf Ihre Unterstützung konnte ich mich während des Studiums und der Doktorarbeit immer verlassen. Und natürlich danke ich meiner Schwester Tanja, die sich sehr viel Zeit genommen hat diese Arbeit Korrektur zu lesen.